Università di Genova

ISTITUTO ITALIANO DI TECNOLOGIA
SMART MATERIALS

PhD Thesis

Porous Materials for Multicomponent Oily Wastewater Purification: Detection, Removal and Recovery of Contaminants

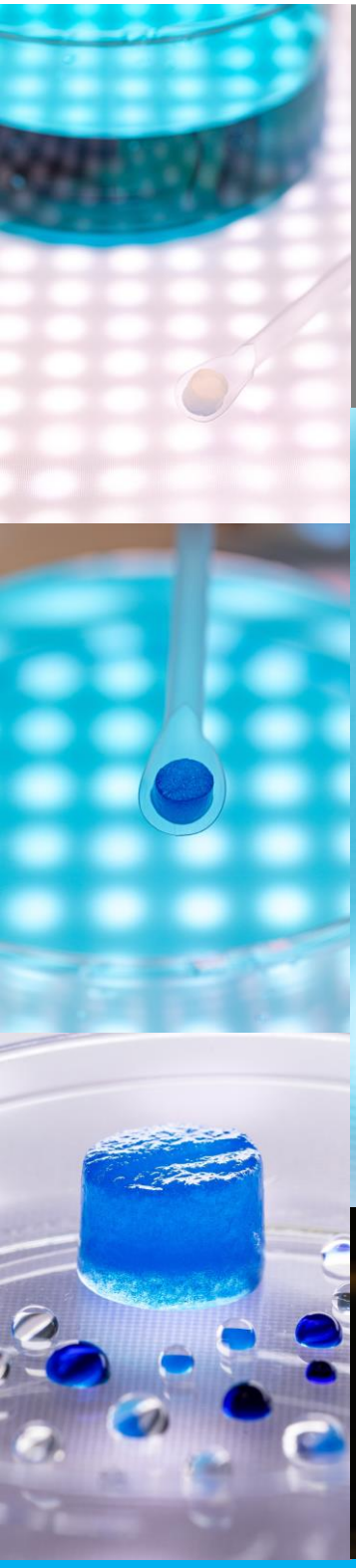

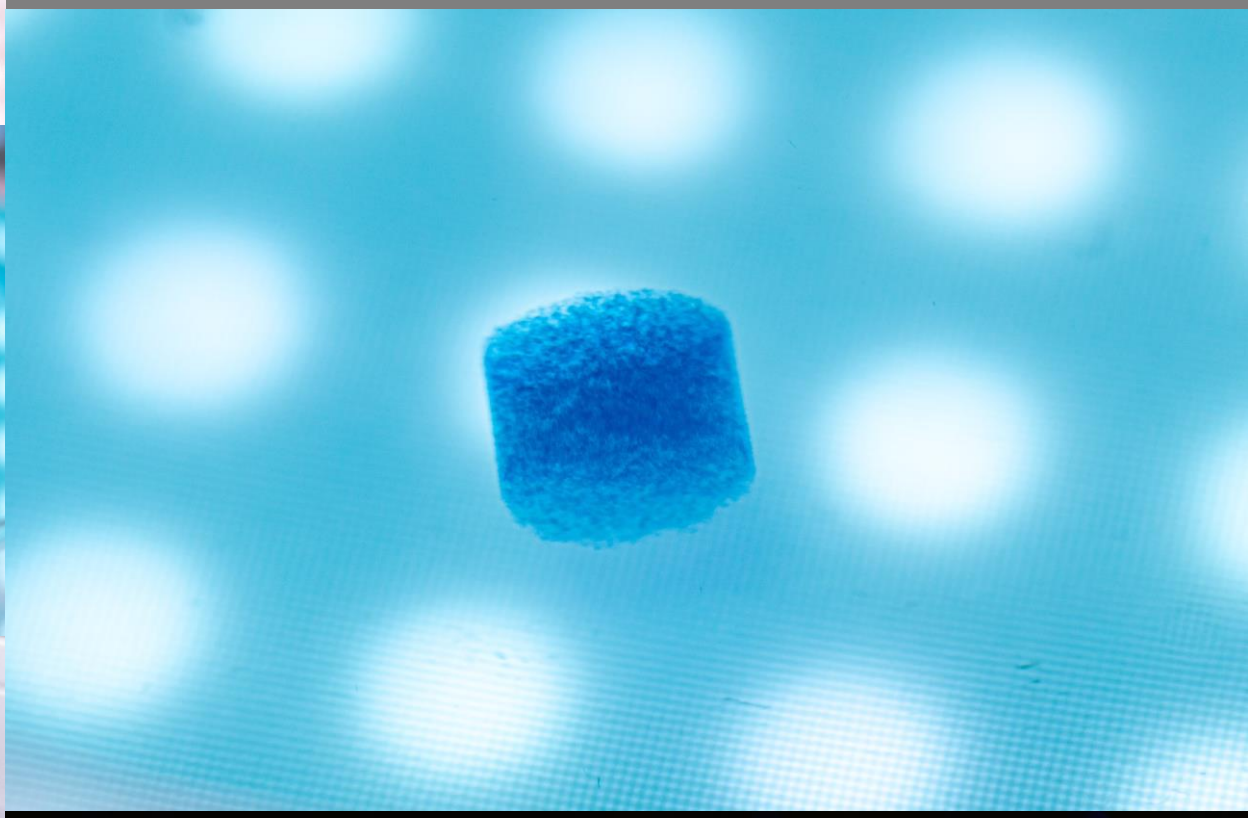

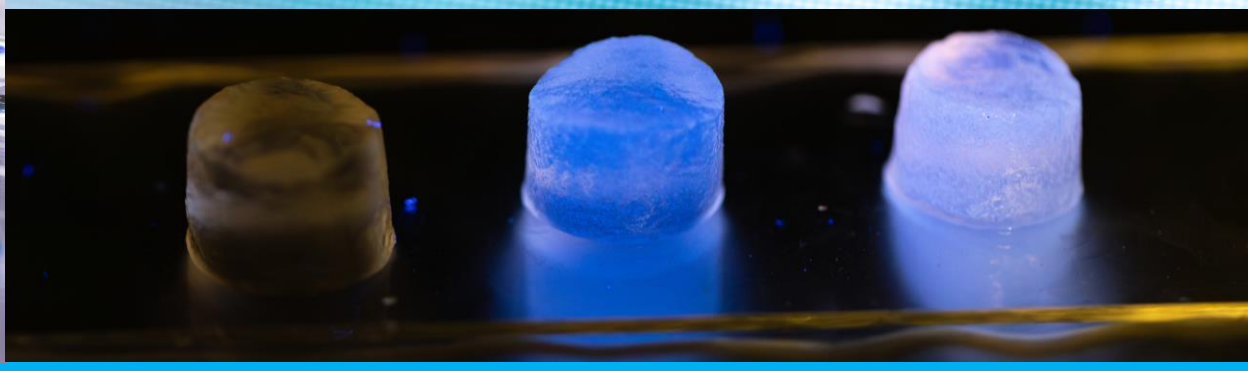

Katarzyna Dziza

University of Genoa, DIBRIS

Affiliation: Italian Institute of Technology, Smart Materials, Genoa

2024

POROUS MATERIALS FOR MULTICOMPONENT OILY WASTEWATER PURIFICATION: DETECTION, REMOVAL AND RECOVERY OF CONTAMINANTS

Katarzyna Adela Dziza

M. Eng. in Materials Engineering

S5089910

Tutors:

Dr. Despina Fragouli

Dr. Athanassia Athanassiou

Cycle XXXVI (2020-2023)

Ph.D. Program in Bioengineering and Robotics

Curriculum: Bionanotechnologies

Abstract

Studies on materials for water treatment and quality monitoring are usually limited to single functions and/or energy-consuming purification processes. This PhD thesis reports the development of a reusable and multifunctional porous material for the detection, removal and recovery of contaminants though gravity-driven filtration. To this aim, poly(sodium) acrylate (PSA) based nanocomposite cryogels containing a functional nanofiller, namely graphitic carbon nitride nanosheets (CNNs), were developed. The obtained PSA/CNN cryogels present appropriate properties for the single-step purification of multicomponent oily wastewater, for the detection of mercury (Hg^{2+}) ions, and for the photodegradation of the sorbed organic pollutants under daylight irradiation. The nanocomposite cryogels were fabricated via cryopolymerization of a mixture of PSA and CNNs, with the CNNs content optimized towards the different functions. Although the tested CNNs concentrations (0.5-3% w/w with respect to the monomer) do not significantly affect the morphology, swelling, or wetting, as well as the mechanical properties of the cryogels, they do influence their optical properties, rendering the cryogels fluorescent and photocatalytically active.

In the filtration process, the purification is mainly attributed to the PSA matrix, which exhibits underwater superoleophobicity, allowing for the water-oil separation, and contains the appropriate functional groups for the effective adsorption of the methylene blue (MB) cationic dye, through electrostatic interactions, and of the Hg^{2+} ions, through Na^{+}-Hg^{2+} ion exchange. We prove that the PSA/CNN cryogel can efficiently and rapidly clean oily wastewater, and its excellent performance is

maintained after diverse filtration cycles, whereas the co-presence of Hg^{2+} ions, oil and MB does not affect the separation efficiencies of any of the pollutants. The sensing properties of the PSA/CNN cryogels are attributed to the CNNs' fluorescence quenching phenomenon occurring upon interaction with the Hg^{2+} ions. Through the optimization of the CNNs concentration within the cryogel, sufficiently low amounts of Hg^{2+} ions can be detected upon the gravity-driven filtration of the wastewater and the subsequent fluorescence intensity evolution monitoring. The sorbed Hg^{2+} ions can be desorbed from the nanocomposite cryogel through a pH-responsive mechanism, and the regenerated cryogel maintains its excellent Hg^{2+} ions separation performance in diverse sorption-desorption cycles. Finally, the photocatalytic self-cleaning property of the composite cryogels, attributed to the CNNs' semiconductive properties, enables it to be regenerated through the degradation of the sorbed organic dye upon exposure to the visible light irradiation for reuse in multiple filtration cycles.

Overall, the herein presented work opens an ample space for the development of multifunctional materials for the cost and energy-efficient integrated water treatment and quality monitoring, as well as for the recovery of the trapped contaminants and the regeneration of the spent filters, going towards a greener alternative to the conventionally used sophisticated and secondary-pollution-causing processes related to water protection.

Table of Contents

List of Figures

List of Tables

List of Abbreviations

ABBREVIATION	MEANING
AAS	atomic absorption spectroscopy
AFS	atomic fluorescence spectroscopy
APS	ammonium persulfate
ATR	attenuated total reflection
BOD5	biochemical oxygen demand
CN	carbon nitride
CNN (CNNs)	graphitic carbon nitride nanosheets
Cu^{2+}	copper (II) ions
$CuCl_2$	copper (II) chloride
FTIR	Fourier Transform Infrared
H_2O	water
Hg	mercury
Hg^{2+}	mercury (II) ions
$HgCl_2$	mercury (II) chloride
HPLC	high-performance liquid chromatography
ICP	inductively coupled plasma
ICP-MS	inductively coupled plasma-mass spectrometry
ICP-AES	inductively coupled plasma-atomic emission spectrometry
ICP-OES	inductively coupled plasma-optical emission spectroscopy
LDH	layered double hydroxide
LIBS	laser induced breakdown spectrometry

LOD	limit of detection
MB	methylene blue
MBA	*N,N'*-methylenebis(acrylamide)
MOF	metal-organic framewroks
NAA	neutron activation analysis
NaOH	sodium hydroxide
NIR	near-infrared
PAH	polycyclic aromatic hydrocarbon
PB	parallel beam
Pb^{2+}	lead (II) ions
$Pb(NO_3)_2$	lead (II) nitrate
PCB	polychlorinated biphenyl
PDMS	polydimethylsiloxane
PES	polyethersulfone
PFAS	per- or poly-fluoroalkyl substances
PSA	poly(sodium acrylate)
PVDF	Polyvinylidene fluoride
RPM	revolutions per minute
SA	sodium acrylate
SAP	superabsorbent polymer
SB oil	soybean oil
SI oil	silicone oil
SDG	Sustainable Development Goal
SEM	scanning electron microscope/y

TEM	trasmission electron microscopy
TEMED	tetramethylethylenedi-amine
UFLP	unfrozen liquid microphase
UOCA	underwater oil contact angle
USA	United States of America
UV	ultraviolet
Vis	visible
XPS	X-ray photoelectron spectroscopy
XRD	X-ray diffraction
XRF	X-ray fluorescence

Statement of Original Authorship

The work contained in this thesis has not been previously submitted to meet requirements for an award at this or any other higher education institution. To the best of my knowledge and belief, the thesis contains no material previously published or written by another person except where due reference is made.

Signature:

Date: 06/01/2024

PREFACE

The 2030 Agenda for Sustainable Development, introduced by the United Nations, sets a series of challenging goals in the improvement of the human health and wildlife protection, with water security management being associated with the majority of the targets, considering that 71% of the Earth's surface is covered by water. SDG6 ("Clean water and sanitation"), as well as SDG14 ("Life below water") are specifically focused on the water sector, and the main motivation of the herein presented thesis is to contribute to these collective initiatives, through the development of smart multifunctional materials for the integration of processes related to wastewater treatment. Indeed, in the era of the environmental crisis we have been facing, and of the fast-paced urbanization and global industrialization, the water usage is constantly increasing by 1% annually since the 1980s[1], together with the water pollution. Therefore, it is of utmost importance to work on the continuous improvement of the technologies used for water treatment and quality monitoring. As a matter of fact, although well-established methods and protocols exist in the field, they suffer from complexity, as well as from high energy consumption and cost, making them unavailable to the great part of the developing countries. This is a serious limitation in managing the problem, taking into account that high contamination of water bodies is usually found in the low-income areas[2–4]. Moreover, ever-growing pollution and wastewater complexity compromise the conventional processes' efficiency, bringing along new challenges[5]. As indicated in the United Nations World Water Development Report 2019, this results in the alarming number of around one third of the population without access to safe potable water, and about 4 billion people suffering for at least

one month yearly from severe water shortage, occurring mainly at those locations that deal with the poor water quality[1,6]. In addition, migration of one billion people is expected to happen due to water-related problems by 2050[7].

Thus, there is an urgent need of simple, energy-saving, cost-effective, and at the same time highly efficient solutions for water remediation and security assurance, and the herein presented work dissertates the use of a novel superabsorbent polymer nanocomposite as a 3D filter with pollutant sensing and recovery properties, highlighting a potential of smart multifunctional composite materials design in tackling the above-discussed problems.

Chapter 1: Introduction

In this chapter the wastewater pollution types and sources, with the focus on certain pollutants of interest and the motivation for their choice in this study for wastewater modelling, as well as the widely used conventional water technologies are introduced. The recent advances in the field of materials for water treatment and pollutant quality monitoring and recovery are also summarized. Special attention is paid to multifunctional materials for the water sector-related applications, especially to those able to simultaneously act as water purifiers and pollutant indicators. Regarding the water treatment functionality, the discussion is focused on emerging materials for a single-step oily wastewater treatment. The motivation, objectives and the scope of this PhD thesis are also presented. The structure- and composition-properties design concept and the fabrication method of the developed material with the potential for integration of multicomponent oily wastewater treatment and pollutant detection and recovery, are introduced as well. The novelty of the work is indicated as well, based on the discussed literature review.

1.1 BACKGROUND

Water pollution is caused by a number of factors, such as continuous industrialization and urbanization of the world, climate change, exponential population growth giving rise to water demand increase, fast-paced life style and globalisation inducing mass food production, as well as poor sanitary conditions and awareness prevailing in developing and under-developed countries[1,5]. Moreover, ecological disasters, such as, for example, commonly occurring oil spills, and either accidental or intentional release of highly concentrated industrial effluents into water bodies, have a deleterious effect

on water safety[8–10]. Another source of disastrous water pollution nowadays are the ongoing conflicts, involving the use of chemical weapons, attacks on chemical factories, wastewater treatment plants, pipelines, or destruction of dams causing flooding of industrial infrastructure and bringing along hazardous substances into the environment at immense scale[11–14]. Globally, around 80% of industrial waste and litter is disposed into water sources, as estimated in the United Nations World Water Development Report 2017[15].

It is notable that the top source of water consumption and withdrawal worldwide is agriculture, and in the low-income countries about 90 % of water resources are used for farming[5,16]. This not only causes the pollution of water with harmful pesticides and fertilizers, but, in some cases, opens the possibility of the contaminated waters' entry into the farmlands. This may have a tremendous effect on food safety, directly associated with human health, especially in the light of the above-mentioned environmental disasters[17–20].

1.1.1 Water pollutants

A wide range of contaminants enters the water bodies, greatly depending on the source of their release. The pollution types fall into the following general categories, i.e. chemical, biological, radioactive, thermal, and solids and sediments[21]. In this work, we focus on the chemical contaminants, which can be classified into two main groups: organic and inorganic. Table 1.1 gathers a list of conventional chemical pollutants, i.e. those commonly involved in the routine monitoring of water/soil samples, with usually known toxic effects to human health, as well as to the environment, and set maximum safe concentration limits. The typical sources of their release into the waters are also presented.

It is important to mention that, even though different families of the conventional pollutants can be distinguished, in each family various substances of different chemical structures, resulting in different behaviours in the environment exist. Certain compounds belonging to a broad pollutant family are part of the general class of persistent pollutants, referring to toxic, bioaccumulative pollutants resistant to photolytic, chemical, and biological degradation[22,23]. This class consists mostly of heavy metals in case of the inorganic persistent pollutants, a wide range of organic compounds in case of the persistent organic pollutants (POPs)[24]. Some examples of the latter ones are azo dyes, phenols, certain pesticides, certain solvents, some insect killer/repellents or pharmaceuticals and personal care products (PPCPs) etc.[22,24–27]

POPs are usually categorized as part of the emerging pollutants group (EPs), described in the following text.

Table 1.1. Examples of organic and inorganic conventional water pollutants and their typical sources.

ORGANIC		**INORGANIC**	
Pollutant	Source	Pollutant	Source
dyes	textile, printing, paint, plastic, food, cosmetics, pharma industries[28]	heavy metals	metallurgical, power plant, electronics, coatings industry, mining[29], agricultural activities[30]
oils, emulsions	domestic sewage, oil spills, paint, food, refinery, cosmetics, mining, metallurgy, automobile, maritime industries, transport[31–34]	sulphates, phosphates, nitrates, ammonium salts	food industry[35], domestic sewage[36], agricultural activities[37], a broad range of chemical industries
surfactants, foaming agents	cosmetics, detergents, emulsifiers, food industries, fire extinguishers[38,39]	ammonia	agricultural activities[40], chemical industries[41]
bisphenol A and its analogues	synthetic polymers, thermal paper[42]	acids, bases	chemical industries, acid rains, analytical labs
solvents (halogenated and non-halogenated)	analytical labs, chemical, pharmaceutical industries[43–45]	halides	treated water, swimming pools[46], medical, domestic sewage [47]
aldehydes	chemical industries, fuel combustion, plastics degradation (by-) products[48]	pyrites	acid rock drainage[49]
petrochemicals	petrochemical refineries	fertilizers	agriculture and fertilizer industry
humic substances	decomposition and transformation of flora and fauna remainings[50]	metal(oid) oxyanions	a very broad range of sources[51]
		asbestos	construction industry

Emerging pollutants (EPs), also referred to as contaminants of emerging concern (CECs), are a broad class of chemical substances that, along with the conventional pollutants, causes threat to the water safety. In particular these are chemical compounds that are not currently (or have only recently been) regulated, and about which concerns exist regarding their impact on human health and the environment. These are not only new chemical pollutants and their biodegradation products/by-products, starting to recently appear in water bodies, but also all those that have been recently detected in the water bodies due to the enhancement of their concentration owed to their prolonged release, to the improvement of the detection processes or the development of new, alternative, monitoring technologies. Moreover, all pollutants with hitherto unidentified hazardous character, as well as those recently identified as toxic, mutagenic, cancerogenic, or endocrine-disruptive, with known or unknown maximum safe concentration limits, also fall into the EPs category. Though, most of these compounds/chemicals are not regulated by law and still remain studied. As very often the conventional wastewater purification methods are inefficient in the removal of EPs, they remain in the environment[5,52,53]. Examples of these pollutants and their sources are shown in Table 1.2.

Table 1.2. Examples of emerging pollutants (EPs)[5,22,24,25,54–56] and their use.

EMERGING POLLUTANTS

Pollutant	Use
POPs*:	
- *azo dyes*	textile, food, pharmaceutical industry[57–59]
- *Endosulfan and derivatives, dibenzofurans*	pesticides/insecticides[24]
- *Dichlorodiphenyltrichloro-ethane (DDT), Heptachlor, Mirex*	insect killer/repellents[24,27]
- *parabens*	cosmetics, pharmaceuticals, food commodities[60]
- *per- and polyfluoroalkyl substances* (*PFAS)*	very broad use[61]
- *phenols*	surfactants[27], polymer resins[62,63], antiseptics[47], pesticides[64]
- *polychlorinated biphenyls (PCBs)*	heat transfer agents, hydraulic fluids, transformers and metal treatment oils, pumps/turbines lubricants[65]
- *polycyclic aromatic hydrocarbons (PAHs)*	products of incomplete combustion of organic materials (e.g. coal, oil, petrol, wood)[66]
- *dioxins/dioxanes*	solvent stabilizers[67]
- *brominanted or organophosphate flame retardants*	plastics, wood, paper, textiles[68]
antibiotics, hormones, anti-diabetics	pharmaceuticals, poultry farms
UV filters	cosmetics
plasticizers	plastics industry
nano/microplastics	cosmetics, products of plastics degradation
artificial sweeteners	food additives

*persistent organic pollutants

1.1.2 Pollutants of subject matter

The focus of this PhD thesis is drawn on selected water pollutants of different chemical nature, namely water-insoluble compounds, such as oils, as well as water-soluble persistent inorganic and organic compounds.

Oils

Oils are one of the most dominant water pollutants. Oily wastewaters are produced not only by industries, offshore oil platforms and ports, but also by households, restaurants, and in such accidents, like oil spills, that become more frequent due to the constant industrialization[33,69]. As viscosity plays an important role in the behaviour of oils, especially during their removal from water, two representatives of high-viscosity and low-viscosity oils are considered in this PhD thesis, namely silicone (SI) oil (500 cSt), and soybean (SB) oil (~50 cSt)[70], respectively.

Persistent inorganic pollutants: heavy metal ions

Concerning the persistent inorganic pollutants, special focus in this PhD work is given to mercury ions (Hg^{2+}), as representative heavy metal ions. Due to the high resistance to degradation, heavy metal ions pose a serious risk for human health and the ecosystem, even if released into the environment in trace quantities[71].

Mercury (Hg) is ranked third of the most toxic elements to human health by the United States (US) Government Agency for Toxic Substances and Disease Registry (ATSDR)[72]. It naturally occurs in the Earth's crust and can be naturally released into the environment through volcanic activity or geological weathering or due to the anthropogenic activities. It is found in soils, rocks, ores, coil, water and oil. Its natural concentration is very low, but the human activities and climate change are continuously inducing its release into the environment at exceedingly high

concentrations, posing a serious threat to the humans and the nature[73]. High-temperature processes, such as combustion in crematories, of municipal and medical waste, sewage sludge, and especially of fossil fuels, as well as the non-ferrous metal smelting, cement and lime production are the main sources of anthropogenic Hg emissions[74,75]. It is also released by a broad range of industries, as well as due to activities, such as ore mining, and the use of pesticides in farming[76–79].

Hg occurs in various forms, such as organic, inorganic, and elemental mercury, which differ in levels of toxicity and exposure pathways. Each of them has different effects on health and requires specifically adapted countermeasures to avoid its exposure in the environment[72].

Hg in general is considered the most toxic heavy metal, mainly due to its capability to be converted into a highly poisonous and cancerogenic organic form, namely monomethyl mercury, produced from its inorganic forms by aquatic bacteria once discharged into nature[80–82]. It is the most frequent form of human exposure to Hg, occurring mostly through aquatic and terrestrial food chains (fish, seafood, fish-consuming animals), due to its structural properties that enable easy bioaccumulation in the fatty tissues of many living organisms[72].

Moreover, human activities enhance mercury methylation by mobilizing the naturally occurring forms, or remobilizing previously emitted mercury. For example, the extensive use of fertilizers causes the acidification of soil, which increases the availability of the heavy metals naturally existing in the ground. Moreover, fertilizers themselves are also a source of heavy metals[83]. Thus, the agricultural activities, which are the top source of wastewater production, as mentioned above in this section, greatly contribute to the contamination of water bodies with heavy metals, including the most toxic monomethyl mercury, one of the main pollutants of concern.

Elemental mercury (Hg^0), also called metallic mercury, occurs in nature and it is mined in the form of mercuric sulphide from cinnabar ore through high temperature treatment which causes its release through vaporization. The cooled vapors form the liquid metal mercury are used for the production of thermometers, electrical parts, dental fillings, as well as sodium hydroxide and chlorine gas[72].

Moreover, small-scale and artisanal gold mining are the source of almost half of the anthropogenic mercury annual emissions globally because of the use of elemental mercury amalgamation to separate gold from the ore. In particular, Hg vapour is oxidized to inorganic mercury (Hg^{2+}) once emitted by the miner or mineral processor into the atmosphere, where it stays for even two years, being distributed across the globe before depositing into water in the form of sediments[84].

Inorganic Hg compounds include mercury chloride, mercury acetate and sulphur sulphide[72]. Coal-fired power plants emit both elemental and inorganic Hg, contributing to more than one-third of global anthropogenic mercury emissions[74]. Direct exposure to the inorganic form of Hg is usually occupational and causes a range of adverse effects on human health[72].

The long range transport (LRT) properties of Hg lead to its presence even in the remote arctic regions, where no atmospheric release occurs[72,85,86]. Its bioaccumulation and biomagnification throughout the food chain, as well as the LRT properties, causes a serious danger to humans, especially in places depending on coil resources, gold mining, and agriculture, which mostly coincide with the impoverished areas[87]. Hence, novel cheap and energy-saving methods of mercury removal from wastewaters and its detection are indispensable in the prevention and efficient management of the alarming Hg pollution problem.

Persistent organic pollutants: azo dyes

In this PhD work methylene blue (MB) is considered as a representative component of the persistent organic pollutants. MB is one of the most widely used organic dyes in textile industry, which belongs to the largest polluters of water globally[88]. At low dosage it also finds medicinal applications, but it is toxic, mutagenic and cancerogenic to humans through the uncontrolled intake via contaminated water, and causes the attenuation of the sunlight transmittance, negatively affecting the aquatic ecosystem[89]. MB is classified as an azo dye, belonging to the category of POPs, and because of its complex aromatic structure (Figure 1.1) typical of this dye family, it is recalcitrant to degradation by traditional biological treatment processes[90].

According to data from 2003, it is estimated that 10–15% of produced dyes is lost and discarded as wastewater[91]. Taking into account that azo dyes, highly persistent in the environment due to their non-biodegradability, represent the most commonly used group of dyes in textile industry, such a scale of losses raises serious concern and can have adverse effects on the human health and the ecosystem for a long period of time. As the major part of textile industry is settled in developing or under-developed areas of the world, novel, cheap and energy-efficient wastewater remediation processes regarding this type of pollutants are urgently needed.

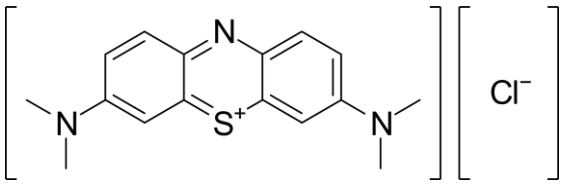

Figure 1.1. The chemical structure of methylene blue (MB).

In conclusion, considering that all the three discussed pollutant types are widely released into the water bodies, and that both MB and Hg^{2+} ions are highly persistent in the environment, they can likely be found together in various types of wastewaters. Hence, simulated wastewater composed of oil, as well as MB and $HgCl_2$ dissolved in water is used in the studies discussed in the following chapters.

1.1.3 Conventional water treatment technologies

Water treatment is typically composed of multiple steps, involving numerous processes and technologies that vary depending on the wastewater type. Industrial and municipal wastewaters purification is usually divided into preliminary, primary, secondary, and tertiary treatment processes[92].

Preliminary Treatment

The preliminary one is designed for the removal of larger materials and particles suspended in the wastewater, such as sand, grit, debris, garbage, other foreign materials, fecal matter, and oils, using coarse screens for their capturing. It involves sedimentation, also referred to as the clarification process, followed by coagulation and flocculation for further removal of the suspended materials[92,93].

Primary Treatment

The primary treatment aims at the preliminary removal of organic, inorganic, and biological pollutants before further refined processes are used, and involves both chemical and physical methods, such as fine screening, sedimentation, centrifugation, chemical precipitation, coagulation, flocculation, flotation, and microfiltration[93,94]. Typically c.ca. 25-50% of the incoming biochemical oxygen demand (BOD5), c.ca 50-70% of the total suspended solids, as well as c.ca 65% of oil and grease is reported

to be removed in the primary treatment. Nonetheless, dissolved constituents or colloids are not efficiently separated in this step[92].

Secondary Treatment

The secondary treatment processes are most commonly used for the removal of organic pollutants, both those occurring in the form of dissolved matter and those organic suspended solids and colloids which did not undergo successful removal in the primary treatment. The secondary processes consist of aerobic and anaerobic treatment utilizing the enzymatically catalyzed metabolic activity of microorganisms, fungi, bacteria, yeasts, or algae in a controlled environment to destroy or convert the pollutants into simpler and safer substances. In case of the aerobic treatment the utilization of a compressor or blower providing continuous flow of oxygen is needed to produce carbon dioxide and biomass, while in the anaerobic process microorganisms convert the pollutants into biogas and biomass in the absence of oxygen. Even though the latter one is an energy-efficient process compared to the aerobic one, its main drawback is very high installation cost. The obtained biomass is removed by liquid-solid separation processes[92,94–96].

These biological treatment technologies used as secondary treatment are performed either as a fixed-film (using trickling filters, rotating biological contactors, membrane biofilm reactors, moving-bed biofilm reactors, or fluidized-bed reactors), or as an activated sludge process, and the latter one shows ability to treat even 10 times more wastewater per unit reactor volume. Thus, it is a widely used technique, but the operation costs are higher than those for the fixed-film one and the excess sludge formation is a serious problem. Treatment and disposal of the as-obtained sludge is one of the biggest challenges in the biological processes of wastewater treatment.

Moreover, it accounts for a significant part of the total operation cost of wastewater treatment plants[95,97].

Generally, the biological treatment of wastewater is a slow process, requiring a large area, which results in high capital and operation costs. Another demerit of the processes used in the secondary treatment is that they may lead to the formation of some unwanted microorganisms producing gases and bad odour[98,99].

Tertiary Treatment

The aim of tertiary processes is conversion of wastewater previously treated by primary and secondary processes into water with quality sufficient for the use for given target purposes, such as drinking, medicinal, industrial, or irrigation water[92,100]. Typically, the major part of dissolved inorganic pollutants is removed in the tertiary treatment. The commonly used tertiary treatment techniques are briefly introduced in the following text.

Chemical oxidation. This method is based on the introduction of an oxidizing agent into the wastewater, resulting in the destruction of the pollutant due to the structural modifications induced by electrons moving from the oxidant to the pollutant. The commonly used oxidants are oxygen, ozone, chlorine, chlorine dioxide, and permanganate. The traditional chemical oxidation processes lead to the formation of by-products, thus for their removal advanced chemical oxidation techniques involving the use of steam stripping or adsorption with activated carbon have been developed[94].

Crystallization and distillation/evaporation. In this technique, the wastewater is brought to its boiling temperature, vaporized and then the obtained steam is condensed resulting in pure water. The concentration of the pollutant separated as the result of the

distillation/evaporation process is gradually increased until its crystallization occurs[94].

Photocatalysis. The mechanism of this method is based on the use of light as a stimulator that enhances the mobility of electrons of a semiconducting material with an electronic structure resulting in photocatalytic activity. In particular, photons from a light source (typically UV light) are absorbed by the surface of a photocatalyst, and once a sufficient frequency of light is provided electrons from the valence band jump to the conduction band, generating free radicals able to undergo secondary reactions, such as reduction (e.g. of heavy metals) or oxidation, i.e. photodegradation (of organic compounds). The commonly used photocatalysts are titanium (IV) oxide (TiO_2), and zinc (II) oxide ZnO[94,101].

Ion Exchange. This method is based on the interchange of ions between an electrolytic solution and a polyelectrolyte solid phase with a high molecular weight, which does not undergo structural changes after the exchange. Typically porous microbeads with high specific surface area pre-saturated with non-toxic cations or anions are used. Polymer ion-exchange resins are the most commonly utilized ion exchangers, and sodium silicates, polystyrene sulfonic acid, zeolites, and acrylic or methacrylic resins are the most widely used ones[93,94,101]. The negatively charged resins are used for anion exchange and positively charged ones for cation interchange. Depending on their functional groups, the ion-exchange resins are classified as acidic or basic, and weak or strong exchangers, and based on these properties the resins may show selectivity towards given ions[93]. Ion exchange is a well-established conventional method for the removal of hardness from drinking water, but nowadays it is also the most frequently applied technique of heavy metal ions separation[93,94]. Ion-exchange resins are fixed in fluidized packed-bed configurations, and once they are saturated the reversibility of

the ion interchange allows for the regeneration by elution of the separated ions, which is especially advantageous in case of the entrapment of precious but toxic and secondary-pollution causing heavy metal ions enabling their recovery from the resin[94,101].

Chemical Precipitation. In this technique pollutants are removed in the form of sediments or precipitates, such as hydroxides, sulphides, or xanthiogenates. They are produced due to bonding of the pollutants with the precipitating agents, which can be chemical, e.g. calcium or sodium oxides, or biological, such as sulfate-reducing bacteria. This method involves filtration or centrifugation of the formed precipitates[101].

Electrochemical Methods. The major part of electrochemical methods use electricity as the main reactant initiating the treatment process[102]. This approach includes different techniques, such as electrocoagulation, electrooxidation, electroflotation, electrodialysis, and electro-Fenton process[101,103]. Electrocoagulation is based on the formation of coagulants in an electrocoagulation cell once the electric current passes through it. It can be used to substitute the traditional chemical coagulation process where chemicals have to be utilized. Electrooxidation functions depending on the mineralization of pollutants through the application of the current, which causes the release of free radicals forming hydroxyl radicals in water and attacking the chemically resistant organic pollutants and causing inactivation of bacteria. Electroflotation is a process used to remove lightweight suspended organic pollutant particles from water using the gas bubbles generated through water electrolysis and depending on the buoyancy of the as-treated pollutants[103]. Electrodialysis is an electrically-driven ion-exchange membrane process, where either cation or anionic membranes are used[93,94]. The electro-Fenton process is based on the oxidation of pollutants with the use of

electro-generated active hydroxyl radicals[103]. Other common electrochemical methods include electrosorption, electrodeposition, and electrodeionization[94].

Membrane Filtration. Numerous membrane-processing technologies are widely used as tertiary wastewater treatment for the removal of various pollutants of different origins[93]. They are classified into ultrafiltration, nanofiltration, reverse osmosis, forward osmosis, and the previously described electrodialysis[94,101]. Most of the membrane filtration technologies rely on pressure-driven processes that can be performed in two configurations, namely as a dead-end or a cross-flow filtration, with the second one giving higher decontamination efficiencies due to the recirculation and re-filtration of the permeate[101]. Ultrafiltration membranes have pore sizes in the range from 10 to 100 nm and are used for the removal of bacteria, pigments, and certain natural organic colloids, but the pore size is larger than the hydrated radius of the heavy metal ions, making such membranes unsuitable for the separation of these pollutants. Nanofiltration membranes have pore size below 10 nm. Thus, they are typically used for the removal of most heavy metals and water hardeners[94]. Reverse osmosis is a process using suitable semipermeable membranes for the separation of pollutants through the application of hydrostatic pressure against the osmotic pressure, which is generated by the differences in the chemical potential of the solvent. Reverse osmosis is effective in the removal of most ions, including heavy metal ones, colloidal matter from inorganic solutions, and colour, nitrates, as well as biotic-factor-like bacteria. Thus, it is widely used for the production of potable water and for domestic wastewater treatment, as well as for the treatment of wastewaters from aerospace, food, oil, gas, galvanic, dairy, pulp and paper and power plants. Moreover, it is the most widely used water desalination technology[93,94]. Forward osmosis is a non-pressure driven membrane filtration process and it is based on osmosis, i.e. on the separation of two

salt solutions with different concentrations through a semipermeable membrane, which allows for the naturally occurring phenomenon of diffusion of the solute from the solution with lower concentration to the solution with higher concentration. This way the pollutants are segregated on one side of the membrane, and pure water is separated on the other side. This technique can be used for the separation of both organic and inorganic contaminants (including heavy metal ions), with the suitable membrane selection[101].

The most commonly used commercial membranes are synthetic polymer ones, such as polyvinylidene floride, polyamide, cellulose acetate, polyethersulfone, polysulfone, polyacrylonitrile, and poly(acrylonitrile)-poly(vinyl chloride) copolymers[101,104].

Adsorption. Due to numerous advantages over the above-described tertiary treatment processes, adsorption is often the purification method of choice. Its main merits are the low cost, no energy consumption, simple design, easy operation, high removal efficiency from dilute solutions, comparatively less complex process, as well as eco-friendliness compared to the chemical/physical methods. The other important advantage of the adsorption method is the reusability, as the adsorbents can be recycled through appropriate desorption activities[105]. The main commercially used adsorbent for wastewater treatment is activated carbon. Nevertheless, due to its extremely high cost, it is still not widely used, and other sorbent materials have been recently applied. Examples include siliceous materials (e.g. perlite, silica beads, alunite), zeolites, clay materials (e.g. bentonite, kaolinite), industrial waste products (such as waste carbon slurries, or metal hydroxide sludge), or agricultural wastes (e.g. coconut shell, rice husk etc.)[106]. However, as the specific area is one of the most important factors in adsorption, new technologies with the use of adsorbents with high chemical activity and higher surface/volume ratio are rapidly emerging. Thus, an extensive amount of

nanoparticle-based sorbents is nowadays appearing but their applications in the wastewater treatment are still limited, as the adsorption technique is a relatively new field recently attracting increased attention[94].

The disadvantages of the above-described tertiary processes are gathered in Table 1.3.

Table 1.3. Conventional tertiary methods of wastewater purification and their drawbacks[93,94,101,107].

Treatment methods	Drawbacks
Chemical oxidation	- high chemicals consumption - requires involvement of adsorption process for the removal of the formed toxic by-products
Chemical precipitation	- high chemicals consumption and secondary pollution (sludge) creation - unsuitability for diluted samples treatment - requires energy-consuming centrifugation or filtration for the removal of the precipitate - high operation cost
Crystallization and distillation/evaporation	- high energy consumption - high operation cost
Photocatalysis	- instability of photocatalysts (rapid recombination of electrons and holes) - low specific surface area limiting the removal efficiency - by-products formation
Ion exchange	- rapid saturation and bead fouling - ineffective for certain pollutants removal (e.g. drugs, dispersed dyes) - compulsory pre-treatment (e.g. the optimal metal ion concentration must be in the range of 10 to 100 mg L^{-1}) - relatively high operation cost
Electrochemical methods	- high energy consumption and high operation costs
Pressure-driven membrane filtration	- high power consumption and operation cost - membrane fouling - low permeation flux
Forward osmosis	- rapid clogging requiring costly membrane regeneration - complex selection process of adequate membranes - possible leakages
Adsorption	- high cost of commonly used sorbents and of the regeneration process - decreased efficiency with the repeated use

Dyes and heavy metals removal

The conventional methods such as biological treatment, coagulation, ozone oxidation, photocatalytic oxidation, Fenton oxidation, and adsorption are used for the removal of organic dyes from wastewater[26,108]. Even though biological and physico-chemical treatments shows high efficiency in the removal of dyes, they suffer from a range of disadvantages, as previously explained. Fenton oxidation is one of the most advanced oxidation processes, where hydroxyl radicals are produced and lead to the oxidation of Fe^{2+} to Fe^{3+} through the formation of ferric hydro-complexes, which contemporaneously act as a coagulant and an oxidant. The advantage of this process is high efficiency and that compared to the traditionally used aluminium salts, iron salts form heavier flocs and are less harmful in case of the coagulant overdose. However, this process results in a yellowish colour of the treated wastewater[108].

In case of heavy metal ions removal the conventional methods include ion exchange, membrane filtration (especially reverse osmosis), chemical precipitation, flocculation, electrodialysis and other electrochemical technologies, as well as evaporation, or adsorption[101,105]. The most commonly used heavy metal ions removal method is the ion exchange, and in case of lower concentrations membrane filtration is typically employed[93]. In case of very high concentrations of the heavy metal ions, tertiary processes are not effective alone, and primary treatment processes, such as microfiltration, coagulation, flocculation, or chemical precipitation have to be firstly applied. This way significant amounts of heavy metals ions can be removed by these cost-effective processes[109].

Concluding, due to the serious limitations of the other conventional wastewater treatment methods, adsorption is becoming the most promising process for the removal

of both organic dyes and heavy metal ions from wastewater. Even though this method brings great potential for tackling different problems associated with the other used processes, the high cost of the hitherto developed sorbents and the loss of efficiency with the repeated use are the main drawbacks, disabling the complete substitution of the complicated, energy consuming, secondary-pollution creating and even more costly conventional processes with adsorption[90,105].

Oils removal

An efficient single-step purification of multicomponent oily wastewater remains a challenge. The commonly utilized water-oil separation methods are based on the pressure-driven membrane separation technologies, such as ultrafiltration, microfiltration or reverse osmosis[110]. The semi-hydrophobic character of the commercial membranes used for such scope hinders their simultaneous application in water-soluble compounds and oil separation, while their short lifetime, due to pore blockage by oils and to surface fouling by hydrophobic pollutants[110–112], makes quite challenging the filtration process. In turn, the use of hydrophilic membranes gives good performance towards the separation of different water-soluble pollutants, but suffers from surface fouling due to the oil cake layer formation on the membranes' surface[113,114].

1.1.4 Conventional heavy metals detection methods

As heavy metals pose a serious threat to humans and the ecosystem even at low concentrations, it is imperative to monitor its presence in the aquatic environment, as well as in the produced wastewaters, and in the post-purification steps of its removal process. In recent decades, several accurate methods have been developed, allowing for the detection of Hg concentrations as low as 1 $\mu g\,L^{-1}$ and 2 $\mu g\,L^{-1}$, fixed as the

concentration limits in drinking and mineral water in Europe and the USA, respectively. The most widely used detection methods include the inductively coupled plasma-mass spectrometry (ICP-MS), ICP-atomic emission spectrometry (ICP-AES), ICP-optical emission spectroscopy (ICP-OES), atomic absorption spectroscopy (AAS), atomic fluoresecence spectroscopy (AFS) , X-ray fluorescence (XRF), as well as neutron activation analysis (NAA), or laser induced breakdown spectrometry (LIBS), and electrochemical methods, such as potentiometric, amperometric, voltammetric, coulometric, impedance measurement and electrochemiluminescent techniques etc. Besides, many different high-performance liquid chromatography (HPLC) techniques are coupled with other ones, such as UV-visible spectrophotometry, gas chromatography, ion chromatography, isotope dilution or AAS[101,105,115]. Even though a vast group of heavy metals detection techniques of high accuracy and sensitivity are available, they exhibit significant drawbacks, as presented in Table 1.4.

Table 1.4. Conventional heavy metals detection methods and their drawbacks[101,116–119].

Detection methods	Drawbacks
ICP	- very high equipment and running cost - time-consuming sample preparation procedure involving high amounts of single-use consumables - secondary pollution from sample digestion with acids - ICP-MS: serious interference of some elements (e.g. K, Ca, Fe, Sa, S) - ICP-AES: large consumption of argon - ICP-OES: complexity in analysis due to spectral interference - real-time detection not possible
AAS	- medium overall cost - non-user-friendly operation requiring lamp source change for each element analysed - real-time detection not possible
AFS	- medium overall cost - scattered light interference - real-time detection not possible
XRF	- medium overall cost - great sensitivity requiring careful sample preparation
NAA	- the use of nuclear reactors, their accessibility and very high cost
electrochemical methods	- often require coupling with electrodes adapted to the analysed element - poor reproducibility and stability - electrode fouling
LIBS	- equipment cost - low signal of liquid samples - often requires sample preparation (solidification) disabling real-time detection
HPLC coupled with other techniques	- high equipment cost - complexity of analysis procedure - use of toxic solvents - time-consuming -real-time detection not possible

To sum up, all of the commonly used heavy metals detection methods suffer from serious limitations, being mainly the use of toxic reagents, complexity of the procedure, time and energy consumption, and the demand a well-equipped lab and highly skilled staff who can perform the analysis. Therefore, it is essential to direct the research towards alternative Hg detection methods development, with the aim of the process simplification, user-friendliness, suitability for in-situ and on-time measurements, as well as cost-cutting and energy and toxic reagents consumption reduction, in order to not only improve their eco-friendliness but also the accessibility, especially in the low-income regions.

1.1.5 Conclusions

In conclusion, due to the fast pace of global industrialization, and ecological disasters, the release of harmful compounds into the aquatic environment is either identified or regulated by law in delay. The list of water contaminants keeps rising, affecting the water treatment and quality monitoring processes efficiency, but also the overall energy consumption, employing additional purification and detection steps, which makes these already complex procedures even more complicated and troublesome. Thus, the integration of these processes into a single-step action for an efficient water treatment is of utmost importance. Taking into account the hitherto problems of many regions worldwide lacking the access to the conventional water technologies due to the economic constraints, it is fundamental to research ways of simplifying the purification processes through cost-effective and energy-saving approaches, starting from the simultaneous oil-water separation and the removal of the most toxic contaminants with a known effect on human health and the ecosystem's balance. This may pave the way for the development of an advanced, simplified water purification and quality monitoring process.

On the top, considering the high exposure to Hg of habitants of the impoverished regions, it is of paramount importance to be able to monitor the presence of Hg using low-cost, and easy to use detection techniques. Another important problem is the non-eco-friendly character of the commonly used heavy metals detection methods, especially in case of the water quality monitoring procedures, being typically a source of secondary pollution with the often used toxic reagents.

Thus, in this PhD thesis the development of a multifunctional purification and sensing system is envisioned and researched as a potential solution to overcome the discussed limits of the current state of the water treatment and quality monitoring processes. As previously highlighted, it is important to conduct studies on water-protection related processes for multicomponent oily mixtures, rather than only on the isolated pollutants, which can give a clearer insight regarding the proposed solution's applicability in the real-case scenarios. Moreover, as a single-step effective purification of multicomponent oily wastewater still remains a challenge, it is of utmost importance to develop a solution to this problem.

1.2 STATE-OF-THE-ART

Continuous efforts are made in order to develop materials for alternative water treatment, quality monitoring and pollutant recovery processes, which could replace, or improve some of the expensive, complicated, non-efficient and secondary-pollution-causing currently used technologies.

1.2.1 Emerging materials for water treatment

Different types of inorganic and organic materials for water treatment have been developed, but polymer materials are considered the most cost-effective and suitable due to their adjustable chemical structure, facile processability, and low cost[120,121].

Among them, porous polymer foams and 2D membranes receive significant attention[122–127].

Nanomaterials are also an emerging group of materials extensively investigated in terms of their suitability for water treatment applications, which is mainly owed to their large specific surface area and high reactivity, enhancing fast and highly efficient separation of pollutants from wastewater[128–130].

Materials for oil-water separation

In the field of oil-water separation enormous attention has been paid to the development of materials targeting oil adsorption. Examples include oil-sorbing sponges made of surface-modified polyurethane or polysiloxane- and organosilane-coated commercial sponges, such as polydimethylsiloxane (PDMS) or melamine ones[131–136]. Such types of materials are especially important for emergency treatments of waters in case of oil spills. Explicitly for such purpose magnetic polymer-based foams are also developed[137,138].

Advanced 2D polymer membranes for oil-water separation prepared through electrospinning, template synthesis, or coating of commercial membranes are also developed. In this field, attention is mostly focused on oil-removing membranes with hydrophobic/oleophilic character, but the oil penetrating through the pores of the material usually causes clogging, and a growing number of studies on water-removing membranes displaying hydrophilic/oleophobic features is now performed[79].

Another type of materials for oil-water separation through oil sorption recently attracting attention are aerogels and xerogels, which are solid materials with a nanoporous open structure, obtained through sol-gel processing and the subsequent drying, in supercritical and in ambient conditions, respectively. Their low-density,

high porosity and large surface area, and strong rigidity make them attractive candidates for such applications[139–141]. Several studies have been recently reported on synthetic and bio-derived polymeric, carbon nanotube, graphene, or biomass-based aerogels and xerogels for oil spills clean-up[135,141–143].

One of the main drawbacks of the developed oil-sorbing porous materials is their poor selectivity for oil and water, resulting in the simultaneous sorption of both phases, which greatly lowers their separation efficiency. For this reason, recently the studies focus on special wetting properties that enable oil sorption and water repellence. Thus, materials showing simultaneous hydrophobicity and oleophilicity are nowadays extensively researched[144,145]. Nonetheless, another disadvantage of oil sorbents is their challenging recycling. The oil-loaded materials are buried or burned, or in case of the fire-resistant sorbents the adsorbed oil is burnt, causing secondary pollution[144,146]. Hence, oil-repellent and water sorbing materials, i.e. hydrophilic and oleophobic materials are also broadly researched for oil-water separation applications different than oil spills removal[114,144,147,148]. Nevertheless, pore blockage, as well as the surface fouling problem previously addressed in Section 1.1.3, are serious limitations in such materials' performance. A promising approach to overcome these drawbacks is the implementation of superwetting materials, which has recently become a hot topic in the oil-water separation field, and will be further discussed in Section 1.2.4[144,149].

Materials for water-soluble pollutants adsorption

Among different water treatment processes, adsorption is considered the most suitable method for an effective removal of low concentrations of organic and inorganic compounds from groundwater, drinking water, and wastewater due to its cost-effectiveness and reliable purification performance. Moreover, very often adsorption

can be reversed, which allows for the regeneration of the sorbent and its extended reuse, limiting the problems of secondary pollution[107].

One of the most important features of sorbent materials is their surface chemistry and surface charge, playing a crucial role in the sorption mechanism, which may occur by various physical or chemical interactions, and in the separation efficiency towards different pollutant types. Besides, another very important property of materials for aqueous pollutants adsorption is hydrophilicity, enabling water permeation and transport of the pollutants through the adsorbent's pores, which leads to their interaction with the material.

There is a large number of studies on hydrophilic 2D membranes for efficient aqueous pollutants adsorption, especially on electrospun nanofibers, and on hydrophilic polymer coatings for hydrophobic electrospun mats or commercial polymer membranes, such as polyethersulfone (PES) or polyvinylidene fluoride (PVDF)[150–154,154].

Recently, superhydrophilic and highly absorbent polymer materials, namely hydrogels are a subject of comprehensive research in the field[155,156]. Their structure consists of a 3D network of cross-linked polymer functional chains with characteristic free space in between the macromolecules, available to interact with water, which allows aqueous solvents to easily penetrate the polymer matrix, filling that space once the dry hydrogel comes in contact with the solvent[155]. Furthermore, hydrogel networks contain numerous active functional groups, which impart high chemical affinity to ions and organic molecules, inherent antibacterial properties, and the ability to embed nanomaterials[156–159]. Owing to such properties hydrogels have proven remarkably high adsorption capacities towards aqueous pollutants and they are considered excellent

sorbents of organic and inorganic pollutants[160–162]. For example, there is an extensive amount of studies focused on the removal of dyes, antibiotics, and heavy metals by chitosan- or cellulose-based hydrogels (prepared as hydrophilic aerogels), pristine or with further enhanced sorption abilities by the embedded graphene oxide[163–166]. Similarly the development of hydrogels prepared in the form of xerogels is investigated for the adsorption of water-soluble pollutants, especially dyes and heavy metals[167–169].

Moreover, some hydrogels display outstandingly high water absorption capability of up to thousands time their original weight and they belong to a new class of superabsorbent polymer (SAP) materials, recently emerging in the water treatment field[170]. Synthetic SAPs are based on polyacrylic acid or polyacrylamide and they are the most widely used, whereas natural ones are based on polysaccharide, polypeptide, starch, cellulose, or chitosan, and hybrid semi-synthetic ones are recently developed by a combination of the two types[171–173]. Both synthetic and hybrid SAPs have shown outstanding adsorption capacities of heavy metal ions and cationic, as well as anionic dyes[174–179].

Another type of materials exhibiting high adsorption capacities towards a wide range of pollutants are the nanostructured ones, such as nanoparticles, nanoscale metal oxides, carbonaceous nanomaterials (e.g. activated carbon, graphene, graphitic carbon nitride, multi/single-walled carbon nanotubes, carbon quantum dots), dendrimers, and nanoscale biopolymers, nanozeolites, as well as the extensively investigated metal organic framework (MOF) and layered double hydroxide (LDH) nanoparticles[129,180–183]. Even though the nanostructured materials hold a great promise for the development of advanced water purification technologies, they also pose challenges, such as

difficult handling, low recovery efficiency causing secondary pollution, and non-economical regeneration, when used in the dispersion form[136,184]. For this reason, there is a large number of studies on magnetic nanoparticles which can be efficiently recovered from the treated wastewater, as well as on porous polymeric nanocomposite 2D and 3D adsorbents where nanostructured materials are embedded into a polymer matrix, which allows for their stabilization and easy handling[121,185–190,191].

1.2.2 Adsorbent regeneration methods

The secondary pollution caused by the spent adsorbent materials is another great problem to tackle in the field of water treatment. Thus, there is a growing number of research works on the development of recyclable adsorbents. Two primary methods of adsorbent regeneration are extensively researched, i.e. desorption and decomposition, with the second one receiving a continuously growing attention. A schematic illustration of the regeneration techniques used in adsorption processes is shown in Figure 1.2.

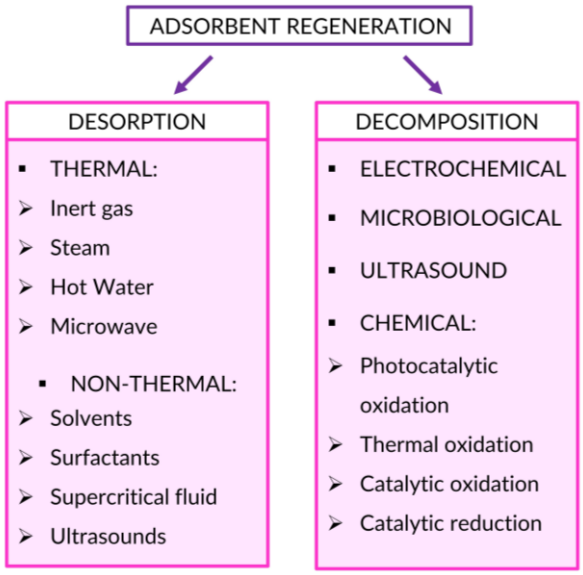

Figure 1.2. Regeneration techniques used in adsorption processes.

Regarding the desorption processes, an appropriate technique has to be adjusted to the type of the adsorbent and the adsorption mechanism. Thus, it is widely studied for different types of materials developed and types of pollutants used. Desorption is a process of detaching the adsorbed components from a solid surface[192]. This method of adsorbent regeneration suffers from certain drawbacks, i.e. in some cases it may affect the overall chemical stability of the adsorbent, and in case of the use of chemical desorption treatment, depending on the eluent type needed, it can be a source of pollution as well. Nevertheless, the chemical desorption has the advantage of being energy-safe and can be performed in-situ.

One of the desorption techniques of great interest is a pH-responsive desorption, where diluted acids or bases can be efficiently used in an eco-friendly way[193]. Nowadays, stimuli-responsive ion adsorbents with reversible ion adsorption/desorption capabilities attract a large number of researchers, with special attention paid to pH-responsive hydrogels which show great ion adsorption capacities and the desorption of heavy metal ions and dyes is typically studied[193–200]. Low pH may favour the desorption of metal cations or cationic organic dyes due to their strong competition with H^+ which causes the displacement and elution of the adsorbates. On the other hand, at high pH, due to the introduced negative charge, electrostatic attraction interactions are disturbed by the electrostatic repulsion, causing the adsorbate displacement[192].

In case of the decomposition methods of adsorbent regeneration, catalytic degradation receives immense interest, allowing for both the regeneration of the adsorbent and the efficient, eco-friendly degradation of the sorbed pollutant[201,202]. Photocatalysis is widely employed for the organic compounds mineralization occurring through the generation of highly reactive free radical species able to destroy the organic pollutants

under UV or visible light irradiation. The typical photocatalysts are TiO_2, SnO_2, and ZrO_2, and nowadays extensive research is ongoing on green metal-free photocatalysts, such as graphene oxide, or graphitic carbon nitride[201,203,204]. Functionalization of porous polymer adsorbents with photocatalysts for the regeneration purposes is now a hot topic in the water research field[205–210]. Very recently, hydrogels have gained attention due to their transparent character improving the photoactivity of the immobilized photocatalysts[211–214].

1.2.3 Emerging materials for heavy metals detection

Due to the significant drawbacks of the conventional heavy metals detection techniques, described in Section 1.1.4, the field of novel detection methods is growing in a fast pace. A vast amount of different detection mechanisms is investigated, such as electrochemical, colorimetric, microfluidic-based, or optical sensing[215,216]. The development of easy-to-handle materials providing inexpensive and facile, user-friendly methods of heavy metals real-time detection without time-consuming preparation procedures is the topic of a continuously growing interest[217].

The development of solid fluorescent materials able to detect heavy metal ions is one of the most promising approaches due to the ease of handling, and high sensitivity. The heavy metal ions fluorosensing mechanism is based on their complexation with the indicator, resulting in the modification of the indicators' emission properties. Typically it is attributed to the intramolecular charge transfer, i.e. photoinduced electron and charge transfers[218].

Photoluminescent electrospun nanofibers and hydrogels are the most frequently reported novel heavy metal ions indicating materials[217–223]. The fluorescent character is usually achieved by the immobilization of luminescent chromophores, such as

rhodamine B derivatives, quantum dots, graphene oxide, as well as gold or silver nanoclusters into a porous optically-inert polymer matrix[223–226]. One of the emerging fluorochromes continuously investigated as a potential heavy metal ions sensor is graphitic carbon nitride (g-C3N4), as it is a relatively inexpensive, metal-free, non-toxic, and at the same time chemically stable alternative[227–230]. Nevertheless, up to date studies on its immobilization into porous polymer substrates for the use as a fluorosensor are not common, but recently an interesting work of Huang et al appeared on the preparation of a g-C3N4 nanofibrous hydrogel for Cu^{2+} fluorosensing, through the thermal evaporation of the bulk g-C3N4 and the self-assembly/gelation of the obtained solution[231].

1.2.4 Multifunctional polymer-based materials for water treatment

Simplification of the water treatment and quality monitoring processes through their integration seems to be an alternative way to deal with the high cost and energy consumption, as well as their complexity. The design of porous polymer-based materials with a multi-purpose character is a promising approach in this regard. Several attempts have been recently made to develop multifunctional polymer-based materials for water treatment, e.g. Saleh et al[232] designed a polymer resin for the simultaneous removal and recovery of toxic metals and dyes, using MB and Hg as model pollutants, and several other works have been performed on multi-purpose polymer materials/composites for the contemporaneous organic and inorganic contaminants removal combined with their recovery, where mostly heavy metals and aromatic compounds, especially dyes, are used[106,233–237].

Multifunctional materials for water-soluble pollutants removal from wastewater, at the same time displaying features, such as photocatalytic self-cleaning and/or antibacterial

properties and/or pollutant recovery, have also attracted a lot of attention of researchers in the last years. For example, Qayum et al[118] and Han et al[119] fabricated multifunctional electrospun polyacrylonitrile-based fibrous membranes functionalized with silver nanoparticles for the removal of various organic pollutants and bacteria, able to photodegrade the adsorbed contaminants under visible light irradiation and to sterilize wastewater. However, the majority of the works on such multifunctionalities is still focused on an isolated pollutant type of choice, with dyes, antibiotics or heavy metal ions being the most commonly studied contaminant groups[240–246].

Moreover, efficient multicomponent oily wastewater treatment remains troublesome as the major part of the so far presented works is based on materials with selective wettability, i.e. on hydrophilic and oleophobic materials for water-soluble wastewater components removal, suffering from the problem of oil fouling, or on hydrophobic and oleophilic materials for oil removal which can only be used for the absorption of the oily phase from wastewater.

The development of porous materials with special wetting properties (superhydrophilicity/superoleophobicity or superhydrophobicity/superoleophilicity), called superwetting materials, for the use as filters or sorbents for one-step oily wastewater purification is a topic of continuously growing interest, giving a great promise in tackling the previously discussed oily wastewater treatment problems[111,247]. Wettability is a peculiar property of a material's surface depending on the surface morphology, roughness and the chemical composition.

Thus, superwetting materials are designed adjusting the structure and the surface energy[248]. The novel superhydrophilic/superoleophobic or superhydrophobic/superoleophilic membranes for oil-water separation are typically prepared through the creation of a rough surface on a commercial or developed

membrane and its modification with low-surface energy substances or nanoparticles[249,250]. The surface modification is usually performed using laser, sol-gel, chemical vapour deposition or electrochemical technologies, which suffer from several drawbacks, such as the complexity of the fabrication procedure, the cost of the used surface properties modifying substances and processes, and the instability of the formed layers[251,252].

Oil-water separation with the use of superwetting surfaces was inspired by the pioneering study from 2004 of Feng et al, who composed a steel mesh spray-coated with a polymer exhibiting superhydrophobic/superoleophilic properties[253].

Nowadays, a vast range of superwetting porous polymer materials, such as hydrogels (aerogels/cryogels), foams, sponges, etc., either neat or embedded with graphene oxides, metal oxides, etc., are extensively researched for the use as membranes with oil-water separation abilities[251]. One of the top emerging materials with the superwetting interfacial features favourable for practical applications in the water sector are hydrogels[156,247]. Both the wetting properties, namely the combination of the underwater superoleophobicity and superhydrophilicity, and their outstandingly high water absorption capacities, as well as the rich active functional groups make them attractive for integrated oily wastewater purification applications[156,254,255]. In fact, the great advantage of hydrogels over the above-discussed novel materials is their intrinsic superwetting character, which does not require further surface modifications. Moreover, their three-dimensional (3D) structure, resulting in large specific surface area, gives superior adsorption abilities compared to the extensively studied 2D materials[252]. For this reason comprehensive research is ongoing on hydrogels and surface engineering of commercial or developed membranes with the use of hydrogel coatings for oil-water separation applications[247,252,256–258].

Nevertheless, only a few studies have been reported so far on multifunctional hydrogels able to efficiently and simultaneously purify water from oil and water-soluble pollutants[158,259–261]. Thus, the development of a simple, single-step and energy-efficient purification method for oily wastewaters containing different water-soluble contaminants, such as metal ions and organic components, still remains a challenge of great importance.

The research on other polymer-based material types able to purify multicomponent oily wastewater is mainly focused on the development of the features favourable for the simultaneous oil separation and aqueous phase purification[262,263]. One of the few works where other functionalities are also developed is the one of Ma et al.[264] who fabricated a composite nanofibrous membrane, based on poly(ethyleneimine) /poly(acrylic acid)/polyacrylonitrile funcionalized with tungsten oxide, with antibacterial activity and able to contemporaneously separate oil, remove different heavy metal ions, as well as remove and photodegrade a dye, namely rhodamine B (RhB). Another example is the study of the same author on a composite nanofibrous polyvinylpyrrolidone/polyacrylonitrile membrane with incorporated metal organic frameworks (MOFs), with similar multi-purpose properties and able to remove stable emulsions[265].

Nevertheless, the research on multi-purpose materials capable of the simultaneous oily wastewater purification from multiple organic and inorganic contaminants and at the same time able to work as pollutant indicators is still very rare and limited. The few reported works focus on the simultaneous removal and detection of one pollutant type by metal organic frameworks, a nanocomposite Ni foam, or a nanocomposite aerogel[79,266,71,267].

1.2.5 Conclusions

It is of utmost importance to develop multifunctional materials for the integration of extremely complicated processes of water treatment and quality monitoring. Due to the adjustable chemical structure and easy processability porous polymer materials are the most widely used for water purification.

Superwetting polymer systems hold a great potential for solving the problem of oil fouling in the oily wastewater filtration, which hinders one-step purification of oily wastewaters. Since the fabrication of superwetting membranes requires complicated surface modifications, hydrogels naturally displaying such features are a great alternative, and a large amount of studies have been recently published on their use for oil-water separation. Nevertheless, in-depth research studies on polymer-based materials applicable for the integration of multicomponent oily wastewater filtration and other processes used in the water sector, are very limited. On the top, reports on the development of multicomponent oily wastewater filters with other important combined functionalities, such as pollutant detection, photodegradation or/and efficient pollutant recovery is still very rare. Moreover, the existing studies on the polymer-based materials able to both purify water and detect pollutants are only devoted to simulated wastewaters composed of the isolated pollutants of interest. Therefore, there is a large gap to be bridged in this regard, and special focus should be paid to hydrogel materials.

1.3 OBJECTIVES AND SCOPE OF THE THESIS

The main objective of this PhD thesis is to stimulate the research on multifunctional materials for processes integration in the studied realm of materials engineering for water-related technologies, where more attention is still paid to single applications, as

indicated in Section 1.2.4. The goal of the work is to propose a more sustainable alternative to the existing energy-consuming and secondary-pollution-causing processes, with cost-effectiveness making it accessible in the areas where financial constrains lead to the lack of proper water-related technologies. To this end, a rational design of a multifunctional superabsorbent polymer-based nanocomposite filter with a chemosensing functionality is proposed.

In particular, the applicability of a highly porous hydrogel material functionalized with graphitic carbon nitride nanosheets (CNNs) is investigated for the simultaneous separation of oil, adsorption of persistent pollutants, such as Hg^{2+} ions and MB dye from multicomponent oily wastewater and the detection of the heavy metal ions' presence in a single gravity-driven filtration step. Moreover, the material is intended to be self-cleaning and reusable through the adsorbed dye's photocatalytic decolorization under daylight irradiation and a pH-responsive mechanism of the adsorbed Hg^{2+} ions recovery in gravity-driven process. Such a design is suitable for the development of an energy-saving and cheap water purification and quality monitoring technology that does not produce secondary pollution from the spent filter and from the Hg^{2+} detection procedure. Thus, the general scope of this thesis is to conduct a comprehensive study on the potential of the material's design to be used as an alternative to the conventional processes used in the water sector.

1.3.1 The developed material's design: composition and motivation

CNNs, with the chemical formula denoted as g-C3N4, are emerging advanced nanomaterials showing great potential in bridging the gaps in the field of multifunctional materials for water sector. Graphitic carbon nitride (CN) possesses a similar structure to graphite exhibiting a stacked 2D structure. As shown in Figure 1.3, it is composed of layered tri-s-triazine units, condensed by tertiary nitrogen atoms,

which interact by van de Waals forces, providing great thermal and chemical stability of the material[268]. The conjugated delocalized system combined with the lone pair electrons of nitrogen gives rise to the interesting electronic structure attracting attention of scientists from different fields. Typically, bulk CN is synthesized through the pyrolysis process of nitrogen-rich precursors such as melamine, thiourea, urea, or dicyandiamide[269].

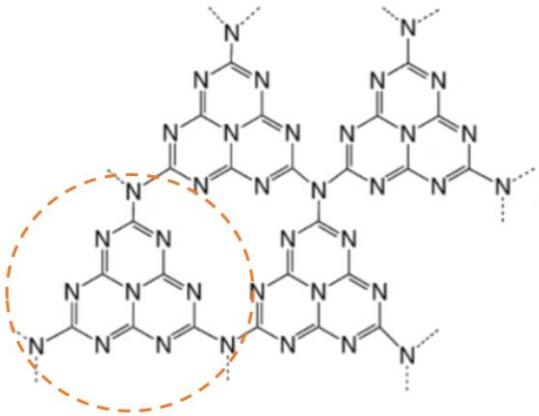

Figure 1.3. The chemical structure of graphitic carbon nitride (g-C3N4) composed of tri-s-triazine units, as marked with the dashed circle.

The multiple interesting properties of CNNs, such as electronic and optical ones (e.g. fluorescence and photocatalytic activity under visible light), their chemically active surface, as well as the non-toxicity, and environmental friendliness containing only C and N atoms which are highly abundant in earth, keep attracting a growing number of researchers studying their potential applications[270–272]. The studies focused on water treatment, have confirmed the CNNs' ability to sorb both organic and inorganic pollutants from water[270,273]. Their metal capture ability is attributed to the surface amino groups, as well as to the negatively charged six nitrogen lone-pair electrons of their highly ordered tri-s-triazine units[274–276].

On the top, there are many reports on the use of CNN dispersions as heavy metals sensors, based on different detection mechanisms[277,278]. One of them is the monitoring of their fluorescence quenching in presence of heavy metal ions, such as for Cu^{2+}, Cr^{6+}, Hg^{2+}, or Ag^{2+} [278–281]. Although with the specific methods heavy metal ions in solutions can be effectively detected, the removal of the dispersed CNNs from the liquid media after their interaction with the pollutants requires several post-processing steps, such as filtration or centrifugation, enhancing the possibility of secondary pollution. Moreover, CNNs aggregation is a serious limitation in their practical applications in the dispersion form[282,283]. In particular, CNNs may aggregate in presence of electrolytes commonly occurring in wastewaters[284,285], while depending on the efficiency of CN exfoliation method, different amounts of residual unexfoliated particles are present in the obtained CNN powders, hindering their stability in aqueous environments[286]. One way of overcoming these problems may be the use of CNNs as functional nanofillers in composite materials. Nonetheless, although many works have been reported on the synthesis and the applications of CN-based materials[287], there is still a limited number of studies on the development of CN porous polymer-based composites for chemosensing alone or combined with the removal of water contaminants[288–294].

Thus, in the herein PhD thesis, through the incorporation of CNN nanofillers into a porous cryogel network, we propose a nanocomposite PSA/CNN 3D filter for oily wastewater purification enabled by the superwetting properties of the cryogel, with heavy metal ions fluorosensing and photocatalytic self-cleaning properties owed to the embedded nanofiller, and reusable via the sorbed metal ions' recovery.

Cryogels are materials with a macroporous 3D structure, produced through the controlled freezing during polymerization, with a highly interconnected polymer network. Cryogels have a unique macroporous network, resulting in the further facilitation of water uptake and inducing fast adsorption kinetics[295,296]. They are obtained through a cryogelation process, which is a gelation process held under semi-frozen conditions, leading to the formation of ice crystals around the crosslinked polymer network with the embedded nanofiller[297]. The illustration of a nanocomposite cryogelation process is shown Figure 1.4. As depicted, the ice crystals play the role of a porogen and an interconnected macroporous structure with highly dense polymer walls is obtained after subsequent thawing.

The interconnected macropores combined with the densely crosslinked polymer network result in excellent flexibility and shape memory properties, being the prominent parameters responsible for the high performance of cryogel structures used as filters[297,298].

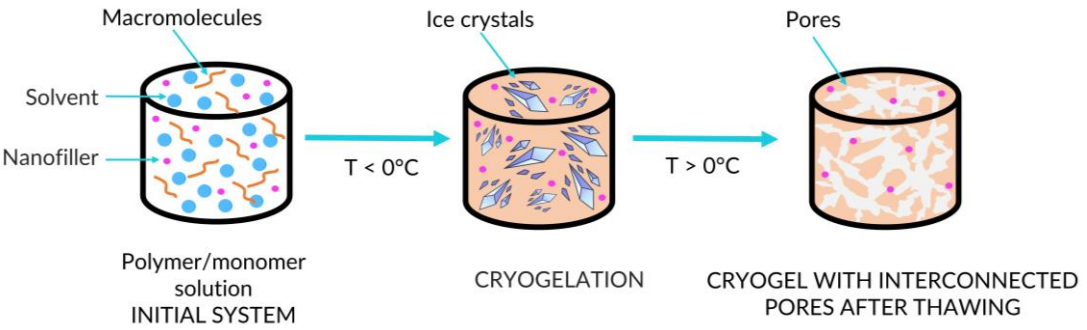

Figure 1.4. A scheme illustrating the cryogelation process of nanocomposites.

The material's polymer matrix is built by crosslinked poly(sodium acrylate) (PSA) chains. The chemical structure of PSA is shown in Figure 1.5. It is a superabsorbent and underwater oleophobic polymer, with sodium carboxylate groups, rendering the polymer anionic, which enables interactions with cationic compounds such as Hg^{2+}

ions and MB.

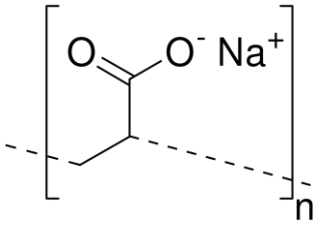

Figure 1.5. The chemical structure of poly(sodium acrylate) (PSA).

The incorporation of the CNNs into the porous structure before the cryopolymerization process facilitates their good distribution within the polymer matrix. Hence, the cryogel matrix serves as a stabilizing platform for the embedded nanofillers. It should be mentioned that the developed multifunctional PSA/CNN cryogel is obtained via a simple one pot synthesis method.

1.3.2 The scope of the thesis

The scope of the present dissertation includes studies on:

1) the applicability of the as-developed PSA/CNN cryogel 3D filter for the multicomponent oily wastewater purification through gravity-driven filtration. Specifically, the performance of the system in the simultaneous oil-water separation and water-soluble persistent inorganic and organic pollutants adsorption is explored, using Hg^{2+} ions and MB as representatives.

2) the reusability of the filter in cyclic oily wastewater gravity-driven filtration, to evaluate the material's anti-fouling properties.

3) the recoverability of the adsorbed Hg^{2+} ions' and the reutilization of the filter.

4) the filter's photocatalytic activity under solar light irradiation, due to the presence of CNNs, with the aim to develop self-cleaning properties of the filter through the sorbed dye's photocatalytic decolorization.

5) the filter's photoluminescence properties, owed to the fluorescence properties of CNNs, for the use as a Hg^{2+} ions fluorosensing filter.

6) the optimization of the CNNs concentration within the cryogel for the satisfactory detection of low Hg^{2+} ions quantities in the integrated filtration and detection process.

7) the mechanism of Hg^{2+} ions and MB adsorption, and the influence of the CNN nanofiller and the co-existence of the aqueous pollutants on the adsorption process.

1.4 NOVELTY AND SIGNIFICANCE

As discussed in Section 1.2.4, the research on multifunctional materials for the water protection field is still at its infant stage. Even though numerous works have been reported on the superwetting materials, such as hydrogels, which show great oily wastewater purification performance, studies on the simultaneous multicomponent oily wastewater treatment and pollutants indication are very rare. Works on the development of other functionalities of a material able to purify multicomponent oily wastewater, such as pollutant recovery or photocatalytic self-cleaning, are also scarce.

CNNs display a great potential for tackling the problem of complexity of the used water technologies due to the various suitable properties. Specifically, the CNNs' photocatalytic activity under daylight, the fluorescence quenching upon the interaction with heavy metal ions, and the ability to sorb certain organic and inorganic pollutants, shade light on the potential multifunctional character of these nanomaterials. Nevertheless, the use of nanomaterials in the form of aqueous dispersions for water treatment suffers from certain drawbacks, such as difficulties in handling, in their recovery and in regeneration after use, the enhanced possibility to form secondary pollution, and, in some cases including CNNs, the aggregation in presence of electrolytes.

However, the incorporation of CNNs within a superwetting hydrogel matrix, combining the multiple interesting features of these two emerging materials, brings a great potential for the development of a system with a superior multifunctional behaviour. To the best of our knowledge, there are no reports on the stabilization of CNNs within a cryogel polymer matrix, making it a novel approach in the field of multi-purpose materials. Moreover, according to our extensive literature research, this is the first study exploring the multifunctionality of a CNN-based polymer composite 3D filter in the water remediation, quality monitoring and pollutant recovery field, opening up the way for more effective and functional integrated processes in the water purification field, and for the potential use of CNNs as a multifunctional component for materials used in the water sector-related applications.

The herein presented work contributes to the scientific community providing a detailed evaluation of the developed PSA/CNN cryogel filter's performance under practical conditions where a multicomponent oily mixture is involved, which is rarely considered in the studies on materials for water treatment. Besides, a large scope of potential applications of the developed material, as well as of their integration into the filtration process is investigated. The work gives an in-depth insight into the applicability of the multifunctional PSA/CNN cryogel filter in the simultaneous multicomponent oily wastewater filtration and Hg^{2+} ions detection, into the filter's performance in regeneration through the photocatalytic self-cleaning from the adsorbed dye and via the pH-responsive recovery of the adsorbed Hg^{2+} ions, and into as-enabled filter's reuse. Crucially, the work focuses not only on the multifunctionality of the developed material, but also on solving the problems associated with wastewater treatment and quality monitoring, such as high energy consumption, high costs, and the complexity of pollutant detection methods involving the use of toxic reagents. For

this reason, the work focuses on gravity-driven filtration, photocatalysis under solar light, and a straightforward, inexpensive, and environmentally-friendly detection method. Proving the success of the proposed approach in obtaining a highly performant multi-purpose filter, the herein thesis offers an inspiration to shift from the studies on single-application materials to the rational design of smart multifunctional nanocomposites, aiming at providing solutions for simplified, energy-efficient, cost-effective, and greener processes in the water protection field.

1.5 THESIS OUTLINE

The outline of the rest of the thesis is as follows.

Chapter 2 describes the fabrication method of the proposed PSA/CNN nanocomposite material, as well as of the neat PSA cryogels, and presents the characterization properties studies, namely the chemical and the morphological analysis, as well as their wetting, and mechanical properties. The differences in the properties between the composite and the neat polymer cryogels, as well as the effect of different CNN nanofillers loadings on those properties is determined.

Chapter 3 is devoted to the investigation on the interaction between the developed cryogels and the cationic pollutants performed in batch conditions. The results of the Hg^{2+} and MB adsorption kinetics studies, as well as of the adsorption capacities evaluation for isolated pollutants are discussed. The obtained results are fitted to the adsorption isotherm and to the adsorption kinetics models, to assess the phenomena governing the sorption process. The adsorption mechanism is also thoroughly investigated by means of chemical analysis and in terms of ion exchange, by the determination of Na^{+} release attributed to Hg^{2+} adsorption, both in case of the single pollutants, as well as in their co-existence. The effect of the presence of different

nanofillers loadings on the adsorption capacities is also determined.

Chapter 4 focuses on the performance of the neat PSA and the PSA/CNN nanocomposite cryogels with different CNN loadings in the oily wastewater purification through the simultaneous adsorption of water-soluble pollutants and oil separation from water, performed through gravity-driven filtration. The performance of both cryogels is systematically studied for different mixtures of the three different types of pollutants used, i.e. SB oil, MB and Hg^{2+} ions. The reusability of the cryogels in various consecutive filtration cycles is evaluated.

Chapter 5 is concentrated on the investigation of the multifunctionality of the nanocomposite cryogel, and the exploration of its suitability for integrated functions, such as multicomponent oily wastewater filtration and Hg^{2+} ions fluorosensing, into a single gravity-driven filtration process. The optimization of the fluorosensing performance by the determination of the nanofillers content effect on the sensitivity of the cryogel filter is discussed.

Other functionalities, such as cyclic regeneration of the spent filter through Hg^{2+} ions recovery via a pH-responsive mechanism, as well as through the photocatalytic decolorization of the adsorbed MB dye, are also explored, and their impact on the filtration performance is evaluated. A detailed study on the sorbed Hg^{2+} ions interactions with the incorporated nanofillers, as well as with the cryogel matrix during the filtration process is performed. The adsorption stability of Hg^{2+} ions is also evaluated. The last part of the thesis concludes the overall results, highlighting the importance of the herein presented work.

Chapter 2: PSA and PSA/CNN cryogels: Fabrication and characterization

This chapter presents the fabrication method of the PSA/CNN, and of the neat PSA cryogels, aiming at the development of highly porous superwetting materials with properties suitable for the application in water treatment and quality monitoring, and at the further enrichment of the material's functionalities by the incorporation of the CNNs, known for several interesting properties, as discussed in Chapter 1:. The successful embedding of the CNNs within the cryogel matrix was confirmed by the chemical analysis of the samples. The highly porous structure of the PSA and the PSA/CNN cryogels was explored revealing the presence of roundish interconnected macropores. The presence of CNNs within the cryogel matrix seems to cause thinning of the polymer walls with the increase of the nanofiller content, and slight pore size reduction evident at the highest studied loading. Nonetheless, these slight microstructure modifications do not affect either the gravity-driven permeability of the materials, showing high water flow rates of ~ 3500-3700 L m^{-2} h^{-1}, or the swelling degree, reaching 159.00±4.48 g g^{-1} – 184.26±14.13 g g^{-1}. Moreover, both types of cryogels exhibit underwater-superoleophobic properties, being completely repellent towards low- and high-viscosity oils. It was also found that the addition of the studied CNNs contents in the polymer network does not affect their mechanical performance. Hence, the obtained cryogels present a set of properties suitable for the use in the water industry sector, allowing to establish the direction of the further works towards the exploration of the materials' performance in the processes used in water industry, and the role of the CNNs in this regard.

2.1 MATERIALS AND METHODS

2.1.1 Materials

Sodium acrylate (SA, 97%), *N,N'*-methylenebis(acrylamide) (MBA, 99%), *N,N,N',N'*-tetramethylethylenedi-amine (TEMED, ≥99%), ammonium persulfate (APS, 98%), and silicone oil (viscosity 500 cPs) were purchased from Sigma-Aldrich. Soybean oil (SB oil) (Bunge) was purchased from a local shop. Graphitic carbon nitride nanosheets (CNNs) were kindly provided by prof. Vassilios Binas from the Institute of Electronic Structure and Laser, Foundation for Research and Technology – Hellas (Greece). All the chemicals were used as received without any further purification. Milli-Q water was used in all the studies.

2.1.2 CNNs synthesis

Porous CNNs were fabricated through thermal polycondensation of melamine and the following thermal exfoliation. The polycondensation reaction was performed in a muffle furnace, heating 50 g of melamine, placed into an alumina crucible with a cover, at 510 °C for 2 h and 530 °C for 2 h under air flow (ramp rate of 2 °C min^{-1}). Then, 5 g of as-synthesised bulk graphitic carbon nitride was placed into an open ceramic container and heated at 580 °C for 2 h (ramp rate of 2 °C min^{-1}) in a muffle furnace to obtain exfoliated graphitic carbon nitride nanosheets.

2.1.3 Cryogels fabrication method

Both the neat PSA and the PSA/CNN nanocomposite cryogels were produced slightly modifying the method introduced by Loo et al[299]. The fabrication principle is based on the cryopolymerization of SA in an aqueous solution. In case of the neat PSA cryogels, the reaction mixture contains SA as a monomer, the crosslinker (MBA), the initiator

(APS) and the activator (TEMED), whereas in case of the PSA/CNN cryogels the mixture is enriched by a specific amount of CNNs.

The general phenomenon responsible for the formation of cryogels is discussed in Chapter 1: (Section 1.3.1). In our case, the cryopolymerization reaction is started in a semi-frozen state, at the temperature close to the nominal water freezing point, leading to a heterogenous system containing both ice crystals and the unfrozen liquid microphase (UFLP)[300–302]. This temperature enables an even distribution of the formed ice crystals within the samples during the water crystallization, at the same time delaying the co-polymerization of MBA and SA, which prevents the formation of the cryogel before water freezes[299,303,304]. Once the mixture is then incubated in subzero temperatures, the majority of the water forms ice crystals and a cryo-concentration phenomenon occurs in the UFLP[305]. In particular, the bound water and the water-soluble substances (SA, MBA, APS, and TEMED) confine in the UFLP due to the freezing-point depression, and the decomposition of persulfate ions of APS into sulfate-free radicals is catalysed by TEMED, initiating the co-polymerization of SA and MBA. While the PSA network is formed, in the case of the PSA/CNN nanocomposites, some of CNNs are expected to be entrapped fully within the PSA matrix and some, accumulated at the UFLP-crystal interfaces, partially[306,307]. Simultaneously, the ice crystals, playing the role of a porogen, grow into contact with each other, leading to the formation of interconnected pores[307,308].

Thus, even though it is a straightforward one-pot synthesis method, the cryopolymerization is a complex process involving ice crystals growth, free radicals formation, and the simultaneous co-polymerization of SA and MBA, leading to gelation, and, in case of the nanocomposite systems, the embedment of the nanofillers.

In order to obtain the reaction solution, firstly an aqueous mixture of SA-MBA (20% w/v of the SA monomer, and 0.05 mol of MBA/mol of SA) was prepared and magnetically stirred until well-dissolved. In case of the PSA/CNN cryogels' fabrication, the CNNs aqueous dispersion was prepared using an ultrasonicator probe (VCX 750, Vibra cell, SONICS) at 40% amplitude for two sonication cycles (10 s on and 15 s off), in an ice bath, and it was added to the SA-MBA solution at the volume ratio of 1:1. In order to obtain cryogels with varying nanofiller loadings, the CNNs were introduced into the mixture at 0.5, 1 or 3% w/w with respect to the monomer and the resulting nanocomposite cryogels are denoted as PSA_CNN0.5, PSA_CNN1 and PSA_CNN3, respectively. The obtained SA-MBA(-CNNs) mixture was then cooled upon stirring in an ice bath prepared in a closed cooler box, and once it reached ~1 °C, the fabrication protocol illustrated in Figure 2.1 was followed. Specifically, free-radical polymerization was initiated by adding APS and TEMED (cooled to ~1 °C in the same ice bath and quickly vortexed before addition) upon stirring, at the respective concentrations of 2.5 mM and 125% v/v in the final reaction mixture. After ~10 s the mixture was quickly transferred into poly(propylene) syringes (1 mL and 5 mm ID), placed in a propylene glycol bath (previously stored in the freezer) at -20 °C, and incubated in the freezer for 24 h to ensure complete polymerization. The same syringe dimensions and reaction mixture volumes were used to assure the reproducibility of the freezing patterns.

Once the polymerization process was completed, the resulting cryogels were cut into small cylindrical disks with a blade, then immersed and vortexed for 30 min in Milli-Q water, and subsequently rinsed with Milli-Q water several times in a vacuum filtration setup to remove any un-reacted components. Next, the samples were frozen at -20 °C in a swollen state, stored overnight at -80°C and dried in a freeze dryer (Base

Unit LIO5P-4K, for 48h at −50 °C). The dry cryogels were stored in poly(propylene) vials and well-sealed with parafilm. The thickness and the mass of the obtained cryogels swollen in Milli-Q water were ~7 mm and ~0.6 g, respectively.

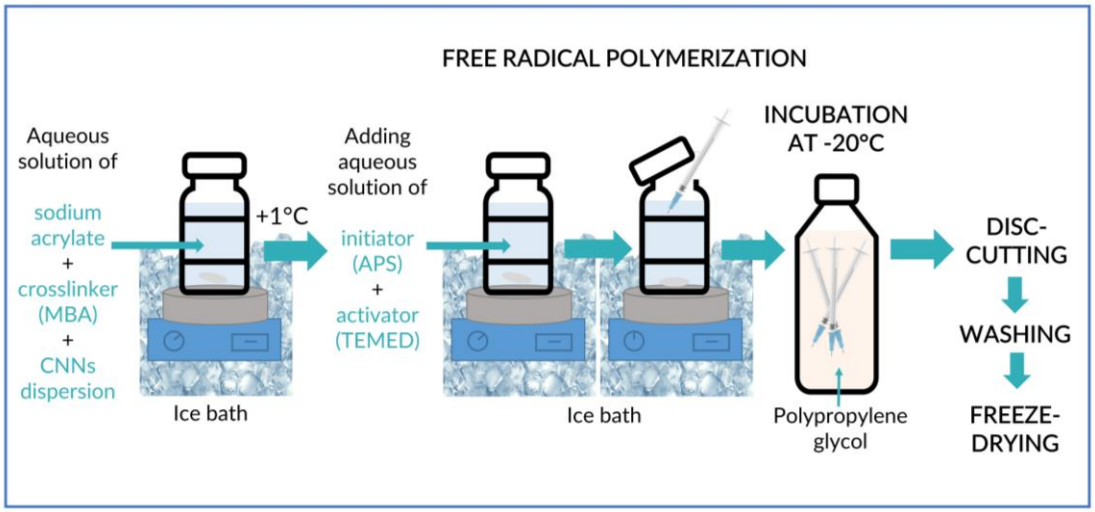

Figure 2.1. A schematic representation of the PSA/CNN nanocomposite cryogels fabrication protocol.

2.1.4 Cryogels characterization

The chemical composition of all the cryogels (in dry conditions), as well as of the bulk CNNs powder, was analyzed with the use of a Fourier Transform Infrared (FTIR) spectrometer (Vertex 70v FT-IR, Bruker) equipped with a single-reflection attenuated total reflection (ATR) accessory (MIRacle ATR, PIKE Technologies). All the spectra were recorded from 4000 to 600 cm^{-1} and 64 repetitive scans were run at a resolution of 4 cm^{-1} with the background spectrum collected for the same number of scans.

The morphology of CNNs was assessed via transmission electron microscopy (TEM; JEOL JEM-2100) equipped with LaB6 filament, operating at 200 kV. The aqueous dispersion of CNNs, prepared with the use of an ultrasonication probe (VCX 750, Vibra cell, SONICS) at 40% amplitude for 20s, was sonicated for 3 min at 59 kHz in

an ultrasonic bath prior to the deposition of 5 uL drop on the carbon film-supported copper TEM grids. After 60 s the remaining volume was blotted off the grid with blotting paper. At the end, the grids were dried at room temperature for a few hours.

The morphological analysis of the freeze-dried neat and nanocomposite cryogels was performed with a scanning electron microscope (SEM, JEOL JSM-6490LA) at an acceleration voltage of 10 kV after coating the samples with a 10-nm Au layer using a high-resolution sputter coater (Cressington 208 HR). For the cross-sectional analysis, prior to the Au coating procedure, the freeze-dried cryogels were treated with liquid nitrogen for several seconds and immediately cut with a blade.

The skeletal density of the different cryogel types was determined using a pycnometer (Pycnomatic ATC) placing the dry cryogels (~0.1 g of each sample), previously dried under dynamic vacuum for 24 h, in a 4 cm^3 cuvette inserted into the pycnometer. The analysis was performed at 20.00±0.01 $^{\circ}C$, using helium as a measuring gas. Ten measurements per sample were run, and the accuracy was set to be ±0.5-0.8 % for each run corresponding to 3-20 measurements (depending on the obtained data stability), where the result for each run is an averaged value from these repetitions.

The swelling degree characterization was performed for the different cryogel types following a procedure of dipping a dry cryogel of known dimensions and mass in Milli-Q water, wiping off the excess surface water with damp paper and subsequently weighing the swollen cryogel (to determine the gravimetric swelling degree Q_w) or measuring its dimensions (to determine the volumetric swelling degree Q_v).

The swelling degrees of the cryogels, Q_w ($g\ g^{-1}$), and Q_v ($cm^3\ cm^{-3}$) were calculated as follows[299]:

$$Q_w = \frac{m_f}{m_0} \tag{2.1}$$

where m_f and m_0 are the masses (g) of the swollen and dry cryogel, respectively.

$$Q_v = \frac{V_f}{V_0} \tag{2.2}$$

where V_f and V_0 are the volumes (cm^3) of the swollen and dry cryogels, respectively. The volume of the swollen cryogel was assessed measuring its dimensions (with a micrometer screw gauge, taking three measurements of the sample's diameter and thickness and calculating their mean values) and assuming the cylindrical shape.

The experimental procedure of determining the porosity of the swollen cryogel followed a published method[309,310], and it is the same as for the above-described swelling degree assessment with the difference that the water-filled in the macropores of the swelled cryogel, i.e. free water, was estimated by the mass decrease of the swelled cryogel after it was subjected to vacuum suction on a microfiltration paper for 30 s.

The porosity, P (%) of the different cryogel types was calculated as follows:

$$P = \frac{(m_f - m_s)}{\rho_{water} \times V_f} \tag{2.3}$$

where m_s is the mass (g) of the cryogel after removing the free water from the pores (through vacuum suction on a microfiltration paper for 30s), V_f is the volume of the swollen cryogel (mL), and ρ_{water} is the water density (0.998 g mL^{-1}).

Water permeability tests were conducted for both the neat and the nanocomposite cryogels in a home-made gravity-driven filtration setup by placing swollen cryogels in between two polyurethane o-rings in a way that no pressure is exerted onto them. The filtration diameter was 6 mm (effective filtration area of 2.83×10^{-5} m^2) and the filtration column volume was 20 mL. Then, 15 mL of water was poured on top and the flow rate (J) was calculated as follows:

$$J = \frac{V}{A \times t} \tag{2.4}$$

where V is the volume of the permeate (L), t is the filtration duration (h), and A is the effective filtration area of the filter (m^2).

The underwater oleophobicity was evaluated using an OCA 20 goniometer (Data-Physics) conducting underwater oil contact angle (UOCA) measurements. The swollen cryogels were fixed on a support and placed under the surface of the Milli-Q water filling a glass cuvette. Then, using an upwards-bent dosing needle, the oil droplet was brought close to the sample's surface at gradually increasing volumes.

Mechanical properties of the different cryogel types were characterized by uniaxial compression tests on an Instron 3365 dual-column dynamometer equipped with a 10 N load cell. Displacement was applied with the rate of 2 mm min^{-1} while the reaction force was recorded until 40% strain was reached. From the stress-strain curves, the Young's modulus (E) was extracted as the slope of the linear region according to the following equation:

$$\frac{F}{\pi \times r^2} = \frac{(E - \Delta h_0)}{h} \tag{2.5}$$

where F is the force applied to cylindrically shaped gels with a cross-sectional area of $\pi \times r^2$ (r: radius), h is the height of the hydrogel during compression, and Δh_0 is the change in height of the sample during compression.

Additionally, the susceptibility to stress relaxation was evaluated through cyclic compressive tests performed on the same setup with the rate of 10 mm min^{-1}, both in loading and in unloading, for the duration of 5 cycles. In each cycle, the peak and valley were set at 40% strain and 0 KPa stress, respectively. The stress relaxation was evaluated as the ratio between each peak and the first one.

All the experimental studies were carried out in triplicates.

2.2 CHEMICAL ANALYSIS OF CNNs AND CRYOGELS

The chemical composition of the pristine PSA, PSA_CNN1, and PSA_CNN3 cryogels, as well as of the used CNNs, was studied by means of FTIR, and the whole wavenumber range of those spectra (up to 4000 cm^{-1}), as well as the low wavenumber range (up to 1750 cm^{-1}) of the obtained spectra is shown in Figure 2.2a, and Figure 2.2b, respectively. For all the cryogel samples, a band of asymmetric stretching vibration of the C=O bond in the carboxyl anion ν_{as}–COO^-, characteristic of the PSA polymer[311], is located at 1547 cm^{-1}. In all the studied cryogel samples, at ca. 1452 cm^{-1} a band of bending vibrations of δ-(CH_2) is present[312,313], whereas at ca. 1400 cm^{-1} a band of symmetric stretching vibrations of the C=O bond in the carboxylate anion, ν_s–COO^- appears[311,312]. The peaks at 1321 cm^{-1} and 849 cm^{-1}, observed in all the cryogel samples, correspond to the C-O stretching vibration of the carboxyl groups (COOH) of the PSA, and the C-COO^- stretching, respectively[313–315].

The main peaks in the spectra of the CNNs at 1321, 1240, 1209, 891 and 812 cm^{-1}, are attributed to the breathing vibrations of the tri-s-triazine units and to the typical stretching modes of the CN heterocycles[259,316–318], and the broad peaks between 3080 and 3290 cm^{-1} are attributed to the stretching mode of the terminal NH_2 or NH groups of the nanosheets [319,320]. Most of these peaks are also observed in the spectra of the PSA/CNN nanocomposites, being more evident in the cryogels with the higher CNNs concentration (Figure 2.2b), which confirms the successful incorporation of the nanofiller into the polymer matrix at increasing loadings. Concerning the peak at 1321 cm^{-1}, in case of the PSA/CNN cryogels, it overlaps with the one ascribed to the C-O stretching vibration of the PSA molecules, but it is slightly more pronounced in the spectra of the cryogels with the highest studied CNNs loading.

In conclusion, although the FTIR spectra confirm the presence of the CNNs within the PSA framework, it is not possible to identify any possible chemical interactions, due to the low intensity of the peaks attributed to the nanofillers and to the high superposition with the characteristic peaks of the PSA, possibly because of the low amount of CNNs in the polymer matrix.

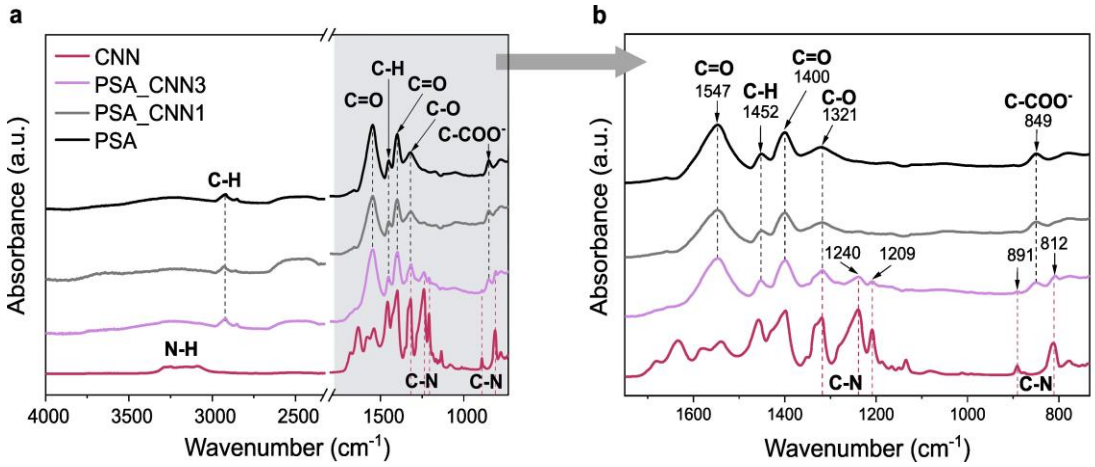

Figure 2.2. The FTIR spectra of the dry pristine PSA, PSA_CNN1 and PSA_CNN3 cryogels in: a) the whole wavenumber range, b) the lower wavenumber range, as indicated by the grey field in a).

2.3 MICROSTRUCTURE OF CNNs AND CRYOGELS

As shown in Figure 2.3, the morphological analysis of the used CNNs, performed by means of transmission electron microscopy (TEM), confirmed the successful exfoliation resulting in the formation of very thin porous nanosheets. Such a nanostructure of the CNNs is highly desired for the use as a functional nanofiller of materials for water treatment and pollutant detection, where the surface active area plays a crucial role in the interactions with the contaminants. In addition, as discussed in Chapter 1: (Section 1.3.1.), the exfoliated CNNs are proved to have higher stability in water, since the self-aggregation, typical for the bulk CN, is hindered. Nevertheless,

as complete exfoliation still remains a challenge, some darker spots, suggesting the aggregation of the residual non-exfoliated CN are observed in the TEM images. Thus, the support of the nanosheets by the porous cryogel matrix is expected to prevent their further aggregation in different aqueous environments, increasing the stability of the CNNs.

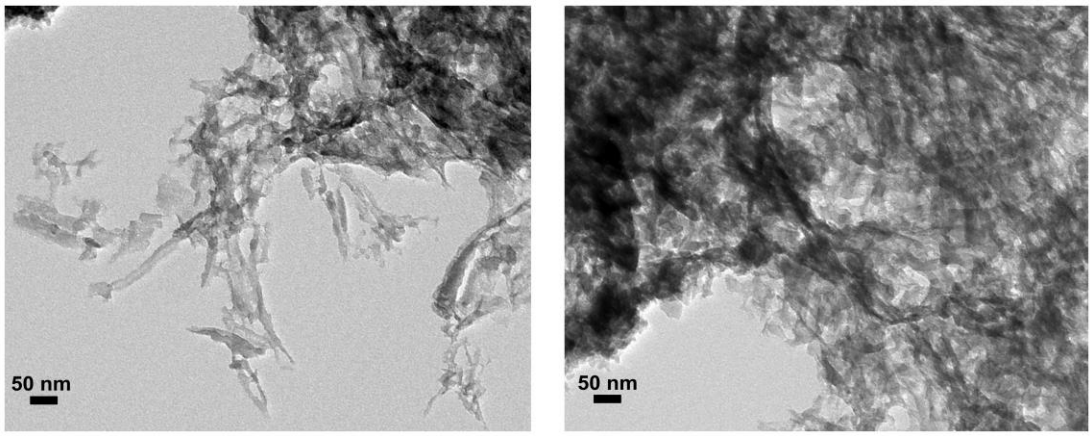

Figure 2.3. TEM images of the used CNNs.

Both the surface and the cross-sectional SEM analysis of the neat PSA and the nanocomposite cryogels with different CNNs loadings (PSA_CNN0.5, PSA_CNN1, PSA_CNN3) was performed. As shown in Figure 2.4 and Figure 2.5, a 3D porous structure with open interconnected roundish macropores was obtained for all the cryogel types, due to the low cryogelation temperature known to be favorable for the formation of highly interconnected pores[299].

As revealed by the microstructural analysis of the different cryogels' surface (Figure 2.4), the addition of the herein defined quantities of CNNs into the polymer matrix does not affect significantly the morphology of the pores and their interconnectivity, under the used fabrication conditions. Nonetheless, the introduction of CNNs at 3 % w/w wrt the monomer, seems to decrease the pore size, suggesting that the presence

of higher amounts of CNNs reduces the freezing temperature of the UFLP, which is known to hinder the ice crystals growth and leads to the rapid formation of smaller pores[321,322].

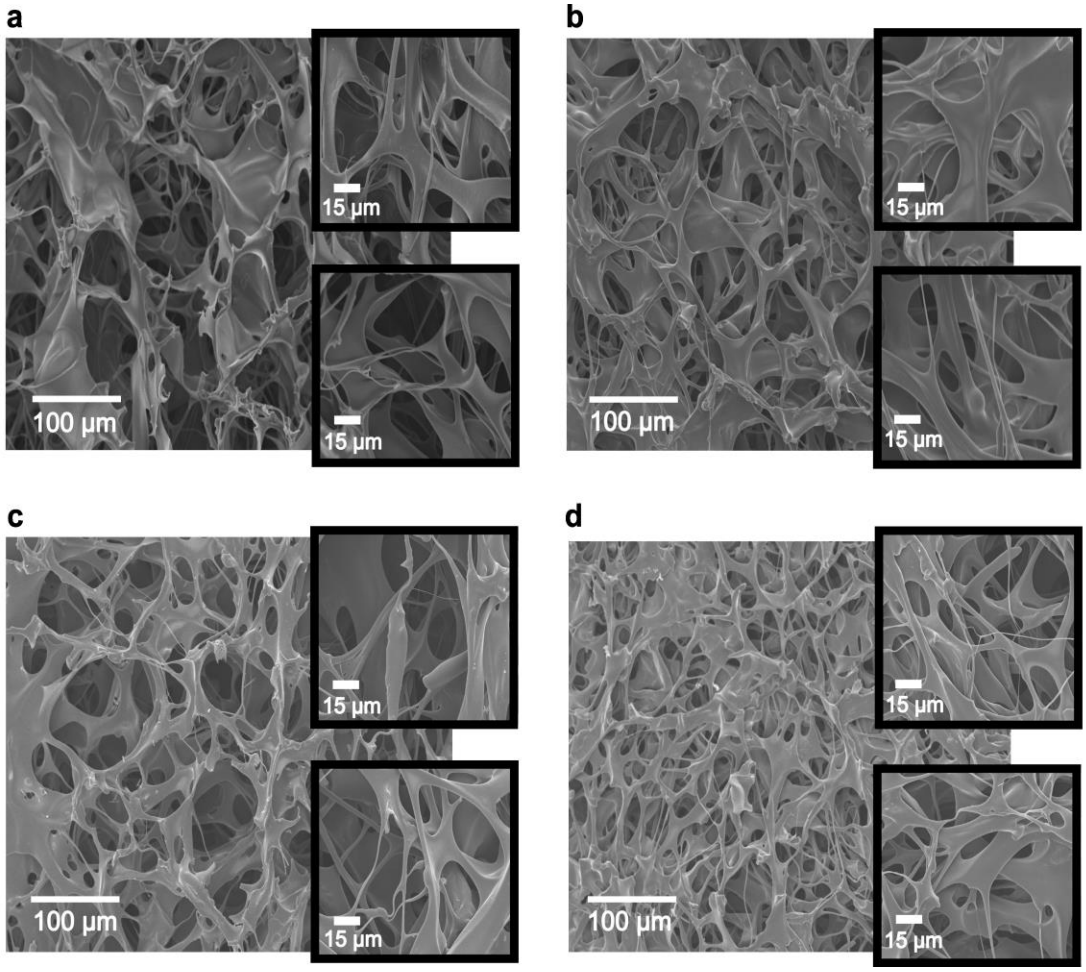

Figure 2.4. SEM images of the surface of a) PSA, b) PSA_CNN0.5, c) PSA_CNN1, d) PSA_CNN3 cryogels, with high magnification insets.

The effect of the pore size reduction in case of the highest used CNNs loading in the cryogel, is also visible in the cross-section images, as shown in Figure 2.5. In addition, the thickness of the PSA matrix walls seems to decrease with the increase of the CNNs content, which is less evident in the SEM images of the cryogels' surface. The thinning of the matrix walls indicates the variation in the ice crystals formation patterns, possibly associated with the previously discussed phenomenon causing the effect of

the pore size reduction, which is apparently better pronounced in case of the PSA_CNN3 cryogels.

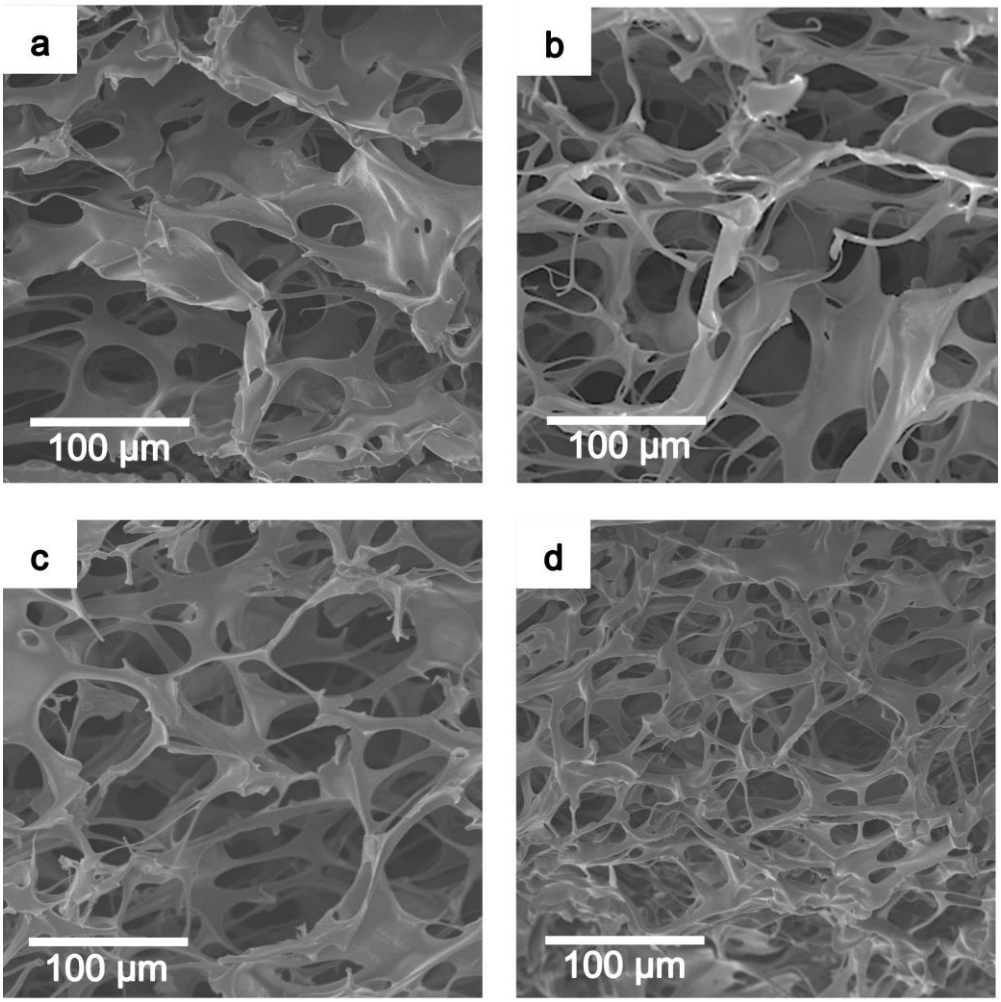

Figure 2.5. SEM cross-sectional images of the a) PSA, b) PSA_ CNN0.5, c) PSA_CNN1, d) PSA_CNN3 cryogels.

The skeletal density of the PSA and the PSA_CNN1 cryogels was measured by means of a pycnometer, and in order to assure the high accuracy of the measurements firstly the drying time of the samples was optimized so as to avoid the effect of any absorbed moisture. The optimization was performed using the PSA cryogels. As shown in Figure 2.6a, after 45 min of drying under vacuum, instability of the data in consecutive runs was observed, whereas after 24 h of vacuum drying the relative stability of the

data was attained (Figure 2.6b). Hence, the measurements after 24 h of drying were performed for both cryogel types.

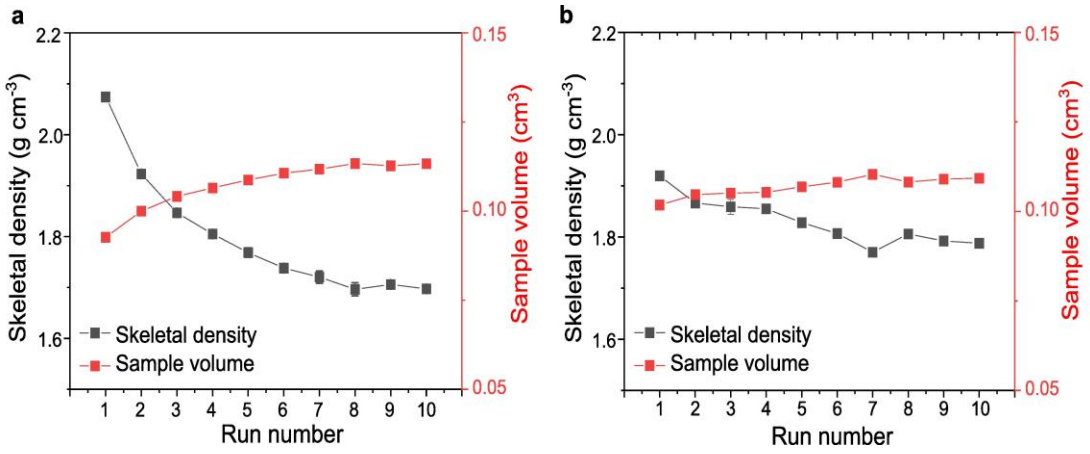

Figure 2.6. Skeletal density and sample volume evolution over consecutive pycnometric measurement runs for PSA cryogels after a vacuum drying time of: a) 45 min, b) 24 h.

Figure 2.7a presents the obtained values of the skeletal densities of the PSA and the PSA_CNN1 cryogels, being slightly higher for the latter one (1.83±0.04 vs. 1.96±0.06 g cm^{-3}). Nonetheless, as presented in Figure 2.7b, high porosity of all the studied cryogels (evaluated following the procedure described in Section 2.1.4.) was unveiled, with no significant effect of the different studied loadings of CNNs' within the polymer matrix (75±3 %, 70±8 %, 78±2 %, and 78±1 % for PSA, PSA_CNN0.5, PSA_CNN1, and PSA_CNN3 cryogels, respectively). This suggests that the presence of CNNs does not influence the relative volume of the ice crystals formed within the polymer matrix during the cryogelation process.

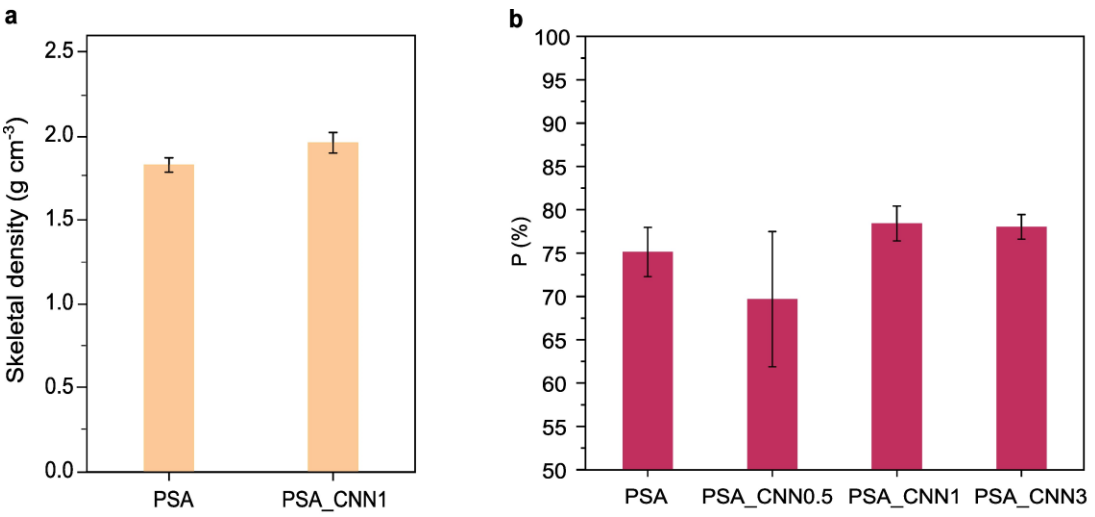

Figure 2.7. a) Skeletal density of the PSA and the PSA_CNN1 cryogels. b) The porosity (P) of the different cryogel types.

2.4 WETTING PROPERTIES OF CRYOGELS

The hydrophilic character of the PSA and the PSA/CNN cryogels was confirmed by the extremely fast time of the samples' swelling in Milli-Q water of ~7 s. The swelling degrees, namely the Q_w and the Q_v of the PSA, PSA_CNN0.5, PSA_CNN1, and PSA_CNN3 cryogels were determined, as demonstrated in Figure 2.8b. While the obtained Q_w values are similar for all the types of cryogels, the Q_v values seem to slightly fluctuate with the modification of the CNNs content in the cryogel without showing a particular trend. Specifically, the Q_w, measuring the uptake of water by the dry hydrogel's network and its macropores, remains in the range of 159.0±4.5 g g^{-1} – 184.3±14.1 g g^{-1}, indicating excellent superabsorbent properties, and Q_v, characterizing the size expansion due to the water uptake solely by the polymer network, falls in the range of 18.0±5.8 cm^3 cm^{-3} – 33.3±6.6 cm^3 cm^{-3}. The fluctuations of the Q_v values may derive from the fact that the volumetric method of swelling determination suffers from certain limitations, such as the effect of minor defects of the samples, e.g. the possible entrapment of some air bubbles during the fabrication

process, and the quite approximate way of the volume measurement.

Figure 2.8b presents the results of the permeability tests conducted for the PSA and the PSA_CNN3 cryogels through gravity driven filtration to study how the pore size and the overall morphology of the two materials can affect their liquid transporting ability. In fact, it strongly depends not only on the pores interconnectivity, but also on their size, which was found to decrease with the introduction of 3 % w/w of CNNs wrt the monomer. The attained results show that the addition of the CNNs into the polymer matrix at the highest studied loading does not influence the water flow rate of the cryogel and values of ~ 3500-3700 L m^{-2} h^{-1} are reached, implying excellent permeability of the obtained cryogels, and enlightening their potential application in the gravity-driven water filtration.

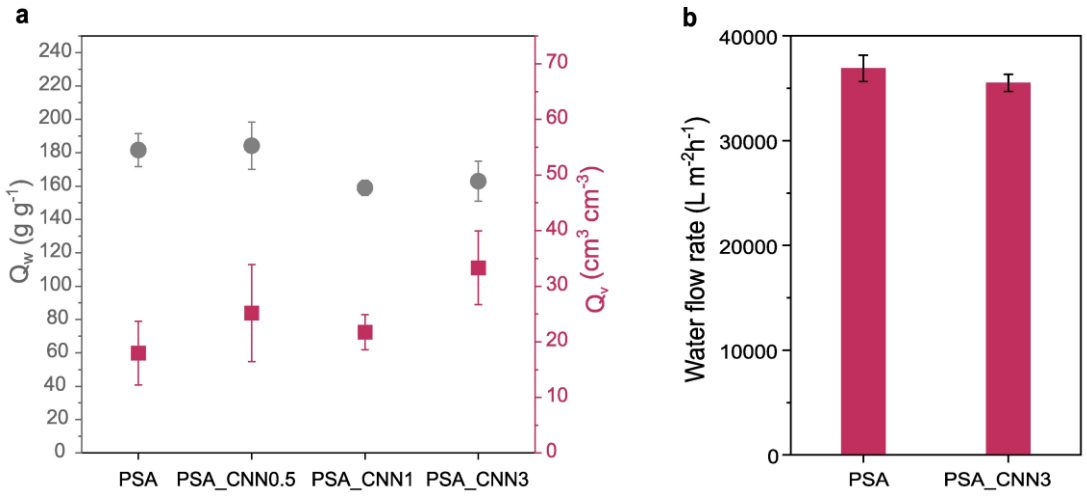

Figure 2.8. a) The gravimetric swelling degrees (Q_w) and the volumetric swelling degrees (Q_v) of the PSA, the PSA_CNN0.5, the PSA_CNN1, and the PSA_CNN3 cryogels with an inset of a photograph of the PSA cryogel in a dry and swollen state. b) The water flow rate of the PSA and the PSA_CNN3 cryogels determined in gravity-driven filtration tests.

Another important property of the developed cryogels, is their underwater oleophobicity, typically exhibited by the hydrogel materials[258,323–325]. The UOCA was

determined for two types of oils: a less viscous SB oil and a highly viscous silicone oil of 500 cPs (Figure 2.9). In case of the former one, the PSA, the PSA_CNN1, and the PSA_CNN3 cryogels were tested, whereas for the latter one the PSA and the PSA_CNN1 cryogels were used. The representative snapshots of the recorded videos are shown in a chronologically numbered order, where the direction of the arrows indicates the direction of the movement of the needle with the oil drop: approaching (up) and distancing (down) from the cryogel's surface. As shown, the study was conducted at different increasing oil drop volumes, as no adhesion of the oil drop to the cryogel surface was occurring at the starting volume of 10 µL. Nonetheless, regardless of the oil and the cryogel types, complete repellence of the oils by the material's surface was observed. This is well visible in the snapshots were the oil drops put in contact with the cryogel's surface were undergoing bending. As shown in step 5, the oil drops did not adhere despite a close contact with the cryogel's surface. This implies that the studied cryogels exhibit superior underwater superoleophobic properties. The combination of the superhydrophilic and underwater superoleophobic properties makes them an excellent candidate for the oil-water separation applications.

Figure 2.9. Video stills from underwater oleophobicity tests performed with SB oil for a) the PSA, b) the PSA_CNN1, c) the PSA_CNN3 representative cryogel samples, and with silicone oil for d) PSA, and e) PSA_CNN1 representative cryogel samples.

2.5 MECHANICAL PROPERTIES OF CRYOGELS

The influence of the CNN fillers presence in the PSA matrix on the mechanical performance was also evaluated for the PSA, the PSA_CNN1, and the PSA_CNN3 cryogels in the swollen state. As in case of the other above-discussed properties, it was found that the nanofillers do not either affect the mechanical properties of the cryogels. In fact, the excellent mechanical stability and flexibility of the cryogels was proved for 5 consecutive compression cycles, where both the PSA and the PSA/CNN nanocomposite cryogels showed the stress relaxation ratio equal to ~1 in all the cycles (Figure 2.10a). On the top, as presented in Figure 2.10b, for all the cryogel types, the hysteresis loops formed during the loading-unloading process of the compression cycle confirm the viscoelastic character of the cryogels[326], while their shape and area do not show significant differences confirming that the viscoelastic properties are not affected by the presence of CNNs. As shown in Figure 2.10c, the Young's modulus (E) is equal to ~2 kPa for all the cryogel types.

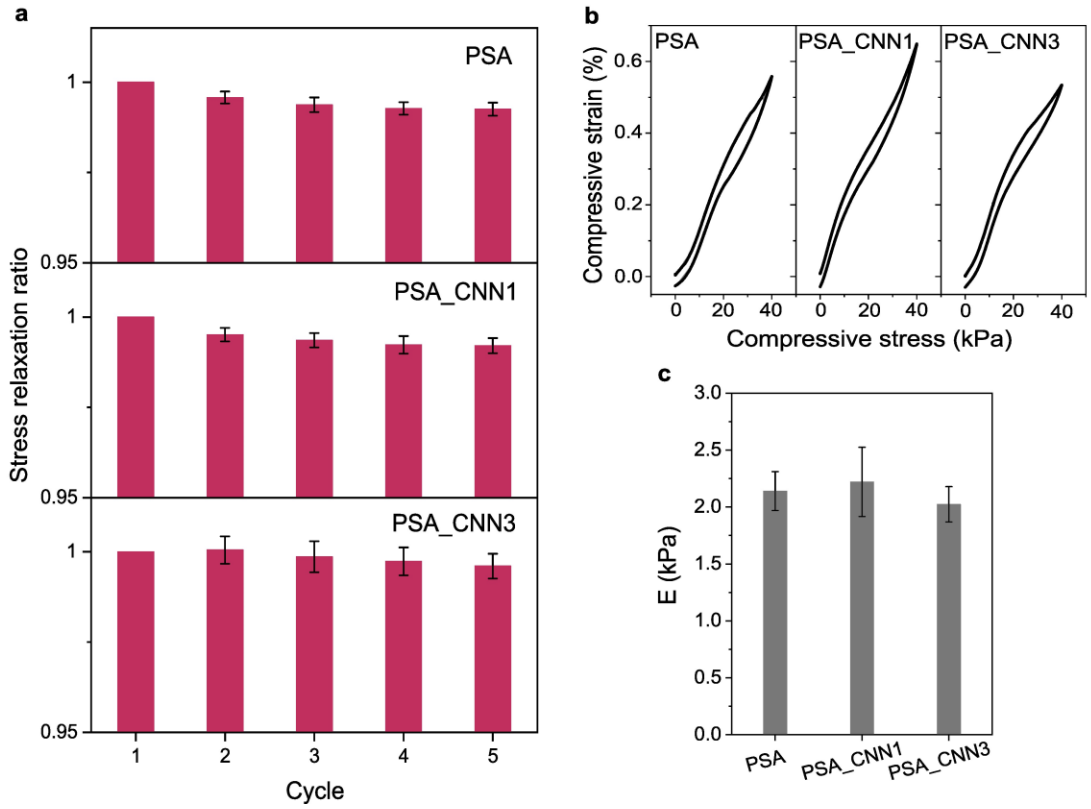

Figure 2.10. Mechanical properties of the PSA, the PSA_CNN1 and the PSA_CNN3 cryogels in swollen state: a) stress relaxation ratio between each compression peak and the compression peak of the first cycle in 5 loading-unloading cycles, b) stress-strain hysteresis loop in the first loading-unloading cycle of the representative PSA, PSA_CNN1 and PSA_CNN3 samples, c) Young's modulus (E) obtained in the compression tests.

2.6 CONCLUSIONS

To sum up, porous neat and nanocomposite cryogels were fabricated through a simple one-step cryopolymerization synthesis method. The chemical composition study, performed by means of FTIR, confirmed the successful incorporation of the CNNs within the cryogel matrix, being more evident with the increase of their content, but it did not reveal any chemical interactions of the PSA polymer chains with the embedded CNNs. The porous CNNs nanosheets, and the roundish interconnected macropores structure of the neat PSA and the PSA/CNN cryogels was revealed through the morphological analysis. It was found that the incorporation of the CNNs into the PSA

framework only slightly affects the morphology of the cryogels, causing thinning of the polymer walls with the CNNs content increase and the pore size reduction in case of the CNNs loading of 3 % w/w wrt the monomer. Importantly, high porosity of all the cryogels, independent of the CNNs content was unveiled, proving the success of the developed method for the support of the CNNs by a highly porous PSA network, and revealing that the CNNs' presence in the cryogels synthesis reaction solution does not influence the relative volume of the formed ice crystals, acting as a porogen. The obtained microstructure of the materials, combined with their hydrophilic character, resulted in excellent gravity-driven water permeability, with high flow rates, which seem not to be affected by the CNNs' presence within the cryogel matrix, staying in the range of ~ 3500-3700 L m^{-2} h^{-1}. On the top, all the cryogel types have shown highly performant and rapid water uptake of 159.0±4.45 g g^{-1} – 184.3±14.1 g g^{-1}, and their underwater superoleophobic character was unveiled towards both low- and high-viscosity oils. All the cryogels proved mechanical stability and flexibility in consecutive compression cycles.

Such superior wetting and swelling properties, combined with good mechanical performance, as well as high porosity and interconnectivity of the pores of the prepared cryogels suggested their potential for the use in water-soluble pollutants adsorption and oil-water separation processes. Moreover, the successful introduction of the CNNs into the polymer network without compromising the above-listed material's properties, opened the way for the studies on their application as a multifunctional nanofiller of polymer cryogels for water treatment and quality monitoring, as will be presented in the following chapters.

Chapter 3: Dye and heavy metal ions adsorption by PSA and PSA/CNN cryogels: Batch conditions studies

In this chapter, the study on the adsorption performance of the neat PSA and the PSA/CNN nanocomposite cryogels towards both organic and inorganic pollutants in batch conditions, i.e. through the sorbents' immersion in their solutions, is discussed. In particular, methylene blue (MB) dye and Hg^{2+} ions were used as representative organic and inorganic contaminants, respectively. The cationic character of both compounds enables their interaction with the anionic poly(sodium acrylate) PSA matrix. As proved, the negatively charged CNN fillers slightly contribute to the sorption process, not affecting significantly the overall performance of the composite cryogel.

The adsorption of Hg^{2+} through the ion exchange mechanism with Na^{+} from the carboxylic groups of PSA, and the adsorption of MB via the electrostatic interactions with PSA were proven. Moreover, in case of the PSA/CNN cryogels, the prevalence of such adsorption mechanism over sorption by the embedded CNNs, was ascertained. The kinetics of the adsorption process of MB and Hg^{2+} as single pollutants was investigated for both cryogel types, and it was found that it is rapid, lasting only several minutes, and the presence of CNNs further accelerates its. For both Hg^{2+} ions and MB adsorption, both the pseudo-first order and the pseudo-second order kinetic models were proved to fit the experimental data for all the studied cryogels, suggesting a complex sorption process including physisorption and chemical interactions. The equilibrium adsorption capacities of both contaminants in a broad concentration range

were also determined, and the maximum adsorption capacities of MB and Hg^{2+} were calculated from the Langmuir isotherm model, which has proven to fit better the experimental data than the Freundlich model. In particular, for Hg^{2+} the maximum adsorption capacities of 615±42, 634 ±49, and 555±33 mg g^{-1} are reached for the PSA, PSA_CNN0.5, and PSA_CNN3 cryogels, respectively, whereas for MB the respective values of 2894.1±237.0, 2913.7±226.2, and 4763.5±474.5 mg g^{-1} were reached for the PSA, PSA_CNN0.5, and PSA_CNN1 cryogels. It has also been found that at moderate concentrations of the pollutants, the incorporation of CNN nanofillers into the polymer matrix slightly enhances the adsorption capacities of the cryogel. The sorption process was studied not only for the single pollutants, but also for their mixture, and only a slight decrease of the equilibrium adsorption capacities of both compounds was observed, whereas there is no significant effect of their co-existence on the sorption mechanism. In conclusion, the excellent adsorption performance of the developed cryogels was unveiled.

3.1 MATERIALS AND METHODS

3.1.1 Materials

Methylene blue (MB) purchased from Sigma-Aldrich, mercury (II) chloride ($HgCl_2$) and lead (II) nitrate ($Pb(NO_3)_2$) were purchased from Sigma-Aldrich and used for the preparation of MB, Hg^{2+} ions and Pb^{2+} ions aqueous solutions. KBr powder purchased from Sigma-Aldrich was used for the preparation of the samples for the FTIR analysis. All the chemicals were used as received without further purification. All the experiments were performed with the use of Milli-Q water.

3.1.2 Adsorption capacity determination

The batch adsorption experiments were conducted through the immersion of one cryogel (~3 mg) in 15 mL of the given pollutant's aqueous solutions of known concentrations. The solutions were kept under continuous agitation in a vortex mixer at 600 rpm. In case of MB, they were left in the dark due to its photosensitivity. For the adsorption kinetics study, same volume aliquots of the solutions were collected at the following immersion time intervals: 1 min, 5 min, 10 min, 15 min, 30 min, 60 min, and 24 h for MB and at: 5 min, 20 min, 45 min, 2 h, 3 h, and 6 hours for Pb^{2+} and Hg^{2+} ions. In case of the study of the adsorption capacity dependence on the pollutant's concentration, the cryogels were immersed for 24 h in the MB solutions and for 5 h in the Hg^{2+} solutions, at given pollutant's concentrations. The adsorption capacity of MB at the concentration range of 10-100 mg L^{-1} was also determined after 6 days from the immersion, in order to evaluate if MB desorption takes place. Apart from the isolated components, also the pollutants mixture was used for the definition of the adsorption capacity. In particular, the MB and Hg^{2+} adsorption capacity was determined after immersing the cryogels for 5h in the aqueous mixtures of the two pollutants (containing i) 5 mg L^{-1} of MB and 5 mg L^{-1} of Hg^{2+} and ii) 10 mg L^{-1} of MB and 20 mg L^{-1} of Hg^{2+}), right after the solutions' preparation, in order to maintain the same conditions in case of the possible interactions between MB and Hg^{2+}. The adsorption kinetics experiments were performed in triplicates, whereas the study of the adsorption dependence on the pollutant's concentration was conducted in duplicate.

The adsorption capacity of the studied pollutants at the equilibrium conditions (q_{e_x}, mg g^{-1} cryogel) or after a specific time of immersion (q_x, mg g^{-1} cryogel), was calculated as follows:

$$q_{e\_x} = \frac{m_{x\_i} - m_{x_f}}{m} \quad (3.1)$$

where m_{x_i} and m_{x_f} are the initial and the final masses (mg) of the given pollutant (x: Pb or Hg or MB) in the analyte solution, respectively, and m (g) is the mass of the dry cryogel.

Regarding the adsorption kinetics study, the adsorption capacity of the given pollutant at determined immersion times, q_{t_x} (mg g^{-1} cryogel) was calculated by Equation (3.1), replacing q_{e_x}, and substituting m_{x_f} with the mass of the pollutant at the specific immersion time (m_{x_t}). The $m_{MB\_i/f}$ values were determined using a Varian Cary 6000i UV–vis–NIR spectrophotometer by recording the absorbance spectra of the MB solutions in the range of 350-800 nm. Subsequently, they were analysed using Origin software to determine the area under the Absorbance-Wavelength curve in a range from 415 to 800 nm, $A_{415\text{-}800nm}$, which was used to calculate the $m_{MB\_i/f}$ as follows:

$$m_{MB\_i/f} = \frac{A_{415-800nm} \times V \times D}{a} \quad (3.2)$$

where V is the total volume of the analyte solution, D is the dilution factor, and a is the slope value of a calibration curve resulting from the linear fitting of $A_{415\text{-}800nm}$ obtained for the absorbance spectra of MB solutions of known concentrations (0 to 4 mg L^{-1}) versus these concentrations. The linear regression equation was $y = a \times x$ (R^2 value of > 0.999), where y is $A_{415\text{-}800nm}$, x is the MB concentration, and a is equal to 18.967.

The $m_{Pb\_i/f}$ and the $m_{Hg\_i/f}$ values were determined measuring the concentration of the Pb^{2+}/Hg^{2+} ions in the heavy metal ions solutions,with an Inductively Coupled Plasma Optical Emission (ICP-OES) spectrometer iCAP (7600 DUO Thermofisher Scientific) at the auxiliary gas, coolant gas and nebulizer gas flows of 0.5 L min^{-1}, 12 L min^{-1}, and 0.5 L min^{-1}, respectively. An internal standard calibration curve was used and 3 scans per sample were conducted. The samples for the analysis were prepared in polypropylene volumetric ICP flasks by adding a specific volume of a Pb^{2+}/Hg^{2+} solution, previously vortexed for 10s, treating it with aqua regia (10% of the volume

flask) and diluting the as-obtained mixture up to the calibration line, followed by filtering it through PTFE syringe filters (diameter 15 mm, pore size 0.45 um, Sartorius, Germany). The Pb^{2+}/Hg^{2+} mass (mg) in the initial solutions (m_{Pb/Hg_i}) and in the collected aliquots (m_{Pb/Hg_f}) was determined as follows:

$$M_{Pb/Hg\_i/f} = c_{Pb/Hg\_i/f} \times V \times D \quad (3.3)$$

where $c_{Pb/Hg\_i/f}$ (mg L^{-1}) is the concentration of Pb^{2+} or Hg^{2+} in the initial solutions/the collected aliquots, determined by means of ICP-OES, and V (L) is the volume of the analyte solution, and D is the dilution factor.

3.1.3 Adsorption isotherm and adsorption kinetics models fitting

The non-linear fittings of the adsorption kinetics models, namely the pseudo-first order, and the pseudo-second order ones, were applied to the acquired datasets of the experimental adsorption capacity at determined immersion time for a given pollutant and initial concentration, and for the different cryogel types using the OriginPro software. To this aim, the pseudo-first order[327] (Eq. 3.4) and pseudo-second order[328] (Eq. 3.5) kinetics models were applied:

$$q_t = q_e\,(1 - e^{(-k_1 t)}) \quad (3.4)$$

$$q_t = \frac{k_2 \times q_e^{\,2} \times t}{1 + k_2 \times q_e^{\,t}} \quad (3.5)$$

where: q_t (mg g^{-1}) is the adsorption capacity at determined immersion times, q_e (mg g^{-1}) is the equilibrium adsorption capacity, k_1 (min^{-1} for MB and h^{-1} for Hg^{2+}) is the pseudo-first order adsorption rate constant, k_2 (g mg^{-1} min^{-1} for MB and g mg^{-1} h^{-1} for Hg^{2+}) is the pseudo-second order adsorption rate constant, and t is the immersion time. The adsorption rate constants, k_1 and k_2, as well as the theoretical equilibrium adsorption capacities for a given pollutant, denoted as $q_{e\_x(calc)}$ (mg g^{-1}), where x: MB or Hg, were derived through the performed fitting.

The acquired datasets of the experimental adsorption capacity for a given pollutant (x: MB or Hg), q_{e_x} vs the concentration of the pollutant in the solution after the sorption process reaches the equilibrium, C_{e_x} (mg L^{-1}), were fitted to the Langmuir and the Freundlich isotherm models for the different cryogel types. To this aim, using the OriginPro software, the linear fittings were performed using Equations (3.8) and(3.7), and for the non-linear fittings Equations (3.8) and (3.9), were used[329,330]:

$$Langmuir\ model\text{:}\ \frac{1}{q_e} = \frac{1}{q_{max}} + \frac{1}{q_{max} \times k_L \times C_e} \tag{3.6}$$

Here the x and the y axis is determined as C_e and $\frac{1}{q_e}$, respectively.

$$Freundlich\ model\text{:}\ \log(q_e) = \log(k_F) + \frac{1}{n}\log(C_e) \tag{3.7}$$

Here the x and the y axis is determined as $\log(c_e)$ and $\log(q_e)$, respectively.

$$Langmuir\ model\text{:}\ q_e = \frac{q_{max}(k_L \times C_e)}{1 + k_L \times C_e} \tag{3.8}$$

Here the x and the y axis is determined as C_e and q_e, respectively.

$$Freundlich\ model\text{:}\ q_e = k_F \times C_e^{1/n} \tag{3.9}$$

Here the x and the y axis is determined as C_e and q_e, respectively.

In all the above Equations (3.6)-(3.9), q_{max} (mg g^{-1}) is the maximum adsorption capacity, i.e. the maximum possible amount of the adsorbate per gram of adsorbent, C_e is the equilibrium concentration (mg L^{-1} and µg L^{-1} in case of Equation (3.7)), whereas k_L (L mg^{-1}) is the Langmuir constant, and k_F ((mg g^{-1})/(mg L^{-1})$^{1/n}$) and n are the Freundlich constants[331].

3.1.4 Na^+-Hg^{2+} molar ratio determination

The release of Na^+ ions from the cryogels, during their immersion in 15 mL of Hg^{2+} aqueous solutions at different concentrations, and during their immersion in 15 mL of the aqueous solutions of MB and MB-Hg^{2+} mixture at a specific concentration of the

pollutants, was determined to explore the possible ion exchange mechanism of Hg^{2+} and MB adsorption by the cryogels. To assure that the Na^+ release is attributed solely to the said exchange, the normalized Na^+ release at the equilibrium conditions, $q_{r(e)\_Na\_ex}$ (mg g^{-1} cryogel), was determined as follows:

$$q_{r_{(e)\_Na\_ex}} = q_{r_{(e)\_Na}} - q_{r_{Na\_w}} \quad (3.10)$$

where $q_{r(e)\_Na}$ (mg g^{-1} cryogel) is the Na^+ release upon the cryogel's immersion for 5 h in 15 mL of the pollutants' aqueous solutions after 5 h, whereas q_{rNa_w} (mg g^{-1} cryogel) is the Na^+ release upon the cryogel's immersion for the same time in 15 mL of pure water, and they were calculated as follows:

$$q_{r_{(e)\_Na/Na\_w}} = \frac{m_{Na\_f} - m_{Na\_i}}{m} \quad (3.11)$$

where m_{Na_f} and m_{Na_i} are the Na^+ mass (mg) after the immersion in the solutions, and the initial Na^+ mass (mg) in those solutions, respectively, while m (g) is the mass of the dry cryogel. The m_{Na_f} and m_{Na_i} determination was performed by the ICP-OES analysis, following the procedure described in Section 3.1.2, substituting $m_{Pb/Hg\_i/f}$ and $c_{Pb/Hg\_i/f}$ in Equation (2.1) with $m_{Na\_i/f}$ and $c_{Na\_i/f}$, respectively.

The kinetics of Na^+ release during the cryogel's immersion in pure water and in Hg^{2+} aqueous solutions at different concentrations was also explored, and the Na^+ release at the specific time of immersion in 15 mL of a Hg^{2+} solution, m_{Na_t} was also determined, using Equation (3.12) where m_{Na_f} is substituted by m_{Na_t}.

Finally, the molar ratio of Na^+ released (solely due to Na^+-Hg^{2+} ion exchange) per 1 mol of Hg^{2+} adsorbed was calculated according to the following equation:

$$\text{molar ratio}_{(Na/Hg)} = \frac{q_{r(e)\_(mol)\_Na}}{q_{e(mol)\_Hg}} \quad (3.12)$$

where $q_{r(mol)\_Na}$ is the Na^+ molar release and $q_{e/t(mol)\_Hg}$ is the Hg^{2+} molar adsorption capacity at the equilibrium (both in mol L^{-1} g^{-1} cryogel), calculated as follows:

$$q_{r(mol)Na} = \frac{q_{r(e)\_Na\_ex}}{M_{Na} \times m} \quad (3.13)$$

$$q_{e(mol)Hg} = \frac{q_{eHg}}{M_{Hg} \times m} \quad (3.14)$$

where q_{eHg} is the Hg^{2+} adsorption capacity at the equilibrium (mg g^{-1}), $M_{Na/Hg}$ (g) is the molecular weight of sodium/mercury, and m (g) is the mass of the dry cryogel.

The experiments of Na^+ release at the equilibrium conditions of the pollutants' adsorption were performed in duplicate, while for all the rest, the experiments were conducted in triplicates and the mean values together with the standard deviations were presented.

3.1.5 Chemical analysis of cryogels after their interaction with the pollutants

The chemical composition of the PSA cryogel (in dry conditions) before and after its immersion in the aqueous solution of MB until the equilibrium adsorption conditions are reached, was analyzed with the use of a Fourier Transform Infrared (FTIR) spectrometer (Vertex 70v FT-IR, Bruker) in transmission mode. All the spectra were recorded from 4000 to 600 cm^{-1} and 64 repetitive scans were run at a resolution of 4 cm^{-1} with the background spectrum collected for the same number of scans. Using the instrument's software the results were transformed from transmittance to absorbance. In order to prepare the samples for the analysis, firstly the neat PSA and MB-loaded PSA cryogels were dried in the oven at 80 °C, until the cryogel could be easily pulverized in a ceramic mortar. Next, KBr powder (previously dried overnight in the oven at 100 ° C due to its hygroscopic character), was added to the pulverized cryogel sample, in the amount of 1 % w/w with respect to the sample's mass, and the mixture was well-grinded in the same mortar, transferred to a pellet press machine, and pressed for 2 min. A KBr pellet was prepared in the same way, for the background correction.

The obtained pellets were dried at 80 °C in the oven directly before recording their spectra, using a solid sample holder.

The absorbance spectra of the swollen PSA and PSA/CNN cryogels before and after their interaction with the aqueous solutions of MB and of MB-Hg^{2+} mixture, at a corresponding concentration of MB in both solutions, were acquired using a Varian Cary 6000i UV-visible-NIR spectrophotometer in the 350-800 nm wavelength range, and utilizing a solid sample holder.

3.2 ADSORPTION KINETICS STUDIES

3.2.1 Dye adsorption kinetics

The kinetics of the adsorption process of MB dye from its aqueous solutions at the c_{0_MB} of 1, 5 and 10 mg L^{-1} was evaluated for the PSA,the PSA_CNN1, and PSA_CNN0.5 cryogels, in the batch conditions. The study allowed determining the time necessary to reach the MB adsorption equilibrium by both cryogel types.

UV-vis absorption spectra of MB aqueous solutions over sorption time

The UV-vis absorbance spectra of the MB solutions at different cryogel's immersion time intervals were analysed in order to determine the q_{t_MB}, as described in Section 3.1.2. Their representative spectra (at the initial MB concentration of 10 mg L^{-1}) are shown in Figure 3.1, revealing the typical UV-vis absorbance spectrum of the monomer (in particular mesomer II) form of $MB^{332,333}$, with the maximum absorbance peak at 664 nm, gradually decreasing in intensity with the increase of the cryogel's immersion time. In case of the PSA cryogel, minor broadening of the spectra, suggesting partial dimerization of $MB^{332,333}$, obtained for the solutions in the first 10 minutes of the immersion is observed (Figure 3.1a), whereas no such effect is visible in case of the PSA_CNN1 cryogel. This can be ascribed to the fact that in aqueous

solutions both the monomer and the dimer form of MB may randomly occur, which is related to the molecules' self-aggregation[332–334]. Nevertheless, at higher immersion times, corresponding to the adsorption equilibrium conditions, the shape of the spectra acquired for both cryogel types does not differ (Figure 3.1c-d).

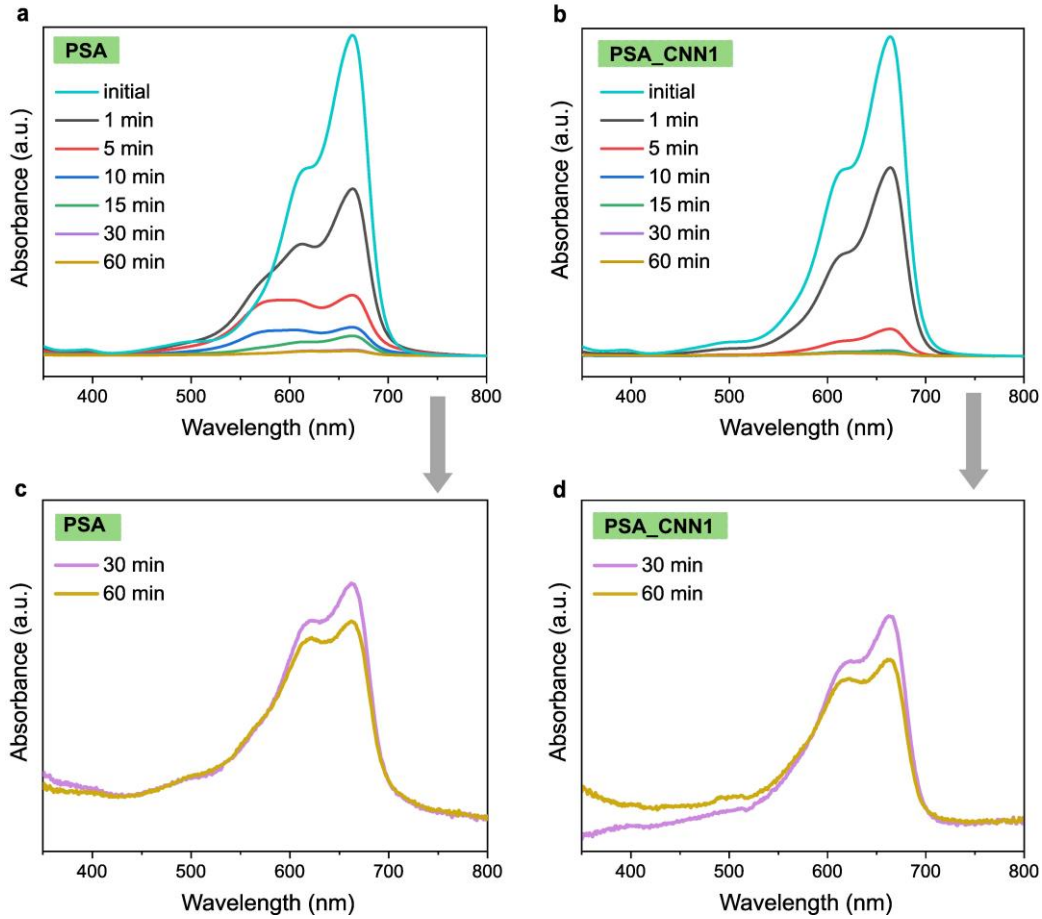

Figure 3.1. Representative spectra of MB aqueous solutions at different time intervals of the: a) PSA, b) PSA_CNN1 cryogel immersion, and c),d) the zoom-in of the corresponding spectra at two higher immersion times.

Time-dependent adsorption capacity of MB

The results of the study of the q_{t_MB} evolution in time are shown in Figure 3.2 (for the first 1h of the cryogels' immersion). As shown, for all the studied c_{0_MB} and cryogel types, the adsorption capacity increases rapidly within the first 5 min and arrives to the equilibrium within several minutes, indicating excellent sorption performance of both

the neat and the nanocomposite cryogels. The study has also revealed that, at the highest studied c_{0_MB} (10 mg L^{-1}), the PSA/CNN cryogels reach the equilibrium adsorption capacities faster than the neat PSA cryogels, i.e. within 10 min, while the neat PSA cryogel arrives to the equilibrium conditions a few minutes later. This implies that CNNs are possibly involved in the MB sorption process, slightly accelerating the time needed to achieve the equilibrium. Nonetheless, at lower MB concentrations (5 mg L^{-1} and 1 mg L^{-1}) the dye adsorption process seems not to be so much influenced by the CNNs presence, indicating that the main role in the sorption process is attributed to the PSA polymer, while the nanofillers interact with the pollutant only when a certain threshold of the sorbed pollutants' amount is reached.

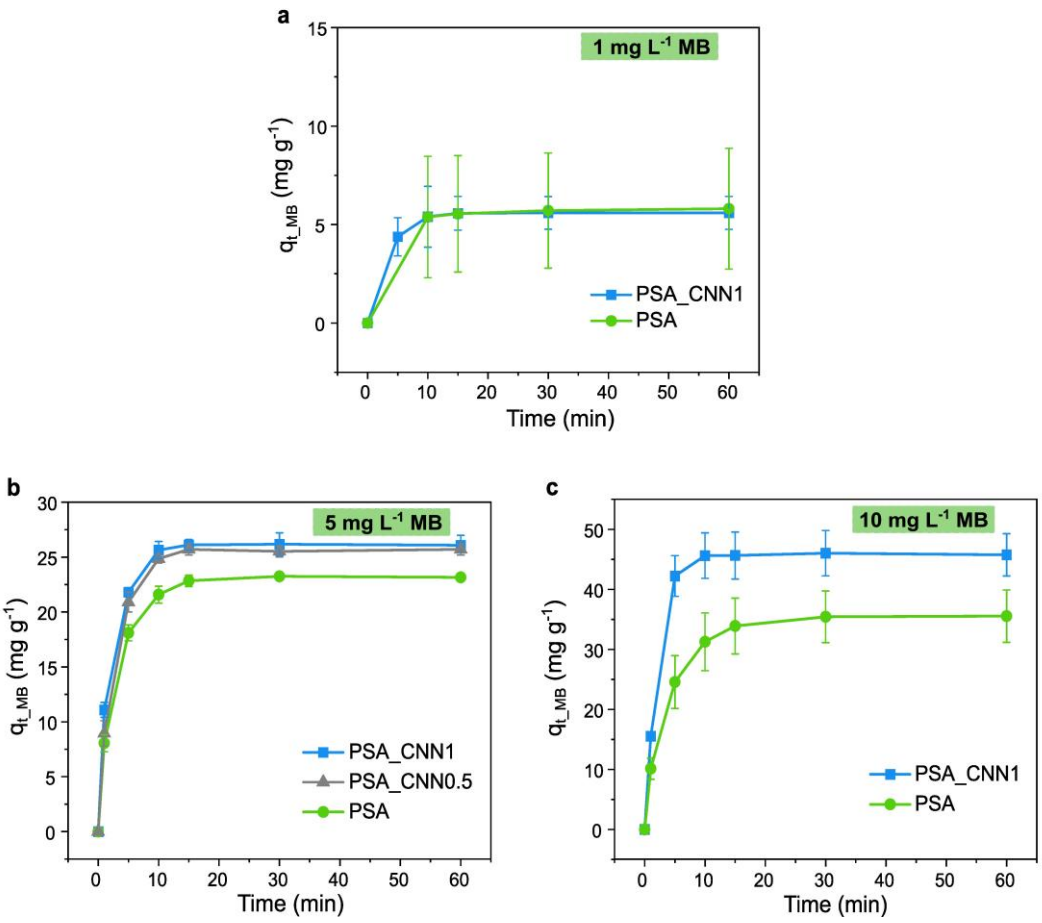

Figure 3.2. Effect of the contact time between the PSA or the PSA/CNN cryogels and a MB aqueous solution (at the initial MB concentrations of 1, 5 and 10 mg L^{-1}) on the MB adsorption capacity (q_{t_MB}).

It is worth noticing that once the equilibrium is reached, no desorption of MB is observed within 24h of the cryogels' immersion (Figure 3.3).

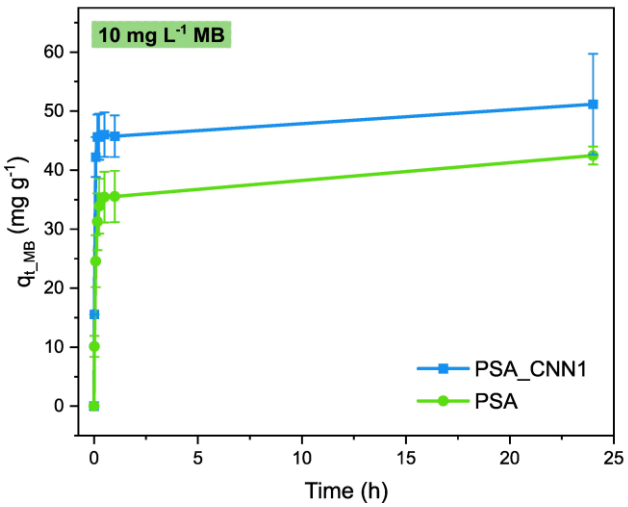

Figure 3.3. The evolution of q_{t_MB} over 24 h of the PSA and the PSA/CNN cryogels immersion in the MB aqueous solution at the initial MB concentration of 10 mg L^{-1}.

Adsorption kinetic models fitting for MB

In order to analyse the MB adsorption mechanism, the pseudo-first order and the pseudo-second order kinetics models were fitted to the obtained experimental data, as shown in Figure 3.4. It has been found that both models seem to fit quite well, exhibiting the coefficient of determination R^2 values of above 0.99 in almost all cases. Taking into consideration the obtained adsorption rate constants reached for a given cryogel type, it may be concluded that, for all cases, lower rate values are obtained for higher concentrations and this is more evident in the case of k_2, indicating that the sorption process is slower, requesting more time to reach equilibrium for higher MB concentrations. In case of k_1 the differences are less pronounced for the studied concentrations (Table 3.1).

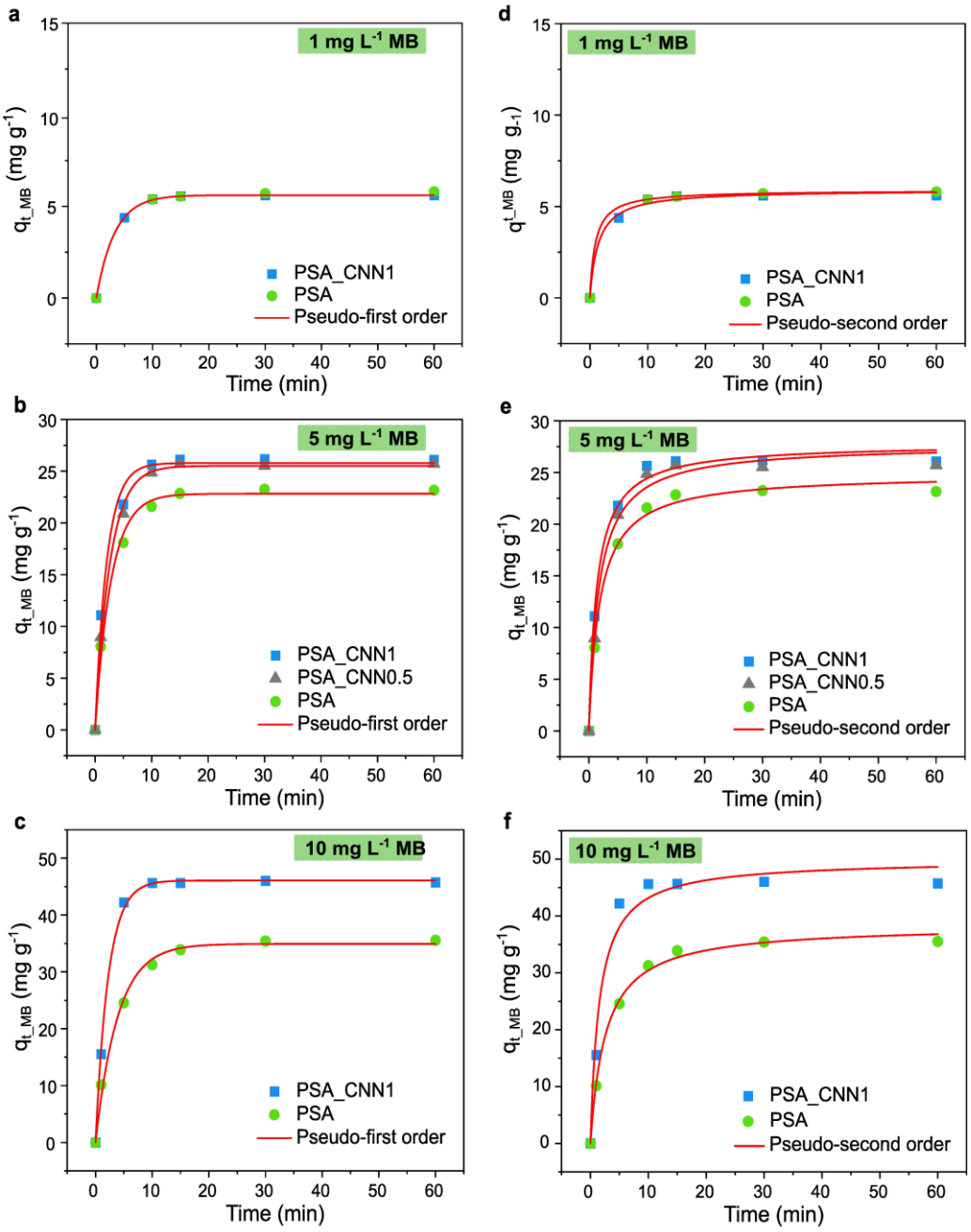

Figure 3.4. a-c) Pseudo-first-order and d-f) pseudo-second order kinetics model fitting curves of q_{t_MB} evolution over time on the data obtained for the PSA and the PSA/CNN cryogels at the initial MB concentrations of 1, 5 and 10 mg L^{-1}.

Table 3.1. Results obtained from the non-linear fitting of the MB adsorption kinetics experimental data by using the pseudo-first and the pseudo-second order kinetic models ($q_{e\_MB(exp)}$ is the experimental MB equilibrium adsorption capacity, and $q_{e\_MB(calc)}$ is the MB equilibrium adsorption capacity calculated from the fitting).

			Pseudo-first-order kinetic model			**Pseudo-second-order kinetic model**		
Sample	c_{0_MB} (mg L^{-1})	$q_{e\_MB(exp)}$ (mg g^{-1})	$q_{e\_MB(calc)}$ (mg g^{-1})	k_1 (min^{-1})	R^2	$q_{e\_MB(calc)}$ (mg g^{-1})	k_2 (g mg^{-1} min^{-1})	R^2
PSA	10	**35.54**±4.35	**34.93**±0.71	0.256±0.024	0.9940	**38.41**±0.76	0.010±0.001	0.9963
	5	**23.16**±0.34	**22.82**±0.41	0.354±0.034	0.9942	**24.85**±0.49	0.021±0.003	0.9955
	1	**5.81**±3.07	**5.62**±0.02	0.310±0.006	0.9999	**5.89**±0.00	0.180±0.001	1.0000
PSA_CNN0.5	5	**25.70**±0.50	**25.51**±0.29	0.380±0.024	0.9976	**27.70**±0.76	0.021±0.004	0.9909
PSA_CNN1	10	**45.75**±3.52	**46.08**±0.36	0.444±0.020	0.9988	**49.90**±2.15	0.013±0.004	0.9766
	5	**26.08**±0.90	**25.79**±0.48	0.483±0.054	0.9925	**27.79**±0.56	0.026±0.004	0.9942
	1	**5.60**±0.84	**5.62**±0.02	0.310±0.006	0.9999	**5.91**±0.17	0.116±0.032	0.9934

Overall, it may be concluded that both pseudo-first and pseudo-second order kinetic models describe well the MB adsorption mechanism in all the studied concentrations. This implies that the adsorption of MB by both cryogel types is governed by a complex sorption process including physisorption and chemical interactions of the MB molecules with the functional groups of the cryogels[335,336].

3.2.2 Heavy metal ions adsorption kinetics

The kinetics of the adsorption process of Pb^{2+} and Hg^{2+} ions from their aqueous solutions at the c_{0_Hg} of 5 and 20 mg L^{-1} was evaluated for the PSA, the PSA_CNN0.5, and the PSA_CNN3 cryogels.

Time-dependent adsorption capacity of Hg^{2+}

Figure 3.5 shows the adsorption kinetics of both the neat PSA and the PSA/CNN cryogels for Hg^{2+} (5 and 20 mg L^{-1}). For each cryogel type the behaviour is the same, regardless of the used c_{0_Hg}, with a rapid adsorption capacity increase in the first 5 min and a following slower adsorption of the heavy metal ions remaining in the solution, until reaching the equilibrium.

Importantly, in case of the PSA cryogel, the adsorption equilibrium is reached within 20 min for 5 mg L^{-1} Hg^{2+}, and within 45 min for 20 mg L^{-1} Hg^{2+}, whereas in the case of the PSA_CNN3 cryogel the sorption process seems faster. These results indicate the involvement of the CNNs in the Hg^{2+} sorption process at the higher studied Hg^{2+} concentration, accelerating it, and decreasing the time necessary to reach the equilibrium adsorption capacity. Thus, as also observed in case of MB sorption (Section 3.2.1), the role of the CNNs in the sorption process is more promoted at higher pollutant concentrations.

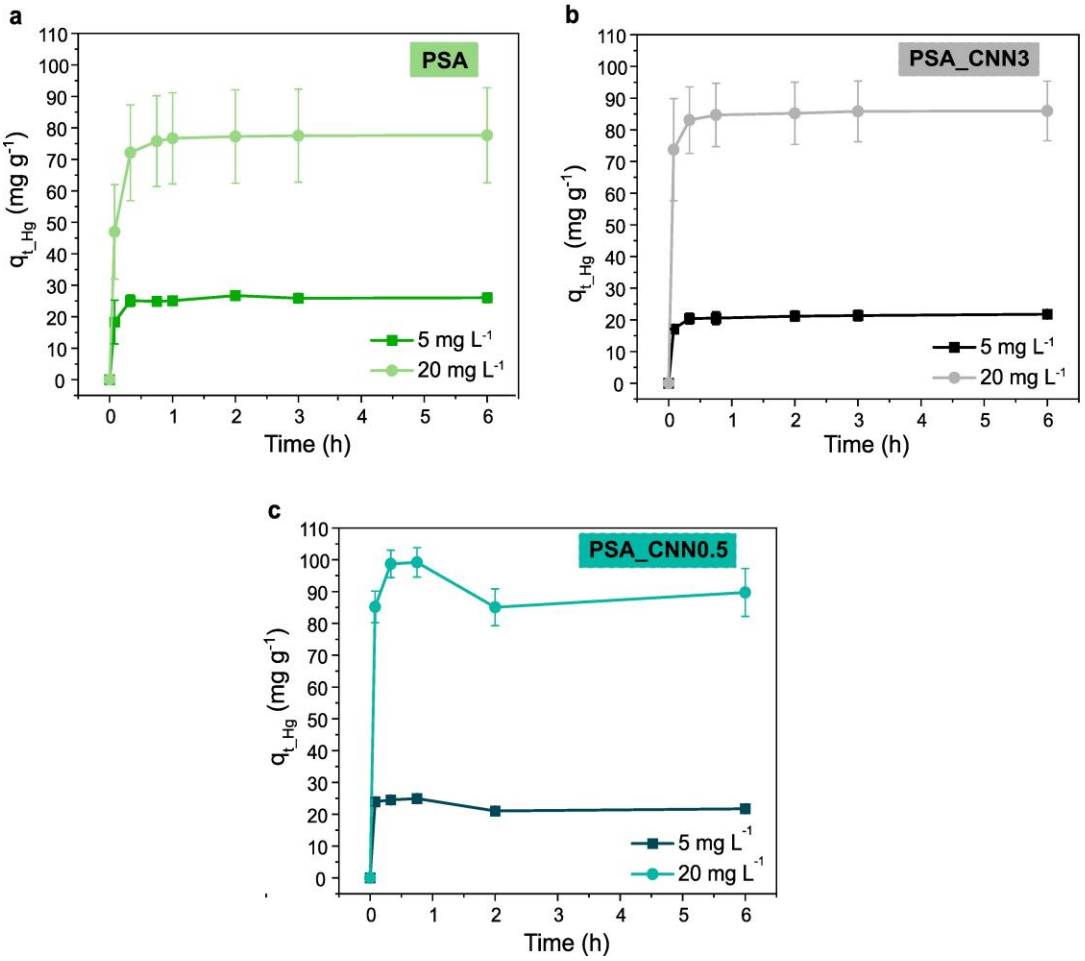

Figure 3.5. Effect of the contact time between the PSA (a) or the PSA/CNN (b-c) cryogels and the Hg^{2+} aqueous solutions (at the initial Hg^{2+} concentrations of 5 and 20 mg L^{-1}) on the Hg^{2+} adsorption capacity (q_{t_Hg}).

Adsorption kinetic models fitting for Hg^{2+}

In order to analyse the Hg^{2+} adsorption mechanism, the pseudo-first and the pseudo-second order kinetic models were fitted to the obtained experimental data, as shown in Figure 3.6a-c) and Figure 3.6d-f), respectively. In case of the PSA and the PSA_CNN3 cryogels, both models seem to fit well, with an exception of the PSA_CNN0.5 cryogel case, due to the unstable experimental data.

In order to further distinguish the best fitting kinetics model of Hg^{2+} adsorption by the cryogels, the values of the parameters derived from the fittings were analysed and presented in

Table 3.2. It has been found that no significant differences were observed between the $q_{e\_Hg(exp)}$ and the $q_{e\_Hg(calc)}$ and in the obtained values of the coefficient of determination R^2 for both models, indicating that, as in the case of MB, also in the present condition both models are valid for the description of the sorption process. Furthermore, as expected, higher initial Hg^{2+} concentrations result in lower sorption rates, while the presence of CNNs makes the sorption rates faster, indicating the role of the nanofillers in the sorption process.

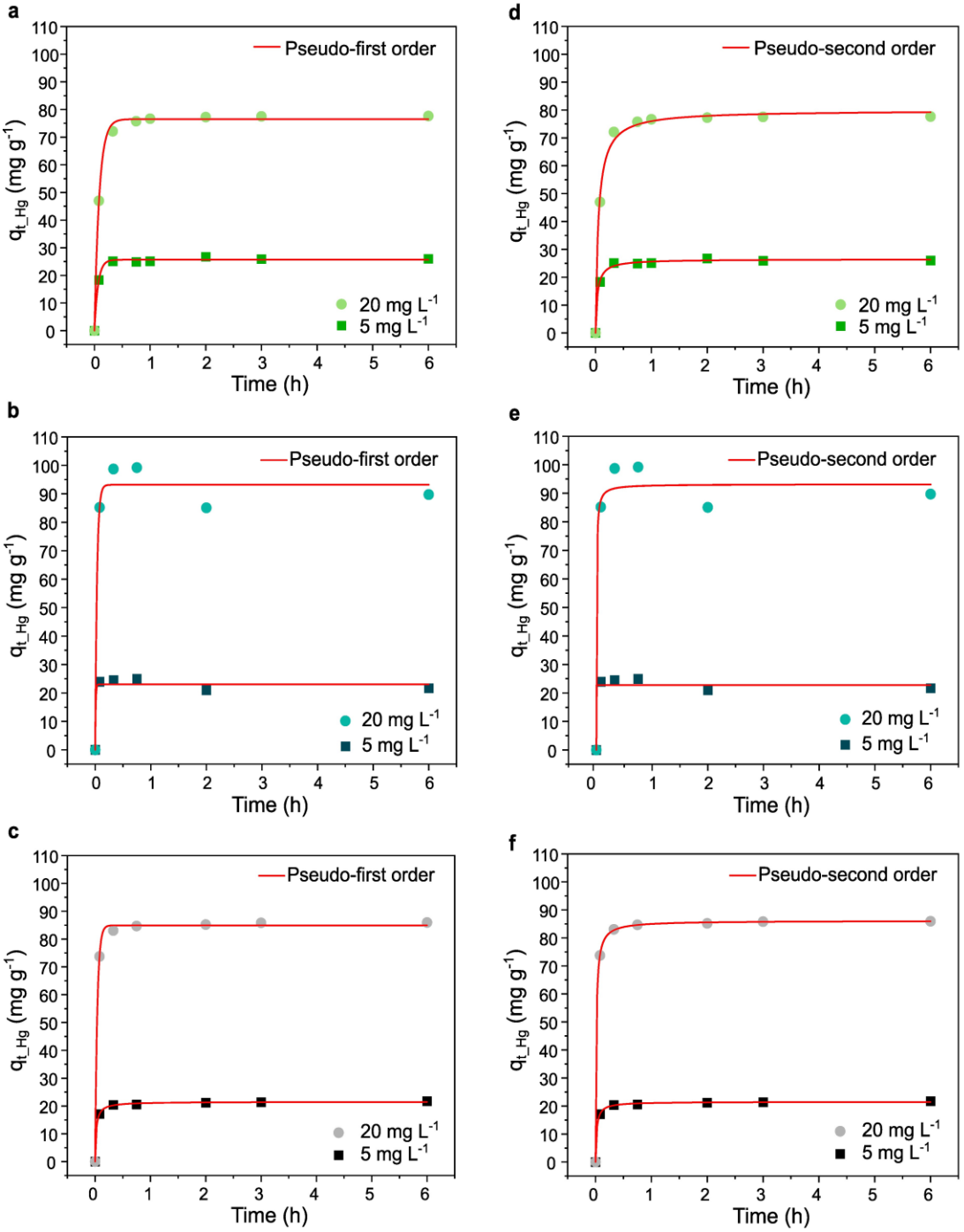

Figure 3.6. A pseudo-first-order and a pseudo-second-order kinetics model fitting curves of the Hg^{2+} adsorption capacity (q_{t_Hg}) evolution over time of the PSA (a,d), the PSA_CNN0.5 (b,e), and the PSA_CNN3 cryogels (c,f) for the initial Hg^{2+} concentrations of 5 and 20 mg L^{-1}.

Table 3.2. Results obtained from the non-linear fitting of the experimental Hg^{2+} adsorption kinetics data by using the pseudo-first and the pseudo-second order kinetics models ($q_{e\_Hg(exp)}$ is the experimental Hg^{2+} equilibrium adsorption capacity, and $q_{e\_Hg(calc)}$ is the Hg^{2+} equilibrium adsorption capacity calculated from the fitting).

			Pseudo-first-order kinetic model			**Pseudo-second-order kinetic model**		
Sample	c_{0_Hg} (mg L^{-1})	$q_{e\_Hg(exp)}$ (mg g^{-1})	$q_{e\_Hg(calc)}$ (mg g^{-1})	k_1 (h^{-1})	R^2	$q_{e\_Hg(calc)}$ (mg g^{-1})	k_2 (g mg^{-1} h^{-1})	R^2
PSA	20	**77.66**±15.09	**76.51**±0.58	11.640±0.590	0.9975	**79.89**±0.86	0.244±0.025	0.9968
	5	**26.03**±1.53	**25.66**±0.26	15.605±1.121	0.9959	**26.47**±0.31	1.125±0.149	0.9959
PSA_CNN0.5	20	**89.73**±7.51	**93.17**±3.01	30.728±10.360	0.9799	**93.20**±3.73	2.030±3.009	0.9761
	5	**21.71**±0.83	**23.04**±0.88	110.35± 7272.72	0.9732	**22.76**±1.02	380770.77± 2.57	0.9714
PSA_CNN3	20	**85.95**±9.41	**84.94**±0.47	25.293±1.250	0.9991	**86.12**±0.10	0.869±0.002	1.0000
	5	**21.77**±1.32	**21.51**±0.13	2.2554±0.188	0.9992	**21.51**±0.13	2.255±0.188	0.9992

Time-dependent adsorption capacity of Pb^{2+}

Figure 3.7 shows the adsorption kinetics of the neat PSA cryogel for Pb^{2+} (20 mg L^{-1}), depicting a rather slow adsorption process, which does not reach the equilibrium within the experimental time of 6 h. Furthermore, the q_{t_Pb} reached after 6 h of the PSA cryogel's immersion is lower compared to the q_{t_Hg} reached by the PSA cryogel (Figure 3.5) at the same time point (60.94±10.45 vs. 77.66±15.10). Therefore, it is evident that the PSA cryogel has significantly higher affinity to Hg^{2+} than to Pb^{2+} in aqueous solutions. Thus, the further studies are focused on Hg^{2+} as a representative inorganic pollutant.

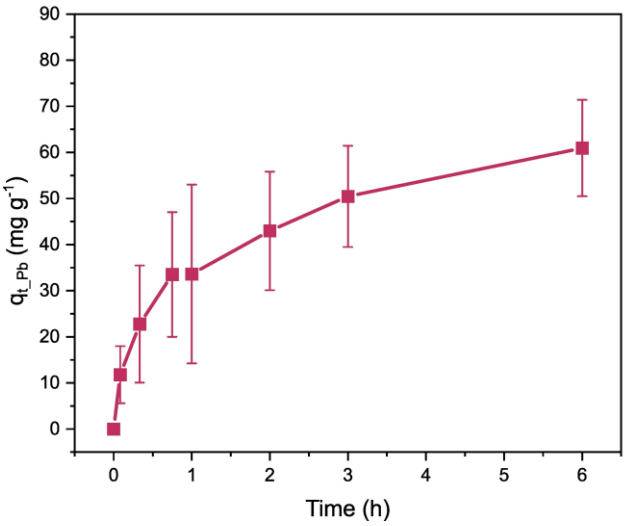

Figure 3.7. Effect of the contact time between the PSA cryogel and a Pb^{2+} aqueous solution (at the initial concentration of 20 mg L^{-1}) on the Pb^{2+} adsorption capacity (q_{t_Pb}).

3.3 ADSORPTION CAPACITY DEPENDENCE ON THE POLLUTANT CONCENTRATION

3.3.1 Adsorption capacity of MB and Hg^{2+} ions as single pollutants

The effect of the initial pollutant concentration to the equilibrium adsorption capacity for MB or Hg^{2+} in water was studied in attempt to assess the maximum adsorption capacity of the studied cryogels.

Concentration-dependent adsorption capacity of MB

Figure 3.8 presents MB adsorption isotherms of the PSA, PSA_CNN0.5 and PSA_CNN1 cryogels under different c_{0_MB} (in the range from 5 to 1300 mg L^{-1}), where the q_{e_MB} of the cryogels increases with the increment of the c_{0_MB} in the whole studied concentrations range. It was revealed that the PSA and the PSA_CNN0.5 cryogels exhibit similar adsorption capacity at different c_{0_MB} in the whole range of the studied concentrations, and they seem to be approaching the equilibrium in the range of ~500-1000 mg L^{-1} MB, whereas the q_{e_MB} of the PSA_CNN1 cryogel keeps increasing above

this concentration range. Nonetheless, both cryogel types exhibit very high q_{e_MB} values. Such an excellent performance might be attributed to the fact that the highly hydrophilic nature and the interconnected pores of the cryogel facilitate the passage of water, that simultaneously transports the MB molecules, and their adsorption by the carboxyl groups of PSA through electrostatic interactions[15], which is the subject of the study discussed in Section 3.4.2. In the presence of the higher amount of CNNs, the nanocomposite's capacity to adsorb MB is further improved, possibly due to the electrostatic attraction between the negative-charged CNNs and the positive-charged MB[337–340].

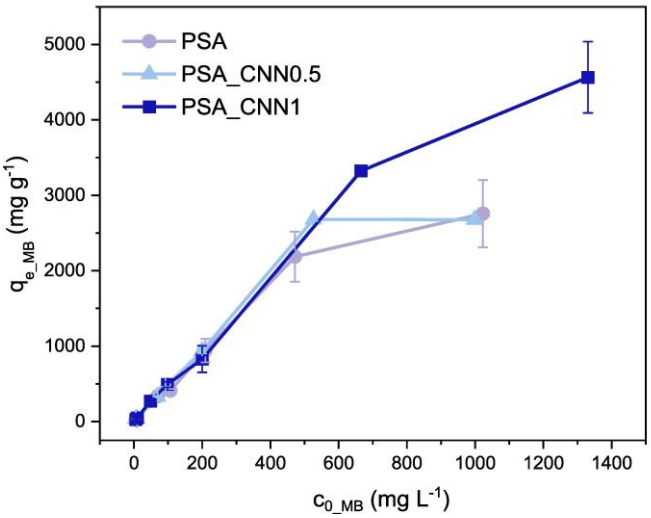

Figure 3.8. Effect of the initial MB concentration (c_{0_MB}) on the equilibrium MB adsorption capacity (q_{e_MB}) after a contact time of 24 h with the PSA and the PSA/CNN cryogels.

The q_{e_MB} values obtained after 24h and 6 days were also compared in the c_{0_MB} range of 10-100 mg L^{-1} and, as presented in Figure 3.9 , and no desorption was observed for any of the cryogels, indicating great stability of the MB adsorption process.

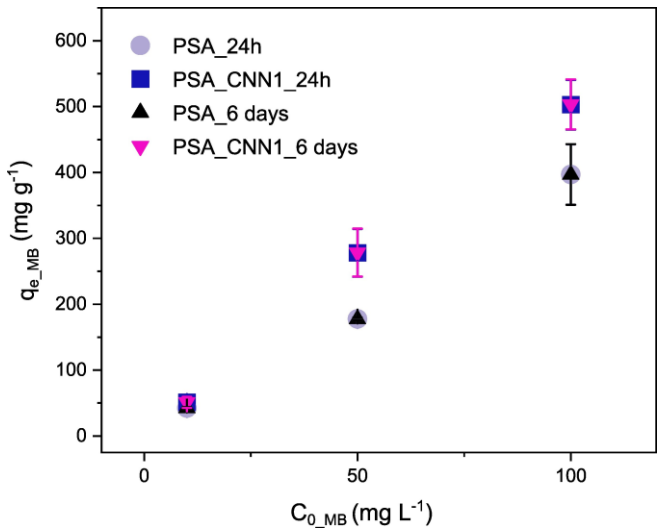

Figure 3.9. Effect of the initial MB concentration (c_{0_MB}) on the equilibrium MB adsorption capacity (q_{e_MB}) after a contact time of 24 h and 6 days with the PSA and the PSA_CNN1 cryogels.

Adsorption isotherm models fitting for MB

In order to further investigate the MB adsorption mechanism, the non-linear fitting to the Langmuir and the Freundlich isotherm models was performed on the equilibrium data, i.e. on the C_{e_MB} vs q_{e_MB} plots, for the different cryogel types, using Equations (3.8) and (3.9) respectively. As presented in Figure 3.10 and Table 3.3, the Langmuir model fits better the experimental data than the Freundlich one for all the studied cryogels. In particular, the R^2 values of 0.94-0.96 are reached in case of the Langmuir model, and the R^2 values as low as 0.64-0.73 are obtained for the fitting to the Freundlich model. Thus, the sorption mechanism is described by the monolayer adsorption on the homogenously distributed adsorption sites[330]. The calculated q_{max_MB} values (Table 3.3) of the PSA, the PSA_CNN0.5, and the PSA_CNN1 cryogels are equal to 2894.1±237.0, 2913.7±226.2, and 4763.5 ±474.5 mg g^{-1}, respectively.

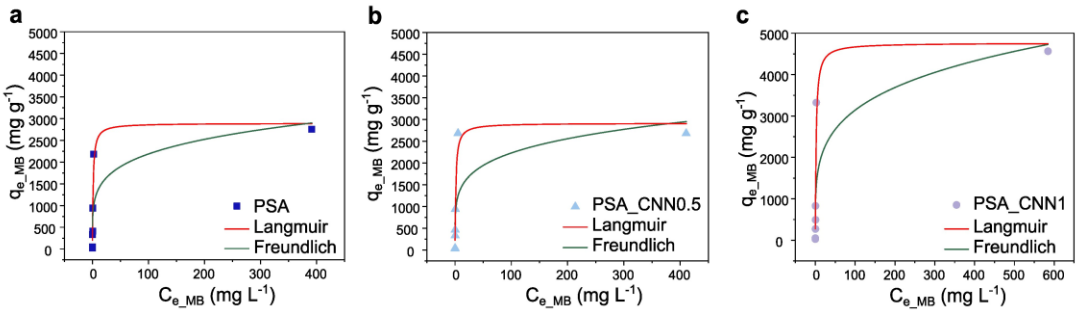

Figure 3.10. Non-linear fitting curves of MB adsorption experimental data to the Langmuir and the Freundlich isotherm models for the a) PSA, b) PSA_CNN0.5, c) PSA_CNN3 cryogels.

Table 3.3. Results obtained from the non-linear fitting of the MB adsorption experimental data by using the Langmuir and the Freundlich isotherm models (q_{max_MB} is the maximum MB adsorption capacity calculated from the fitting).

	Langmuir isotherm model			**Freundlich isotherm model**		
Sample	q_{max_MB} (mg g^{-1})	k_L (L mg^{-1})	R^2	1/n	k_F (mg g^{-1})/(mg L^{-1})$^{1/n}$	R^2
PSA	**2894.1**±237.0	0.774±0.199	0.9588	0.207±0.066	843.317±286.000	0.7009
PSA_CNN0.5	**2913.7**±226.2	0.717±0.210	0.9615	0.199±0.074	893.094±333.436	0.6410
PSA_CNN3	**4763.5** ±474.5	0.486±0.154	0.9426	0.232±0.074	1081.696±458.288	0.7294

Concentration-dependent adsorption capacity of Hg^{2+}

Figure 3.11 shows the Hg^{2+} adsorption isotherms of the PSA, PSA_CNN0.5 and PSA_CNN3 cryogels under different c_{0_Hg} (in the range from 5 to 400 mg L^{-1}). It has been found that both the neat PSA and the PSA/CNN cryogels are able to adsorb large amounts of Hg^{2+}, without significant differences in the q_e obtained by the different cryogel types. The overall excellent adsorption capacity of the cryogels is possibly attributed to the chemical nature of the PSA molecules and their functional groups of $-COO^-Na^+$ allowing for a Na^+-Hg^{2+} ion exchange. Indeed, the $–COO^-Na^+$-containing materials, including polyacrylates, have proven to be an efficient ion exchanger in the

sorption of heavy metal ions[312,341–346].

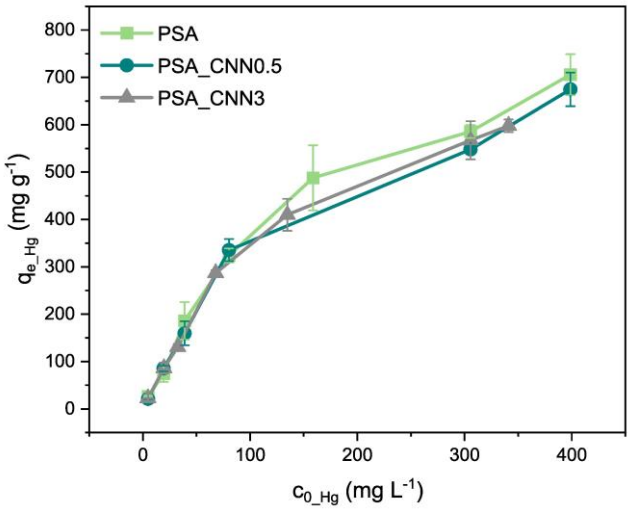

Figure 3.11. Effect of the initial Hg^{2+} concentration (c_{0_Hg}) on the equilibrium Hg^{2+} adsorption capacity (q_{e_Hg}) after a contact time of 5 h with the PSA and the PSA/CNN cryogels.

Adsorption isotherm models fitting for Hg^{2+}

In order to further investigate the Hg^{2+} adsorption mechanism, the non-linear fitting to the Langmuir and the Freundlich isotherm models was performed on the equilibrium data, i.e. on the q_{e_Hg} vs C_{e_Hg} plots, for the different cryogel types, using Equations (3.8) and (3.9), respectively. As presented in Figure 3.12 and Table 3.4, the Freundlich model fits better the data of the higher concentration values while the Langmuir model fits better the data of the lower part of the graphs, i.e. at lower pollutant concentrations, indicating that none of the adopted models is appropriate to represent the sorption process.

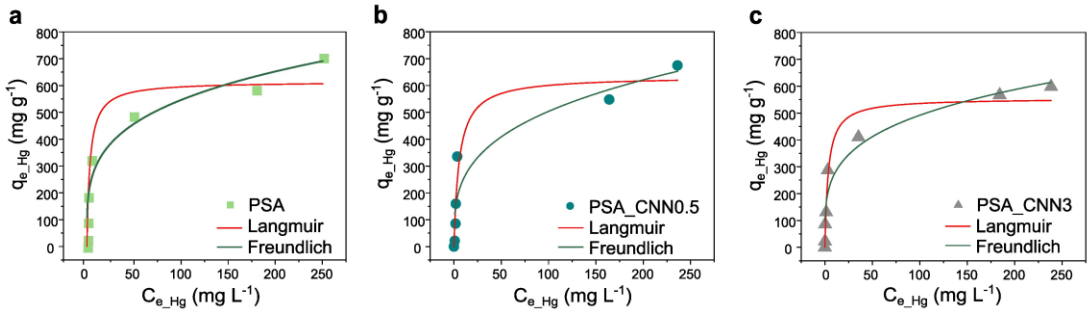

Figure 3.12. Non-linear fitting curves of Hg^{2+} adsorption experimental data to the Langmuir and the Freundlich isotherm models for the a) PSA, b) PSA_CNN0.5, c) PSA_CNN3 cryogels.

Overall, the parameters derived from the fittings and presented in Table 3.4, reveal that R^2 is slightly higher in case of the Langmuir isotherm model. Nevertheless, for both models the R^2 values are not satisfactory. To further validate the obtained results, linear fittings of both models were performed in the lower concentrations range, using Equations(3.6) and (3.7), as an indirect method of distinguishing between the two models, based on their different behaviour at low adsorption sites coverage. In particular, in such conditions, unlike the Freundlich isotherm, the Langmuir one follows a linear trend[347–350]. Based on the attained R^2 values (>0.99 for the Langmuir isotherm model vs. 0.86-0.95 for the Freundlich isotherm model), as shown in Figure 3.13, for all the cryogels the linear form of the Langmuir equation fits the data better than the linear form of the Freundlich equation. Hence, the modelling results suggest that at low Hg^{2+} concentrations the sorption mechanism is described by the monolayer adsorption on the homogenously distributed adsorption sites[330]. Nevertheless, in case of higher concentrations none of these two models can explain the process, indicating more complex adsorption processes, while the calculated q_{max_Hg} (Table 3.4) can only serve as a rough estimate. However, it seems that there is no significant influence of the CNNs presence in the polymer matrix on the q_{max_Hg} of the cryogels.

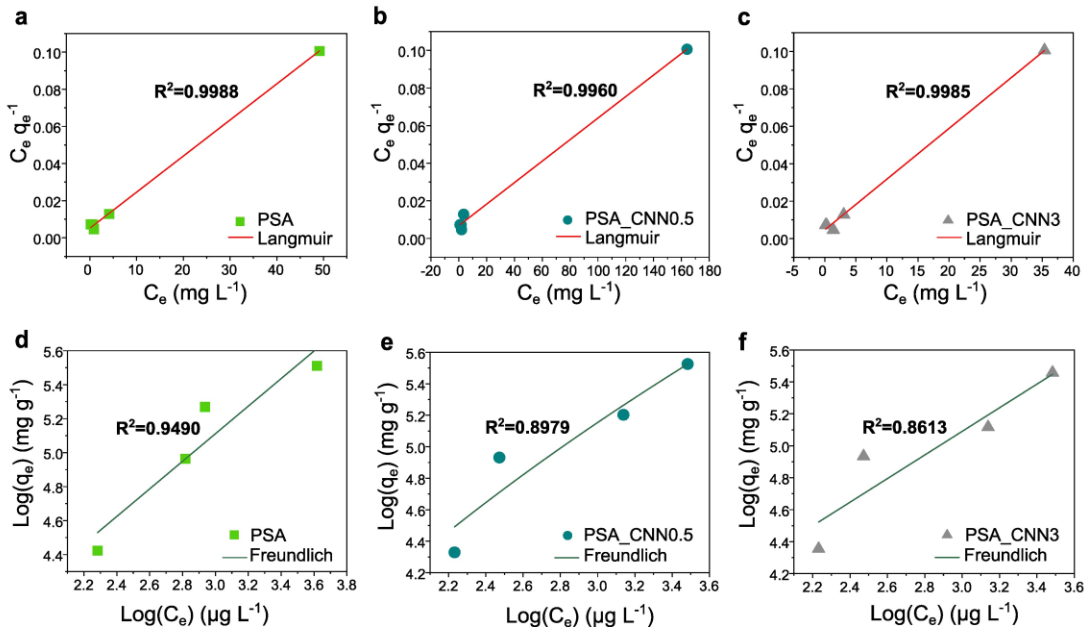

Figure 3.13. Linear fitting curves of Hg^{2+} adsorption in the lower initial Hg^{2+} concentration range for the PSA and PSA/CNN cryogels to a-c) the Langmuir and d-f) the Freundlich isotherm models.

Importantly, it should be noticed that since the ion exchange can be hypothesized as a highly probable Hg^{2+} adsorption mechanism of the cryogels, its applicability to the Langmuir isotherm model should be considered. According to the performed literature review, there is no consensus in the studies on whether the non-extended version of the Langmuir equation can be representative or not of the adsorption process based on the ion exchange[351–353]. Hence, further investigations of the adsorption mechanism, evaluating the possible ion exchange between the Na^{+} ions of the PSA molecules and the sorbed Hg^{2+} (further discussed in Section 3.4.1.), can give a clearer overview of the adsorption mechanism.

Table 3.4. Results obtained from the non-linear fitting of the Hg^{2+} adsorption experimental data by using the Langmuir and the Freundlich isotherm models (q_{max_Hg} is the maximum Hg^{2+} adsorption capacity calculated from the fitting).

	Langmuir isotherm model			**Freundlich isotherm model**		
Sample	q_{max_Hg} (mg g^{-1})	k_L (L mg^{-1})	R^2	1/n	k_F (mg g^{-1})/(mg L^{-1})$^{1/n}$	R^2
PSA	**614.78**±42.28	0.298±0.098	0.9567	0.256±0.039	167.693±31.651	0.9463
PSA_CNN0.5	**634.02**±49.41	0.179±0.058	0.9445	0.302±0.073	125.628±46.116	0.8271
PSA_CNN3	**554.98**±33.11	0.277±0.085	0.9617	0.256±0.037	151.277±27.133	0.9508

3.3.2 Adsorption capacity of Hg^{2+} ions and MB dye in their co-existence

The effect of the co-presence of Hg^{2+} and MB on the sorption performance of the cryogels was studied by determining the equilibrium sorption capacities after immersing the cryogels in Hg^{2+}-MB mixtures for 5h, as shown in Figure 3.14Figure 3.14. Even though the adsorption kinetics study was not performed in the present case, based on the so far performed studies on the isolated pollutants (Sections 3.2.1 and 3.2.2), it can be assumed that the adsorption capacities attained for the Hg^{2+}-MB mixture correspond to the equilibrium conditions and are comparable with the results obtained for the single pollutant solutions.

Figure 3.14a and Figure 3.14b present the q_{e_Hg} of the PSA, the PSA_CNN0.5, and the PSA_CNN3 cryogels upon immersion in Hg^{2+} and Hg^{2+}-MB solutions, respectively. The depicted results reveal that for the mixture of 5 mg L^{-1} Hg^{2+} –5 mg L^{-1} MB and for the solution of 5 mg L^{-1} Hg^{2+} all the studied cryogels exhibit similar q_{e_Hg}, regardless of the solution's composition. However, once the initial Hg^{2+} concentration increases, for the mixture of 20 mg L^{-1} Hg^{2+} –10 mg L^{-1} MB the q_{e_Hg} values are slightly

lower compared to the ones obtained for the 20 mg L^{-1} Hg^{2+} solutions. Nevertheless, this decrease is becoming less significant with the increase of the CNNs content within the cryogel's matrix, suggesting the possible contribution of the CNNs to the Hg^{2+} sorption process.

This is also the case for the adsorption behaviour of MB. The q_{e_MB} obtained for the 5 mg L^{-1} Hg^{2+} – 5 mg L^{-1} MB mixture does not significantly differ from the one attained for 5 mg L^{-1} MB without the presence of Hg^{2+}, for all the cryogels. The increase of the MB concentration in the pollutants mixture (i.e. 10 mg L^{-1} MB as a single pollutant and a 20 mg L^{-1} Hg^{2+} – 10 mg L^{-1} MB mixture) highlights the slight effect of the MB adsorption capacity enhancement by the presence of CNNs within the cryogel matrix Moreover, for the PSA/CNN cryogels the q_{e_MB} is slightly lower in presence of Hg^{2+} compared to the situation when MB is sorbed as a single pollutant.

In conclusion, at higher concentrations of both MB and Hg^{2+}, the decrease of the adsorption capacities of each of them is observed in their co-presence, which may be due to the cationic character of both contaminants leading to the electrostatic repulsion. Moreover, unlike in case of MB sorbed as a single pollutant, in co-existence of MB and Hg^{2+}, CNNs do not significantly contribute to the adsorption capacity of the pollutants.

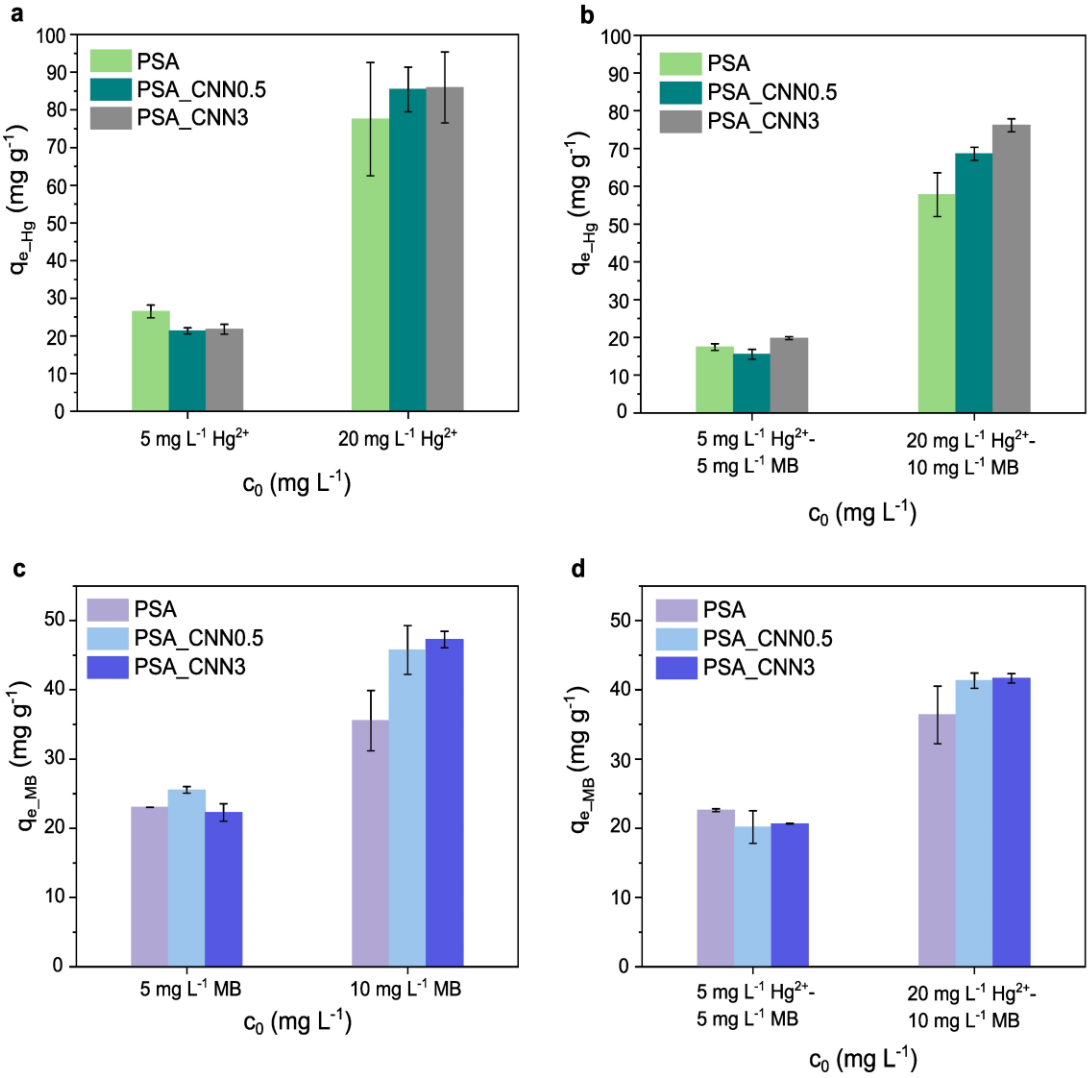

Figure 3.14. The Hg^{2+} equilibrium adsorption capacity (q_{e_Hg}) for: a) Hg^{2+} aqueous solutions at different initial concentrations (c_0), b) Hg^{2+}-MB mixture aqueous solutions at different combinations of the initial concentrations of each pollutant (c_0). The MB equilibrium adsorption capacity (q_{e_MB}) for: c) MB aqueous solutions at different initial concentrations (c_0), d) Hg^{2+}-MB mixture aqueous solutions at different combinations of the initial concentrations of each pollutant (c_0), after a contact time of 5 h with the PSA and the PSA/CNN cryogels.

3.4 ADSORPTION MECHANISM

3.4.1 Hg^{2+} ions adsorption mechanism

The already mentioned possible Hg^{2+} ions adsorption through Na^{+}-Hg^{2+} ion exchange was systematically studied, analysing the Na^{+} release ($q_{r(t)\_Na}$) over the PSA and the

PSA_CNN3 cryogels' immersion time in the aqueous solutions of Hg^{2+} (5 and 20 mg L^{-1}) and in pure water (as a blank test).

Na^+ release kinetics: in water and in presence of Hg^{2+}

As presented in Figure 3.15, the Na^+ release is observed for both cryogel types in pure water, as well as in Hg^{2+} solutions. Furthermore, in both liquids, the Na^+ release does not reach the equilibrium within 24h of cryogel immersion. Given the fact that the Hg^{2+} adsorption equilibrium is reached within 20-45 min, as described in Section 3.2.2 (Figure 3.5), these results indicate that Na^+ release due to the exchange with H^+ of water molecules occurs[354].

For the PSA cryogel, within the first 45 min of the dipping process, falling into the Hg^{2+} adsorption time range until reaching the equilibrium, as seen in Figure 3.5a, the $q_{r(t)\_Na}$ is higher in Hg^{2+} solutions than in pure water, while after the equilibrium time-point is crossed, the values of the Na^+ release in Hg^{2+} solutions and in pure water do not vary significantly, which indicates that two different mechanisms are involved in Na^+ release over time, namely Na^+-Hg^{2+} (in the first 45 min), as well as Na^+-H^+ exchange (over the whole immersion time). Such behaviour is observed at both studied Hg^{2+} initial concentrations. However, in case of the PSA_CNN3 cryogels, at the lower studied c_{0_Hg}, within the whole immersion time, the Na^+ release is lower in the Hg^{2+} solutions than in pure water, which may be caused by the entrapment of the exchanged Na^+ ions by the CNNs, preventing the release of Na^+ into the solution. Indeed, CNNs have been reported to be able to sorb Na^+ ions[355–358], and in pure water no effect of CNNs incorporation within the polymer matrix on the cryogel's Na^+ release ability is observed. Thus, the presence of Hg^{2+} within the nanocomposite cryogel matrix seems to influence the embedded CNN's propensity towards Na^+ sorption. In case of the higher studied c_{0_Hg} for PSA_CNN3 cryogels, the $q_{r(t)\_Na}$ values are similar to those

reached in pure water, meaning that lower amounts of the exchanged Na^+ ions are sorbed by the CNNs compared to the situation observed at the lower c_{0_Hg}. This can be explained by the fact that the higher the sorbed Hg^{2+} content, the higher the amount of CNNs involved in the interaction with Hg^{2+} making the nanofillers less available to entrap Na^+ ions. In fact, as previously discussed in Section 3.2.2, CNNs interact with Hg^{2+} only once a sufficient amount of the heavy metal ions is available (Hg^{2+} adsorption capacity enhancement by CNNs at c_{0_Hg} of 20 mg L^{-1} vs. no enhancement at c_{0_Hg} of 5 mg L^{-1}).

In Hg^{2+} solutions, at given concentrations, the lower Na^+ release reached by the PSA_CNN3 compared to the one of the neat PSA cryogels may be due to the interactions of CNNs with the sorbed Hg^{2+}, as well as due to the above-mentioned Na^+ entrapment by CNNs.

However, it should be noted that for a given cryogel type, the observed differences between Na^+ release values obtained through the immersion in pure water and in Hg^{2+} solutions, are relatively low (below 10 mg g^{-1} for both cryogel types in the first 45 min), which indicates that marginal amounts of Na^+ are released due to Na^+-Hg^{2+} exchange at the studied conditions (solution volume of 15 mL and c_{0_Hg} of 5 and 20 mg L^{-1}).

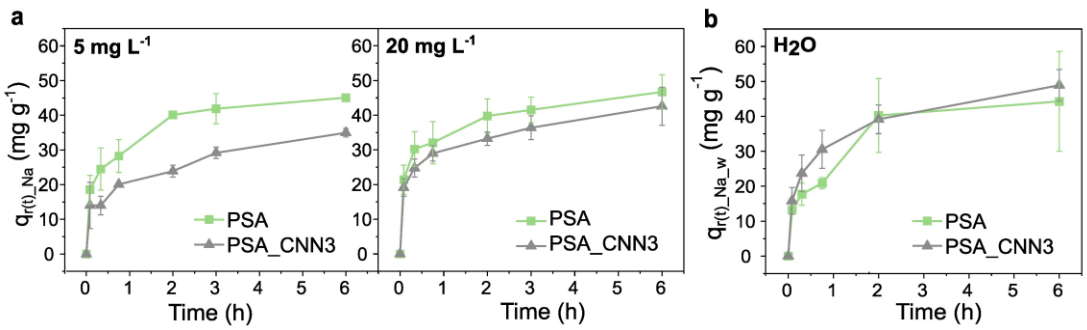

Figure 3.15. Na^+ ions release ($q_{r(t)\_Na}$) over the time of the PSA and the PSA_CNN3 cryogels' immersion in a) the aqueous solutions of Hg^{2+} (at the initial concentrations of 5 mg L^{-1} and 20 mg L^{-1}) and in b) pure water.

Na^+-Hg^{2+} ion exchange molar ratio determination

Since at lower Hg^{2+} concentrations the Na^+-H^+ exchange seems to be prevalent over the Na^+-Hg^{2+}, the Na^+ release was studied at higher c_{0_Hg} and, as shown in Figure 3.16, it was possible to determine the $q_{r(e)\_Na\_ex}$ for both the PSA and the PSA_CNN3 cryogels (a higher amount of Na^+ is released due to the exchange with Hg^{2+} than with H^+). Figure 3.16a shows that, unlike in case of the lower c_{0_Hg} (Figure 3.15), in the herein studied c_{0_Hg} range the $q_{r(e)\_Na\_ex}$ increases with the increase of the Hg^{2+} concentration. Based on the obtained $q_{r(e)\_Na\_ex}$ and the q_{e_Hg} attained at the corresponding c_{0_Hg} (Figure 3.11), the molar $ratio_{(Na/Hg)}$ was determined, using Equations (3.12(3.14), and it was found that in case of the PSA cryogel ~2.3-2.5 mols of Na^+ are exchanged with 1 mol of Hg^{2+} whereas for the PSA_CNN3 cryogel ~2.1-2.3 mols of Na^+ are exchanged with Hg^{2+}. The slightly lower molar ratio observed for the PSA_CNN3 cryogel could be attributed to the effect of the exchanged Na^+ entrapment by CNNs, discussed above in this section. Nevertheless, relatively high error bars suggest that the obtained values are comparable for both cryogels and one Hg^{2+} ion interacts with two $–COO^-$ groups of the PSA network.

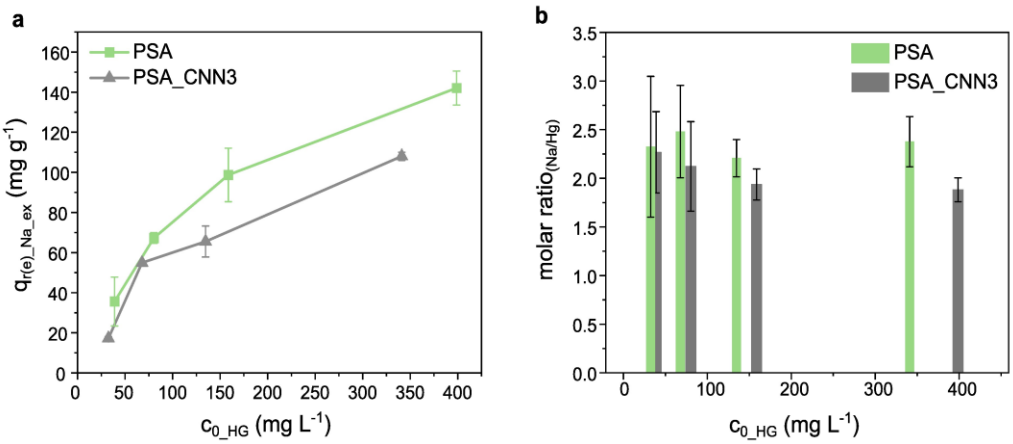

Figure 3.16. a) The normalized Na^+ release from the PSA and the PSA_CNN3 cryogels at the equilibrium conditions ($q_{r(e)\_Na\_ex}$ at 5h of cryogel immersion) for different initial Hg^{2+} concentrations (c_{0_Hg}). b) The molar ratio of Na^+-Hg^{2+} ion exchange calculated based on data shown in a).

3.4.2 Methylene blue adsorption mechanism

The FTIR spectra of the pristine PSA cryogel and the PSA cryogels after the adsorption of MB from its aqueous solutions at two different concentrations were analysed in order to investigate the mechanism of MB adsorption by the cryogel's matrix. As demonstrated in Figure 3.17, the typical PSA spectra, discussed in Chapter 2:, Section 2.2, is revealed. The slight differences compared to the spectrum presented in Figure 2.2 derive from the different used methods: the ATR mode for the PSA chemical characterization, and the transmission mode for the herein discussed MB adsorption mechanism study. In case of the MB-loaded PSA cryogels, no difference in the PSA spectrum is observed, apart from the substantial increase of the relative intensity of the peak at 3441 cm^{-1}, ascribed to the –OH stretching mode of the terminal -COOH groups of PSA, with respect to the peak at 1574 cm^{-1}, along with a slight peak shape modification suggesting the formation of another peak in the same range. Such a phenomenon is observed for both initial MB concentrations, and considering the fact that before the measurements all the samples underwent oven drying (as described in Section 3.1.5), the effect of the absorbed moisture, possible in the discussed range, can be eliminated. Thus, the observed modifications may be attributed to MB, exhibiting a strong peak in the same range[359,360]. Moreover, with respect to the peak at 1574 cm^{-1} the relative intensity of the peak at 2936 cm^{-1} (ascribed to the $–CH_2$ stretching of the alkane groups of PSA), observed in the spectrum of the pristine PSA cryogel, is significantly increased in the MB-loaded PSA cryogels, and slightly shifted to 2930 cm^{-1}. This might be due to the closely overlapped –CH stretching bands of PSA and MB[361,362]. The other typical peaks of MB are not evident, which suggests the overlapping with the peaks ascribed to PSA.

In conclusion, although the FTIR spectra confirm the presence of MB entrapped by the PSA framework, other typical peaks of MB are not evident, which might be due to the high superposition with the characteristic peaks of the PSA. Thus, the possible chemical interaction of PSA and MB cannot be identified based on the obtained FTIR spectra.

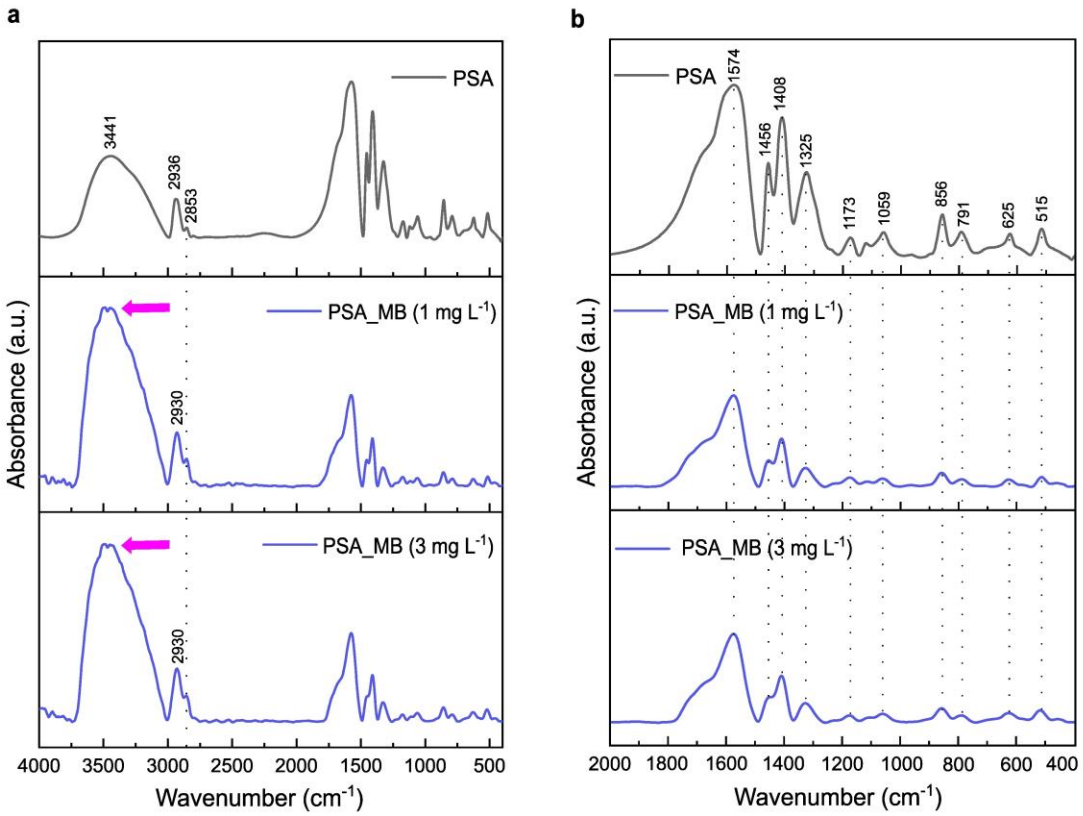

Figure 3.17. a) The whole wavenumber range FTIR spectra of the pristine PSA cryogel and the PSA cryogels loaded with MB after 24h of immersion in 15 mL of the MB aqueous solutions at the initial concentrations of 1 mg L^{-1} and 3 mg L^{-1}. b) The zoom-in on the low wavenumber range of the corresponding FTIR spectra.

3.4.3 Influence of the co-existence of Hg^{2+} ions and MB on the adsorption mechanism

In this section the mechanism of MB and Hg^{2+} adsorption in their co-existence is studied. To this aim the $q_{r(e)\_Na\_ex}$ was determined for the process of MB sorption from

the aqueous solutions of 10 mg L^{-1} MB and of a Hg^{2+}-MB mixture (20 mg L^{-1}-10 mg L^{-1}), and the results are presented in Figure 3.18. Since MB adsorption via the exchange with Na^+ ions due to the cationic nature of the dye has been reported in the literature[363–365], it was also considered in the study, so as to verify the obtained FTIR results where chemical interactions between MB and PSA were not visible (Section 3.4.2). It has been observed that in case of the MB aqueous solution no release of Na^+ due to the exchange with MB occurs, with negligibly lower overall amount of Na^+ released than in pure water, for both the PSA and the PSA_CNN3 cryogels. Instead, in case of the Hg^{2+}-MB aqueous solution, Na^+ release attributed to the ion exchange is evident for both cryogel types. Hence, it can be concluded that, as the adsorption of MB is not driven by the ion exchange with Na^+, the $q_{r(e)\_Na\_ex}$ obtained for the Hg^{2+}-MB mixture derives solely from Hg^{2+} sorption, and the heavy metal ions' adsorption mechanism is not affected by the presence of MB.

Next, the effect of the co-existence of MB and Hg^{2+} in the sorbate solution on the adsorption mechanism of MB was investigated. In particular, a possible interaction between the adsorbed Hg^{2+} and MB, indicated in some studies, was evaluated. Specifically, Raj et al[366] reported the complexation effect between MB and mercury(II) salts, including $HgCl_{(2)}$ used in this study, and Saleh et al[232] observed a synergistic adsorption effect due to the chemical interactions between MB and Hg^{2+} in their co-presence. Considering the fact that MB is very sensitive to changes in its surrounding microenvironment, which can be reflected in its UV-vis spectrum[367], the spectrophotometric analysis of the MB-loaded and (Hg^{2+}-MB)-loaded PSA and PSA_CNN3 cryogels, in the range corresponding to MB absorption peaks range, was performed, as presented in Figure 3.18b. For both cryogel and solution types, the same MB concentration was used. The measurements revealed that in the studied

wavelength range no peaks deriving from the cryogels' chemical composition are present, and the typical spectra of the dimer form of MB are obtained[332]. The dimerization of MB upon its sorption by a porous structure has been discussed by Handa et al[368], and it may be ascribed to the changes in the effective polarity of the dye.

In case of the PSA cryogel, no difference was observed in the spectra of MB adsorbed from its aqueous solution and from the Hg^{2+}-MB aqueous solution, suggesting that the two adsorbed components do not interact with each other. In case of the PSA_CNN3 cryogel, in co-existence of the two pollutants, a bathochromic shift of 10 nm is observed with respect to the high-intensity peak at 596 nm in the spectrum of the MB-loaded PSA_CNN3 cryogel. Since no interaction of MB and Hg^{2+} adsorbed by the PSA network occurs, and the adsorption studies revealed the possible interaction of the CNNs incorporated into the PSA matrix with both MB and Hg^{2+} (Section 3.2), the observed shift seems to be induced by the presence of the CNNs and the interactions between MB, Hg^{2+} and the nanosheets. Even if they involve capturing one pollutant type by another one adsorbed by the CNNs, such a hypothetical synergistic effect is negligible due to the fact that no contribution of the CNNs to the adsorption capacity of MB in its co-presence with Hg^{2+} has been observed (Figure 3.14c-d).

Hence, it can be concluded that the prevalent adsorption mechanism does not differ for the single pollutant and the pollutant mixture scenarios, which is in agreement with the studies on the effect of Hg^{2+} and MB co-existence on the adsorption capacity of each of them (Section 3.3.2).

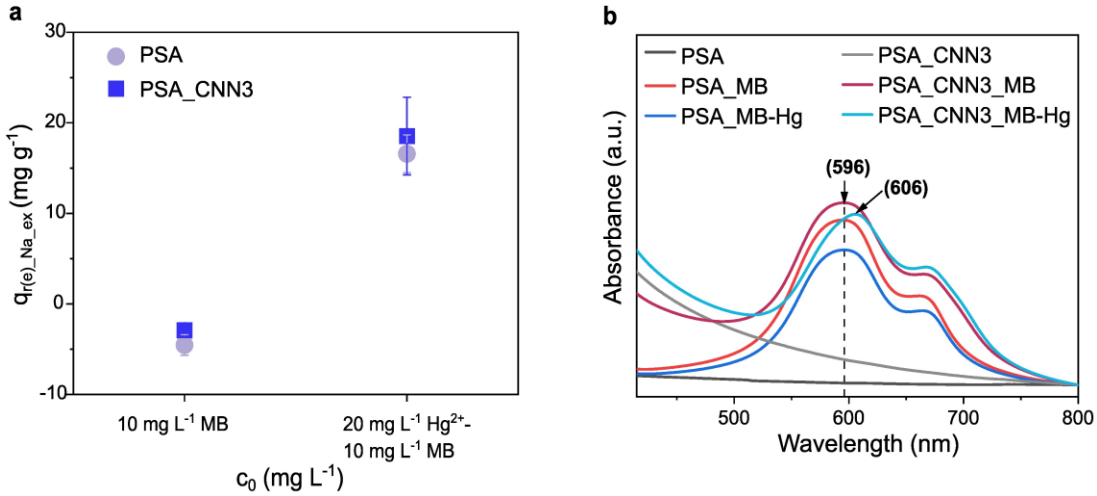

Figure 3.18. a) The normalized Na^+ release from the PSA and the PSA_CNN3 cryogels at the equilibrium conditions ($q_{r(e)\_Na\_ex}$ at 5h of cryogel immersion) for a MB aqueous solution (10 mg L^{-1}) and a Hg^{2+}-MB aqueous mixture (20 mg L^{-1}-10 mg L^{-1}). b) The UV-vis spectra of the PSA and the PSA_CNN3 cryogels after 5h of immersion in MB and Hg^{2+}-MB mixture aqueous solutions with the same MB concentrations.

3.5 CONCLUSIONS

To sum up, the study of the adsorption of MB and Hg^{2+} in batch conditions allowed to understand in detail the adsorption mechanisms of the two studied compounds, giving a clear indication of the contributions of their interactions between each other, with the PSA matrix, and with the embedded CNNs, to the MB/Hg^{2+} adsorption capacities of the neat PSA and the nanocomposite PSA/CNN cryogels. For the neat cryogels, the Hg^{2+} adsorption mechanism was found to be based on Na^+-Hg^{2+} ion exchange, with ~2 moles of Na^+ released per 1 mol of Hg^{2+} adsorbed. In case of the PSA/CNN cryogels, the same adsorption mechanism prevails, even though CNNs seem to participate in the sorption process at moderate pollutant concentrations, slightly enhancing the adsorption capacities and reducing the time need to reach the adsorption equilibrium. The co-existence of MB and Hg^{2+} does not affect the adsorption mechanism, but slightly decreases the adsorption capacities of both cryogels.

Nevertheless, both material types have proven to be excellent sorbents of organic and inorganic cationic pollutants, with the respective maximum adsorption capacities reaching 2894.1±237.0, 2913.7±226.2, and 4763.5±474.5 mg g^{-1} cryogel for the PSA, the PSA_CNN0.5, and the PSA_CNN1 cryogels in case of MB, and 554.98-634.02 mg g^{-1} cryogel for Hg^{2+}, depending on the cryogel's composition. Despite a rapid uptake of both MB and Hg^{2+} by the neat cryogel, the incorporation of CNNs into the PSA matrix further reduced the time needed to reach the adsorption equilibrium for both pollutants.

These findings, combined with the unveiling of the cryogels' interesting functional properties, such as underwater oleophobicity, and excellent water flow rate (as presented in Chapter 1:), paved the path to the work on the development of PSA/CNN cryogels for the filtration of multicomponent oily wastewater, integrated with the detection and the recovery of the adsorbed Hg^{2+}, as well as the photocatalytic decolorization of the sorbed dye, as discussed in the next chapters.

Chapter 4: Multicomponent oily wastewater purification performance of PSA and PSA/CNN cryogels: Gravity-driven filtration

This chapter focuses on the performance of the neat PSA and the PSA/CNN nanocomposite cryogels in the simultaneous adsorption of water-soluble pollutants and in the oil separation from water, both performed through gravity-driven filtration. As the study presented in Chapter 3: proved the successful uptake of MB and Hg^{2+} by the developed cryogels in batch conditions, the filtration ability of the cryogels towards the same pollutants is studied in the herein presented work. Two types of oils are used for the evaluation of the cryogels' behaviour during oily wastewater filtration, namely a highly viscous SI oil (500 cPs), and SB oil, being a lower viscosity oil. The study unveils the excellent performance of both cryogel types in the adsorption of MB and Hg^{2+} through the filtration process, with the adsorption capacities reaching those determined at the equilibrium in the batch conditions studies, despite the short contact time with the pollutants during the filtration. Regarding the separation of the oil phase, for both the PSA and the PSA/CNN cryogels the separation efficiencies of almost 100% are reached in case of the non-emulsified SI/SB oil-water mixtures whereas the surfactant-stabilized oil-in-water emulsions filtration performance is not satisfactory indicating that the developed filters are better fitted for free oil-in-water mixtures.

The reusability of both cryogels in multiple filtration cycles of SB oil-water and SB-oil-water-MB mixtures is studied and excellent oil separation efficiency of nearly 100 % for SB oil, and of $\geq$ 98 % in case of MB is evidenced in all cases.

Finally, the herein study corroborates the versatility of the PSA and the PSA/CNN cryogels in the gravity-driven filtration of the simulated multicomponent oily wastewater, composed of MB dye, Hg^{2+} ions and SB oil, reaching very high efficiency of ≥ 97 % for all the components of the mixtures. The influence of the contaminants' co-presence on the filtration performance is also evaluated and no effect is observed. In all the filtration studies, the embedded CNNs do not show any effect on the separation efficiencies of the cryogel towards the different studied pollutants.

In conclusion, in this work the applicability of the developed neat and nanocomposite cryogel materials as highly efficient gravity-driven 3D filters for the simultaneous oil-water separation and the purification of the aqueous phase from both organic and inorganic cationic pollutants is proved.

4.1 MATERIALS AND METHODS

4.1.1 Materials

Methylene blue (MB) and mercury (II) chloride ($HgCl_2$), silicone oil (SI oil) (viscosity 500 cPs), and Polyoxyethylene (20) sorbitan monooleate (Tween 80) were purchased from Sigma-Aldrich. Soybean oil (SB oil) (Bunge) was bought in a local shop. All these compounds were used for the preparation of aqueous solutions, oil-in water mixtures or stabilized emulsions as filtration feeds. All the chemicals were used as received without further purification. All the experiments were performed with the use of Milli-Q water.

4.1.2 Filtration procedure

The swollen cryogels were used as filters in gravity-driven filtration performed in a homemade setup composed of a filtration column, funnel, and a clip, as shown in

Figure 4.1. The cryogels were placed in between two polyurethane o-rings in a way that no pressure is exerted onto them. The filtration diameter, indicated with the arrows in Figure 4.1c, was 6 mm (effective filtration area of 2.83×10^{-5} m^2), and the filtration column volume was 20 mL.

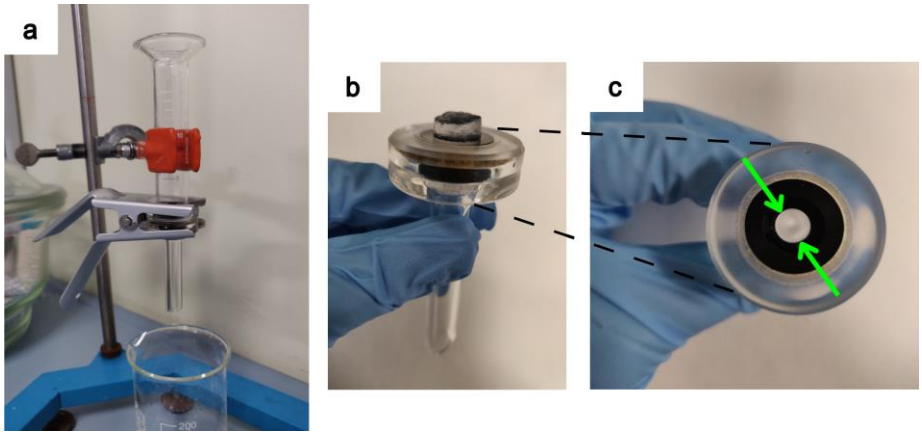

Figure 4.1. Photographs presenting: a) the gravity-driven filtration setup, b) the funnel with an inserted cryogel, c) the upper part of the funnel equipped with a polyurethane o-ring (the green arrows indicate the filtration dimeter).

The performance of both the PSA and the PSA/CNN cryogels in wastewater purification during gravity-driven filtration was evaluated for different mixtures, i.e. for water-Hg^{2+}, oil-water, oil-water-MB, water-Hg^{2+}-MB, as well as oil-water-MB-Hg^{2+} (5 mg L^{-1} Hg^{2+}, 1 mg L^{-1} MB, 30 % w/w oil in water, with respect to the total mixture volume, pH=6.0 in all cases). In case of the oil-water system, SB oil-water and SI oil-water mixtures were used, and for the other systems SB oil was utilized as a chosen representative oil. The oil-containing feeds were vigorously shaken manually for 15 s and then immediately poured on top of the swollen cryogel. The filtration process consisted of two steps: i) permeation of 15 mL of pure water, as a control test of the material's permeation performance, and ii) filtration of 15 mL of the simulated wastewater.

Reusability of the PSA and the PSA/CNN cryogels was evaluated carrying out five consecutive gravity-driven permeation/filtration cycles, with each of them composed of two successive steps: i) permeation of 15 mL of water, and ii) permeation of 15 mL of the oil-water mixture or filtration of the oil-water-MB mixture (0.5 mg L^{-1} of MB, 30% w/w SB oil with respect to the total mixture volume). In case of the oil-water mixture, reusability tests were conducted for one sample, and in case of the oil-water-MB mixture the tests were performed in triplicate.

The performance of the PSA/CNN cryogel in the gravity-driven filtration of surfactant-stabilized oil in water (O/W) emulsions (30 % w/w and 10 % w/w SB oil using Tween 80 (8×10^{-5} M) as a non-ionic surfactant) was also assessed. The surfactant's choice was dictated by its common use for the production of O/W emulsions[369–371]. In order to confirm the effectiveness of the chosen surfactant concentration in stabilizing the emulsions, and to investigate the influence of the water-oil weight ratio on the stability of the emulsions, the prepared emulsions were monitored at the following time intervals: 0 min, 5 min, 10 min, 15 min, 30 min, 45 min, 60 min, 85-90 min and 18h (and re-controlled after 2 weeks), by measuring the relative emulsion volume, V_{em}/V_{tot} (where V_{em} is the emulsion volume, and V_{tot} is the total mixture volume).

The emulsions for the stability-in-time study and for the filtration process were prepared with the use of two 12 mL polypropylene syringes connected through a 16 mm long syringe connector with an inner diameter of 4.4 mm. One syringe was filled with SB oil and another one with the aqueous solution of Tween 80 surfactant, and the total volume of the mixture was 15 mL. The emulsions were formed by applying twenty sequential cycles of pushing the mixture through the connector from one

syringe to the other one. The tests were performed on one sample for each emulsion composition.

Unless differently stated, the experiments were performed in triplicate.

4.1.3 Separation efficiency and adsorption capacity determination

For each mixture type, the oil, MB or Hg^{2+} separation efficiencies (E_{ff_x} %, with x; SB or MB or Hg) were calculated as follows:

$$E_{ff\_x} = (m_{x\_i} - m_{x\_f}) / m_{x\_i} \times 100\% \quad (4.1)$$

where m_{x_i} is the mass (mg) of the specific component in the feed solution, whereas m_{x_f} is the mass (mg) of the component in the permeate. In case of the water-soluble compounds, these masses were determined following procedures described in Section 3.1.2.

For the analysis of oil content in the permeate solutions (m_{SB/SI_f}), the absorption spectra were recorded in a range of 200-350 nm for SB oil and 900-1800 nm for SI oil, using a Varian Cary 6000i UV–vis–NIR spectrophotometer. To do so, the analytes were prepared by dissolving the oil in heptane through mixing 4 mL of the permeate (V_f) in a specific volume of heptane ($V_{heptane}$) and vortexing the as-obtained mixture for 1 min. Next, the mixture was centrifuged for 10 min at 4800 RPM to separate the oil-heptane and water phases. The supernatant was then carefully collected with a pipette and its absorption spectrum was recorded.

To determine the oil mass from the UV-vis absorption spectra, in a preliminary step, the absorption spectra of the oils were obtained for the set of the prepared oil-in-heptane solutions with known oil concentrations ranging from 0 to 4000 mg L^{-1}. In case of SB oil, the absorbance at the wavelength of 269 nm (Abs_{269}) of oil-in-heptane solutions[372] was plotted versus the concentration of the oil, and in case of SI oil the

area under the peak at the wavelength of 1183 nm ($A_{1172\text{-}1190\ nm}$) was plotted vs. the concentration of the oil. Subsequently, the linear fitting was performed and in the resulting equations of $y = a \times x$, (where y is the absorbance at the wavelength of 269 nm for SB oil or the area under the peak at 1183 nm for SI oil, and x is the concentration), for SB oil a was equal to 0.000254, and for the SI oil it was 0.00000461. The values of the coefficient of determination (R^2) were > 0.99 for SB oil and 0.98 for SI oil.

Then, for SB oil the $m_{SB\_f,}$ was determined as follows:

$$m_{SB_f} = \frac{A_{269\,nm} \times V_{heptane} \times V_T}{V_f \times a} \quad (4.2)$$

For the SI oil the $m_{SI\_f,}$ was determined as follows:

$$m_{SI\_f} = \frac{A_{1172-1190\,nm} \times V_{heptane} \times V_T}{V_f \times a} \quad (4.3)$$

where V_T is the total volume of the permeate and a is the slope of the linear regression equation of the obtained calibration curves of the oil-in-heptane. The oil mass in the feed (m_{SB/SI_i}) was determined based on the known weight of the oil added to water.

For each mixture type, the MB or Hg^{2+} adsorption capacities (q_x (mg g^{-1} cryogel) with x; MB or Hg) were calculated as follows:

$$q_x = \frac{m_{x\_i} - m_{x\_f}}{m} \quad (4.4)$$

where m (g) is the mass of the dry cryogel.

4.1.4 Separation performance evaluation for stabilized emulsions

In order to assess the separation performance of the PSA/CNN cryogels in the gravity-driven filtration of surfactant-stabilized O/W emulsions, a polarized microscope (LEICA DM2500M, 10x objective lens) was used, and images of the emulsions were taken right after their formation, when they were completely emulsified. Then, their

gravity-driven filtration through the PSA_CNN1 cryogel was performed and subsequently the permeate was analysed under the microscope. The samples were analysed casting an emulsion drop onto a glass slide blocked by two other glass slides inserted on the sides.

4.2 OIL SEPARATION PERFORMANCE AND FILTER REUSABILITY

Oil separation ability of the PSA and the PSA_CNN1 cryogels in the process of the gravity-driven filtration was studied using SI and SB oil. The oil content in the feed and permeate solutions was analysed by means of spectrophotometric studies of the supernatants obtained following the procedure of oil extraction in heptane from the permeate, as explained in Section 4.1.3. Figure 4.2a presents zoomed-in NIR spectra of SI oil and its extracts from 30 % w/w SI oil-water mixture permeates at the wavelength corresponding to the peak at 1183 nm. As it can be seen, no peak is observed in case of the permeate extract samples for both cryogel types, suggesting complete oil separation. The UV-vis spectra of the water-SB oil permeate extracts from the permeate solutions are shown in Figure 4.2b, and the SB oil content in the corresponding permeates was determined based on the intensities of the peak at 269 nm.

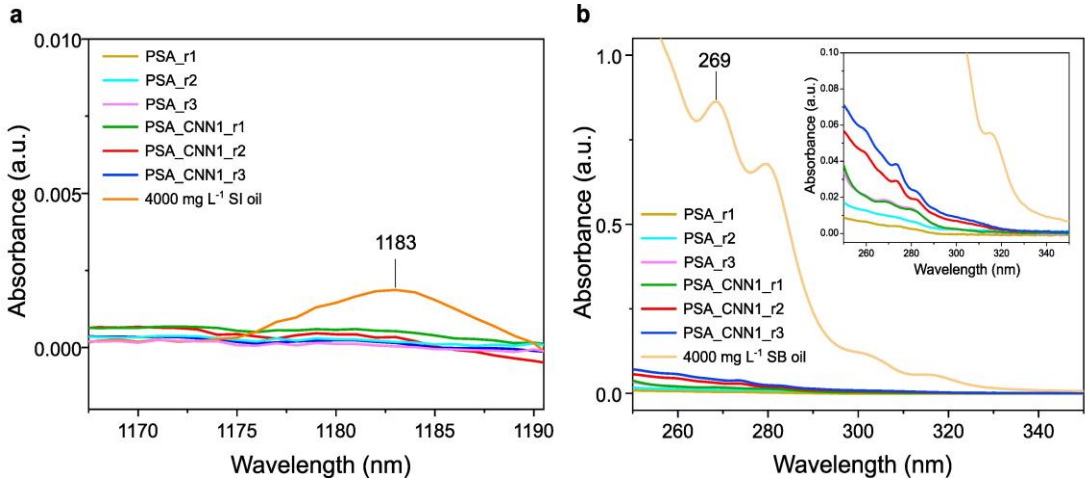

Figure 4.2. a) NIR spectra of a) 4000 mg L^{-1} SI oil dissolved in heptane, and the supernatants obtained following the procedure of oil extraction in heptane from the permeate of 30 % w/w SI oil-water mixture of the PSA and the PSA_CNN1 cryogels. b) UV-vis spectra of 4000 mg L^{-1} SB oil dissolved in heptane, and the supernatants obtained following the procedure of oil extraction in heptane from the permeate of 30 % w/w SB oil-water mixture of the PSA and the PSA_CNN1 cryogels. Symbols r1-r3 indicate filtration replicates using three samples.

With oil fouling being one of the biggest challenges in the commonly used filtration systems designed to separate oils, as addressed in Section 1.1.3, the reusability of the developed cryogels in oily wastewater filtration seems to be fundamental. Thus, the separation performance of the PSA and the PSA_CNN1 cryogels in five consecutive filtration cycles was evaluated for SB oil–water and SB oil-MB-water mixtures.

Figure 4.3a-b show that for both types of feed solutions, the E_{ff_SB} of both the PSA and the PSA_CNN1 cryogels remains > 99.81 %. Moreover, as presented in Figure 4.3c, both cryogel types can simultaneously separate oil and MB even after multiple filtration cycles, achieving E_{ff_MB} of 97.83-99.19 %.

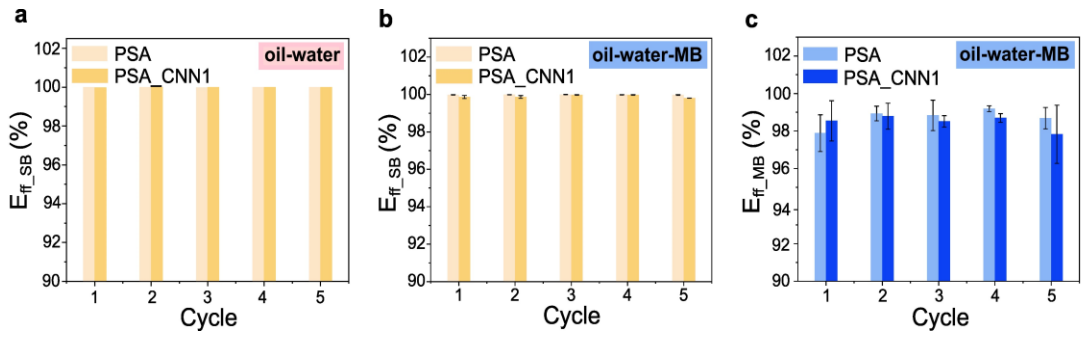

Figure 4.3. Reusability of the PSA and the PSA_CNN1 cryogels in five consecutive gravity-driven filtration cycles. a) SB oil separation efficiencies (E_{ff_SB}) of the cryogels for an oil-water mixture (30 % w/w SB oil). Separation efficiencies of the cryogels for an oil-water-dye mixture (0.5 mg L-1 MB, 30 % w/w SB oil) for: b) SB oil (E_{ff_SB}), c) MB (E_{ff_MB}).

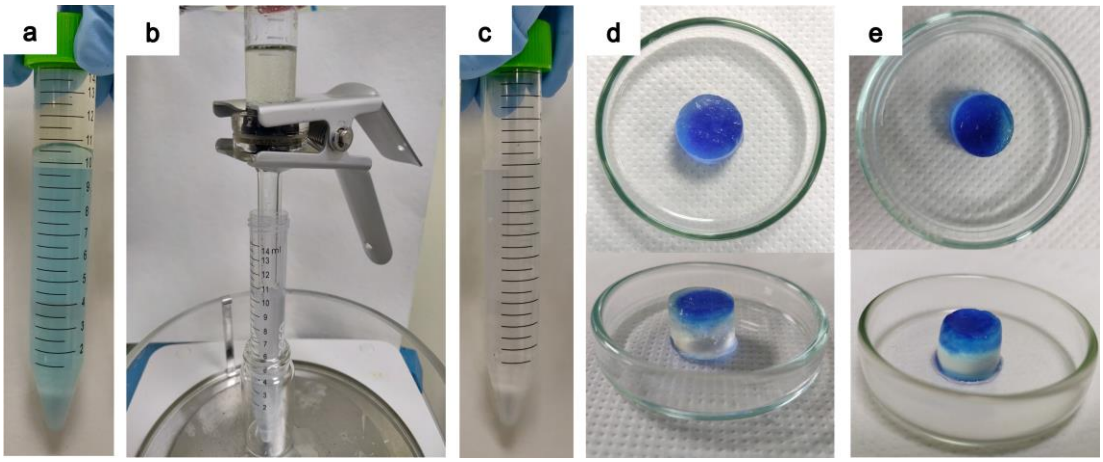

Figure 4.4 presents the images of the SB oil-MB-water filtration feed and permeate, as well as the separation of oil in the filtration setup, and the PSA cryogel after the first and the fifth consecutive filtration cycle of the oil-water-dye mixture. As shown, with the increasing amount of the sorbed MB the cryogels adsorb the dye layer-wise, i.e. from the top surface, being in direct contact with the wastewater, towards its bottom, and the filter is stable after multiple filtrations.

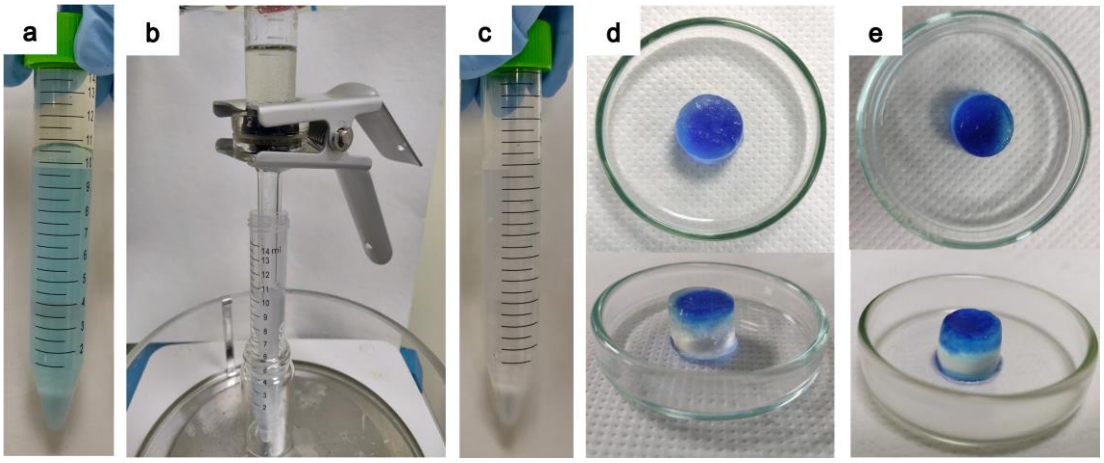

Figure 4.4. The filtration of an oil-water-dye mixture (0.5 mg L^{-1} MB, 30 % w/w SB oil). Photographs of: a) the filtration feed, b) oil separated in the filtration column at the end of the filtration, c) the permeate solution, d) the PSA cryogel after the first filtration cycle (top and side view), e) the PSA cryogel after the fifth filtration cycle (top and side view).

4.3 FILTRATION PERFORMANCE: FROM SINGLE POLLUTANT TO MULTICOMPONENT OILY WASTEWATER

The findings discussed in the above section paved the path for the study on the application of the developed cryogels as versatile filters for the purification of multicomponent oily wastewater containing not only organic, but also inorganic pollutants. Due to the chemical nature of the developed materials, the interactions of cationic heavy metal ions with the anionic PSA network and the incorporated CNNs are favoured, as proven in Section 3.4. Hence, the performance of the PSA and the PSA_CNN3 cryogels in the adsorption of Hg^{2+} ions from its aqueous solution during the gravity-driven filtration process was explored, and high E_{ff_Hg} values > 93 % were reached for both material types, as shown in Figure 4.5a. Similar results were obtained in case of the filtration of a water-Hg^{2+}-MB mixture at the corresponding Hg^{2+} concentration, while the MB separation performance seemed not to be significantly affected by the co-presence of Hg^{2+}, with respect to the so far obtained results (i.e Figure 4.3c and Figure 4.5a-b). Thus, in the next step the performance of the cryogels

in the gravity-driven filtration of the simulated oily wastewater containing MB and enriched by Hg^{2+} ions was investigated for the PSA and the PSA_CNN3 cryogels. As demonstrated in Figure 4.5c, the separation efficiencies reached by both cryogels for each pollutant (SB oil, MB, Hg^{2+}) during the oil-water-dye-heavy metal mixture filtration are in all cases higher than c.a. 97%. These values are not significantly modified by the co-presence of all the three pollutants, meaning that the developed cryogels can effectively remove the studied contaminants without being affected by the type of the wastewater tested. This suggests that the adsorption process is not competitive for the studied pollutant concentrations. The good affinity of both MB and Hg^{2+} ions to the active sites of the cryogels in their co-presence can derive from their positive charge allowing for the electrostatic attraction to the negatively charged carboxylate groups (COO^-) of the PSA polymer. Furthermore, the incorporation of CNNs into the cryogel matrix did not show any significant effect on the separation efficiency of the PSA, for any of the pollutants in the different studied solutions. It is worth noticing that the filtration process is fast, lasting ~90s in case of the aqueous solutions and ~60s for the oily solutions.

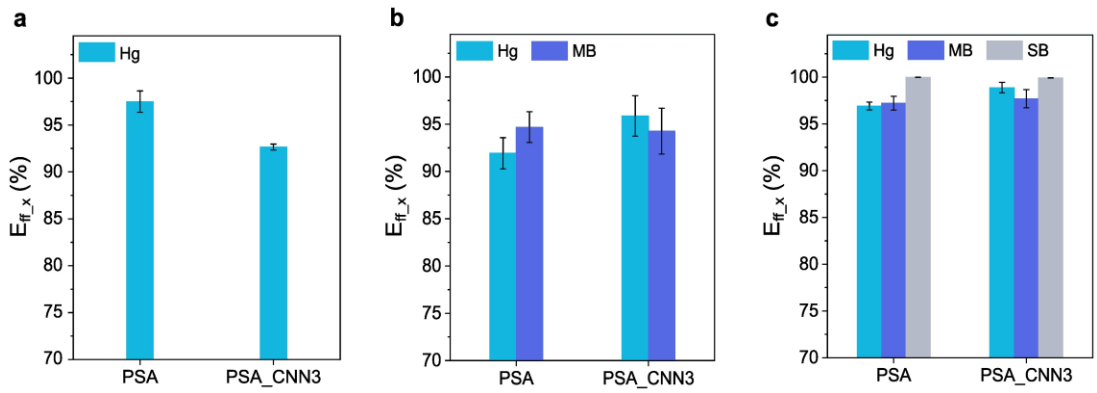

Figure 4.5. Separation efficiencies (E_{ff_x}) of the cryogels in the filtration of: a) a water-heavy metal mixture, b) a water-dye-heavy metal mixture, c) an oil-water-dye-heavy metal mixture. In all cases the concentrations of pollutants in the feed solutions are: 30% w/w SB oil, 1 mg L^{-1} MB, 5 mg L^{-1} Hg^{2+}.

The MB and Hg^{2+} adsorption capacities of the PSA and the PSA_CNN3 cryogels after the filtrations of the above-discussed pollutant mixtures were studied and the results are presented in Figure 4.6. It was found that, regardless of the wastewater composition and the cryogel type, the q_x remained similar (~ 20-24 mg g^{-1} for Hg^{2+} and ~ 5 mg g^{-1} for MB), with the values comparable to those reached at the equilibrium in the batch experiments at the corresponding MB and Hg^{2+} concentrations (Section 3.2, Figures Figure 3.2 Figure 3.3). Hence, despite the short contact time with the solution during the filtration process, the materials are able to uptake the same amounts of the pollutants as in case of the prolonged contact. This proves the excellent performance of the material in the energy-saving gravity-driven filtration process.

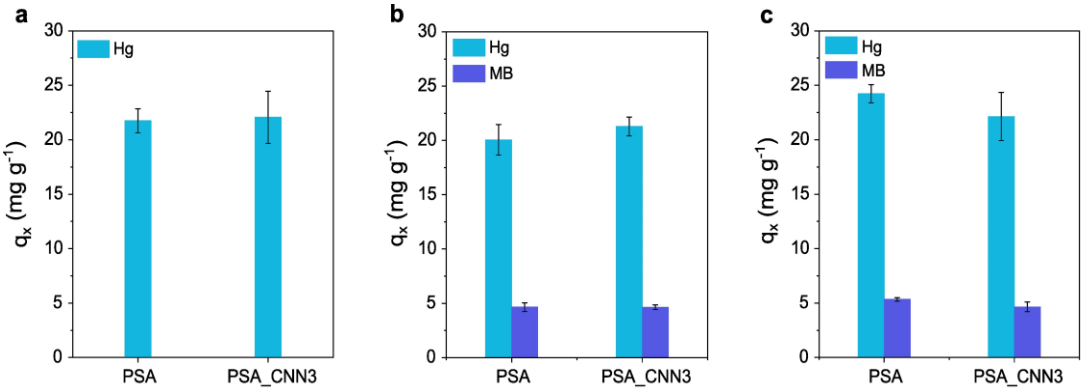

Figure 4.6. Adsorption capacities (q_x) of the cryogels in the filtration of: a) a water-heavy metal mixture, b) a water-dye-heavy metal mixture, c) an oil-water-dye-heavy metal mixture. In all cases the concentrations of pollutants in the feed solutions are: 30% w/w SB oil, 1 mg L^{-1} MB, 5 mg L^{-1} Hg^{2+}.

4.4 STABILIZED EMULSIONS FILTRATION PERFORMANCE

Before starting the O/W emulsion filtration tests, the emulsion stability was studied to ascertain the full emulsification of the filtration feed with the used Tween 80

surfactant. As shown in Figure 4.7a, emulsions with SB oil contents of 10 % w/w and 30 % w/w in water were relatively stable within the first 30 min after the preparation. Subsequently, the emulsion with the lower oil content underwent drastic destabilization, maintaining at the equilibrium only ~0.25 of the initial emulsion volume, whereas at the higher oil content the emulsion's stability continued to decrease gradually, until it reached the equilibrium at around half of the initial volume. The volumes reached after around 40 min for 10% w/w oil emulsion and after 60 min for 30% w/w oil emulsion were maintained after 2 weeks. Thus, the stabilizing effect of the surfactant was confirmed, and the filtration tests with the use of the PS_CNN1 cryogel filter were carried out for both emulsions, right after their formation.

As presented in Figure 4.7b-c, at both compositions of the emulsions, a milky turbid permeate was obtained, suggesting the permeation of the emulsion through the filter. The permeation process was concluded within ~1.5 min. Nevertheless, the cryogel's color change after the permeation, depicted in Figure 4.7d, indicates the filter's fouling by stable emulsions. However, the results of the microscopic analysis, shown in Figure 4.7 do not indicate any significant difference between the feed and the permeate in the dimensions and amount of the oil droplets dispersed in the water continuous phase. Hence, to make the developed material able to separate emulsions, apart from the favorable wetting properties, the further engineering of the porous structure is necessary, due to the low size of the oil drops in a stably emulsified system, resulting in their passage through the macropores of the cryogel.

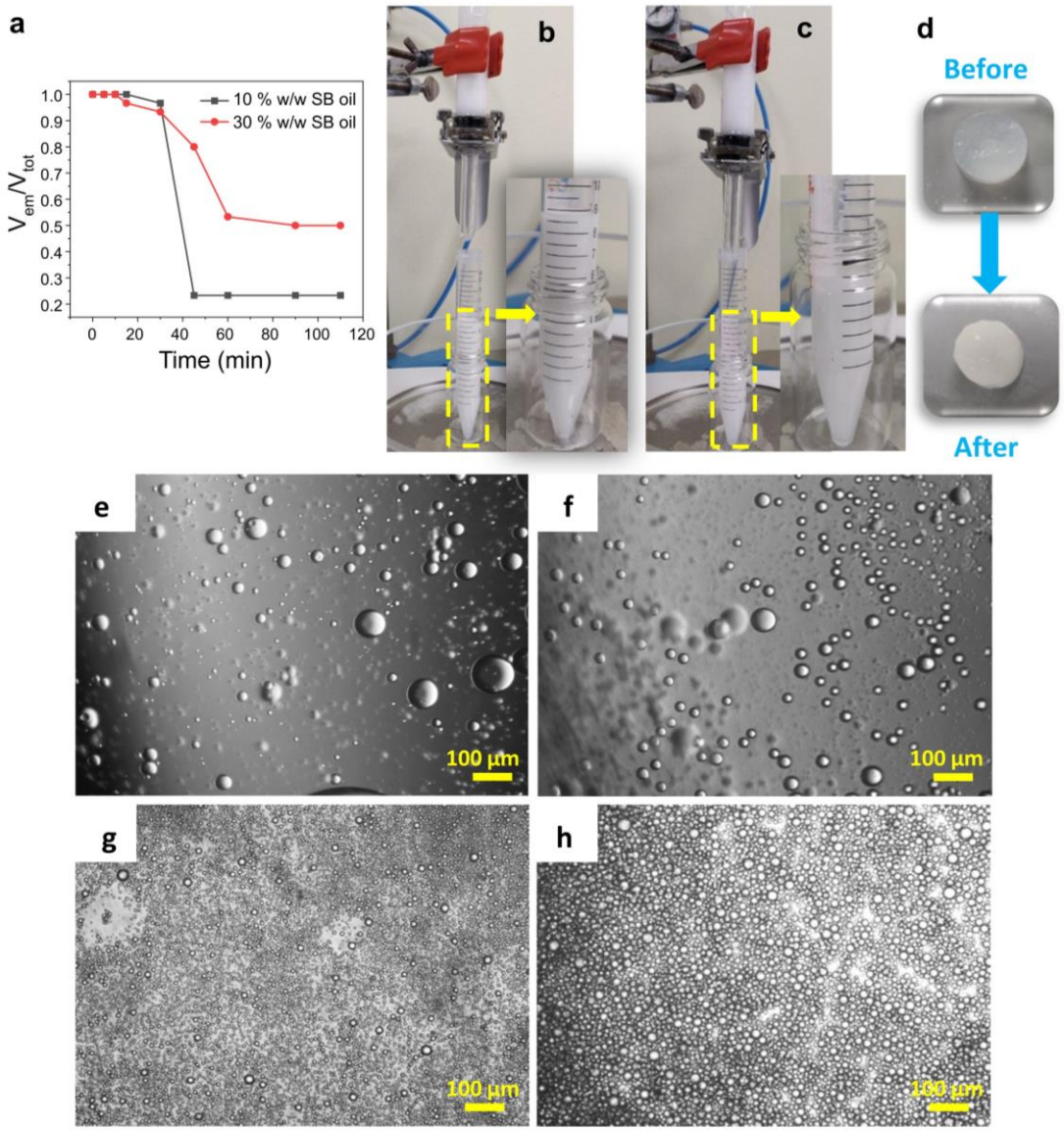

Figure 4.7. Filtration performance of the PSA_CNN1 cryogel for SB oil-in-water emulsions stabilized by Tween 80 (8×10^{-5} M). a) Stability of 30 % w/w and 10 % w/w O/W emulsions over time. b) 30 % w/w O/W emulsion feed and permeate photo. c) 10 % w/w O/W emulsion feed and permeate photo. d) Photo depicting the cryogel's fouling after the 10 % w/w O/W emulsion filtration. e-h) Polarized microscopy images of: 30 % w/w O/W emulsion feed (e) and permeate (f), 10 % w/w O/W emulsion feed (g) and permeate (h).

4.5 CONCLUSIONS

In conclusion, owing to the underwater superoleophobicity of the fabricated PSA and PSA/CNN cryogels, both high- and low-viscosity oils can be efficiently separated through the gravity-driven filtration of oily mixtures. Both cryogel types showed remarkable stability, without oil fouling, when applied in multiple filtration cycles of oil-water and oil-dye-water mixtures, with outstanding separation efficiencies of almost 100 % for SB oil, and ≥ 98 % in case of MB. Moreover, both the PSA and the PSA/CNN cryogels are highly performant in the gravity-driven filtration of multicomponent oily wastewater containing not only organic but also inorganic pollutants, reaching very high efficiency in the simultaneous separation of MB dye, Hg^{2+} ions and SB oil (≥ 97 % for each pollutant), without significant interference of the pollutants' co-presence with the cryogel's filtration performance. As in case of Hg^{2+} and MB adsorption studied in batch conditions (Chapter 3:), also in the filtration process the presence of CNNs in the PSA matrix was proven not to affect the cryogel's adsorption capacities of these pollutants, regardless of the wastewater's composition. On the top, for both cryogel types the Hg^{2+} and MB adsorption capacities reached in the filtration process were in accordance with the equilibrium adsorption capacities obtained in case of the batch conditions studies, which proves that despite the short contact time with the pollutants during the filtration process, the developed cryogel filters maintain an excellent adsorption performance. Thus, both the developed PSA and the PSA/CNN 3D filters can efficiently purify multicomponent oily wastewaters, simultaneously sorbing water-soluble pollutants of different chemical nature and separating oils. The developed materials can serve as a valuable alternative to the multi-step and energy-consuming wastewater purification processes.

Chapter 5: Multifunctionality of PSA/CNN cryogels: Dye Photocatalytic Decolorization, Mercury Detection and Recovery

In this chapter, the results of the studies exploring the multifunctional potential of the developed PSA/CNN cryogels are discussed. In particular, the applicability of the material for the purification of wastewater containing Hg^{2+} ions and the simultaneous indication of their presence through gravity-driven filtration has been investigated. The sensing properties are attributed to the graphitic carbon nitride nanosheets (CNNs), present as nanofillers of the nanocomposite filter, which modulate its fluorescence upon interaction with the Hg^{2+} ions. It has been found that although the different loadings of CNNs into the PSA matrix barely affect any of the pollutants' separation efficiencies, as proved in the studies presented in Chapter 4:, their fluorescence-based detection can be significantly modified. Through the optimization of the CNNs concentration within the cryogel, sufficiently low amounts of Hg^{2+} ions could be detected upon the gravity-driven filtration of the wastewater and the subsequent fluorescence intensity evolution monitoring of the nanocomposite cryogel. The study on the mechanism of Hg^{2+} ions adsorption by the PSA/CNN cryogel in the gravity-driven filtration process proved that it is dominated by the Na^{+}-Hg^{2+} ion exchange. This is in accordance with the findings of the same study performed in the batch conditions (Chapter 3:), suggesting that the short interaction time during the filtration process does not affect the Hg^{2+} ions sorption mechanism. The analysis of the Hg^{2+} ions adsorption capacities and of the fluorescence intensity changes, obtained in the

integrated filtration and fluorosensing process performed for cryogels with different CNN loadings, revealed that the fluorosensing mechanism is based on the interaction of the Hg^{2+} ions adsorbed by the PSA matrix with the embedded CNNs. Based on the chemical and structural analysis of the CNNs' interactions with Hg^{2+} they are driven by the electrostatic forces.

Apart from the detection of the adsorbed Hg^{2+} ions, the nanocomposite cryogel has also proven the applicability for their pH-responsive recovery via the permeation of a $NaOH_{(aq)}$ solution, which leads to the effective desorption of the heavy metal ions, allowing at the same time for the regeneration of the filter. Moreover, the PSA/CNN cryogel has shown great Hg^{2+} ions adsorption stability in consecutive gravity-driven water permeation cycles, and a stable Hg^{2+} ions recovery and separation performance was unveiled in various sorption-desorption cycles. On the top, the recovery process does not affect the fluorescence properties of the PSA/CNN cryogel in any of the cycles, making possible the simultaneous separation and detection of Hg^{2+} ions after each heavy metal ions recovery cycle.

Furthermore, the PSA/CNN cryogel's self-cleaning ability, owed to the photocatalytic activity of CNNs under daylight, was also revealed carrying out gravity-driven filtration of a SB oil-water-MB mixture, and subsequently exposing the as-obtained MB-loaded nanocomposite cryogel to the visible light irradiation. A stable MB photocatalytic decolorization as well as the oil and MB separation performance was proved in repeated filtration-photocatalysis cycles. Importantly, no effect of the photocatalytic process on the cryogel's texture and chemical stability was observed.

In conclusion, the studies presented in this chapter prove a promising versatile character of the developed PSA/CNN cryogel for the use in the integrated water treatment, pollutants recovery, photocatalytic self-cleaning, and water quality

monitoring process.

5.1 MATERIALS AND METHODS

5.1.1 Materials

Methylene blue (MB) and sodium hydroxide (NaOH) were purchased from Sigma-Aldrich. For the preparation of the heavy metal solutions, mercury (II) chloride ($HgCl_2$) and lead (II) nitrate ($Pb(NO_3)_2$) purchased from Sigma-Aldrich, and copper (II) chloride ($CuCl_2$) from Alfa Aesar were used. Soybean oil (SB oil) (Bunge) was bought in a local shop. All the chemicals were used as received without further purification. All the experiments were performed with the use of Milli-Q water.

5.1.2 Materials characterization

The X-ray diffraction (XRD) study was performed using an X-ray powder diffractometer (PANalytical Empyrean) equipped with a 1.8 kW CuKα ceramic X-ray tube (λ=1.5418 Å) operating at 40 mA and 45 kV and PIXcel^{3D} area detector (2 × 2 mm^2). The divergent X-ray beam was converted into a parallel beam (PB) with the use of the poly-capillary X-ray lens and the CuKα radiation was suppressed using a Ni filter. The diffraction patterns were acquired in air at room temperature at 2θ range of 10-70 °, with a step size of 0.026 ° and a step time of 435.18 s.

The surface chemistry of the materials involved in this work was studied with X-ray photoelectron spectroscopy (XPS) using an electron spectrometer (Lab2, Specs, Berlin, Germany) equipped with a monochromatic X-ray source (set at 1486 eV) and with a hemispherical energy analyzer (Phoibos, HSA3500, also from Specs). The applied voltage of the Al Kα X-ray source was 13 kV and the applied current was set at 8 mA. The pressure in the analysis chamber was ≈ 1 × 10^{-9} mbar. The large area lens mode was utilized for both wide and narrow scans. In the wide scan, the energy pass

and step were 90 eV and 1 eV, respectively, and in the narrow high-resolution scan, the energy pass and step were 30 eV and 0.1 eV, respectively. A flood gun, with the energy of 7 eV and the filament current of 2.2 A, was used to neutralize the surface charge. For the XPS characterization of the cryogels before and after the purification process, the adsorption process was executed in batch conditions through the immersion of cryogels in 15 mL of Hg^{2+} aqueous solution at 300 mg L^{-1} for 5 h using continuous shaking at 600 rpm.

The chemical composition of all the cryogels (in dry conditions): pristine, after the permeation of 100 mL of water, and after the filtration of 100 mL of Hg^{2+} aqueous solution at 8 mg L^{-1} (which followed the permeation of 100 mL of water), as well as of the bulk CNNs powder, was analyzed with the use of a Fourier Transform Infrared (FTIR) spectrometer (Vertex 70v FT-IR, Bruker) equipped with a single-reflection attenuated total reflection (ATR) accessory (MIRacle ATR, PIKE Technologies). All the spectra were recorded from 4000 to 600 cm^{-1} and 64 repetitive scans were run at a resolution of 4 cm^{-1} with the background spectrum collected for the same number of scans.

Fluorescence emission spectra were obtained utilizing a FluoroMax spectrofluorometer (Horiba Scientific, USA) using the slit width of 5 nm, and an excitation wavelength of 310 nm. The fluorescence measurements of the cryogels were performed by blocking a swelled cryogel in a cuvette. Six runs per sample were conducted, and the fluorescence peak intensity values were averaged.

The UV-visible absorption analysis, for the determination of MB and SB oil concentrations in the feeds and permeates, was performed utilizing a Varian Cary 6000i UV-visible-NIR spectrophotometer (the detailed procedure is described in

Section 3.1.2).

The concentration of Hg^{2+} and Na^{+} ions in the feeds and permeates was measured with an Inductively Coupled Plasma Optical Emission (ICP-OES) spectrometer iCAP (7600 DUO Thermofisher Scientific) at the auxiliary gas, coolant gas and nebulizer gas flows of 0.5 L min^{-1}, 12 L min^{-1}, and 0.5 L min^{-1}, respectively. An internal standard calibration curve was used and 3 scans per sample were conducted. The detailed procedure of the calculation of the Hg^{2+} and Na^{+} ions content in the solutions is described in Section 3.1.2.

5.1.3 Fluorosensing study

The photoluminescence properties of the CNNs were firstly confirmed by acquiring the fluorescence emission spectra of their aqueous dispersion (10 µg mL^{-1}). The excitation wavelength of 310 nm was chosen based on the obtained UV-vis absorbance spectrum of the CNNs (Figure 5.1), and it was used for all the herein presented spectrofluorometric studies.

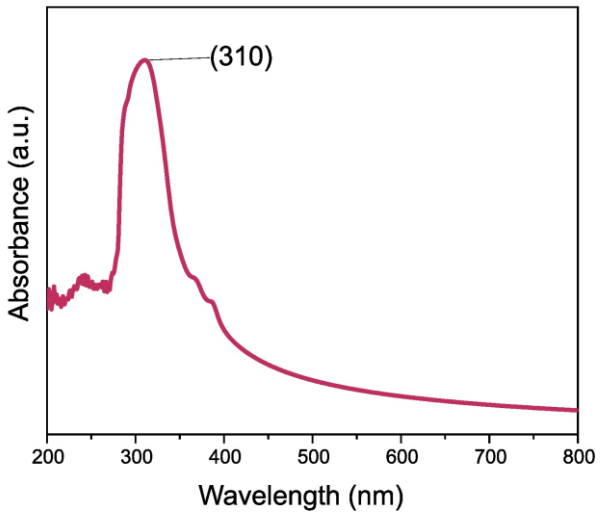

Figure 5.1. UV-vis spectrum of the CNNs dispersion.

Next, the fluorescence emission spectra were monitored for aqueous dispersions of 10 mg L^{-1} CNNs in the presence of 10 mg L^{-1} of the different heavy metal ions aqueous solutions. The as-obtained mixtures were sonicated with an ultrasonic probe for 5 s at the amplitude of 40 % prior to the fluorescence measurement.

Subsequently, the photoluminescence properties of the CNNs incorporated into the PSA matrix were studied, and it was explored how they are affected after the adsorption of Hg^{2+} ions. The fluorescence intensity change of the peak at 442 nm in the presence of the adsorbed ions, ΔFI (%) was determined as follows:

$$\Delta\text{FI}\ (\%) = \frac{\text{FI}_0 - \text{FI}}{\text{FI}_0} \times 100\% \tag{5.1}$$

where FI_0 and FI are the fluorescence intensities of the swelled cryogel before and after the Hg^{2+} adsorption, respectively. The adsorption process was performed by the gravity–driven filtration of 100 mL Hg^{2+} aqueous solutions at different concentrations (1, 2, 3, 5, 8 mg L^{-1}, pH: 5.9-6.0). Given the fact that the volume of the filtration column was 20 mL, the filtration process was carried out by continuous pouring of the feed in the filtration column. In brief, for each case, the procedure consisted of four consecutive steps: i) recording the fluorescence emission spectrum of the swollen PSA/CNN cryogel, ii) permeation of 100 mL of pure water, as a control test of the material's permeation performance, iii) filtration of 100 mL of Hg^{2+} solution at a given concentration, iv) recording the fluorescence emission spectrum of the swelled PSA/CNN cryogel. As a reference sample, the neat PSA cryogel was also used for the filtration of 100 mL of Hg^{2+} solutions at the above-mentioned concentrations, following only the steps ii) and iii).

The Hg^{2+} separation efficiency, E_{eff_Hg} (%), and the Hg^{2+} adsorption capacity, q_{Hg} (mg g^{-1} cryogel) were calculated as described in Section 4.1.3.

5.1.4 Study of the interactions of Hg^{2+} ions with the cryogels

The release of Na^+ from the cryogels during the filtration of the aqueous solutions of Hg^{2+} was determined to explore the adsorption mechanism. To assure that the Na^+ release is attributed solely to the Hg^{2+}-Na^+ exchange, the normalized Na^+ release, $q_{r\_Na\_ex}$ (mg g^{-1} cryogel), was determined as follows:

$$q_{r\_Na\_ex} = q_{r\_Na} - q_{r\_Na\_w} \quad (5.2)$$

where q_{r_Na} is the Na^+ release (mg g^{-1} cryogel) upon the filtration of 100 mL of Hg^{2+} aqueous solution (corresponding to step iii) in the procedure described in Section 5.1.3, whereas $q_{r\_Na\_w}$ (mg g^{-1} cryogel) is the Na^+ release (mg g^{-1} cryogel) upon the permeation of 100 mL of pure water, after step ii), in the procedure described in Section 5.1.3.

The values of q_{r_Na} (mg g^{-1} cryogel), and q_{r_Na/Na_w} (mg g^{-1} cryogel) were determined as follows:

$$q_{r_{Na/Na\_w}} = \frac{m_{Na\_f} - m_{Na\_i}}{m} \quad (5.3)$$

where m_{Na_f} and m_{Na_i} are the Na^+ mass (mg) in the Hg^{2+} ions solution/pure water permeate and the feed, respectively, and m_0 is the mass (g) of the dry cryogel. The procedures of m_{Na_f} and m_{Na_i} determination are described in Section 3.1.2.

Finally, the molar ratio of Na^+ released (solely due to Na^+-Hg^{2+} ion exchange) per 1 mol of Hg^{2+} adsorbed was calculated according to the following equation:

$$\text{molar ratio}_{(Na/Hg)} = \frac{q_{r(mol)\_Na}}{q_{(mol)\_Hg}} \quad (5.4)$$

where $q_{r(mol)\_Na}$ is the Na^+ molar release and $q_{(mol)\_Hg}$ is the Hg^{2+} molar adsorption capacity (both in mol L^{-1} g^{-1} cryogel), calculated as follows:

$$q_{r(mol)\_Na} = \frac{q_{r\_Na\_ex}}{M_{Na} \times m} \quad (5.5)$$

$$q_{(mol)\_Hg} = \frac{q_{\_Hg}}{M_{Hg} \times m} \quad (5.6)$$

where $M_{Na/Hg}$ (g) is the molecular weight of sodium/mercury, and m (g) is the mass of the dry cryogel.

5.1.5 Study of the interactions of Hg^{2+} ions with the CNNs

In order to examine the nature of the interactions occurring between the pure CNNs and Hg^{2+} ions, XPS and XRD studies were performed, using the same assemblies and the parameters as described in Section 5.1.2. The samples were prepared by adding 5 mL of a 100 mg L^{-1} Hg^{2+} solution to aqueous dispersions of 5 mL CNNs (400 mg L^{-1}). After 15 min of the interaction time, 1 ml of the mixture (containing 0.2 mg of CNNs) was centrifuged for 20 min at 15300 rpm and 20°C, using Centrisart® G-16C centrifuge (Sartorius, Germany). Then the supernatant was removed, together with any non-reacted Hg^{2+} present. A few samples prepared in this way were subsequently unified and re-dispersed in 1 mL of Milli-Q water upon vortexing for 30s. The centrifugation and supernatant removal process was repeated once more, to assure the complete removal of any residuals of non-reacted Hg^{2+}. Subsequently, the wet pellet was deposited on a silicon wafer and dried for further studies. Bulk CNNs powder without any previous treatments served as a reference sample.

5.1.6 Desorption and Reusability Study

To investigate the stability of the interactions occurring between the cryogel filters and the Hg^{2+} ions, three consecutive pure water permeation cycles (15 mL each) were performed on the cryogels loaded with Hg^{2+} ions after the filtration of 15 mL of 5 mg L^{-1} Hg^{2+} aqueous solution. The Hg^{2+} desorption efficiency ($D_{Hg\_w(n)}$ %) in the n-th pure water permeation cycle was calculated as follows:

$$D_{Hg\_w(n)} = \frac{m_{des\_w(n)}}{m_{0\_w(n)}} \times 100\% \quad (5.7)$$

where $m_{des\_w\,(n)}$ and $m_{0\_w(n)}$ are the desorbed Hg^{2+} mass and the initial mass of Hg^{2+} in the cryogel in the n-th cycle (mg), respectively, and $m_{0\_w(n)}$ (mg) is calculated as follows:

$$m_{0\_\,w(n)} = m_{0\_\,w(n-1)} - m_{des\_w(n)} \quad (5.8)$$

where $m_{0\_\,w(n-1)}$ is the initial mass (mg) of Hg^{2+} in the cryogel in the previous cycle.

To evaluate the regeneration and reusability of the Hg^{2+}-loaded 3D cryogel filters three Hg^{2+} adsorption-desorption cycles were carried out and they consisted of the following steps: i) filtration of 15 ml of Hg^{2+} (5 mg L^{-1}) aqueous solution, ii) Hg^{2+} recovery via permeation of 100 mL of $NaOH_{(aq)}$ solution (pH=12), iii) cryogel washing via the permeation of 100 mL of pure water. Before the first cycle, pure water permeation (15ml) was performed to control the permeation performance of the cryogels. The experiments were performed in duplicates. The contents of the heavy metal ions in the filtration feeds and the permeates were determined as described in Section 3.1.2. Figure 5.2 presents a schematic representation of the adsorption-desorption cycles indicating the denotation of the Hg^{2+} ions mass in the feeds and the permeates, as well as the adsorbed and the desorbed Hg^{2+} ions mass at the consecutive steps.

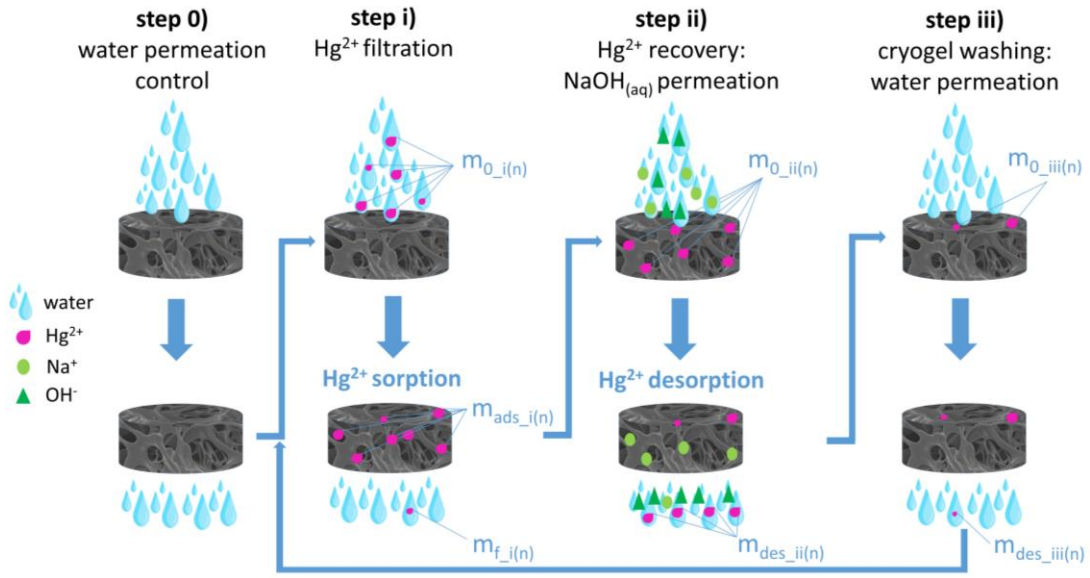

Figure 5.2. Schematic representation of the Hg^{2+} ions adsorption-desorption cycles including the denotations of the Hg^{2+} ions mass in the initial solutions, permeates, as well as adsorbed and desorbed at the consecutive steps.

The Hg^{2+} desorption capacity in the Hg^{2+} recovery step ii), ($q_{D\_Hg\_ii(n)}$ mg g^{-1} cryogel), as well as the Hg^{2+} desorption efficiency in the washing step iii) ($D_{Hg\_iii(n)}$ %), of the n-th reuse cycles, were calculated as follows.

The determination of $q_{D\_Hg\_ii(n)}$ for each of the reuse cycles:

The Hg^{2+} desorption capacity in the recovery step ii) of the n-th reuse cycle ($q_{D\_Hg\_ii(n)}$ mg g^{-1} cryogel) was determined as follows:

$$q_{D\_Hg\_ii(n)} = m_{\_des\_ii(n)} / m \quad (5.9)$$

where: m is the mass (g) of the dry cryogel, and $m_{\_des\_ii(n)}$ is the desorbed Hg^{2+} mass (mg) in the Hg^{2+} recovery step ii) of the n-th reuse cycle.

The initial mass of Hg^{2+} in the cryogel in the recovery step ii) of the first reuse cycle (n=1), $m_{0\_ii(n)}$ (mg) was calculated as follows:

$$m_{0\_ii(1)} = m_{ads\_i(1)} \quad (5.10)$$

where $m_{ads\_i(n)}$ is the mass (mg) of Hg^{2+} adsorbed by the cryogel from the Hg^{2+} aqueous

solution of the filtration step i) in the n-th reuse cycle, and:

$$m_{ads\_i(n)} = m_{0\_i(n)} - m_{f\_i(n)} \quad (5.11)$$

where $m_{0\_i(n)}$ is the Hg^{2+} mass (mg) in the feed solution, and $m_{f\_i(n)}$ is the Hg^{2+} mass (mg) in the permeate in step i) of the n-th reuse cycle.

The determination of $D_{Hg\_iii(n)}$ for each of the reuse cycles:

The Hg^{2+} desorption efficiency in the washing step iii), ($D_{Hg\_iii(n)}$ %) of the n-th reuse cycle was calculated as follows:

$$D_{Hg\_iii(n)} = (m_{des\_iii(n)} / m_{0\_iii(n)}) \times 100\% \quad (5.12)$$

where $m_{des\_iii(n)}$ and $m_{0\_iii(n)}$ are the desorbed Hg^{2+} mass and the initial mass of Hg^{2+} in the cryogel (mg), in the washing step (iii) of the n-th reuse cycle, respectively and:

for n=1: $$m_{0\_iii(1)} = m_{ads\_i(1)} - m_{des\_ii(1)} \quad (5.13)$$

for n=2: $$m_{0\_iii(2)} = m_{0\_iii(1)} - m_{des\_iii(1)} + m_{ads\_i(2)} - m_{des\_ii(2)} \quad (5.14)$$

for n=3: $$m_{0\_iii(3)} = m_{0\_iii(2)} - m_{des\_iii(2)} + m_{ads\_i(3)} - m_{des\_ii(3)} \quad (5.15)$$

where $m_{des\_ii(n)}$ and $m_{des\_iii(n)}$ are the desorbed Hg^{2+} mass (mg) in the recovery step ii) and washing step iii) of the n-th reuse cycle, respectively.

The influence of the $NaOH_{(aq)}$ treatment on the cryogel's q_{Hg} in the filtration step i) of each reuse cycle were evaluated following Equation (4.4) Moreover, the stability of the material's photoluminescent behaviour after the successive $NaOH_{(aq)}$ treatments was investigated, i.e. the fluorescence emission spectra were recorded for the cryogel before any treatment, after Hg^{2+} ions sorption (step i) and at the end of each cycle (step iii). The volumes of the cryogel samples before and after the $NaOH_{(aq)}$ treatment were assessed, according to the procedure described in Section 2.1.4.

Unless differently stated, all values presented in this chapter are the mean values of three measurements at three different samples. All the Hg^{2+} solutions used in this work were prepared in the form of $HgCl_{2(aq)}$.

5.1.7 Photocatalytic performance study

The photocatalytic decolorization of the MB dye adsorbed by the cryogels during the gravity-driven filtration of 15 mL of the oil-water-MB mixture (0.5 mg L^{-1} MB, 30 % w/w SB oil with respect to the total mixture volume) was studied by means of a Varian Cary 6000i UV–vis–NIR spectrophotometer. One filtration cycle consisted of two consecutives steps: i) permeation of 15 mL of pure water, and ii) filtration of 15 mL of the oil-water-MB mixture. The UV-vis absorbance spectra of the swollen cryogels after the dye adsorption were recorded, then the dye-loaded cryogels were immersed in small glass Petri dishes with 2.5 mL of Milli-Q water, and placed under fluorescent lamps connected to a climatic chamber (ICH 110 L, Memmert) and emitting in the wavelength range between 400 nm to 600 nm, at a distance of 15 cm. The evolution of the MB concentration in the cryogel was monitored by recording the UV-vis absorbance spectra of the swollen cryogels at given time intervals (7 h and 24 h), and the decolorization efficiency (%) was calculated as follows:

$$\text{decolorization efficiency} = \frac{A_t}{A_0} \times 100\% \tag{5.16}$$

where A_0 and A_t are the areas under the MB Absorbance-Wavelength curve, initial and at determined time intervals, respectively. The fully swollen cryogels were fixed in a solid samples holder, and three measurements were taken re-positioning the gels for each of them. The areas under the curve were calculated by integrating the Absorbance-Wavelength curve in the range of 415-800 nm, using the Origin Lab software, and the obtained values were averaged.

The morphology and the chemical composition of a PSA/CNN cryogel were analysed after the filtration cycle consisting of two consecutive steps: i) permeation of 15 mL of pure water, and ii) filtration of 15 mL of the water-MB mixture (0.5 mg L^{-1} MB), followed by 24 h of the exposure to the visible light irradiation in the climatic chamber, as described above in this section. To this end, SEM analysis of the cross-sectional morphology of the subsequently freeze-dried cryogel was performed with JEOL JSM-6490LA, at an acceleration voltage of 10 kV, after coating the samples with a 10-nm Au layer using a high-resolution Cressington 208 HR sputter coater. The FTIR analysis of the freeze-dried cryogel after the visible light irradiation was also performed, as described in Section 5.1.2. For comparison reasons, a PSA/CNN cryogel subjected to solely two consecutive permeations of 15 mL of pure water was also analysed by means of SEM and FTIR.

Prior to the morphological and chemical analysis both cryogels were dried in a freeze dryer (Base Unit LIO5P-4K, for 48h at −50 °C) after being stored overnight at -80°C.

5.2 MERCURY FLUOROSENSING PERFORMANCE

Mercury fluorosensing properties of the PSA/CNN cryogels are expected owing to the photoluminescence of CNNs.

Even though the studies on the filtration performance of the cryogels (Section 4.3) revealed that the presence of CNNs in the cryogels composition does not affect the Hg^{2+} separation efficiencies at the studied filtration conditions, the entrapped heavy metal ions interact with the CNN nanofillers of the cryogel, influencing their photoluminescence properties, which is in accordance with what was observed for the pure CNNs dispersions (Figure 5.3).

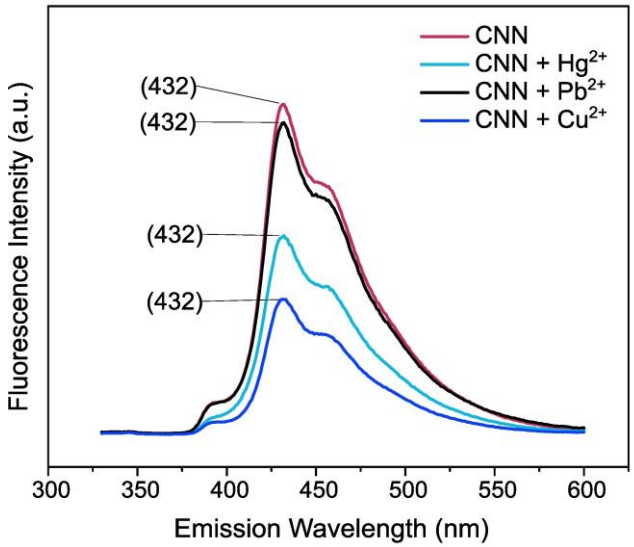

Figure 5.3. Fluorescence spectra of the CNN 10 mg L^{-1} aqueous dispersions: pristine and in presence of 10 mg L^{-1} Pb^{2+}, Hg^{2+} and Cu^{2+} chloride salts.

As presented in Figure 5.4, the non-fluorescent neat PSA cryogel becomes fluorescent after embedding 1 and 3 % w/w of CNNs into its porous structure. The fluorescence spectra of the PSA/CNN nanocomposites show a 10 nm bathochromic shift of the maximum peak (442 nm) with respect to the peak position obtained for the pure CNNs aqueous dispersion, possibly due to the changes in the CNNs surrounding

microenvironment[373–375]. After the adsorption of Hg^{2+} ions by the PSA/CNN nanocomposite cryogels, their fluorescence intensity significantly decreases, without further modification of the spectrum profile, indicating a quenching effect induced by the interaction of the sorbed ions with the CNN nanofillers. This behaviour can be attributed exclusively to the CNNs-Hg^{2+} ions interactions as the interaction of the neat PSA cryogel with Hg^{2+} does not affect its non-fluorescent character (Figure 5.4).

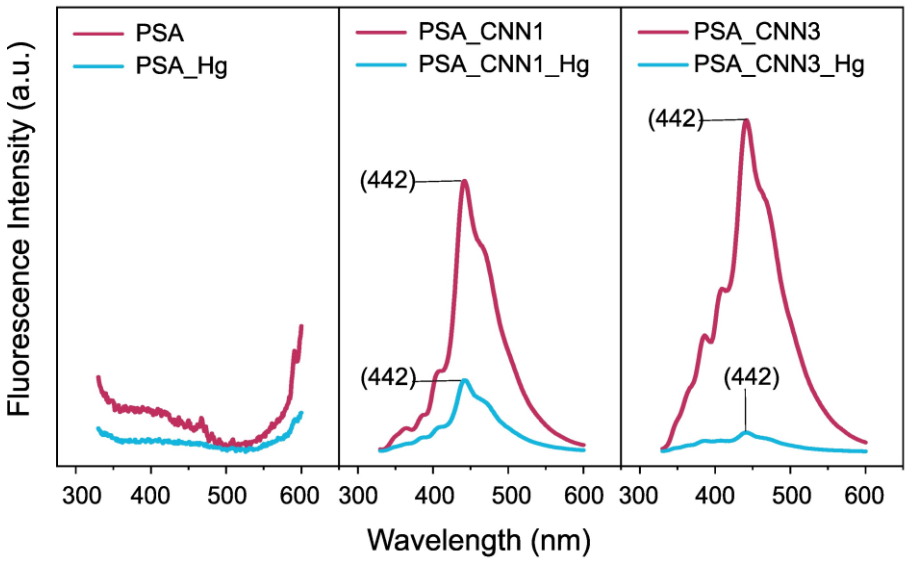

Figure 5.4. Representative fluorescence spectra of the PSA, PSA_CNN1 and PSA_CNN3 cryogels before and after the filtration of 100 mL of 8 mg L^{-1} Hg^{2+} aqueous solution.

The fluorescent response of the PSA/CNN cryogels upon the filtration of 100 mL of Hg^{2+} ions aqueous solutions and its relation to the q_{Hg} of the cryogels, were systematically studied at different concentrations of the heavy metal ions and CNNs loadings within the polymer matrix. As shown in Figure 5.5, q_{Hg} increases with the increase of Hg^{2+} initial concentration in the feed solution for both the neat PSA and the PSA/CNN cryogels, showing an effective uptake process. Both cryogel types reach similar q_{Hg} values at the given Hg^{2+} concentrations in the feeds, with a slight effect of the nanofillers on the Hg^{2+} adsorption performance of the cryogels evident only at the

highest studied CNNs content and Hg^{2+} concentration in the feed, where the q_{Hg} of the PSA_CNN3 is ~10% higher than the one achieved by the PSA and the PSA_CNN1. On the other hand, Figure 5.5b-c shows that even though the q_{Hg} is similar for the three cryogels tested, the higher the amount of CNNs in their composition, the higher is the ΔFI, possibly due to the higher density of the nanofillers in the cryogel that makes them more readily available to interact with the sorbed ions. Alternatively, for each nanocomposite cryogel type, the higher the concentration of Hg^{2+} in the feed solution, the higher is ΔFI, due to the higher amount of the sorbed ions, which enhances the possibility to interact with the englobed CNNs. These evidences can be further confirmed by the fact that even though for both nanocomposite cryogels the minimum Hg^{2+} concentration in the feed solutions where the fluorescence quenching occurs is 3 mg L^{-1}, a more significant response is observed for the PSA_CNN3 (ΔFI=66.40±8.31 %) compared to the PSA_CNN1 (ΔFI=34.60±5.99 %). Overall, the fluorescence of the nanocomposite cryogels is quenched after the interaction with the feed solutions due to the successful entrapment of the heavy metal ions by the PSA matrix and to their subsequent interaction with the CNN fillers. Thus, the englobed CNNs are able to effectively interact with the sorbed Hg^{2+} ions and act as a fluorosensing nanofiller.

Importantly, fluorescence quenching upon the interaction with Hg^{2+} ions increases not only with the increment of the CNNs content in the cryogel and of the heavy metal ions concentration, but also with the increase of the feed solution volume. In particular, in case of the PSA_CNN3 cryogel and the Hg^{2+} concentration of 5 mg L^{-1}, ΔFI of 17.74±8.43 % was achieved with the feed volume of 15 mL, and, as shown in Figure 5.5c, ΔFI of 76.30±2.09 % was reached with the feed volume of 100 mL. Hence, at the given Hg^{2+} ions concentration and CNNs loading, a significant improvement of the fluorescence-based response could be achieved with the higher feed volume. This

indicates that further optimization of the detection performance might be possible via the modulation of the filtration feed volume and the CNNs loadings within the polymer matrix. In any case, the limit of detection (LOD) of 3 mg L^{-1} Hg^{2+} attained with the feed volume of 100 mL is sufficiently low for industrial wastewaters from specific sectors where effluents of mercury are typically found, such as the wastewaters coming from metallurgical or chloro-alkali industry and fuel combustion plants[74–79].

It is worth noting that the filtration process of 100 mL of Hg^{2+} aqueous solutions lasts around 5 min (regardless of the Hg^{2+} concentration) and the fluorescence spectra were recorded immediately after the filtration process, which reveals a quick response of the 3D filter, making it a suitable candidate for the use as an alternative to the commonly utilized, sophisticated, and time-consuming heavy metal ions detection methods.

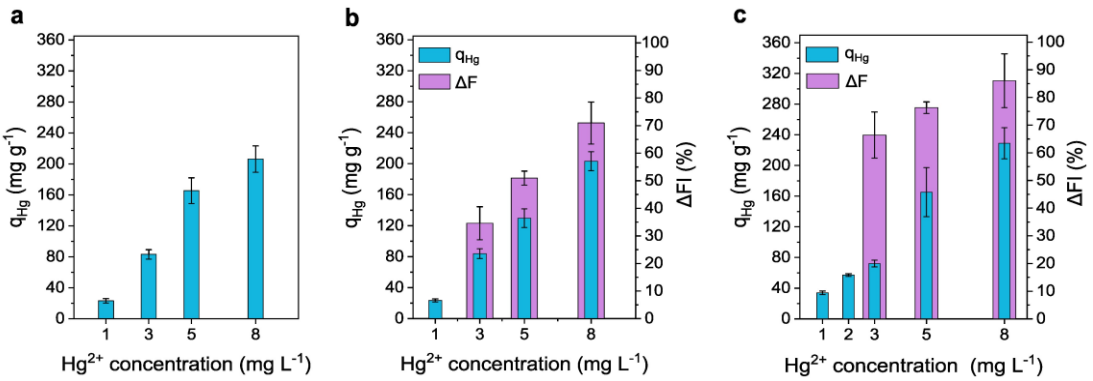

Figure 5.5. Hg^{2+} fluorosensing performance of the cryogels and its relation with the Hg^{2+} adsorption capacity. a) Adsorption capacity (q_{Hg}) after the filtration of Hg^{2+} aqueous solutions using the neat PSA cryogel. b-c) q_{Hg} and fluorescence quenching (ΔFI) after the filtration of Hg^{2+} aqueous solutions using the PSA_CNN1 (b) and PSA_CNN3 (c) cryogel filters. For all cases the feed volume was 100 mL.

Additionally, as shown in Figure 5.6, high E_{eff_Hg} are reached by the PSA, PSA_CNN1 and the PSA_CNN3 cryogels upon the filtration of 100 ml solutions of Hg^{2+} ions at

the different concentrations. No effect of Hg^{2+} concentration in the feed solution and of the CNN nanofiller at different loadings on the separation efficiency of the cryogel filter is observed.

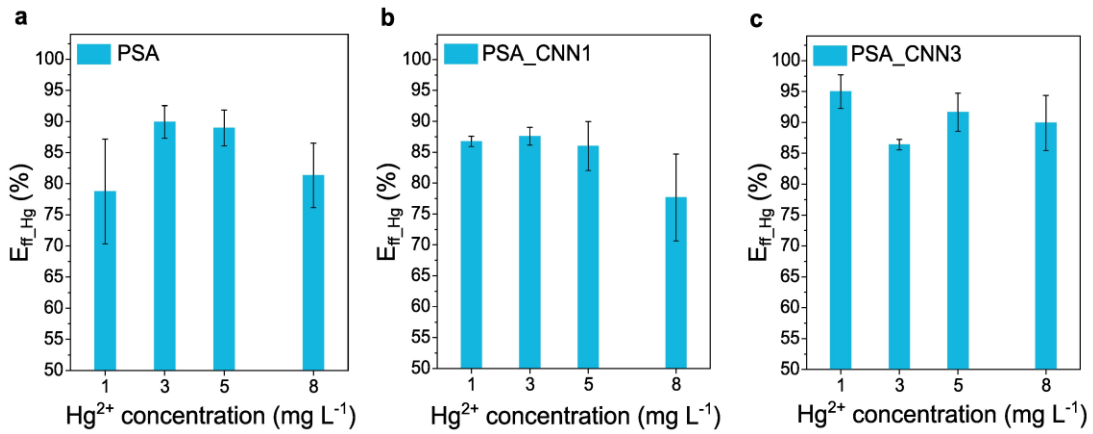

Figure 5.6. Hg^{2+} separation efficiency during the filtration of 100 mL of Hg^{2+} aqueous solutions at the different concentrations, reached by the a) PSA, b) PSA_CNN1, and c) PSA_CNN3 cryogels.

5.3 MERCURY ADSORPTION MECHANISM

5.3.1 Hg^{2+} ions interactions with the PSA and the PSA/CNN cryogels upon filtration

Na^+ release during the filtration of water and of Hg^{2+} ions aqueous solutions

Based on the Na^+ release studies performed in batch conditions for the different cryogel types, their interaction with Hg^{2+} through the ion exchange with Na^+, coming from the $–COO^-Na^+$ groups of the PSA structure, is expected[312,345,346,376]. Nevertheless, the interaction time of the cryogels with the Hg^{2+} ions solution during the gravity-driven filtration process is shorter compared to the case of Hg^{2+} ions uptake by the cryogels' through immersion in their solution until the equilibrium adsorption capacity is reached. For this reason, the Na^+ release from the cryogels to the permeate upon the

filtration of Hg^{2+} aqueous solutions was also determined. As presented in Figure 5.7 apart from the possible ion exchange between Hg^{2+} and Na^{+}, there is also the possibility of the Na^{+} exchange with H^{+} of the water molecules present in the feed solutions[354]. This is in accordance with the findings of the study on the Hg^{2+} ions mechanism adsorption in batch conditions, presented in Section 3.4.1. For the definition of Hg^{2+} sorption mechanism during the gravity-driven filtration process a detailed experimental process was followed, as described in the Section 5.1.4.

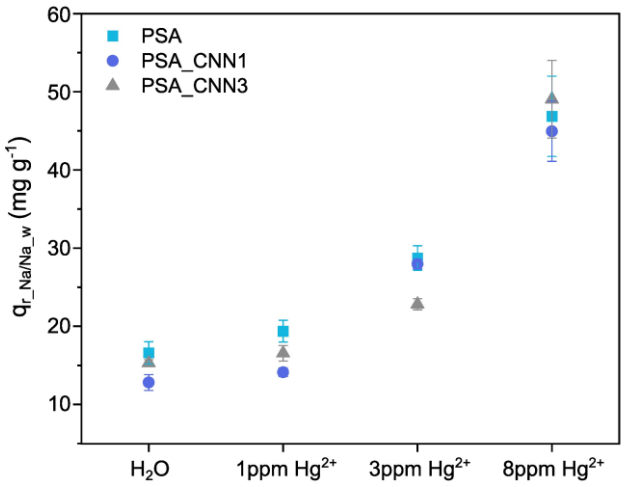

Figure 5.7. Na^{+} release after the permeation of 100 mL of pure water ($q_{r\_Na\_w}$) and after the subsequent filtration of 100 mL of Hg^{2+} aqueous solutions of given concentrations (q_{r_Na}).

As demonstrated in Figure 5.8, in case of the neat PSA cryogel, the molar $ratio_{(Na/Hg)}$ remains unchanged for all the reported Hg^{2+} concentrations in the feed solutions (~1.3), indicating that for 1.0 mol of Hg^{2+} ions sorbed, 1.3 mols of Na^{+} ions are released into the permeate. Regarding the nanocomposite cryogels, even if the Hg^{2+} adsorption capacity is barely affected by the presence of the CNNs (Figure 5.5), the molar $ratio_{(Na/Hg)}$ starts from lower values compared to PSA, and it increases as the concentration of Hg^{2+} in the feed solutions increases. This is more evident in the PSA_CNN3 sample with the molar $ratio_{(Na/Hg)}$ gradually growing from ~0.5 for

1 mg L^{-1} Hg^{2+} to ~0.8 for 3 mg L^{-1}, until it finally reaches a value similar to the one achieved by the neat PSA for 8 mg L^{-1}. Such behaviour may be attributed to the capability of the CNNs to entrap Na^{+} [355–358], preventing their release into the permeate after their exchange with the Hg^{2+} ions. This phenomenon can be more evident at the lowest studied Hg^{2+} concentrations in the feed, where, as observed in the fluorescence study, the englobed CNNs barely interact with the adsorbed Hg^{2+} ions (Figure 5.5b-c). The effect of the CNNs' presence on the exchanged Na^{+} release may be further confirmed by the fact that the PSA_CNN1 reaches the molar $ratio_{(Na/Hg)}$ value of the neat PSA at a lower Hg^{2+} feed concentration compared to the PSA_CNN3. These findings are in accordance with the observations from the Na^{+}-Hg^{2+} ion exchange study performed in the batch conditions at lower Hg^{2+} concentrations.

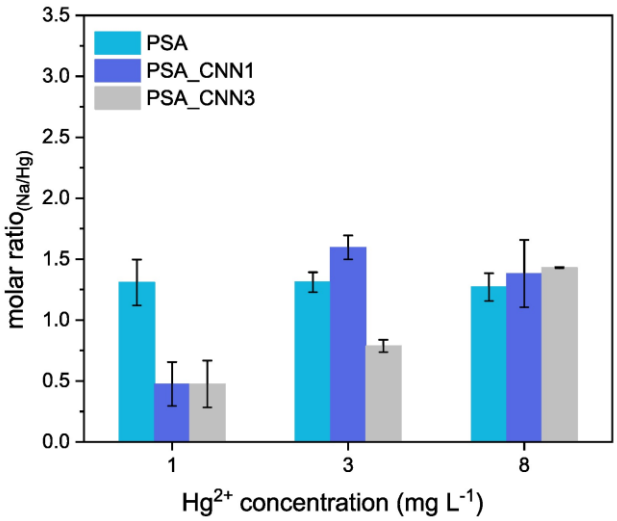

Figure 5.8. Molar ratio of Na^{+} in the permeate released solely due to the ion exchange with Hg^{2+}, per 1 mol of Hg^{2+} adsorbed upon the filtrations of 100 mL of Hg^{2+} aqueous solutions of different concentrations.

Chemical analysis of the interactions between Hg^{2+} ions and the cryogels

Figure 5.9 presents the FTIR spectra of the pure CNNs and of the cryogels at the two steps of the filtration process, described in Section 5.1.3 (step ii): after pure water

permeation, and step iii): after the subsequent filtration of Hg^{2+} aqueous solution, both at the same volume). The characteristic peaks of the embedded CNNs between 3080 and 3290 $cm^{-}1$, attributed to the stretching mode of the terminal NH_2 or NH groups of the nanosheets[319,320], and at 1317-1321, 1240, 1209 and 891 and 812 cm^{-1}, attributed to the breathing vibrations of the tri-s-triazine units and to the typical stretching modes of the CN heterocycles[259,317,318,337], are observed in the PSA_CNN nanocomposites after both filtration procedure steps. As in case of the pristine cryogels (Chapter 2:, Section 2.2), these peaks are more evident in the cryogels with the higher CNN concentration (Figure 5.9b). The absorption band at around 1665 cm^{-1} for PSA can be attributed to the -ONa group or to the C=O stretching vibration of the hydrogen-bonded carboxyl groups (C=O···HO) of PSA[313,377,378]. The observed shift of this peak towards higher wavenumbers in the PSA/CNN nanocomposite cryogels but also after the interaction with the Hg^{+2} ions, indicates the weakening of the hydrogen bonds between the carboxyl groups, suggesting the modification of the polymer's configuration in the presence of the fillers and of the metal ion. A band of asymmetrical stretching vibration of the C=O bond in the carboxyl anion ν_{as}–COO^{-}, typical of the PSA polymer[311], is located at 1553 cm^{-1} in the PSA spectrum and at ca. 1555-1560 cm^{-1} in the spectra of the PSA/CNN nanocomposites. Upon the interaction with Hg^{2+} ions, this band shifts towards lower wavenumbers (1543-1547 cm^{-1}), indicating an interaction of the polymer's carboxyl groups (COO^{-}) with the heavy metal ions, due to the replacement of Na^{+} ions of the $COO^{-}Na^{+}$ groups with the Hg^{2+} ions, confirming what we previously observed. The peaks at ca. 1452 cm^{-1}, ca. 1400 cm^{-1}, and at 1171-1175 cm^{-1} appear in all the studied cryogel samples, after both filtration procedure steps, and they correspond to the bending vibrations of δ-(CH_2)[312,313], the symmetric

stretching vibrations of the C=O bond in the carboxylate anion, ν_s–COO^- [311,312], and the C-O stretching vibration of the carboxyl groups, respectively.

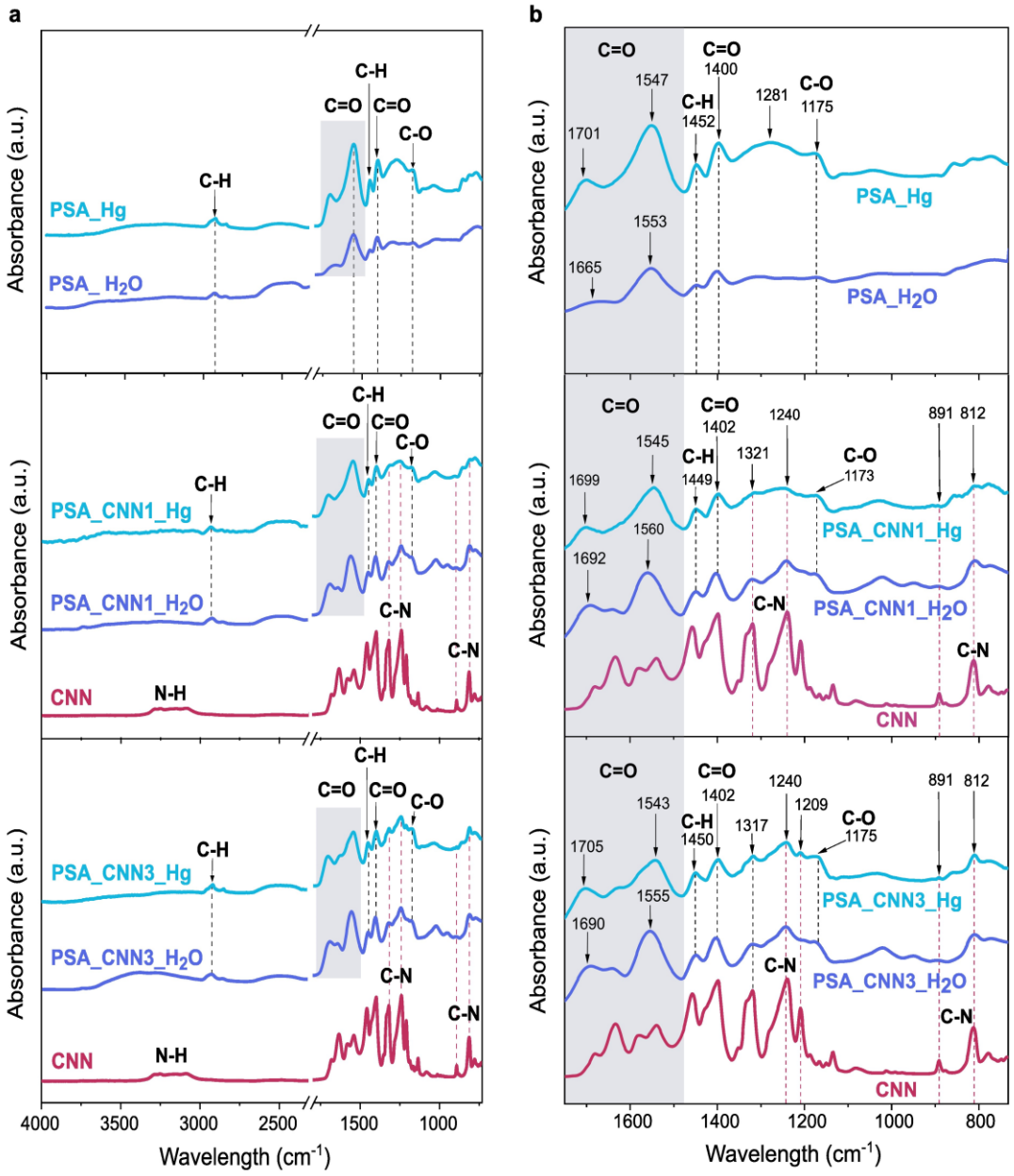

Figure 5.9 The whole (a) and the low (b) wavenumber range FTIR spectra of the CNNs and the cryogels after the filtration of 100 mL of pure water (PSA_H_2O, PSA_CNN1_H_2O, PSA_CNN3_H_2O) and after the subsequent filtration of 100 mL of Hg^{2+} aqueous solution at 8 mg L^{-1} (PSA_Hg, PSA_CNN1_Hg, PSA_CNN3_Hg). The grey field indicates the peak shifts.

The XPS survey spectra of the cryogels before and after Hg^{2+} adsorption are shown in Figure 5.10, where it is clearly evident that after the sorption process, the Hg element appears on the surface of the cryogels, while the Na^{+} content is decreased, confirming the adsorption mechanism through ion exchange (Table 5.1).

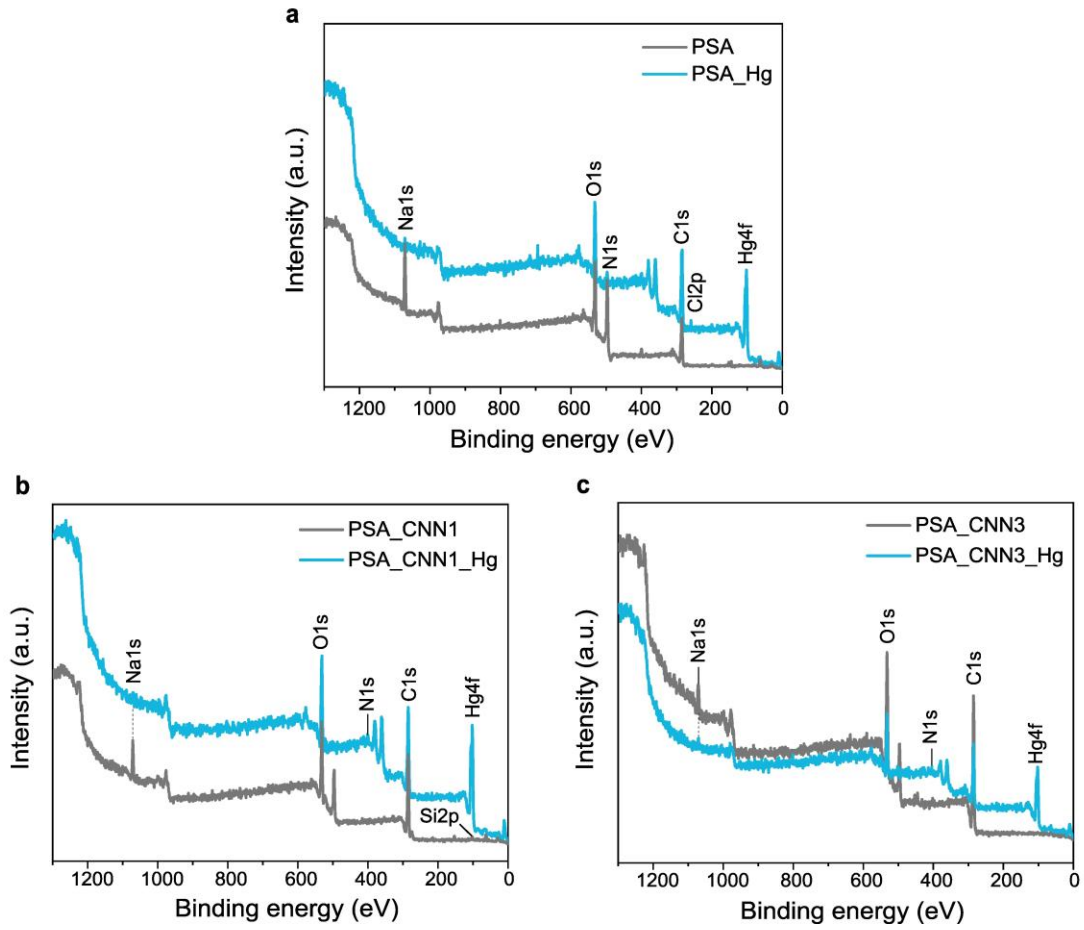

Figure 5.10. XPS survey spectra of a) the PSA, b) the PSA_CNN1, c) the PSA_CNN3 cryogels before any treatment and after the adsorption of 300 mg L^{-1} Hg^{2+} through the immersion in 15 mL of its aqueous solution at continuous shaking at 600 rpm for 5 h (PSA_Hg, PSA_CNN1_Hg, PSA_CNN3_Hg).

Table 5.1. XPS analysis of the peak areas percentage for the different components in the pristine cryogels before any treatment and after Hg^{2+} adsorption 15 mL of its 300 mg L^{-1} aqueous solution at continuous shaking at 600 rpm for 5h.

Element	Cryogel type					
	PSA	PSA_Hg	PSA_CNN1	PSA_CNN1_Hg	PSA_CNN3	PSA_CNN3_Hg
C1s	56.35	67.73	69.22	67.53	71.84	69.04
O1s	30.44	22.15	23.37	23.25	23.87	24.21
N1s	4.15	3.26	0.61	1.60	1.40	1.50
Na1s	**9.06**	**1.10**	**4.200**	**0.41**	**2.89**	**0.80**
Si2p	-	-	2.61	-	-	-
Cl2p	-	1.03	-	-	-	-
Hg4f	-	4.74	-	7.20	-	4.45

Nonetheless, no other change is observed in the surface chemical composition profile of the cryogels indicating that the adsorption of Hg^{2+} ions is not a chemisorption process but it is rather attributed to the electrostatic interactions (Figure 5.11).

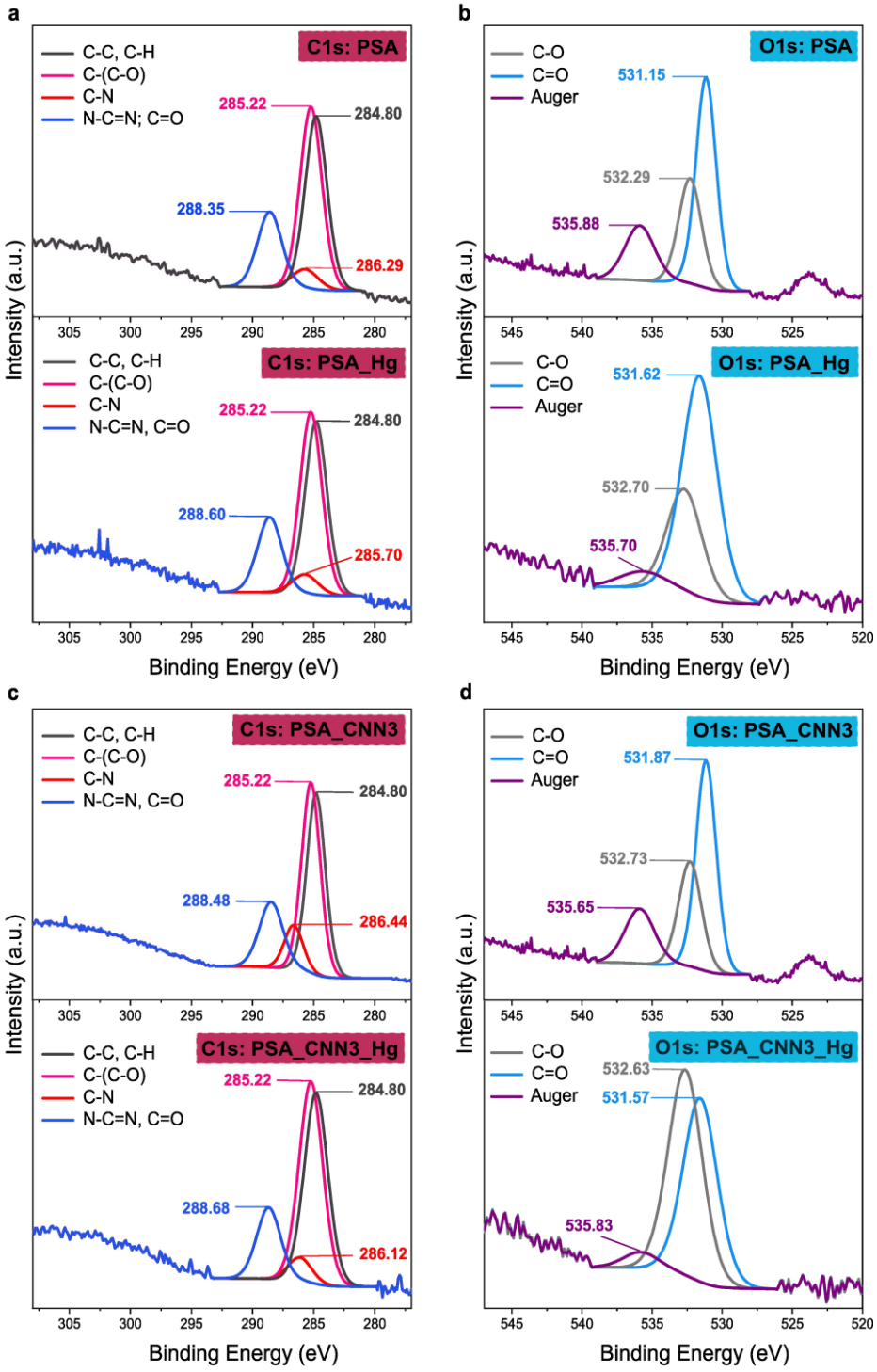

Figure 5.11. High resolution XPS spectra before any treatment and after the adsorption of 300 mg L^{-1} Hg^{2+} through the immersion in 15 mL of its aqueous solution at continuous shaking at 600 rpm for 5h for the PSA cryogel: a) of C1s component and b) of O1s component, and for the PSA_CNN cryogel: c) of C1s component and d) of O1s component. The appearance of the small peak at around 286 eV, in the C1s component of both the PSA and the PSA/CNN nanocomposite cryogels, ascribed to C-N bonds, derives from the MBA crosslinker.

5.3.2 Hg^{2+} ions interactions with the CNNs

Chemical analysis of the interactions of Hg^{2+} ions with the CNNs

To investigate the nature of the interactions of the CNNs with the Hg^{2+} ions that affect their photoluminescence properties, the XPS survey spectra of the pure CNNs and the CNN-Hg mixture were studied, and the results are shown in Figure 5.12a. The characteristic C1s and N1s peaks of the CNNs, are observed in both survey spectra, and the Hg element is also evident in the CNN-Hg mixture, confirming the effective interaction of the Hg^{2+} ions with the CNNs. The peak ascribed to the O1s component in the CNN-Hg sample may derive from CO_2 or from humidity sorbed by the sample from the air during the drying process of the preparation for the measurement[280]. Figure 5.12b depicts the high resolution spectra of the C1s component, which demonstrate the significant increase of the contribution of the peak at 284.80 eV in the presence of Hg^{2+} ions (Table 5.2). This indicates the formation of new C-C bonds in the CNNs structure, possibly due to the nanosheets' structure reorganization with the involvement of the graphitic carbon[379]. Such structural changes may suggest the nanosheets layers' alignment modification or aggregation in presence of the heavy metal, but they may also derive from the differences in the experimental procedure. In fact, the pure CNN powder was analysed as obtained, and it did not undergo the same protocol of repeated dispersing and centrifuging in an aqueous solution, as in case of the preparation of the CNN-Hg mixture (the details can be found in Section 5.1.5). The peak positions around 288 and at 286 eV, typical for CNNs (arising from the N-C=N coordination and the C-NH_2 bond), are not significantly modified by the presence of Hg^{2+} ions. Finally, no differences are observed in the peak positions of N2C and N3C components of the N1s deconvoluted spectra of CNNs and the CNN-Hg mixture, attributed to the N atoms between two tri-s-triazine rings and the N atoms building the

s-triazine rings, respectively (Figure 5.12c). Overall, it can be concluded that no chemical interactions occur between the Hg^{2+} ions and the CNNs, and the possible structural reorganization of the nanosheets layers was further verified by means of XRD, as discussed below.

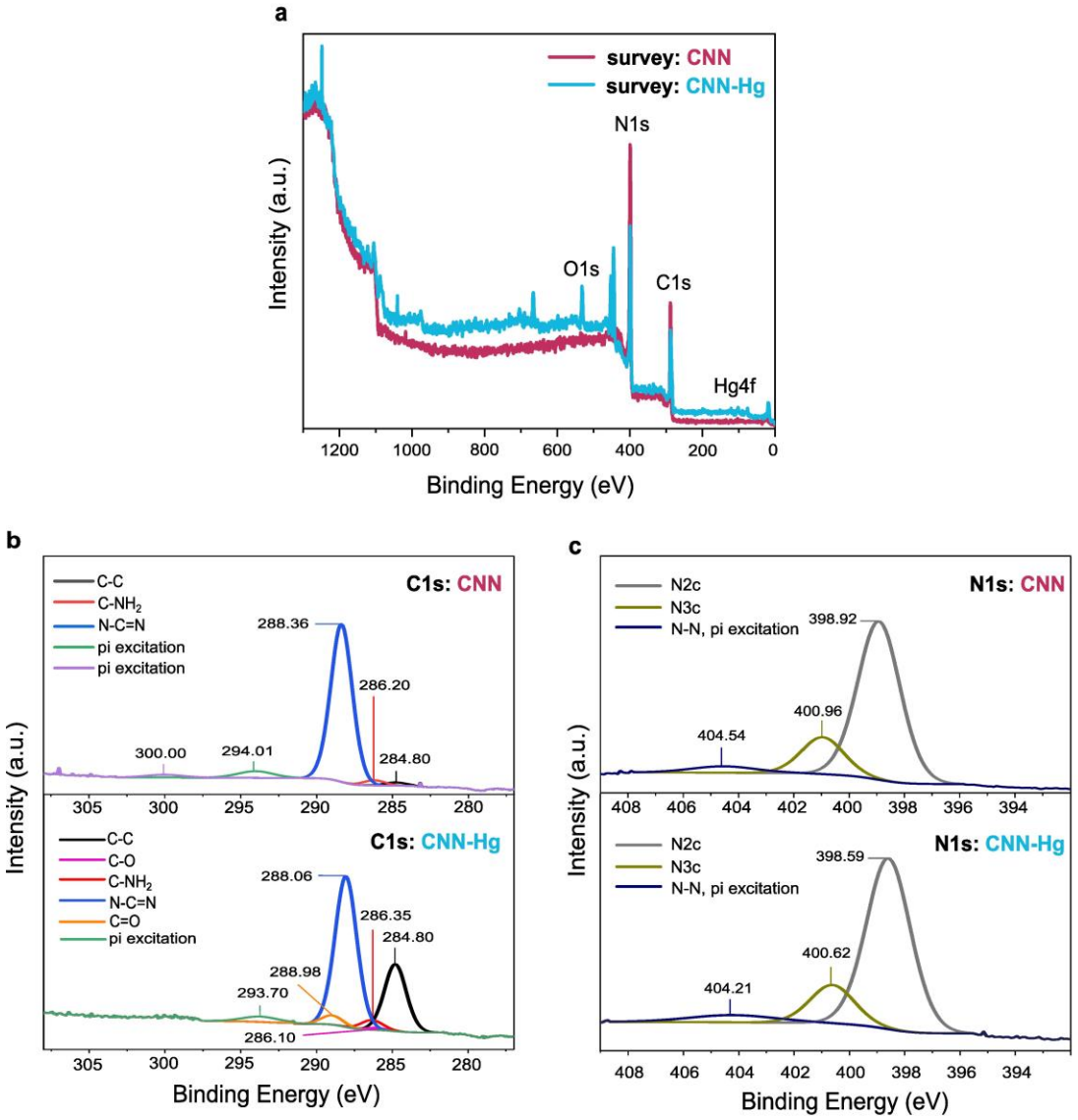

Figure 5.12. a) XPS survey spectra of the pure CNNs before and after the adsorption of Hg^{2+} by mixing 200 mg L^{-1} CNN- 50 mg L^{-1} Hg^{2+} (CNN-Hg). High resolution XPS spectra of the pure CNNs and the CNN-Hg mixture: b) C1s spectra: for the CNN-Hg mixture the two peaks at 288.98 and 286.10 eV, ascribed to C=O and C-O bonds, respectively, are attributed to the interaction of CNNs with oxygen, possibly deriving from CO_2 or from humidity sorbed by the sample from air in the drying process of the preparation for the measurement. c) N1s spectra.

Table 5.2. XPS analysis of the peak areas percentage for the different binding energies of the C1, N1, O1 and Hg 4f components in pure CNN and CNN-Hg mixture.

Components		Area (%)	Area (%)
		CNN	CNN-Hg
C1s	C-C	1.85	27.09
	C-O	-	0.86
	C-NH_2	2.89	3.94
	N-C=N	86.59	60.78
	C=O	-	3.73
	pi excitation	6.04	3.60
	pi excitation	2.64	-
N1s	N2C	77.21	76.34
	N3C	18.03	17.33
	N-N, pi excitation	4.77	6.34
O1s	C=O	-	27.35
	C-O	-	72.65
Hg4f	Hg^0 4f 7/2	-	11.41
	Hg^0 4f 5/2	-	8.57
	Hg^{2+} 4f 7/2	-	45.71
	Hg^{2+} 4f 5/2	-	34.31

Structural analysis of the interactions of Hg^{2+} ions with the CNNs

Regarding the crystal structure of CNNs, the X-ray diffractograms of the CNN and the CNN-Hg mixture powders reveal that it is not affected by the presence of Hg^{2+} ions, as shown in Figure 5.13. Both patterns present the characteristic peaks of CNNs, in particular at 12.9° and 28.0°, corresponding to the (100) and (002) planes, respectively. The first one is related to the in-plane structural repeating of the tri-s-triazine units, and the latter one is attributed to interlayer stacking of conjugated aromatic rings, typical of graphite materials[319,380]. The corresponding peaks of the two samples do not differ in width, which implies no modification of the dimensions of the crystal domains in the presence of the Hg^{2+} ions, and, therefore, no penetration of the ions into the

nanosheets layers.

In conclusion, the results of the herein presented structural and chemical analysis suggest that the CNNs interact with Hg^{2+} ions solely through the electrostatic forces, and the new peaks, corresponding to the C-C bonds, appearing in the XPS spectra of the CNN-Hg mixture are rather not attributed to the modification of the nanosheets' structural organization induced by the heavy metal ions.

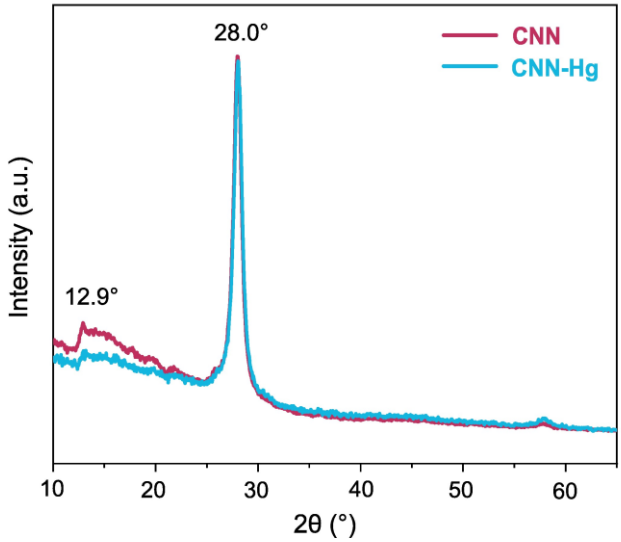

Figure 5.13. XRD spectra of CNNs before and after the adsorption of Hg^{2+} by mixing 200 mg L^{-1} CNN-50 mg L^{-1} Hg^{2+} (CNN-Hg).

5.4 MERCURY ADSORPTION STABILITY

As shown in Figure 5.14, insignificant leaching of the adsorbed Hg^{2+} ions from the PSA and PSA/CNN3 cryogels occurs in 3 consecutive pure water permeation cycles, with the $D_{Hg\_w(n)}$ respective values ranging between 0.5 % and 3.0 % depending on the filtration cycle and the sample type. The slightly higher Hg^{2+} desorption efficiency for both types of the material in the first cycle may be attributed to the entrapment of the Hg^{2+} ions within the polymer network pores without a strong interaction with the

functional groups of the material, causing their facilitated release upon the application of the pure water flux. Based on the values obtained in the next two filtration cycles, it can be concluded that, for both PSA and PSA_CNN3, the following permeation cycles of pure water through the Hg^{2+}-loaded cryogel filters do not affect their stability, indicating the ability of the materials to effectively entrap Hg^{2+} ions in their structure.

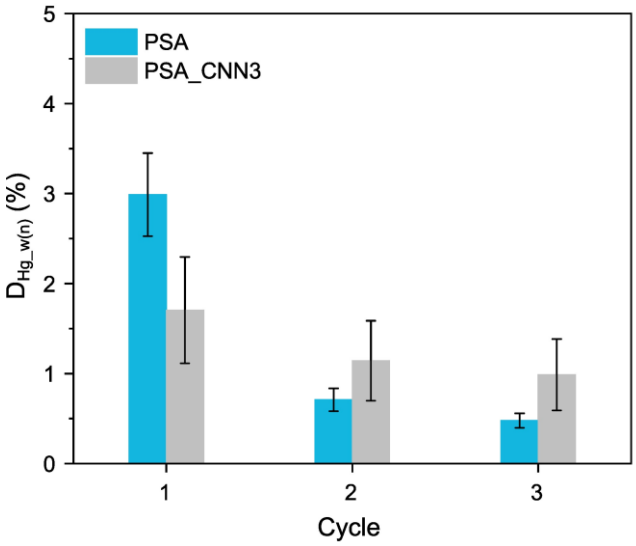

Figure 5.14. Hg^{2+} ions desorption efficiency, $D_{Hg\_w(n)}$, in three consecutive cycles of pure water permeation for PSA and PSA_CNN3 cryogels loaded with Hg^{2+} during the filtration of a Hg^{2+} aqueous solution.

5.5 MERCURY RECOVERY AND CRYOGELS' REUSABILITY

Three reusability cycles were performed on the PSA_CNN3 cryogel filter through Hg^{2+} sorption-desorption sequences. To successfully induce the release of the adsorbed Hg^{2+} ions, the $NaOH_{(aq)}$ gravity-driven permeation has been performed (no significant differences between the feed's and filtrate's pH were observed). As it can be seen in Figure 5.15, the $q_{D\_Hg\_ii(n)}$ remains stable in all the three cycles (~16 mg g^{-1} cryogel), and is lower than the corresponding q_{Hg} (~22 mg g^{-1} cryogel), indicating the incomplete recovery of Hg^{2+}. Nonetheless, this does not affect the separation

performance in the consecutive cycles. The Hg^{2+} ions release process could be possibly attributed to the changes in the charge distribution due to the introduction of the OH^- groups in the cryogels during the NaOH permeation, and due to the modification of the osmotic pressure resulting in the polymer chains rearrangement[381–386]. Indeed, the PSA's volume expansion (by ~6%) was observed during the NaOH treatment. In addition, these results indicate the PSA_CNN3 cryogel's chemical stability in alkaline harsh conditions. The ability of the cryogel filter to repetitively desorb a significant amount of the adsorbed Hg^{2+} ions allows for the effective reuse before reaching its saturation point. It should also be noted that in the washing steps (performed through the pure water permeation) applied after each treatment with $NaOH_{(aq)}$, the cryogel desorbs only trace amounts of Hg^{2+} (below 0.75 %), as shown in Table 5.3 . Thus, it can be concluded that the developed PSA_CNN3 cryogel shows great potential for the application in the repetitive integrated separation and recovery of heavy metal ions, in order to tackle the secondary pollution caused by the spent filters loaded with toxic contaminants and to collect and, eventually, reutilize the heavy metal ions from wastewater.

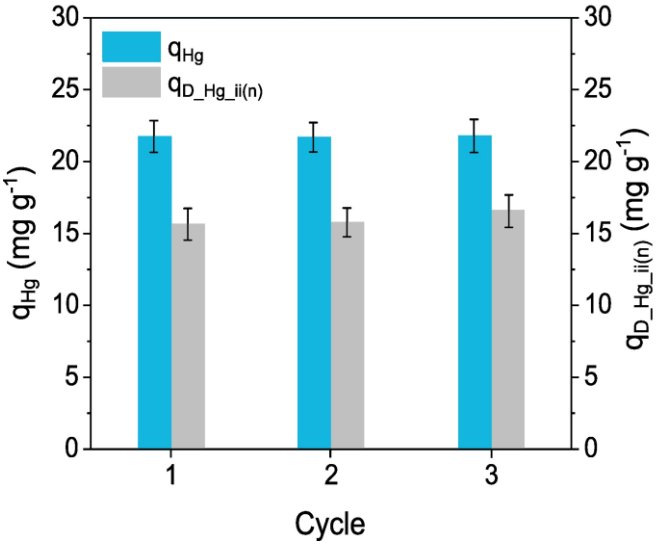

Figure 5.15. Hg^{2+} recovery from PSA_CNN3 and the cryogel's reusability. Hg^{2+} (5 mg L^{-1}) adsorption capacity in step i), (q_{Hg}) and Hg^{2+} desorption capacity in step ii), ($q_{D\_Hg\_ii(n)}$) for three consecutive adsorption-desorption cycles.

Table 5.3. Hg^{2+} desorption efficiency ($D_{Hg\_iii(n)}$) reached by the PSA_CNN3 cryogel in the washing steps of each reuse cycle.

Cycle	Hg^{2+} desorption efficiency $D_{Hg\_iii(n)}$ (%)	Standard deviation (%)
1	0.75	0.56
2	0.18	0.25
3	0.09	0.13

In addition, as presented in Figure 5.16, the fluorescent properties in the course of all the sorption-desorption cycles of the PSA_CNN3 were not significantly affected, making possible the simultaneous separation and detection of Hg^{2+} ions after each process of the heavy metal ions recovery.

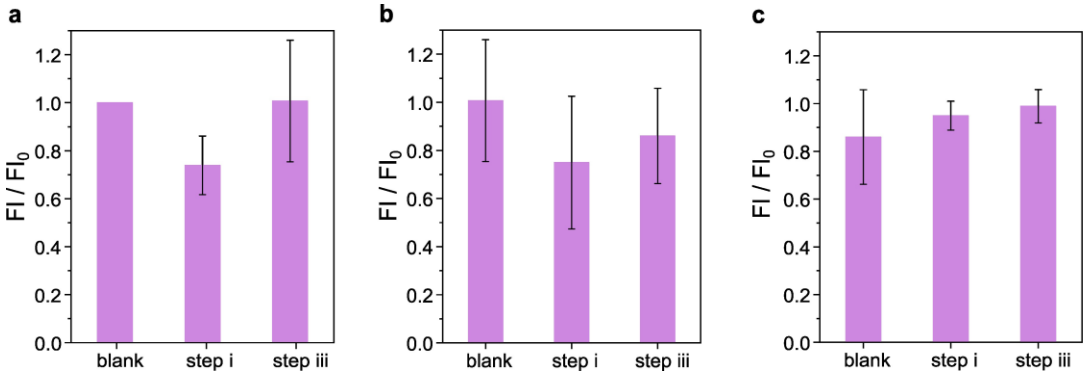

Figure 5.16. Relative fluorescence intensities (FI/FI_0) of the PSA/CNN3 cryogel after each Hg^{2+} ions sorption step (i) and desorption step (iii) in the first (a), second (b), and third (c) consecutive sorption-desorption cycles. FI and FI_0 are the fluorescence intensities of the cryogel after a given step, and before that step, respectively, whereas for the blank measurements in the first cycle $FI = FI_0$.

5.6 PHOTOCATALYTIC DECOLORIZATION OF THE ADSORBED METHYLENE BLUE

The reusability of the cryogels was further analysed conducting two cycles of SB oil-water-MB mixture filtration and the adsorbed MB dye photocatalytic decolorization under the visible light irradiation.

Firstly, based on the transparent character of the different PSA/CNN cryogels (PSA_CNN1, and PSA_CNN3), playing an important role in the materials' ability to absorb the light, PSA_CNN1 was chosen for the experiments, exhibiting visibly higher transparency than the PSA_CNN3 sample (Figure 5.17).

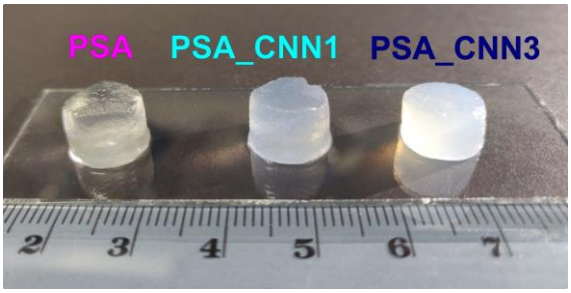

Figure 5.17. A photograph of the PSA, the PSA_CNN1 and the PSA_CNN3 cryogels in the swollen state, evidencing decreasing transparency of the cryogel with the addition of increasing amounts of the CNN nanofiller.

As shown in Figure 5.18, the relative MB absorbance intensity decreases with time under visible light irradiation. Even though the relative absorbance intensities of MB adsorbed by the PSA cryogel after the first and the second cycle indicate the occurrence of a self-decolorization effect, it is not stable, decreasing from 31.65 ± 7.45 % to 20.77 ± 11.21 % reached after 24 h of the exposure to the visible light in the first and the second cycle, respectively. However, in case of the PSA_CNN1 cryogel, not only higher decolorization efficiency was reached compared to that of the PSA cryogel, but also similar values were obtained in the two cycles. In particular, 42.75 ± 2.49 % and 41.36 ± 9.20 % of the adsorbed MB is decolorized after the first and after the second photocatalysis cycle, respectively. This evidences the photocatalytic ability of the PSA_CNN1 hybrid to decolorize the adsorbed MB due to the presence of CNNs. In fact, it has been reported that photoexcited CNNs produce direct electron injection to the MB, which typically initiates the degradation of cationic dyes[387]. The reason why the PSA_CNN1 cryogel could not reach decolorization efficiencies higher than 43% might be the encapsulation of some CNNs into the PSA scaffold, limiting their contact with MB and inhibiting the photocatalytic process, and/or to the relatively dense cryogel surface that hinders the interaction of the visible light with the exposed CNNs[388]. Despite the fact that the PSA_CNN1 could not

achieve higher decolorization efficiencies, it did exhibit photocatalytic properties that can play a complementary role in the filtration process, extending the reusability of the cryogel filter.

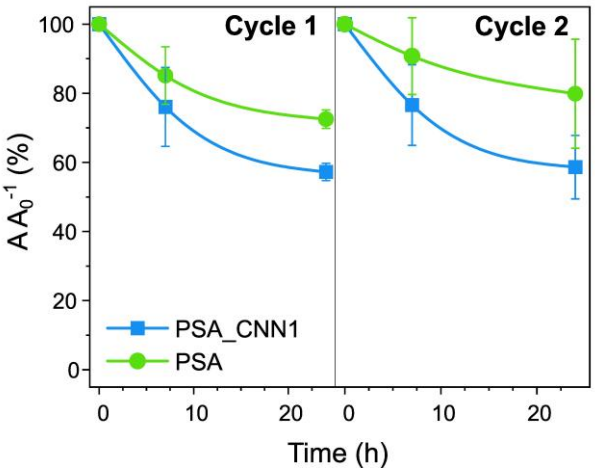

Figure 5.18. Photocatalytic decolorization curves of MB adsorbed by the PSA and the PSA_CNN1 cryogels over 24 h under visible light irradiation. AA_0^{-1} is the relative MB absorbance intensity.

Apart from a stable self-cleaning performance, the nanocomposite cryogel showed a stable filtration performance, maintaining high separation efficiencies for the SB oil-water-MB mixture filtration in the second filtration-dye photocatalytic decolorization cycle. Specifically, 99.97 ± 0.00% and 98.22 ± 0.42% were reached for SB oil and for MB, respectively (Figure 5.19). Similarly, the PSA cryogel's E_{ff_SB} and E_{ff_MB} were not affected by the self-decolorization of the dye under the visible light irradiation and after one filtration-dye decolorization cycle 99.98 ± 0.01% and 97.87 ± 1.64% were reached for SB oil and for MB, respectively (Figure 5.19).

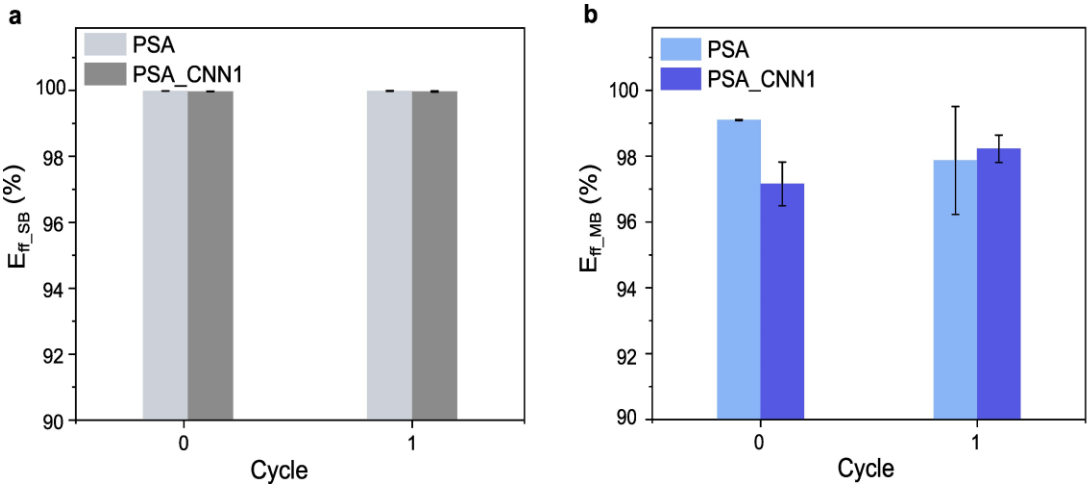

Figure 5.19. a) SB oil (E_{ff_SB}) and b) MB separation efficiency (E_{ff_MB}), reached by the PSA and the PSA_CNN1 cryogel in the filtration of an oil-water-MB mixture (0.5 mg L^{-1} MB, 30 % w/w SB oil with respect to the total mixture volume) before and after one filtration-MB dye decolorization cycle.

Moreover, the cryogel's texture as well as its chemical composition are not significantly affected by the light irradiation, as revealed by a comparative morphological and chemical analysis of the reference samples: PSA_CNN- before any treatment, and/or PSA_CNN1_water – after water permeation, as described in Section 5.1.7, and of the PSA_CNN1 cryogel after the MB aqueous solution filtration (in a procedure described in Section 5.1.7), followed by the adsorbed MB photocatalytic decolorization (PSA_CNN1_MB).

The SEM images of the PSA_CNN1_water and PSA_CNN1_MB samples are shown in Figure 5.20. Both samples were subjected to freeze drying for the analysis purposes, as described in Section, which resulted in a different morphology compared to that of the pristine cryogels (Chapter 2: Section 2.3).

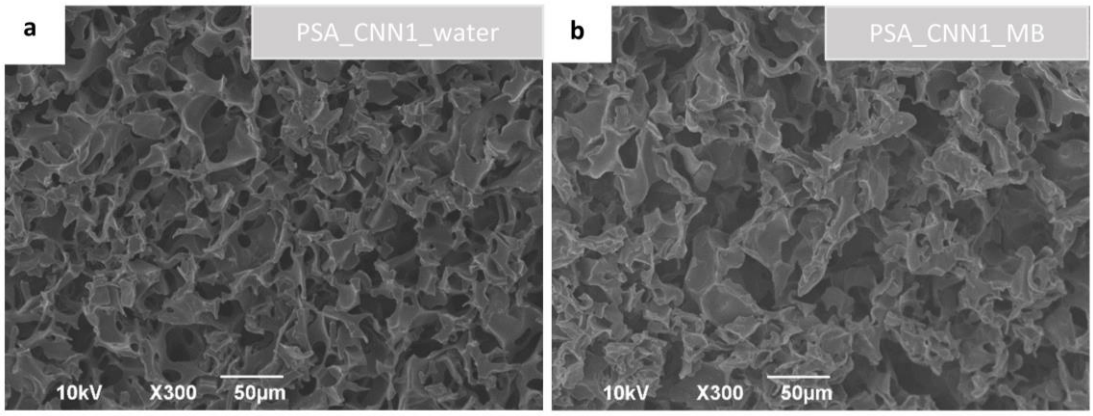

Figure 5.20. SEM images showing the cross-section of PSA_CNN1 cryogels after a) water permeation, b) MB filtration and the subsequent visible light irradiation for the photodegradation of the adsorbed MB.

As stated above, the chemical analysis did not reveal any effect of the adsorbed MB dye photocatalytic decolorization on the chemical structure of the PSA/CNN1 cryogel. The FTIR spectra of PSA_CNN1, PSA_CNN1_water, and PSA_CNN1_MB samples are shown in Figure 5.21, and no differences are observed, apart from the peaks at 1022 cm^{-1} and at 955 cm^{-1} appearing in the spectrum of the PSA_CNN1_MB sample, which can be attributed to the C-H and N-O vibrations of the MB molecules that are not completely decomposed upon the photocatalytic process[359,389].

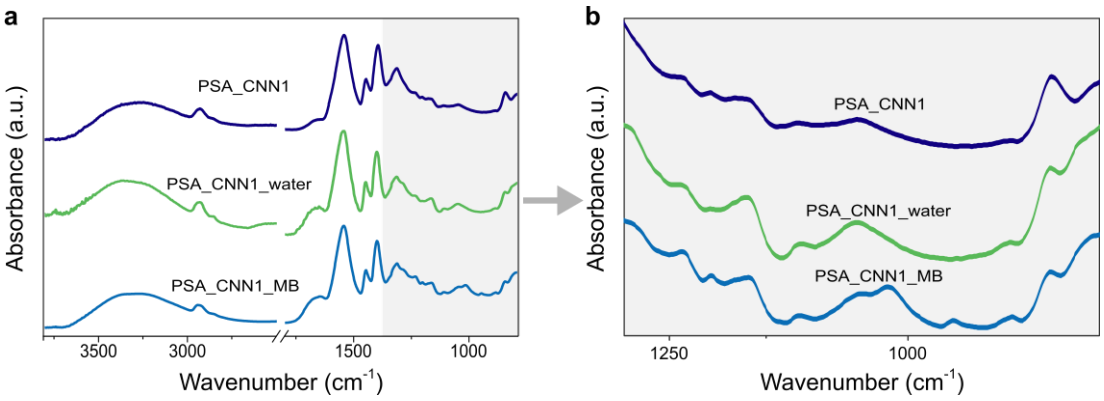

Figure 5.21. FTIR analysis of PSA_CNN1 samples before and after the photocatalytic decolorization of the adsorbed MB dye. a) FTIR spectra of the PSA_CNN1 cryogel after water permeation (PSA_CNN1_water, green line) and after the filtration of a MB aqueous solution and subsequent light irradiation for the decolorization of the adsorbed MB molecules (PSA_CNN1_MB, light blue line). The dark blue line refers to the spectrum of the PSA_CNN1 before any interaction with water. b) Zoom-in of the gray-shaded area of a).

In conclusion, the self-cleaning properties, and the excellent filtration performance and stability of the PSA_CNN1 cryogel after the photocatalytic-decolorization further confirm a facile regeneration and the potential long-term operation of the developed PSA/CNN filter.

5.7 CONCLUSIONS

To sum up, the successful expansion of the PSA/CNN cryogel filter's applications related to the water protection sector was achieved. Moreover, the different explored functions of the cryogel, such as Hg^{2+} ions fluorosensing and recovery, as well as the photocatalytic self-cleaning were integrated with the gravity-driven filtration process and a stable performance of the cryogel in terms of the various functionalities has been proved in multiple cycles of reuse for the integrated processes.

In particular, owing to the fluorosensing properties of the CNN nanofiller, the developed cryogel nanocomposite has shown fluorescence quenching upon the interaction with Hg^{2+} ions during the filtration process. It has been found that the detection response can be significantly modified varying the filtration feed volume and the CNN nanofiller's loading in the polymer matrix, and that the PSA/CNN cryogel's fluorosensing mechanism is based on the electrostatic interaction of the Hg^{2+} ions adsorbed by the PSA matrix with the embedded CNNs. The LOD of 3 mg L^{-1} Hg^{2+}, attained using the PSA/CNN3 cryogel and a feed volume of 100 mL, is applicable for a rapid and facile quality monitoring during the purification of wastewaters coming from industries typically releasing Hg.

Furthermore, the PSA/CNN cryogel has shown great Hg^{2+} ions adsorption stability in the consecutive gravity-driven water permeation cycles and the applicability for the pH-responsive recovery of the adsorbed Hg^{2+} via the gravity-driven permeation of a $NaOH_{(aq)}$ solution, resulting in the effective desorption of the heavy metal ions. The material shows a stable performance in various Hg^{2+} sorption-desorption cycles. The ability of the PSA/CNN cryogel to be used for the simultaneous separation and detection of Hg^{2+} ions after each heavy metal ions recovery process was proven, as the fluorescence properties were maintained in all the recovery and reuse cycles.

Moreover, the PSA/CNN cryogel's self-cleaning ability, owed to the photocatalytic activity of CNNs under daylight, was achieved without affecting the cryogel's texture and chemical stability upon the photocatalytic process. In particular, the material has shown a stable MB photocatalytic decolorization and separation performance in repeated filtration-photocatalysis cycles.

Both the pH-responsive recovery and the photocatalytic self-cleaning properties of the PSA/CNN cryogel allow for its regeneration and the extended reuse.

In conclusion, the use of CNNs as a multifunctional nanofiller of a PSA cryogel filter has proven to be a successful approach in the development of a versatile and recyclable multi-purpose material for the integrated wastewater filtration and Hg^{2+} indication as well as recovery, exhibiting a photocatalytic self-cleaning ability under the visible light irradiation. Such a PSA/CNN nanocomposite cryogel offers an inspiration for the development of multifunctional materials as a valuable alternative to the sophisticated processes related to water protection.

Chapter 6: FINAL REMARKS AND FUTURE PERSPECTIVES

In summary, PSA and nanocomposite PSA/CNN cryogels were fabricated using a simple one-pot cryopolymerization synthesis method. The successful incorporation of graphitic carbon nitride nanosheets (CNNs) into the PSA cryogel matrix was confirmed. The addition of CNNs had a minimal impact on the cryogels' morphology, preserving their high porosity and roundish interconnected macropores, and the CNNs' presence in the synthesis reaction solution had no effect on the relative volume of the generated ice crystals acting as a porogen. Both the neat and the nanocomposite cryogels showed hydrophilic character and rapid water uptake with remarkable swelling degrees, as well as high water permeability rates, underwater superoleophobicity, and good mechanical stability and flexibility upon cyclic compression.

The adsorption study of methylene blue (MB) and mercury ions (Hg^{2+}) in batch conditions revealed detailed insights into the adsorption mechanisms. This study allowed for the identification of the precise roles that the interactions between the compounds, the PSA matrix, and the embedded CNNs played in the MB/Hg^{2+} adsorption by the cryogels. The MB and Hg^{2+} ions adsorption kinetics study revealed a rapid sorption of the two pollutants by both cryogel types. Both the pseudo-first order and pseudo-second order kinetic models were proved to fit the experimental data of Hg^{2+} ions and MB time-dependent adsorption for all the cryogels under study, indicating a complex sorption process involving physisorption and chemical interactions. The Hg^{2+} ions adsorption mechanism of both cryogel types was

discovered to be based on Na^+-Hg^{2+} ion exchange, releasing ~2 moles of Na^+ for every 1 mol of Hg^{2+} adsorbed. However, the embedded CNNs appeared to contribute to the sorption process at moderate pollutant concentrations, marginally increasing the adsorption capacities and shortening the time required to reach the adsorption equilibrium, both in case of MB and Hg^{2+}ions uptake. The co-existence of MB and Hg^{2+} was found to slightly reduce both cryogels' adsorption capacity, having no effect on the adsorption mechanism. The Langmuir isotherm model was proved to better describe the adsorption process of MB and Hg^{2+} than the Freundlich one, for both the PSA and the PSA/CNN nanocomposite cryogels. Both material types demonstrated excellent sorption performance for organic and inorganic cationic pollutants, with remarkable maximum adsorption capacities, which could be derived from the fitting to the Langmuir isotherm model.

The described properties suggested potential applications in water-soluble pollutant adsorption and oil-water gravity-driven filtration separation processes. Indeed, the cryogels demonstrated efficient separation of both high- and low-viscosity oils from water in a gravity-driven process. Furthermore, they maintained stability and high separation efficiencies in multiple filtration cycles for oil-water and oil-dye-water mixtures. Additionally, the cryogels exhibited excellent performance in the purification of multicomponent oily wastewater containing Hg^{2+} and MB, demonstrating the ability to simultaneously adsorb water-soluble pollutants of different chemical nature, and separate oil from water. Notably, the obtained adsorption capacities were consistent with the ones obtained at equilibrium conditions in batch conditions studies, indicating suitability of the developed materials to be used in the filtration process, where the contact time of the sorbent with the contaminants during the permeation is limited.

A successful integration of the filtration process with other functions enabled by the incorporation of CNNs into the polymer matrix was also proven. In particular, the detection of Hg^{2+} ions through the fluorescence quenching phenomenon occurring for the nanosheets upon the interaction with heavy metal ions, and the photocatalytic self-cleaning through the decolorization of the adsorbed dye under visible light were made possible due to the suitable optical properties of CNNs preserved upon their incorporation into the cryogel matrix. Moreover, the functionalities of the developed nanocomposite cryogels were further expanded by the recovery of the adsorbed Hg^{2+} ions through a pH-responsive desorption mechanism, extending their reuse as filtration systems. The PSA/CNN cryogels demonstrated a stable performance in sorption-desorption cycles, maintaining at the same time the fluorescent properties.

While the use of nanomaterials in the form of aqueous dispersions for water treatment and quality monitoring suffers from certain limitations, such as complicated recovery and regeneration after use, a risk of secondary pollution, and, in certain situations, such as in case of CNNs, aggregation in the presence of electrolytes, the embedment of CNNs into a superwetting hydrogel matrix allows for their successful application in the field. Such approach presents a significant opportunity for the development of a system for water protection field with superior multifunctional behaviour integrating the many intriguing aspects of these two novel materials.

In addition to examining the wide range of potential applications of the developed PSA/CNN cryogel and their integration into the filtration process, the herein presented PhD thesis offers a thorough assessment of the filter's performance in real-world scenarios involving multicomponent oily mixtures, which is rarely taken into account in research on materials for water treatment. Most importantly, the work addresses issues related to wastewater treatment and quality monitoring, including high energy

consumption, high costs, and the intricacy of pollutant detection techniques involving the use of toxic reagents. This is why the study focuses on solar-light photocatalysis, gravity-driven filtering, and an easy-to-use, low-cost, and ecologically friendly detection technique.

We believe that the produced multifunctional PSA/CNN nanocomposite cryogel provides an inspiration for the development of solutions for more straightforward, economical, environmentally friendly, and energy-efficient water protection processes. Besides, the thorough study on the performance of the cryogel filters under practical conditions, where multiple contaminants are involved provides a deep understanding of the proposed material's properties and applicability for water treatment.

Nonetheless, the effect of the interference of other cations typically present in wastewaters on the pollutants separation efficiency, on the detection of Hg^{2+} ions, and on the material's chemosensing selectivity, as well as the scale-up filtration experiments are considered important future steps for the validation of the proposed material.

Bibliography

(1) https://unesdoc.unesco.org/ark:/48223/pf0000367306 (accessed 2023-12-14).

(2) Carlton, E. J.; Liang, S.; McDowell, J. Z.; Li, H.; Luo, W.; Remais, J. V. Regional Disparities in the Burden of Disease Attributable to Unsafe Water and Poor Sanitation in China. *Bull World Health Organ* **2012**, *90* (8), 578–587. https://doi.org/10.2471/BLT.11.098343.

(3) Azizullah, A.; Khattak, M. N. K.; Richter, P.; Häder, D.-P. Water Pollution in Pakistan and Its Impact on Public Health — A Review. *Environment International* **2011**, *37* (2), 479–497. https://doi.org/10.1016/j.envint.2010.10.007.

(4) Shayo, G. M.; Elimbinzi, E.; Shao, G. N.; Fabian, C. Severity of Waterborne Diseases in Developing Countries and the Effectiveness of Ceramic Filters for Improving Water Quality. *Bull Natl Res Cent* **2023**, *47* (1), 113. https://doi.org/10.1186/s42269-023-01088-9.

(5) Mahmoud, A. E. D.; Fawzy, M.; Khan, N. A. *Artificial Intelligence and Modeling for Water Sustainability: Global Challenges*; CRC Press, 2023.

(6) Salehi, M. Global Water Shortage and Potable Water Safety; Today's Concern and Tomorrow's Crisis. *Environment International* **2022**, *158*, 106936. https://doi.org/10.1016/j.envint.2021.106936.

(7) *Water, Climate, Conflict, and Migration: Coping with One Billion People on the Move by 2050 - Our World*. https://ourworld.unu.edu/en/water-climate-conflict-migration-coping-with-1-billion-people-on-the-move-by-2050 (accessed 2023-12-14).

(8) Soares, M. O.; Rabelo, E. F. Severe Ecological Impacts Caused by One of the Worst Orphan Oil Spills Worldwide. *Marine Environmental Research* **2023**, *187*, 105936. https://doi.org/10.1016/j.marenvres.2023.105936.

(9) Sobieraj, J.; Metelski, D. Insights into Toxic Prymnesium Parvum Blooms as a Cause of the Ecological Disaster on the Odra River. *Toxins* **2023**, *15* (6), 403. https://doi.org/10.3390/toxins15060403.

(10) Bhattacharjee, S.; Dutta, T. Chapter 1 - An Overview of Oil Pollution and Oil-Spilling Incidents. In *Advances in Oil-Water Separation*; Das, P., Manna, S., Pandey, J. K., Eds.; Elsevier, 2022; pp 3–15. https://doi.org/10.1016/B978-0-323-89978-9.00014-8.

(11) Qandeel, M.; Sommer, J. Syria Conflict and Its Impact: A Legal and Environmental Perspective. *Journal of International Humanitarian Legal Studies* **2022**, *13* (2), 275–296. https://doi.org/10.1163/18781527-bja10057.

(12) Kitowski, I.; Sujak, A.; Drygaś, M. The Water Dimensions of Russian – Ukrainian Conflict. *Ecohydrology & Hydrobiology* **2023**, *23* (3), 335–345. https://doi.org/10.1016/j.ecohyd.2023.05.001.

(13) Rawtani, D.; Gupta, G.; Khatri, N.; Rao, P. K.; Hussain, C. M. Environmental Damages Due to War in Ukraine: A Perspective. *Science of The Total Environment* **2022**, *850*, 157932. https://doi.org/10.1016/j.scitotenv.2022.157932.

(14) Pereira, P.; Bašić, F.; Bogunovic, I.; Barcelo, D. Russian-Ukrainian War Impacts the Total Environment. *Science of The Total Environment* **2022**, *837*, 155865. https://doi.org/10.1016/j.scitotenv.2022.155865.

(15) https://unesdoc.unesco.org/ark:/48223/pf0000247153 (accessed 2023-12-15).

(16) Wu, B.; Tian, F.; Zhang, M.; Piao, S.; Zeng, H.; Zhu, W.; Liu, J.; Elnashar, A.; Lu, Y. Quantifying Global Agricultural Water Appropriation with Data Derived

from Earth Observations. *Journal of Cleaner Production* **2022**, *358*, 131891. https://doi.org/10.1016/j.jclepro.2022.131891.

(17) Lu, Y.; Song, S.; Wang, R.; Liu, Z.; Meng, J.; Sweetman, A. J.; Jenkins, A.; Ferrier, R. C.; Li, H.; Luo, W.; Wang, T. Impacts of Soil and Water Pollution on Food Safety and Health Risks in China. *Environment International* **2015**, *77*, 5–15. https://doi.org/10.1016/j.envint.2014.12.010.

(18) Di Stefano, V.; Avellone, G. Food Contaminants. *Journal of Food Studies* **2014**, *3* (1), 88. https://doi.org/10.5296/jfs.v3i1.6192.

(19) Lin, L.; Yang, H.; Xu, X. Effects of Water Pollution on Human Health and Disease Heterogeneity: A Review. *Frontiers in Environmental Science* **2022**, *10*.

(20) Thompson, L. A.; Darwish, W. S. Environmental Chemical Contaminants in Food: Review of a Global Problem. *Journal of Toxicology* **2019**, *2019*, e2345283. https://doi.org/10.1155/2019/2345283.

(21) Singh, J.; Yadav, P.; Pal, A. K.; Mishra, V. Water Pollutants: Origin and Status. In *Sensors in Water Pollutants Monitoring: Role of Material*; Pooja, D., Kumar, P., Singh, P., Patil, S., Eds.; Advanced Functional Materials and Sensors; Springer: Singapore, 2020; pp 5–20. https://doi.org/10.1007/978-981-15-0671-0_2.

(22) Titchou, F. E.; Zazou, H.; Afanga, H.; El Gaayda, J.; Akbour, R. A.; Hamdani, M. Removal of Persistent Organic Pollutants (POPs) from Water and Wastewater by Adsorption and Electrocoagulation Process. *Groundwater for Sustainable Development* **2021**, *13*, 100575. https://doi.org/10.1016/j.gsd.2021.100575.

(23) Harrad, S. *Persistent Organic Pollutants*; John Wiley & Sons, 2009.

(24) Tufail, M. A.; Iltaf, J.; Zaheer, T.; Tariq, L.; Amir, M. B.; Fatima, R.; Asbat, A.; Kabeer, T.; Fahad, M.; Naeem, H.; Shoukat, U.; Noor, H.; Awais, M.; Umar, W.; Ayyub, M. Recent Advances in Bioremediation of Heavy Metals and

Persistent Organic Pollutants: A Review. *Science of The Total Environment* **2022**, *850*, 157961. https://doi.org/10.1016/j.scitotenv.2022.157961.

(25) do Vale-Júnior, E.; da Silva, D. R.; Fajardo, A. S.; Martínez-Huitle, C. A. Treatment of an Azo Dye Effluent by Peroxi-Coagulation and Its Comparison to Traditional Electrochemical Advanced Processes. *Chemosphere* **2018**, *204*, 548–555. https://doi.org/10.1016/j.chemosphere.2018.04.007.

(26) Bafana, A.; Devi, S. S.; Chakrabarti, T. Azo Dyes: Past, Present and the Future. *Environ. Rev.* **2011**, *19* (NA), 350–371. https://doi.org/10.1139/a11-018.

(27) Jones, K. C.; de Voogt, P. Persistent Organic Pollutants (POPs): State of the Science. *Environmental Pollution* **1999**, *100* (1), 209–221. https://doi.org/10.1016/S0269-7491(99)00098-6.

(28) Shitu, A.; A., I. Removal of Methylene Blue Using Low Cost Adsorbent: A Review. *Research journal of chemical Sciences* **2014**, *4*, 2231–2606.

(29) Das, T. K.; Poater, A. Review on the Use of Heavy Metal Deposits from Water Treatment Waste towards Catalytic Chemical Syntheses. *International Journal of Molecular Sciences* **2021**, *22* (24), 13383. https://doi.org/10.3390/ijms222413383.

(30) Alloway, B. J. Sources of Heavy Metals and Metalloids in Soils. In *Heavy Metals in Soils: Trace Metals and Metalloids in Soils and their Bioavailability*; Alloway, B. J., Ed.; Environmental Pollution; Springer Netherlands: Dordrecht, 2013; pp 11–50. https://doi.org/10.1007/978-94-007-4470-7_2.

(31) Rubio, J.; Souza, M. L.; Smith, R. W. Overview of Flotation as a Wastewater Treatment Technique. *Minerals Engineering* **2002**, *15* (3), 139–155. https://doi.org/10.1016/S0892-6875(01)00216-3.

(32) Zhao, C.; Zhou, J.; Yan, Y.; Yang, L.; Xing, G.; Li, H.; Wu, P.; Wang, M.; Zheng, H. Application of Coagulation/Flocculation in Oily Wastewater Treatment:

A Review. *Science of The Total Environment* **2021**, *765*, 142795. https://doi.org/10.1016/j.scitotenv.2020.142795.

(33) Adetunji, A. I.; Olaniran, A. O. Treatment of Industrial Oily Wastewater by Advanced Technologies: A Review. *Appl Water Sci* **2021**, *11* (6), 98. https://doi.org/10.1007/s13201-021-01430-4.

(34) Putatunda, S.; Bhattacharya, S.; Sen, D.; Bhattacharjee, C. A Review on the Application of Different Treatment Processes for Emulsified Oily Wastewater. *Int. J. Environ. Sci. Technol.* **2019**, *16* (5), 2525–2536. https://doi.org/10.1007/s13762-018-2055-6.

(35) Long, N.; Gál, R.; Buňka, F. Use of Phosphates in Meat Products. *African Journal of Biotechnology* **2011**, *10* (86), 19874–19882. https://doi.org/10.5897/AJBX11.023.

(36) Kundu, S.; Coumar, M. V.; Rajendiran, S.; Rao, A.; Rao, A. S. Phosphates from Detergents and Eutrophication of Surface Water Ecosystem in India. *Current Science* **2015**, *108* (7), 1320–1325.

(37) Barr, D. B.; Bravo, R.; Weerasekera, G.; Caltabiano, L. M.; Whitehead, R. D.; Olsson, A. O.; Caudill, S. P.; Schober, S. E.; Pirkle, J. L.; Sampson, E. J.; Jackson, R. J.; Needham, L. L. Concentrations of Dialkyl Phosphate Metabolites of Organophosphorus Pesticides in the U.S. Population. *Environmental Health Perspectives* **2004**, *112* (2), 186–200. https://doi.org/10.1289/ehp.6503.

(38) Arora, J.; Ranjan, A.; Chauhan, A.; Biswas, R.; Rajput, V. D.; Sushkova, S.; Mandzhieva, S.; Minkina, T.; Jindal, T. Surfactant Pollution, an Emerging Threat to Ecosystem: Approaches for Effective Bacterial Degradation. *Journal of Applied Microbiology* **2022**, *133* (3), 1229–1244. https://doi.org/10.1111/jam.15631.

(39) Courtens, E. N. P.; Meerburg, F.; Mausen, V.; Vlaeminck, S. E. When the Smoke Disappears: Dealing with Extinguishing Chemicals in Firefighting Wastewater. *Water Science and Technology* **2014**, *69* (8), 1720–1727. https://doi.org/10.2166/wst.2014.081.

(40) Sapek A. Ammonia Emissions from Non-Agricultural Sources. *Pol. J. Environ. Stud. 22* (1), 63–70.

(41) El Diwani, G.; El Rafie, Sh.; El Ibiari, N. N.; El-Aila, H. I. Recovery of Ammonia Nitrogen from Industrial Wastewater Treatment as Struvite Slow Releasing Fertilizer. *Desalination* **2007**, *214* (1), 200–214. https://doi.org/10.1016/j.desal.2006.08.019.

(42) Liu, J.; Zhang, L.; Lu, G.; Jiang, R.; Yan, Z.; Li, Y. Occurrence, Toxicity and Ecological Risk of Bisphenol A Analogues in Aquatic Environment – A Review. *Ecotoxicology and Environmental Safety* **2021**, *208*, 111481. https://doi.org/10.1016/j.ecoenv.2020.111481.

(43) Henry, M. P.; Donlon, B. A.; Lens, P. N.; Colleran, E. M. Use of Anaerobic Hybrid Reactors for Treatment of Synthetic Pharmaceutical Wastewaters Containing Organic Solvents. *Journal of Chemical Technology & Biotechnology* **1996**, *66* (3), 251–264. https://doi.org/10.1002/(SICI)1097-4660(199607)66:3<251::AID-JCTB496>3.0.CO;2-S.

(44) Płotka-Wasylka, J.; Rutkowska, M.; Owczarek, K.; Tobiszewski, M.; Namieśnik, J. Extraction with Environmentally Friendly Solvents. *TrAC Trends in Analytical Chemistry* **2017**, *91*, 12–25. https://doi.org/10.1016/j.trac.2017.03.006.

(45) López-Grimau, V.; Guadayol, J. M.; Griera, J. A.; Gutiérrez, M. C. Determination of Non Halogenated Solvents in Industrial Wastewater Using Solid

Phase Microextiraction (SPME) and GC-MS. *Latin American applied research* **2006**, *36* (1), 49–55.

(46) Rivera-Utrilla, J.; Sánchez-Polo, M.; Polo, A. M. S.; López-Peñalver, J. J.; López-Ramón, M. V. New Technologies to Remove Halides from Water: An Overview. In *Advanced Research in Nanosciences for Water Technology*; Prasad, R., Karchiyappan, T., Eds.; Nanotechnology in the Life Sciences; Springer International Publishing: Cham, 2019; pp 147–180. https://doi.org/10.1007/978-3-030-02381-2_7.

(47) Kanduti, D.; Sterbenk, P.; Artnik, B. FLUORIDE: A REVIEW OF USE AND EFFECTS ON HEALTH. *Mater Sociomed* **2016**, *28* (2), 133–137. https://doi.org/10.5455/msm.2016.28.133-137.

(48) Dąbrowska, A.; Nawrocki, J. Aldehyde Concentrations in Wet Deposition and River Waters. *Science of The Total Environment* **2013**, *452–453*, 1–9. https://doi.org/10.1016/j.scitotenv.2013.02.037.

(49) Rimstidt, J. D.; Vaughan, D. J. Pyrite Oxidation: A State-of-the-Art Assessment of the Reaction Mechanism. *Geochimica et Cosmochimica Acta* **2003**, *67* (5), 873–880. https://doi.org/10.1016/S0016-7037(02)01165-1.

(50) Zhu, X.; Liu, J.; Li, L.; Zhen, G.; Lu, X.; Zhang, J.; Liu, H.; Zhou, Z.; Wu, Z.; Zhang, X. Prospects for Humic Acids Treatment and Recovery in Wastewater: A Review. *Chemosphere* **2023**, *312*, 137193. https://doi.org/10.1016/j.chemosphere.2022.137193.

(51) Weidner, E.; Ciesielczyk, F. Removal of Hazardous Oxyanions from the Environment Using Metal-Oxide-Based Materials. *Materials (Basel)* **2019**, *12* (6), 927. https://doi.org/10.3390/ma12060927.

(52) Inyinbor, A. A.; Bello, O. S.; Dada, O. A.; Oreofe, T. A. Emerging Water Pollutants and Wastewater Treatments. In *Two-Dimensional (2D) Nanomaterials in Separation Science*; Das, R., Ed.; Springer Series on Polymer and Composite Materials; Springer International Publishing: Cham, 2021; pp 13–42. https://doi.org/10.1007/978-3-030-72457-3_2.

(53) Ahamad, A.; Madhav, S.; Singh, A. K.; Kumar, A.; Singh, P. Types of Water Pollutants: Conventional and Emerging. In *Sensors in Water Pollutants Monitoring: Role of Material*; Pooja, D., Kumar, P., Singh, P., Patil, S., Eds.; Advanced Functional Materials and Sensors; Springer Singapore: Singapore, 2020; pp 21–41. https://doi.org/10.1007/978-981-15-0671-0_3.

(54) Ahmad, H. A.; Ahmad, S.; Cui, Q.; Wang, Z.; Wei, H.; Chen, X.; Ni, S.-Q.; Ismail, S.; Awad, H. M.; Tawfik, A. The Environmental Distribution and Removal of Emerging Pollutants, Highlighting the Importance of Using Microbes as a Potential Degrader: A Review. *Science of The Total Environment* **2022**, *809*, 151926. https://doi.org/10.1016/j.scitotenv.2021.151926.

(55) Balakrishnan, A.; Sillanpää, M.; Jacob, M. M.; Vo, D.-V. N. Metformin as an Emerging Concern in Wastewater: Occurrence, Analysis and Treatment Methods. *Environmental Research* **2022**, *213*, 113613. https://doi.org/10.1016/j.envres.2022.113613.

(56) Lorenzo, M.; Campo, J.; Picó, Y. Analytical Challenges to Determine Emerging Persistent Organic Pollutants in Aquatic Ecosystems. *TrAC Trends in Analytical Chemistry* **2018**, *103*, 137–155. https://doi.org/10.1016/j.trac.2018.04.003.

(57) Noman, M.; Shahid, M.; Ahmed, T.; Niazi, M. B. K.; Hussain, S.; Song, F.; Manzoor, I. Use of Biogenic Copper Nanoparticles Synthesized from a Native

Escherichia Sp. as Photocatalysts for Azo Dye Degradation and Treatment of Textile Effluents. *Environmental Pollution* **2020**, *257*, 113514. https://doi.org/10.1016/j.envpol.2019.113514.

(58) Yamjala, K.; Nainar, M. S.; Ramisetti, N. R. Methods for the Analysis of Azo Dyes Employed in Food Industry – A Review. *Food Chemistry* **2016**, *192*, 813–824. https://doi.org/10.1016/j.foodchem.2015.07.085.

(59) Tiwari, A.; Joshi, M.; Salvi, N.; Gupta, D.; Gandhi, S.; Rajpoot, K.; Tekade, R. K. Chapter 21 - Toxicity of Pharmaceutical Azo Dyes. In *Pharmacokinetics and Toxicokinetic Considerations*; Tekade, R. K., Ed.; Advances in Pharmaceutical Product Development and Research; Academic Press, 2022; Vol. 2, pp 569–603. https://doi.org/10.1016/B978-0-323-98367-9.00004-4.

(60) Błędzka, D.; Gromadzińska, J.; Wąsowicz, W. Parabens. From Environmental Studies to Human Health. *Environment International* **2014**, *67*, 27–42. https://doi.org/10.1016/j.envint.2014.02.007.

(61) Glüge, J.; Scheringer, M.; T. Cousins, I.; C. DeWitt, J.; Goldenman, G.; Herzke, D.; Lohmann, R.; A. Ng, C.; Trier, X.; Wang, Z. An Overview of the Uses of Per- and Polyfluoroalkyl Substances (PFAS). *Environmental Science: Processes & Impacts* **2020**, *22* (12), 2345–2373. https://doi.org/10.1039/D0EM00291G.

(62) Rappoport, Z. V. I. *The Chemistry of Phenols*; John Wiley & Sons, 2004.

(63) McDonnell, G.; Russell, A. D. Antiseptics and Disinfectants: Activity, Action, and Resistance. *Clinical Microbiology Reviews* **1999**, *12* (1), 147–179. https://doi.org/10.1128/cmr.12.1.147.

(64) J. Michałowicz, W. Duda. Phenols – Sources and Toxicity. *Pol. J. Environ. Stud. 16* (3), 347–362.

(65) Borja, J.; Taleon, D. M.; Auresenia, J.; Gallardo, S. Polychlorinated Biphenyls and Their Biodegradation. *Process Biochemistry* **2005**, *40* (6), 1999–2013. https://doi.org/10.1016/j.procbio.2004.08.006.

(66) Abdel-Shafy, H. I.; Mansour, M. S. M. A Review on Polycyclic Aromatic Hydrocarbons: Source, Environmental Impact, Effect on Human Health and Remediation. *Egyptian Journal of Petroleum* **2016**, *25* (1), 107–123. https://doi.org/10.1016/j.ejpe.2015.03.011.

(67) Kumar, M.; Borah, P.; Devi, P. Priority and Emerging Pollutants in Water. In *Inorganic Pollutants in Water*; Elsevier, 2020; pp 33–49. https://doi.org/10.1016/B978-0-12-818965-8.00003-2.

(68) Alaee, M.; Arias, P.; Sjödin, A.; Bergman, Å. An Overview of Commercially Used Brominated Flame Retardants, Their Applications, Their Use Patterns in Different Countries/Regions and Possible Modes of Release. *Environment International* **2003**, *29* (6), 683–689. https://doi.org/10.1016/S0160-4120(03)00121-1.

(69) Yu, J.; Zhou, D.; Yu, M.; Yang, J.; Li, Y.; Guan, B.; Wang, X.; Zhan, C.; Wang, Z.; Qu, F. Environmental Threats Induced Heavy Ecological Burdens on the Coastal Zone of the Bohai Sea, China. *Science of The Total Environment* **2021**, *765*, 142694. https://doi.org/10.1016/j.scitotenv.2020.142694.

(70) Paul, A. K.; Achar, S. K.; Dasari, S. R.; Borugadda, V. B.; Goud, V. V. Analysis of Thermal, Oxidative and Cold Flow Properties of Methyl and Ethyl Esters Prepared from Soybean and Mustard Oils. *J Therm Anal Calorim* **2017**, *130* (3), 1501–1511. https://doi.org/10.1007/s10973-017-6424-z.

(71) Ahmadijokani, F.; Molavi, H.; Rezakazemi, M.; Aminabhavi, T. M.; Arjmand, M. Simultaneous Detection and Removal of Fluoride from Water Using Smart

Metal-Organic Framework-Based Adsorbents. *Coordination Chemistry Reviews* **2021**, *445*, 214037. https://doi.org/10.1016/j.ccr.2021.214037.

(72) Budnik, L. T.; Casteleyn, L. Mercury Pollution in Modern Times and Its Socio-Medical Consequences. *Science of The Total Environment* **2019**, *654*, 720–734. https://doi.org/10.1016/j.scitotenv.2018.10.408.

(73) Rodríguez Martín, J. A.; Nanos, N. Soil as an Archive of Coal-Fired Power Plant Mercury Deposition. *Journal of Hazardous Materials* **2016**, *308*, 131–138. https://doi.org/10.1016/j.jhazmat.2016.01.026.

(74) Liu, H.; Ruan, W.; Zhang, Z.; Zhou, Y.; Shen, F.; Liu, J.; Yang, H. Performance and Mechanism of CuS-Modified MWCNTs on Mercury Removal: Experimental and Density Functional Theory Study. *Fuel* **2022**, *309*, 122238. https://doi.org/10.1016/j.fuel.2021.122238.

(75) Panagos, P.; Jiskra, M.; Borrelli, P.; Liakos, L.; Ballabio, C. Mercury in European Topsoils: Anthropogenic Sources, Stocks and Fluxes. *Environmental Research* **2021**, *201*, 111556. https://doi.org/10.1016/j.envres.2021.111556.

(76) Beckers, F.; Rinklebe, J. Cycling of Mercury in the Environment: Sources, Fate, and Human Health Implications: A Review. *Critical Reviews in Environmental Science and Technology* **2017**, *47* (9), 693–794. https://doi.org/10.1080/10643389.2017.1326277.

(77) Pavithra, K. G.; SundarRajan, P.; Kumar, P. S.; Rangasamy, G. Mercury Sources, Contaminations, Mercury Cycle, Detection and Treatment Techniques: A Review. *Chemosphere* **2023**, *312*, 137314. https://doi.org/10.1016/j.chemosphere.2022.137314.

(78) Attari, M.; Bukhari, S. S.; Kazemian, H.; Rohani, S. A Low-Cost Adsorbent from Coal Fly Ash for Mercury Removal from Industrial Wastewater. *Journal of*

Environmental Chemical Engineering **2017**, *5* (1), 391–399. https://doi.org/10.1016/j.jece.2016.12.014.

(79) Zhang, L.; Wang, J.; Wang, H.; Zhang, W.; Zhu, W.; Du, T.; Ni, Y.; Xie, X.; Sun, J.; Wang, J. Rational Design of Smart Adsorbent Equipped with a Sensitive Indicator via Ligand Exchange: A Hierarchical Porous Mixed-Ligand MOF for Simultaneous Removal and Detection of Hg2+. *Nano Res.* **2021**, *14* (5), 1523–1532. https://doi.org/10.1007/s12274-020-3211-0.

(80) Jaishankar, M.; Tseten, T.; Anbalagan, N.; Mathew, B. B.; Beeregowda, K. N. Toxicity, Mechanism and Health Effects of Some Heavy Metals. *Interdiscip Toxicol* **2014**, *7* (2), 60–72. https://doi.org/10.2478/intox-2014-0009.

(81) Say, R.; Birlik, E.; Erdemgil, Z.; Denizli, A.; Ersöz, A. Removal of Mercury Species with Dithiocarbamate-Anchored Polymer/Organosmectite Composites. *Journal of Hazardous Materials* **2008**, *150* (3), 560–564. https://doi.org/10.1016/j.jhazmat.2007.03.089.

(82) Fitzgerald, W. F.; Lamborg, C. H.; Hammerschmidt, C. R. Marine Biogeochemical Cycling of Mercury. *Chem. Rev.* **2007**, *107* (2), 641–662. https://doi.org/10.1021/cr050353m.

(83) Khan, M. N.; Mobin, M.; Abbas, Z. K.; Alamri, S. A. Fertilizers and Their Contaminants in Soils, Surface and Groundwater. In *Encyclopedia of the Anthropocene*; Elsevier, 2018; pp 225–240. https://doi.org/10.1016/B978-0-12-809665-9.09888-8.

(84) Gulley, A. L. Valuing Environmental Impacts of Mercury Emissions from Gold Mining: Dollar per Troy Ounce Estimates for Twelve Open-Pit, Small-Scale, and Artisanal Mining Sites. *Resources Policy* **2017**, *52*, 266–272. https://doi.org/10.1016/j.resourpol.2017.03.009.

(85) Braune, B.; Chételat, J.; Amyot, M.; Brown, T.; Clayden, M.; Evans, M.; Fisk, A.; Gaden, A.; Girard, C.; Hare, A.; Kirk, J.; Lehnherr, I.; Letcher, R.; Loseto, L.; Macdonald, R.; Mann, E.; McMeans, B.; Muir, D.; O'Driscoll, N.; Poulain, A.; Reimer, K.; Stern, G. Mercury in the Marine Environment of the Canadian Arctic: Review of Recent Findings. *Science of The Total Environment* **2015**, *509–510*, 67–90. https://doi.org/10.1016/j.scitotenv.2014.05.133.

(86) Kirk, J. L.; Lehnherr, I.; Andersson, M.; Braune, B. M.; Chan, L.; Dastoor, A. P.; Durnford, D.; Gleason, A. L.; Loseto, L. L.; Steffen, A.; St. Louis, V. L. Mercury in Arctic Marine Ecosystems: Sources, Pathways and Exposure. *Environmental Research* **2012**, *119*, 64–87. https://doi.org/10.1016/j.envres.2012.08.012.

(87) Esdaile, L. J.; Chalker, J. M. The Mercury Problem in Artisanal and Small-Scale Gold Mining. *Chemistry* **2018**, *24* (27), 6905–6916. https://doi.org/10.1002/chem.201704840.

(88) Behera, M.; Nayak, J.; Banerjee, S.; Chakrabortty, S.; Tripathy, S. K. A Review on the Treatment of Textile Industry Waste Effluents towards the Development of Efficient Mitigation Strategy: An Integrated System Design Approach. *Journal of Environmental Chemical Engineering* **2021**, *9* (4), 105277. https://doi.org/10.1016/j.jece.2021.105277.

(89) Oladoye, P. O.; Ajiboye, T. O.; Omotola, E. O.; Oyewola, O. J. Methylene Blue Dye: Toxicity and Potential Elimination Technology from Wastewater. *Results in Engineering* **2022**, *16*, 100678. https://doi.org/10.1016/j.rineng.2022.100678.

(90) Wang, X.; Zhang, P.; Xu, F.; Sun, B.; Hong, G.; Bao, L. Adsorption of Methylene Blue on Azo Dye Wastewater by Molybdenum Disulfide

Nanomaterials. *Sustainability* **2022**, *14* (13), 7585. https://doi.org/10.3390/su14137585.

(91) Hunger, K. *Industrial Dyes: Chemistry, Properties, Applications*; John Wiley & Sons, 2007.

(92) Sonune, A.; Ghate, R. Developments in Wastewater Treatment Methods. *Desalination* **2004**, *167*, 55–63. https://doi.org/10.1016/j.desal.2004.06.113.

(93) Koul, B.; Yadav, D.; Singh, S.; Kumar, M.; Song, M. Insights into the Domestic Wastewater Treatment (DWWT) Regimes: A Review. *Water* **2022**, *14* (21), 3542. https://doi.org/10.3390/w14213542.

(94) Bolisetty, S.; Peydayesh, M.; Mezzenga, R. Sustainable Technologies for Water Purification from Heavy Metals: Review and Analysis. *Chem. Soc. Rev.* **2019**, *48* (2), 463–487. https://doi.org/10.1039/C8CS00493E.

(95) Murshid, S.; Antonysamy, A.; Dhakshinamoorthy, G.; Jayaseelan, A.; Pugazhendhi, A. A Review on Biofilm-Based Reactors for Wastewater Treatment: Recent Advancements in Biofilm Carriers, Kinetics, Reactors, Economics, and Future Perspectives. *Science of The Total Environment* **2023**, *892*, 164796. https://doi.org/10.1016/j.scitotenv.2023.164796.

(96) Roy, M.; Saha, R. 6 - Dyes and Their Removal Technologies from Wastewater: A Critical Review. In *Intelligent Environmental Data Monitoring for Pollution Management*; Bhattacharyya, S., Mondal, N. K., Platos, J., Snášel, V., Krömer, P., Eds.; Intelligent Data-Centric Systems; Academic Press, 2021; pp 127–160. https://doi.org/10.1016/B978-0-12-819671-7.00006-3.

(97) Wei, Y.; Van Houten, R. T.; Borger, A. R.; Eikelboom, D. H.; Fan, Y. Minimization of Excess Sludge Production for Biological Wastewater Treatment.

Water Research **2003**, *37* (18), 4453–4467. https://doi.org/10.1016/S0043-1354(03)00441-X.

(98) Ahmed Hussain. *Biological Wastewater Treatment - an overview | ScienceDirect Topics*. https://www.sciencedirect.com/topics/chemical-engineering/biological-wastewater-treatment (accessed 2024-01-06).

(99) Gandhi, V.; Shah, K. *Advances in Wastewater Treatment I*; Materials Research Forum LLC, 2021.

(100) Kumar Gupta, V.; Ali, I.; A. Saleh, T.; Nayak, A.; Agarwal, S. Chemical Treatment Technologies for Waste-Water Recycling—an Overview. *RSC Advances* **2012**, *2* (16), 6380–6388. https://doi.org/10.1039/C2RA20340E.

(101) Punia, P.; Bharti, M. K.; Dhar, R.; Thakur, P.; Thakur, A. Recent Advances in Detection and Removal of Heavy Metals from Contaminated Water. *ChemBioEng Reviews* **2022**, *9* (4), 351–369. https://doi.org/10.1002/cben.202100053.

(102) Sillanpää, M.; Shestakova, M. Chapter 3 - Emerging and Combined Electrochemical Methods. In *Electrochemical Water Treatment Methods*; Sillanpää, M., Shestakova, M., Eds.; Butterworth-Heinemann, 2017; pp 131–225. https://doi.org/10.1016/B978-0-12-811462-9.00003-7.

(103) AlJaberi, F. Y.; Ahmed, S. A.; Makki, H. F.; Naje, A. S.; Zwain, H. M.; Salman, A. D.; Juzsakova, T.; Viktor, S.; Van, B.; Le, P.-C.; La, D. D.; Chang, S. W.; Um, M.-J.; Ngo, H. H.; Nguyen, D. D. Recent Advances and Applicable Flexibility Potential of Electrochemical Processes for Wastewater Treatment. *Science of The Total Environment* **2023**, *867*, 161361. https://doi.org/10.1016/j.scitotenv.2022.161361.

(104) Lee, A.; W. Elam, J.; B. Darling, S. Membrane Materials for Water Purification: Design, Development, and Application. *Environmental Science:*

Water Research & Technology **2016**, *2* (1), 17–42. https://doi.org/10.1039/C5EW00159E.

(105) Malik, L. A.; Bashir, A.; Qureashi, A.; Pandith, A. H. Detection and Removal of Heavy Metal Ions: A Review. *Environ Chem Lett* **2019**, *17* (4), 1495–1521. https://doi.org/10.1007/s10311-019-00891-z.

(106) Alaba, P. A.; Oladoja, N. A.; Sani, Y. M.; Ayodele, O. B.; Mohammed, I. Y.; Olupinla, S. F.; Daud, W. M. W. Insight into Wastewater Decontamination Using Polymeric Adsorbents. *Journal of Environmental Chemical Engineering* **2018**, *6* (2), 1651–1672. https://doi.org/10.1016/j.jece.2018.02.019.

(107) Anderson, A.; Anbarasu, A.; Pasupuleti, R. R.; Manigandan, S.; Praveenkumar, T. R.; Aravind Kumar, J. Treatment of Heavy Metals Containing Wastewater Using Biodegradable Adsorbents: A Review of Mechanism and Future Trends. *Chemosphere* **2022**, *295*, 133724. https://doi.org/10.1016/j.chemosphere.2022.133724.

(108) Nawaz, M. S.; Ahsan, M. Comparison of Physico-Chemical, Advanced Oxidation and Biological Techniques for the Textile Wastewater Treatment. *Alexandria Engineering Journal* **2014**, *53* (3), 717–722. https://doi.org/10.1016/j.aej.2014.06.007.

(109) Zinicovscaia, I. Conventional Methods of Wastewater Treatment. In *Cyanobacteria for Bioremediation of Wastewaters*; Zinicovscaia, I., Cepoi, L., Eds.; Springer International Publishing: Cham, 2016; pp 17–25. https://doi.org/10.1007/978-3-319-26751-7_3.

(110) Abuhasel, K.; Kchaou, M.; Alquraish, M.; Munusamy, Y.; Jeng, Y. T. Oily Wastewater Treatment: Overview of Conventional and Modern Methods,

Challenges, and Future Opportunities. *Water* **2021**, *13* (7), 980. https://doi.org/10.3390/w13070980.

(111) Dmitrieva, E. S.; Anokhina, T. S.; Novitsky, E. G.; Volkov, V. V.; Borisov, I. L.; Volkov, A. V. Polymeric Membranes for Oil-Water Separation: A Review. *Polymers (Basel)* **2022**, *14* (5), 980. https://doi.org/10.3390/polym14050980.

(112) Kumar, R.; Ismail, A. F. Fouling Control on Microfiltration/Ultrafiltration Membranes: Effects of Morphology, Hydrophilicity, and Charge. *Journal of Applied Polymer Science* **2015**, *132* (21). https://doi.org/10.1002/app.42042.

(113) Ismail, N. H.; Salleh, W. N. W.; Ismail, A. F.; Hasbullah, H.; Yusof, N.; Aziz, F.; Jaafar, J. Hydrophilic Polymer-Based Membrane for Oily Wastewater Treatment: A Review. *Separation and Purification Technology* **2020**, *233*, 116007. https://doi.org/10.1016/j.seppur.2019.116007.

(114) Zhu, X.; Loo, H.-E.; Bai, R. A Novel Membrane Showing Both Hydrophilic and Oleophobic Surface Properties and Its Non-Fouling Performances for Potential Water Treatment Applications. *Journal of Membrane Science* **2013**, *436*, 47–56. https://doi.org/10.1016/j.memsci.2013.02.019.

(115) Jin, M.; Yuan, H.; Liu, B.; Peng, J.; Xu, L.; Yang, D. Review of the Distribution and Detection Methods of Heavy Metals in the Environment. *Anal. Methods* **2020**, *12* (48), 5747–5766. https://doi.org/10.1039/D0AY01577F.

(116) You, Z.; Li, X.; Huang, J.; Chen, R.; Peng, J.; Kong, W.; Liu, F. Agarose Film-Based Liquid–Solid Conversion for Heavy Metal Detection of Water Samples by Laser-Induced Breakdown Spectroscopy. *Molecules* **2023**, *28* (6), 2777. https://doi.org/10.3390/molecules28062777.

(117) Basharat R., K. V. *A Mini-review on Ultra Performance Liquid Chromatography - ProQuest*.

https://www.proquest.com/docview/2807982948?pq-origsite=gscholar&fromopenview=true&sourcetype=Scholarly%20Journals (accessed 2023-12-18).

(118) Cui, L.; Wu, J.; Ju, H. Electrochemical Sensing of Heavy Metal Ions with Inorganic, Organic and Bio-Materials. *Biosensors and Bioelectronics* **2015**, *63*, 276–286. https://doi.org/10.1016/j.bios.2014.07.052.

(119) March, G.; Nguyen, T. D.; Piro, B. Modified Electrodes Used for Electrochemical Detection of Metal Ions in Environmental Analysis. *Biosensors* **2015**, *5* (2), 241–275. https://doi.org/10.3390/bios5020241.

(120) Werber, J. R.; Osuji, C. O.; Elimelech, M. Materials for Next-Generation Desalination and Water Purification Membranes. *Nat Rev Mater* **2016**, *1* (5), 16018. https://doi.org/10.1038/natrevmats.2016.18.

(121) Khodakarami, M.; Bagheri, M. Recent Advances in Synthesis and Application of Polymer Nanocomposites for Water and Wastewater Treatment. *Journal of Cleaner Production* **2021**, *296*, 126404. https://doi.org/10.1016/j.jclepro.2021.126404.

(122) de Souza Neves Ellendersen, L.; Milinsk, M. C.; Feroldi, M.; Volkweis Zadinelo, I.; Dena dos Santos, L.; Bolzón de Muniz, G. I.; Gasparrini, L. J.; Alves, H. J. Biopolymer Foam for Remediation of Aquatic Environments Contaminated with Particulates and Heavy Metals. *Journal of Environmental Chemical Engineering* **2018**, *6* (5), 6131–6138. https://doi.org/10.1016/j.jece.2018.09.019.

(123) Udayakumar, K. V.; Gore, P. M.; Kandasubramanian, B. Foamed Materials for Oil-Water Separation. *Chemical Engineering Journal Advances* **2021**, *5*, 100076. https://doi.org/10.1016/j.ceja.2020.100076.

(124) Gama, N. V.; Ferreira, A.; Barros-Timmons, A. Polyurethane Foams: Past, Present, and Future. *Materials* **2018**, *11* (10), 1841. https://doi.org/10.3390/ma11101841.

(125) Liao, Y.; Loh, C.-H.; Tian, M.; Wang, R.; Fane, A. G. Progress in Electrospun Polymeric Nanofibrous Membranes for Water Treatment: Fabrication, Modification and Applications. *Progress in Polymer Science* **2018**, *77*, 69–94. https://doi.org/10.1016/j.progpolymsci.2017.10.003.

(126) Lee, J.-W.; Jung, J.; Cho, Y. H.; Yadav, S. K.; Baek, K. Y.; Park, H. B.; Hong, S. M.; Koo, C. M. Fouling-Tolerant Nanofibrous Polymer Membranes for Water Treatment. *ACS Appl. Mater. Interfaces* **2014**, *6* (16), 14600–14607. https://doi.org/10.1021/am503874b.

(127) Suja, P. S.; Reshmi, C. R.; Sagitha, P.; Sujith, A. Electrospun Nanofibrous Membranes for Water Purification. *Polymer Reviews* **2017**, *57* (3), 467–504. https://doi.org/10.1080/15583724.2017.1309664.

(128) Khan, N. A.; Khan, S. U.; Ahmed, S.; Farooqi, I. H.; Dhingra, A.; Hussain, A.; Changani, F. Applications of Nanotechnology in Water and Wastewater Treatment: A Review. *AJW* **2019**, *16* (4), 81–86. https://doi.org/10.3233/AJW190051.

(129) Patanjali, P.; Singh, R.; Kumar, A.; Chaudhary, P. Nanotechnology for Water Treatment: A Green Approach. In *Green Synthesis, Characterization and Applications of Nanoparticles*; Elsevier, 2019; pp 485–512. https://doi.org/10.1016/B978-0-08-102579-6.00021-6.

(130) Bora, T.; Dutta, J. Applications of Nanotechnology in Wastewater Treatment—A Review. *Journal of Nanoscience and Nanotechnology* **2014**, *14* (1), 613–626. https://doi.org/10.1166/jnn.2014.8898.

(131) Zhang, Z.; Sèbe, G.; Rentsch, D.; Zimmermann, T.; Tingaut, P. Ultralightweight and Flexible Silylated Nanocellulose Sponges for the Selective Removal of Oil from Water. *Chem. Mater.* **2014**, *26* (8), 2659–2668. https://doi.org/10.1021/cm5004164.

(132) Al-Khalaf, A. A.; Al-Lami, H. S.; Abbas, A. F. Flexible Polyurethane Foam with Improved Oleophilic and Hydrophobic Properties for Oil Spill Cleaning. *Petroleum Science and Technology* **2024**, *42* (3), 287–302. https://doi.org/10.1080/10916466.2022.2118774.

(133) Ge, J.; Zhao, H.-Y.; Zhu, H.-W.; Huang, J.; Shi, L.-A.; Yu, S.-H. Advanced Sorbents for Oil-Spill Cleanup: Recent Advances and Future Perspectives. *Advanced Materials* **2016**, *28* (47), 10459–10490. https://doi.org/10.1002/adma.201601812.

(134) Ko, S. W.; Moon, J. Y.; Bae, S. M.; Kim, C. S.; Park, C. H. A Sponge-Type Oil Skimmer for Highly Efficient Removal of Floating Oils: Superabsorbent and Oleophilic Sponge with Nano-Scale Interface Roughness. *Applied Surface Science* **2022**, *606*, 154750. https://doi.org/10.1016/j.apsusc.2022.154750.

(135) Fragouli, D. Foams and Aerogels for Remediation and Recovery of Oil Spillage. In *Oil−Water Mixtures and Emulsions, Volume 2: Advanced Materials for Separation and Treatment*; ACS Symposium Series; American Chemical Society, 2022; Vol. 1408, pp 51–76. https://doi.org/10.1021/bk-2022-1408.ch003.

(136) Khosravi, M.; Azizian, S. Synthesis of a Novel Highly Oleophilic and Highly Hydrophobic Sponge for Rapid Oil Spill Cleanup. *ACS Appl. Mater. Interfaces* **2015**, *7* (45), 25326–25333. https://doi.org/10.1021/acsami.5b07504.

(137) Furlan, P. Y.; Ackerman, B. M.; Melcer, M. E.; Perez, S. E. Reusable Magnetic Nanocomposite Sponges for Removing Oil from Water Discharges. *Journal of*

Ship Production and Design **2017**, *33* (03), 227–236. https://doi.org/10.5957/JSPD.33.3.160017.

(138) Yu, J.; Cao, C.; Liu, S.; Pan, Y. Eco-Friendly Magneto-Photothermal Sponge for the Fast Recovery of Highly Viscous Crude Oil Spill. *Separation and Purification Technology* **2022**, *298*, 121668. https://doi.org/10.1016/j.seppur.2022.121668.

(139) Smirnova, I.; Gurikov, P. Aerogel Production: Current Status, Research Directions, and Future Opportunities. *The Journal of Supercritical Fluids* **2018**, *134*, 228–233. https://doi.org/10.1016/j.supflu.2017.12.037.

(140) Tüysüz, H.; Schüth, F. Chapter Two - Ordered Mesoporous Materials as Catalysts. In *Advances in Catalysis*; Gates, B. C., Jentoft, F. C., Eds.; Academic Press, 2012; Vol. 55, pp 127–239. https://doi.org/10.1016/B978-0-12-385516-9.00002-8.

(141) Li, Z.; Zhong, L.; Zhang, T.; Qiu, F.; Yue, X.; Yang, D. Sustainable, Flexible, and Superhydrophobic Functionalized Cellulose Aerogel for Selective and Versatile Oil/Water Separation. *ACS Sustainable Chem. Eng.* **2019**, *7* (11), 9984–9994. https://doi.org/10.1021/acssuschemeng.9b01122.

(142) Jiang, Y.-H.; Zhang, Y.-Q.; Gao, C.; An, Q.-D.; Xiao, Z.-Y.; Zhai, S.-R. Superhydrophobic Aerogel Membrane with Integrated Functions of Biopolymers for Efficient Oil/Water Separation. *Separation and Purification Technology* **2022**, *282*, 120138. https://doi.org/10.1016/j.seppur.2021.120138.

(143) Thakkar, S. V.; Pinna, A.; Carbonaro, C. M.; Malfatti, L.; Guardia, P.; Cabot, A.; Casula, M. F. Performance of Oil Sorbents Based on Reduced Graphene Oxide–Silica Composite Aerogels. *Journal of Environmental Chemical Engineering* **2020**, *8* (1), 103632. https://doi.org/10.1016/j.jece.2019.103632.

(144) Ma, Q.; Cheng, H.; Fane, A. G.; Wang, R.; Zhang, H. Recent Development of Advanced Materials with Special Wettability for Selective Oil/Water Separation. *Small* **2016**, *12* (16), 2186–2202. https://doi.org/10.1002/smll.201503685.

(145) Zhang, W.; Liu, N.; Cao, Y.; Lin, X.; Liu, Y.; Feng, L. Superwetting Porous Materials for Wastewater Treatment: From Immiscible Oil/Water Mixture to Emulsion Separation. *Advanced Materials Interfaces* **2017**, *4* (10), 1600029. https://doi.org/10.1002/admi.201700029.

(146) Xue, Z.; Cao, Y.; Liu, N.; Feng, L.; Jiang, L. Special Wettable Materials for Oil/Water Separation. *J. Mater. Chem. A* **2014**, *2* (8), 2445–2460. https://doi.org/10.1039/C3TA13397D.

(147) Brown, P. S.; Atkinson, O. D. L. A.; Badyal, J. P. S. Ultrafast Oleophobic–Hydrophilic Switching Surfaces for Antifogging, Self-Cleaning, and Oil–Water Separation. *ACS Appl. Mater. Interfaces* **2014**, *6* (10), 7504–7511. https://doi.org/10.1021/am500882y.

(148) Wang, Y.; Dugan, M.; Urbaniak, B.; Li, L. Fabricating Nanometer-Thick Simultaneously Oleophobic/Hydrophilic Polymer Coatings via a Photochemical Approach. *Langmuir* **2016**, *32* (26), 6723–6729. https://doi.org/10.1021/acs.langmuir.6b00802.

(149) Chu, Z.; Feng, Y.; Seeger, S. Oil/Water Separation with Selective Superantiwetting/Superwetting Surface Materials. *Angewandte Chemie International Edition* **2015**, *54* (8), 2328–2338. https://doi.org/10.1002/anie.201405785.

(150) Miller, D. J.; Dreyer, D. R.; Bielawski, C. W.; Paul, D. R.; Freeman, B. D. Surface Modification of Water Purification Membranes. *Angewandte Chemie*

International Edition **2017**, *56* (17), 4662–4711. https://doi.org/10.1002/anie.201601509.

(151) Rana, D.; Matsuura, T.; Narbaitz, R. M.; Feng, C. Development and Characterization of Novel Hydrophilic Surface Modifying Macromolecule for Polymeric Membranes. *Journal of Membrane Science* **2005**, *249* (1), 103–112. https://doi.org/10.1016/j.memsci.2004.09.034.

(152) Asmatulu, R.; Muppalla, H.; Veisi, Z.; Khan, W. S.; Asaduzzaman, A.; Nuraje, N. Study of Hydrophilic Electrospun Nanofiber Membranes for Filtration of Micro and Nanosize Suspended Particles. *Membranes* **2013**, *3* (4), 375–388. https://doi.org/10.3390/membranes3040375.

(153) Pan, S.-F.; Dong, Y.; Zheng, Y.-Ming.; Zhong, L.-B.; Yuan, Z.-H. Self-Sustained Hydrophilic Nanofiber Thin Film Composite Forward Osmosis Membranes: Preparation, Characterization and Application for Simulated Antibiotic Wastewater Treatment. *Journal of Membrane Science* **2017**, *523*, 205–215. https://doi.org/10.1016/j.memsci.2016.09.045.

(154) Park, M. J.; Gonzales, R. R.; Abdel-Wahab, A.; Phuntsho, S.; Shon, H. K. Hydrophilic Polyvinyl Alcohol Coating on Hydrophobic Electrospun Nanofiber Membrane for High Performance Thin Film Composite Forward Osmosis Membrane. *Desalination* **2018**, *426*, 50–59. https://doi.org/10.1016/j.desal.2017.10.042.

(155) Darban, Z.; Shahabuddin, S.; Gaur, R.; Ahmad, I.; Sridewi, N. Hydrogel-Based Adsorbent Material for the Effective Removal of Heavy Metals from Wastewater: A Comprehensive Review. *Gels* **2022**, *8* (5), 263. https://doi.org/10.3390/gels8050263.

(156) Loo, S.-L.; Vásquez, L.; Athanassiou, A.; Fragouli, D. Polymeric Hydrogels—A Promising Platform in Enhancing Water Security for a Sustainable Future. *Advanced Materials Interfaces* **2021**, *8* (24), 2100580. https://doi.org/10.1002/admi.202100580.

(157) Jia, Z.; Shu, Y.; Huang, R.; Liu, J.; Liu, L. Enhanced Reactivity of nZVI Embedded into Supermacroporous Cryogels for Highly Efficient Cr(VI) and Total Cr Removal from Aqueous Solution. *Chemosphere* **2018**, *199*, 232–242. https://doi.org/10.1016/j.chemosphere.2018.02.021.

(158) Dai, L.; Cheng, T.; Xi, X.; Nie, S.; Ke, H.; Liu, Y.; Tong, S.; Chen, Z. A Versatile TOCN/CGG Self-Assembling Hydrogel for Integrated Wastewater Treatment. *Cellulose* **2020**, *27* (2), 915–925. https://doi.org/10.1007/s10570-019-02834-x.

(159) Jia, B.; Li, G.; Cao, E.; Luo, J.; Zhao, X.; Huang, H. Recent Progress of Antibacterial Hydrogels in Wound Dressings. *Materials Today Bio* **2023**, *19*, 100582. https://doi.org/10.1016/j.mtbio.2023.100582.

(160) Samaddar, P.; Kumar, S.; Kim, K.-H. Polymer Hydrogels and Their Applications Toward Sorptive Removal of Potential Aqueous Pollutants. *Polymer Reviews* **2019**, *59* (3), 418–464. https://doi.org/10.1080/15583724.2018.1548477.

(161) Isobe, N.; Chen, X.; Kim, U.-J.; Kimura, S.; Wada, M.; Saito, T.; Isogai, A. TEMPO-Oxidized Cellulose Hydrogel as a High-Capacity and Reusable Heavy Metal Ion Adsorbent. *Journal of Hazardous Materials* **2013**, *260*, 195–201. https://doi.org/10.1016/j.jhazmat.2013.05.024.

(162) Huai-Ping Cong. *Thermoresponsive Poly(N-isopropylacrylamide)/Graphene/Au Nanocomposite Hydrogel for Water Treatment by a Laser-Assisted Approach - Cong - 2015 - Small - Wiley Online*

Library. https://onlinelibrary.wiley.com/doi/abs/10.1002/smll.201401651 (accessed 2023-12-19).

(163) Yao, Q.; Fan, B.; Xiong, Y.; Jin, C.; Sun, Q.; Sheng, C. 3D Assembly Based on 2D Structure of Cellulose Nanofibril/Graphene Oxide Hybrid Aerogel for Adsorptive Removal of Antibiotics in Water. *Sci Rep* **2017**, *7* (1), 45914. https://doi.org/10.1038/srep45914.

(164) Lyu, W.; Li, J.; Trchová, M.; Wang, G.; Liao, Y.; Bober, P.; Stejskal, J. Fabrication of Polyaniline/Poly(Vinyl Alcohol)/Montmorillonite Hybrid Aerogels toward Efficient Adsorption of Organic Dye Pollutants. *Journal of Hazardous Materials* **2022**, *435*, 129004. https://doi.org/10.1016/j.jhazmat.2022.129004.

(165) Mei, J.; Zhang, H.; Mo, S.; Zhang, Y.; Li, Z.; Ou, H. Prominent Adsorption of Cr(VI) with Graphene Oxide Aerogel Twined with Creeper-like Polymer Based on Chitosan Oligosaccharide. *Carbohydrate Polymers* **2020**, *247*, 116733. https://doi.org/10.1016/j.carbpol.2020.116733.

(166) Wei, X.; Huang, T.; Nie, J.; Yang, J.; Qi, X.; Zhou, Z.; Wang, Y. Bio-Inspired Functionalization of Microcrystalline Cellulose Aerogel with High Adsorption Performance toward Dyes. *Carbohydrate Polymers* **2018**, *198*, 546–555. https://doi.org/10.1016/j.carbpol.2018.06.112.

(167) Moura, A. L. A.; Oliveira, L. K. de; Ciuffi, K. J.; Molina, E. F. Influence of the Hydrophilic/Hydrophobic Nature of Polyetheramines on the Interaction between Amine–Alcohol–Silicate Hybrids and Anionic Dyes for Effective Water Cleaning. *J. Mater. Chem. A* **2015**, *3* (31), 16020–16032. https://doi.org/10.1039/C5TA04022A.

(168) Chen, S.; De Guzman, M. R.; Tsou, C.-H.; Li, M.; Suen, M.-C.; Gao, C.; Tsou, C.-Y. Hydrophilic and Absorption Properties of Reversible Nanocomposite

Polyvinyl Alcohol Hydrogels Reinforced with Graphene-Doped Zinc Oxide Nanoplates for Enhanced Antibacterial Activity. *Polym J* **2023**, *55* (1), 45–61. https://doi.org/10.1038/s41428-022-00711-2.

(169) Mondal, B.; Bairagi, D.; Nandi, N.; Hansda, B.; Das, K. S.; Edwards-Gayle, C. J. C.; Castelletto, V.; Hamley, I. W.; Banerjee, A. Peptide-Based Gel in Environmental Remediation: Removal of Toxic Organic Dyes and Hazardous Pb2+ and Cd2+ Ions from Wastewater and Oil Spill Recovery. *Langmuir* **2020**, *36* (43), 12942–12953. https://doi.org/10.1021/acs.langmuir.0c02205.

(170) Zhang, M.; Zhang, S.; Chen, Z.; Wang, M.; Cao, J.; Wang, R. Preparation and Characterization of Superabsorbent Polymers Based on Sawdust. *Polymers* **2019**, *11* (11), 1891. https://doi.org/10.3390/polym11111891.

(171) Ostrand, M. S.; DeSutter, T. M.; Daigh, A. L. M.; Limb, R. F.; Steele, D. D. Superabsorbent Polymer Characteristics, Properties, and Applications. *Agrosystems, Geosciences & Environment* **2020**, *3* (1), e20074. https://doi.org/10.1002/agg2.20074.

(172) Qi, Z.; Hu, X. Waterabsorbency of Super Absorbent Polymer Based on Flexible Polymeric Network. *European Polymer Journal* **2022**, *166*, 111045. https://doi.org/10.1016/j.eurpolymj.2022.111045.

(173) Mignon, A.; De Belie, N.; Dubruel, P.; Van Vlierberghe, S. Superabsorbent Polymers: A Review on the Characteristics and Applications of Synthetic, Polysaccharide-Based, Semi-Synthetic and 'Smart' Derivatives. *European Polymer Journal* **2019**, *117*, 165–178. https://doi.org/10.1016/j.eurpolymj.2019.04.054.

(174) Ge, H.; Hua, T. Synthesis and Characterization of Poly(Maleic Acid)-Grafted Crosslinked Chitosan Nanomaterial with High Uptake and Selectivity for Hg(II)

Sorption. *Carbohydrate Polymers* **2016**, *153*, 246–252. https://doi.org/10.1016/j.carbpol.2016.07.110.

(175) Bhattacharyya, R.; Ray, S. K. Micro- and Nano-Sized Bentonite Filled Composite Superabsorbents of Chitosan and Acrylic Copolymer for Removal of Synthetic Dyes from Water. *Applied Clay Science* **2014**, *101*, 510–520. https://doi.org/10.1016/j.clay.2014.09.015.

(176) Bai, W.; Fan, L.; Zhou, Y.; Zhang, Y.; Shi, J.; Lv, G.; Wu, Y.; Liu, Q.; Song, J. Removal of Cd2+ Ions from Aqueous Solution Using Cassava Starch–Based Superabsorbent Polymers. *Journal of Applied Polymer Science* **2017**, *134* (17). https://doi.org/10.1002/app.44758.

(177) Shah, L. A.; Khan, M.; Javed, R.; Sayed, M.; Khan, M. S.; Khan, A.; Ullah, M. Superabsorbent Polymer Hydrogels with Good Thermal and Mechanical Properties for Removal of Selected Heavy Metal Ions. *Journal of Cleaner Production* **2018**, *201*, 78–87. https://doi.org/10.1016/j.jclepro.2018.08.035.

(178) Ur Rehman, T.; Ali Shah, L.; Khan, M.; Irfan, M.; Saeed Khattak, N. Zwitterionic Superabsorbent Polymer Hydrogels for Efficient and Selective Removal of Organic Dyes. *RSC Advances* **2019**, *9* (32), 18565–18577. https://doi.org/10.1039/C9RA02488C.

(179) Mu, Z.; Liu, D.; Lv, J.; Chai, D.-F.; Bai, L.; Zhang, Z.; Dong, G.; Li, J.; Zhang, W. Insight into the Highly Efficient Adsorption towards Cationic Methylene Blue Dye with a Superabsorbent Polymer Modified by Esterified Starch. *Journal of Environmental Chemical Engineering* **2022**, *10* (5), 108425. https://doi.org/10.1016/j.jece.2022.108425.

(180) Raza, A.; Altaf, S.; Ali, S.; Ikram, M.; Li, G. Recent Advances in Carbonaceous Sustainable Nanomaterials for Wastewater Treatments. *Sustainable*

Materials and Technologies **2022**, *32*, e00406. https://doi.org/10.1016/j.susmat.2022.e00406.

(181) Ozer, D.; Tunca, E. T. Chapter 3 - Design and Construction of MOF Nanomaterials. In *Metal-Organic Framework-Based Nanomaterials for Energy Conversion and Storage*; Gupta, R. K., Nguyen, T. A., Yasin, G., Eds.; Micro and Nano Technologies; Elsevier, 2022; pp 35–65. https://doi.org/10.1016/B978-0-323-91179-5.00032-2.

(182) Zamel, D.; Khan, A. U.; Waris, A.; Ebrahim, A.; Abd El-Sattar, N. E. A. Nanomaterials Advancements for Enhanced Contaminant Removal in Wastewater Treatment: Nanoparticles, Nanofibers, and Metal-Organic Frameworks (MOFs). *Results in Chemistry* **2023**, *6*, 101092. https://doi.org/10.1016/j.rechem.2023.101092.

(183) Cohen, Y. *Advances In Water Desalination Technologies*; World Scientific, 2021.

(184) Baskar, A. V.; Bolan, N.; Hoang, S. A.; Sooriyakumar, P.; Kumar, M.; Singh, L.; Jasemizad, T.; Padhye, L. P.; Singh, G.; Vinu, A.; Sarkar, B.; Kirkham, M. B.; Rinklebe, J.; Wang, S.; Wang, H.; Balasubramanian, R.; Siddique, K. H. M. Recovery, Regeneration and Sustainable Management of Spent Adsorbents from Wastewater Treatment Streams: A Review. *Science of The Total Environment* **2022**, *822*, 153555. https://doi.org/10.1016/j.scitotenv.2022.153555.

(185) Bassyouni, M.; Abdel-Aziz, M. H.; Zoromba, M. Sh.; Abdel-Hamid, S. M. S.; Drioli, E. A Review of Polymeric Nanocomposite Membranes for Water Purification. *Journal of Industrial and Engineering Chemistry* **2019**, *73*, 19–46. https://doi.org/10.1016/j.jiec.2019.01.045.

(186) Pendergast, M. M.; Hoek, E. M. V. A Review of Water Treatment Membrane Nanotechnologies. *Energy Environ. Sci.* **2011**, *4* (6), 1946–1971. https://doi.org/10.1039/C0EE00541J.

(187) Akram, S.; Naddeo, V.; Rehan, Z.; Zahid, M.; Rashid, A.; Razzaq, W. A Comprehensive Review on Polymeric Nano-Composite Membranes for Water Treatment. *Journal of Membrane Science & Technology* **2018**, *08*. https://doi.org/10.4172/2155-9589.1000179.

(188) Elrasheedy, A.; Nady, N.; Bassyouni, M.; El-Shazly, A. Metal Organic Framework Based Polymer Mixed Matrix Membranes: Review on Applications in Water Purification. *Membranes* **2019**, *9* (7), 88. https://doi.org/10.3390/membranes9070088.

(189) Hibino, T. Facile Synthesis of Layered Double Hydroxide/Superabsorbent Polymer Composites for Water and Wastewater Treatment. *Applied Clay Science* **2021**, *211*, 106188. https://doi.org/10.1016/j.clay.2021.106188.

(190) Rasheed, T. Magnetic Nanomaterials: Greener and Sustainable Alternatives for the Adsorption of Hazardous Environmental Contaminants. *Journal of Cleaner Production* **2022**, *362*, 132338. https://doi.org/10.1016/j.jclepro.2022.132338.

(191) Sharma, R.; Arizaga, G. G. C.; Saini, A. K.; Shandilya, P. Layered Double Hydroxide as Multifunctional Materials for Environmental Remediation: From Chemical Pollutants to Microorganisms. *Sustainable Materials and Technologies* **2021**, *29*, e00319. https://doi.org/10.1016/j.susmat.2021.e00319.

(192) Shanker, U.; Rani, M. *Liquid and Crystal Nanomaterials for Water Pollutants Remediation*; CRC Press, 2022.

(193) Li, N.; Hou, J.; Ou, R.; Yeo, L.; Choudhury, N. R.; Zhang, H. Stimuli-Responsive Ion Adsorbents for Sustainable Separation Applications. *ACS Nano* **2023**, *17* (18), 17699–17720. https://doi.org/10.1021/acsnano.3c04942.

(194) Abdeen, Z. U.; Saeed, R. Kinetics and Mechanism of pH Responsive Cationic Desorption from Poly(Vinyl Alcohol)-Borate Hydrogel. *Polym. Sci. Ser. A* **2016**, *58* (5), 689–696. https://doi.org/10.1134/S0965545X16050011.

(195) Kuroiwa, T.; Takada, H.; Shogen, A.; Saito, K.; Kobayashi, I.; Uemura, K.; Kanazawa, A. Cross-Linkable Chitosan-Based Hydrogel Microbeads with pH-Responsive Adsorption Properties for Organic Dyes Prepared Using Size-Tunable Microchannel Emulsification Technique. *Colloids and Surfaces A: Physicochemical and Engineering Aspects* **2017**, *514*, 69–78. https://doi.org/10.1016/j.colsurfa.2016.11.046.

(196) Wang, W.; Hu, J.; Zhang, R.; Yan, C.; Cui, L.; Zhu, J. A pH-Responsive Carboxymethyl Cellulose/Chitosan Hydrogel for Adsorption and Desorption of Anionic and Cationic Dyes. *Cellulose* **2021**, *28* (2), 897–909. https://doi.org/10.1007/s10570-020-03561-4.

(197) Jana, S.; Ray, J.; Mondal, B.; Pradhan, S. S.; Tripathy, T. pH Responsive Adsorption/Desorption Studies of Organic Dyes from Their Aqueous Solutions by Katira Gum-Cl-Poly(Acrylic Acid-Co-N-Vinyl Imidazole) Hydrogel. *Colloids and Surfaces A: Physicochemical and Engineering Aspects* **2018**, *553*, 472–486. https://doi.org/10.1016/j.colsurfa.2018.06.001.

(198) Wei, R.; Song, W.; Yang, F.; Zhou, J.; Zhang, M.; Zhang, X.; Zhao, W.; Zhao, C. Bidirectionally pH-Responsive Zwitterionic Polymer Hydrogels with Switchable Selective Adsorption Capacities for Anionic and Cationic Dyes. *Ind.*

Eng. Chem. Res. **2018**, *57* (24), 8209–8219. https://doi.org/10.1021/acs.iecr.8b01027.

(199) Yao, G.; Bi, W.; Liu, H. pH-Responsive Magnetic Graphene Oxide/Poly(NVI-Co-AA) Hydrogel as an Easily Recyclable Adsorbent for Cationic and Anionic Dyes. *Colloids and Surfaces A: Physicochemical and Engineering Aspects* **2020**, *588*, 124393. https://doi.org/10.1016/j.colsurfa.2019.124393.

(200) Upadhyay, A.; Rao, C. P. Porous, pH-Responsive, and Reusable Hydrogel Beads of Bovine Serum Albumin_Au Hybrid as Smart Nanofactories for the Removal of Organic and Inorganic Pollutants from Water: A Detailed Demonstration by Spectroscopy and Microscopy. *ACS Appl. Mater. Interfaces* **2019**, *11* (8), 7965–7973. https://doi.org/10.1021/acsami.8b20027.

(201) Zanella, O.; Tessaro, I. C.; Féris, L. A. Desorption- and Decomposition-Based Techniques for the Regeneration of Activated Carbon. *Chemical Engineering & Technology* **2014**, *37* (9), 1447–1459. https://doi.org/10.1002/ceat.201300808.

(202) Kung, M. C.; Ye, J.; Kung, H. H. 110th Anniversary: A Perspective on Catalytic Oxidative Processes for Sustainable Water Remediation. *Ind. Eng. Chem. Res.* **2019**, *58* (37), 17325–17337. https://doi.org/10.1021/acs.iecr.9b04581.

(203) Lopes, J. L.; Martins, M. J.; Nogueira, H. I. S.; Estrada, A. C.; Trindade, T. Carbon-Based Heterogeneous Photocatalysts for Water Cleaning Technologies: A Review. *Environ Chem Lett* **2021**, *19* (1), 643–668. https://doi.org/10.1007/s10311-020-01092-9.

(204) Zhou, L.; Zhang, H.; Sun, H.; Liu, S.; Tade, M. O.; Wang, S.; Jin, W. Recent Advances in Non-Metal Modification of Graphitic Carbon Nitride for

Photocatalysis: A Historic Review. *Catal. Sci. Technol.* **2016**, *6* (19), 7002–7023. https://doi.org/10.1039/C6CY01195K.

(205) Salama, A.; Abouzeid, R.; Leong, W. S.; Jeevanandam, J.; Samyn, P.; Dufresne, A.; Bechelany, M.; Barhoum, A. Nanocellulose-Based Materials for Water Treatment: Adsorption, Photocatalytic Degradation, Disinfection, Antifouling, and Nanofiltration. *Nanomaterials* **2021**, *11* (11), 3008. https://doi.org/10.3390/nano11113008.

(206) Kumar, N.; Gusain, R.; Pandey, S.; Ray, S. S. Hydrogel Nanocomposite Adsorbents and Photocatalysts for Sustainable Water Purification. *Advanced Materials Interfaces* **2023**, *10* (2), 2201375. https://doi.org/10.1002/admi.202201375.

(207) Kuroda, K.; Lu, B.; Hama, Y.; Yang, Y. Recent Progress in Photocatalysts for Oxidation of As(III) and Photocatalyst-Impregnated Adsorbents for Removing Aqueous Arsenic. *Current Opinion in Environmental Science & Health* **2023**, *35*, 100498. https://doi.org/10.1016/j.coesh.2023.100498.

(208) Liao, W.; Zhao, M.; Rong, H.; Jiang, P.; Liao, Q.; Zhang, C.; Chen, Y. Photocatalyst Immobilized by Hydrogel, Efficient Degradation and Self Regeneration: A Review. *Materials Science in Semiconductor Processing* **2022**, *150*, 106929. https://doi.org/10.1016/j.mssp.2022.106929.

(209) Seida, Y.; Tokuyama, H. Hydrogel Adsorbents for the Removal of Hazardous Pollutants—Requirements and Available Functions as Adsorbent. *Gels* **2022**, *8* (4), 220. https://doi.org/10.3390/gels8040220.

(210) Joseph, A.; Vijayanandan, A. Review on Support Materials Used for Immobilization of Nano-Photocatalysts for Water Treatment Applications.

Inorganica Chimica Acta **2023**, *545*, 121284. https://doi.org/10.1016/j.ica.2022.121284.

(211) Li, J.; Boyer, C.; Zhang, X. 3D Printing Based on Photopolymerization and Photocatalysts: Review and Prospect. *Macromolecular Materials and Engineering* **2022**, *307* (8), 2200010. https://doi.org/10.1002/mame.202200010.

(212) Sawut, A.; Wu, T.; Simayi, R.; Jiao, X.; Feng, Y. Preparation and Photocatalytic Performance of Sodium Alginate/Polyacrylamide/Polypyrrole-TiO2 Nanocomposite Hydrogels. *Polymers* **2023**, *15* (20), 4174. https://doi.org/10.3390/polym15204174.

(213) Hou, X.; Mu, L.; Chen, F.; Hu, X. Emerging Investigator Series: Design of Hydrogel Nanocomposites for the Detection and Removal of Pollutants: From Nanosheets, Network Structures, and Biocompatibility to Machine-Learning-Assisted Design. *Environ. Sci.: Nano* **2018**, *5* (10), 2216–2240. https://doi.org/10.1039/C8EN00552D.

(214) Jayakumar, A.; Jose, V. K.; Lee, J.-M. Hydrogels for Medical and Environmental Applications. *Small Methods* **2020**, *4* (3). https://doi.org/10.1002/smtd.201900735.

(215) Zulkifli, S. N.; Rahim, H. A.; Lau, W.-J. Detection of Contaminants in Water Supply: A Review on State-of-the-Art Monitoring Technologies and Their Applications. *Sensors and Actuators B: Chemical* **2018**, *255*, 2657–2689. https://doi.org/10.1016/j.snb.2017.09.078.

(216) Aragay, G.; Pons, J.; Merkoçi, A. Recent Trends in Macro-, Micro-, and Nanomaterial-Based Tools and Strategies for Heavy-Metal Detection. *Chem. Rev.* **2011**, *111* (5), 3433–3458. https://doi.org/10.1021/cr100383r.

(217) Rasheed, T.; Bilal, M.; Nabeel, F.; Iqbal, H. M. N.; Li, C.; Zhou, Y. Fluorescent Sensor Based Models for the Detection of Environmentally-Related Toxic Heavy Metals. *Science of The Total Environment* **2018**, *615*, 476–485. https://doi.org/10.1016/j.scitotenv.2017.09.126.

(218) Korent Urek, Š.; Frančič, N.; Turel, M.; Lobnik, A. Sensing Heavy Metals Using Mesoporous-Based Optical Chemical Sensors. *Journal of Nanomaterials* **2013**, *2013*, e501320. https://doi.org/10.1155/2013/501320.

(219) Terra, I. A. A.; Mercante, L. A.; Andre, R. S.; Correa, D. S. Fluorescent and Colorimetric Electrospun Nanofibers for Heavy-Metal Sensing. *Biosensors* **2017**, *7* (4), 61. https://doi.org/10.3390/bios7040061.

(220) Sethi, S.; Medha; Singh, G.; Sharma, R.; Kaith, B. S.; Sharma, N.; Khullar, S. Fluorescent Hydrogel of Chitosan and Gelatin Cross-Linked with Maleic Acid for Optical Detection of Heavy Metals. *Journal of Applied Polymer Science* **2022**, *139* (15), 51941. https://doi.org/10.1002/app.51941.

(221) Zhang, D.; Zhang, Y.; Lu, W.; Le, X.; Li, P.; Huang, L.; Zhang, J.; Yang, J.; Serpe, M. J.; Chen, D.; Chen, T. Fluorescent Hydrogel-Coated Paper/Textile as Flexible Chemosensor for Visual and Wearable Mercury(II) Detection. *Advanced Materials Technologies* **2019**, *4* (1), 1800201. https://doi.org/10.1002/admt.201800201.

(222) Chen, B.-Y.; Kuo, C.-C.; Cho, C.-J.; Liang, F.-C.; Jeng, R.-J. Novel Fluorescent Chemosensory Filter Membranes Composed of Electrospun Nanofibers with Ultra-Selective and Reversible pH and Hg2+ Sensing Characteristics. *Dyes and Pigments* **2017**, *143*, 129–142. https://doi.org/10.1016/j.dyepig.2017.04.023.

(223) Chen, B.-Y.; Lung, Y.-C.; Kuo, C.-C.; Liang, F.-C.; Tsai, T.-L.; Jiang, D.-H.; Satoh, T.; Jeng, R.-J. Novel Multifunctional Luminescent Electrospun Fluorescent Nanofiber Chemosensor-Filters and Their Versatile Sensing of pH, Temperature, and Metal Ions. *Polymers* **2018**, *10* (11), 1259. https://doi.org/10.3390/polym10111259.

(224) Feng, H.; Qian, Z. Functional Carbon Quantum Dots: A Versatile Platform for Chemosensing and Biosensing. *The Chemical Record* **2018**, *18* (5), 491–505. https://doi.org/10.1002/tcr.201700055.

(225) Pourreza, N.; Ghomi, M. In Situ Synthesized and Embedded Silver Nanoclusters into Poly Vinyl Alcohol-Borax Hydrogel as a Novel Dual Mode "on and off" Fluorescence Sensor for Fe (III) and Thiosulfate. *Talanta* **2018**, *179*, 92–99. https://doi.org/10.1016/j.talanta.2017.10.035.

(226) Senthamizhan, A.; Celebioglu, A.; Uyar, T. Flexible and Highly Stable Electrospun Nanofibrous Membrane Incorporating Gold Nanoclusters as an Efficient Probe for Visual Colorimetric Detection of Hg(II). *J. Mater. Chem. A* **2014**, *2* (32), 12717–12723. https://doi.org/10.1039/C4TA02295E.

(227) Hussen, A. Review on G-C_3N_4 Based Fluorescence Chemical Sensor for Detection of Heavy Metal Ions. Rochester, NY 2021. https://papers.ssrn.com/abstract=3857063 (accessed 2023-12-20).

(228) Patel, M. R.; Kailasa, S. K. Carbon Nitride Nanomaterials: Properties, Synthetic Approaches and New Insights in Fluorescence Spectrometry for Assaying of Metal Ions, Organic and Biomolecules. *ChemistrySelect* **2022**, *7* (27), e202201849. https://doi.org/10.1002/slct.202201849.

(229) Talukdar, M.; Deb, P. Recent Progress in Research on Multifunctional Graphitic Carbon Nitride: An Emerging Wonder Material beyond Catalyst. *Carbon* **2022**, *192*, 308–331. https://doi.org/10.1016/j.carbon.2022.02.060.

(230) Wang, X.; Yang, X.; Wang, N.; Lv, J.; Wang, H.; Choi, M. M. F.; Bian, W. Graphitic Carbon Nitride Quantum Dots as an "off-on" Fluorescent Switch for Determination of Mercury(II) and Sulfide. *Microchim Acta* **2018**, *185* (10), 471. https://doi.org/10.1007/s00604-018-2994-0.

(231) Huang, Z.; Yan, F.-W.; Yuan, G. A Fluorescent Carbon Nitride Nanofibrous Hydrogel for Selective Sensing of Cu 2+. *RSC Advances* **2017**, *7* (3), 1318–1325. https://doi.org/10.1039/C6RA26136A.

(232) Saleh, T. A.; Rachman, I. B.; Ali, S. A. Tailoring Hydrophobic Branch in Polyzwitterionic Resin for Simultaneous Capturing of Hg(II) and Methylene Blue with Response Surface Optimization. *Sci Rep* **2017**, *7* (1), 4573. https://doi.org/10.1038/s41598-017-04624-6.

(233) Qin, X.; Bai, L.; Tan, Y.; Li, L.; Song, F.; Wang, Y. β-Cyclodextrin-Crosslinked Polymeric Adsorbent for Simultaneous Removal and Stepwise Recovery of Organic Dyes and Heavy Metal Ions: Fabrication, Performance and Mechanisms. *Chemical Engineering Journal* **2019**, *372*, 1007–1018. https://doi.org/10.1016/j.cej.2019.05.006.

(234) Bagbi, Y.; Pandey, A.; Solanki, P. R. Chapter 10 - Electrospun Nanofibrous Filtration Membranes for Heavy Metals and Dye Removal. In *Nanoscale Materials in Water Purification*; Thomas, S., Pasquini, D., Leu, S.-Y., Gopakumar, D. A., Eds.; Micro and Nano Technologies; Elsevier, 2019; pp 275–288. https://doi.org/10.1016/B978-0-12-813926-4.00015-X.

(235) Yan, J.; Li, K. A Magnetically Recyclable Polyampholyte Hydrogel Adsorbent Functionalized with β-Cyclodextrin and Graphene Oxide for Cationic/Anionic Dyes and Heavy Metal Ion Wastewater Remediation. *Separation and Purification Technology* **2021**, *277*, 119469. https://doi.org/10.1016/j.seppur.2021.119469.

(236) Zhang, M.; Zhang, Z.; Peng, Y.; Feng, L.; Li, X.; Zhao, C.; Sarfaraz, K. Novel Cationic Polymer Modified Magnetic Chitosan Beads for Efficient Adsorption of Heavy Metals and Dyes over a Wide pH Range. *International Journal of Biological Macromolecules* **2020**, *156*, 289–301. https://doi.org/10.1016/j.ijbiomac.2020.04.020.

(237) Salih, S. S.; Mohammed, H. N.; Abdullah, G. H.; Kadhom, M.; Ghosh, T. K. Simultaneous Removal of Cu(II), Cd(II), and Industrial Dye onto a Composite Chitosan Biosorbent. *J Polym Environ* **2020**, *28* (1), 354–365. https://doi.org/10.1007/s10924-019-01612-x.

(238) Qayum, A.; Wei, J.; Li, Q.; Chen, D.; Jiao, X.; Xia, Y. Efficient Decontamination of Multi-Component Wastewater by Hydrophilic Electrospun PAN/AgBr/Ag Fibrous Membrane. *Chemical Engineering Journal* **2019**, *361*, 1255–1263. https://doi.org/10.1016/j.cej.2018.12.161.

(239) Han, N.; Wang, W.; Lv, X.; Zhang, W.; Yang, C.; Wang, M.; Kou, X.; Li, W.; Dai, Y.; Zhang, X. Highly Efficient Purification of Multicomponent Wastewater by Electrospinning Kidney-Bean-Skin-like Porous H-PPAN/rGO-g-PAO@Ag+/Ag Composite Nanofibrous Membranes. *ACS Appl. Mater. Interfaces* **2019**, *11* (50), 46920–46929. https://doi.org/10.1021/acsami.9b16889.

(240) Pandey, B.; Singh, P.; Kumar, V. Photocatalytic-Sorption Processes for the Removal of Pollutants from Wastewater Using Polymer Metal Oxide Nanocomposites and Associated Environmental Risks. *Environmental*

Nanotechnology, Monitoring & Management **2021**, *16*, 100596. https://doi.org/10.1016/j.enmm.2021.100596.

(241) Nayak, S.; Prasad, S. R.; Mandal, D.; Das, P. Carbon Dot Cross-Linked Polyvinylpyrrolidone Hybrid Hydrogel for Simultaneous Dye Adsorption, Photodegradation and Bacterial Elimination from Waste Water. *Journal of Hazardous Materials* **2020**, *392*, 122287. https://doi.org/10.1016/j.jhazmat.2020.122287.

(242) Li, M.; Zhao, H.; Lu, Z.-Y. Porphyrin-Based Porous Organic Polymer, Py-POP, as a Multifunctional Platform for Efficient Selective Adsorption and Photocatalytic Degradation of Cationic Dyes. *Microporous and Mesoporous Materials* **2020**, *292*, 109774. https://doi.org/10.1016/j.micromeso.2019.109774.

(243) Shah, S. S.; Ramos, B.; Otubo, L.; Teixeira, A. C. S. C. Deep Removal and Subsequent Photodegradation of Methylene Blue Dye Using Biodegradable Superabsorbent Polymer Hydrogel Composite Incorporated with Activated Charcoal and Tio2 Nanoparticles. Rochester, NY October 24, 2023. https://doi.org/10.2139/ssrn.4612013.

(244) Das, R. S.; Kumar, A.; Wankhade, A. V.; Peshwe, D. R. ZrO2@chitosan Composite for Simultaneous Photodegradation of Three Emerging Contaminants and Antibacterial Application. *Carbohydrate Polymers* **2022**, *278*, 118940. https://doi.org/10.1016/j.carbpol.2021.118940.

(245) Yang, F.; Ding, G.; Wang, J.; Liang, Z.; Gao, B.; Dou, M.; Xu, C.; Li, S. Self-Cleaning, Antimicrobial, and Antifouling Membrane via Integrating Mesoporous Graphitic Carbon Nitride into Polyvinylidene Fluoride. *Journal of Membrane Science* **2020**, *606*, 118146. https://doi.org/10.1016/j.memsci.2020.118146.

(246) Kusworo, T. D.; Budiyono; Kumoro, A. C.; Utomo, D. P. Photocatalytic Nanohybrid Membranes for Highly Efficient Wastewater Treatment: A Comprehensive Review. *Journal of Environmental Management* **2022**, *317*, 115357. https://doi.org/10.1016/j.jenvman.2022.115357.

(247) Lv, Y.; Xi, X.; Dai, L.; Tong, S.; Chen, Z. Hydrogel as a Superwetting Surface Design Material for Oil/Water Separation: A Review. *Advanced Materials Interfaces* **2021**, *8* (7), 2002030. https://doi.org/10.1002/admi.202002030.

(248) Chen, C.; Weng, D.; Mahmood, A.; Chen, S.; Wang, J. Separation Mechanism and Construction of Surfaces with Special Wettability for Oil/Water Separation. *ACS Appl. Mater. Interfaces* **2019**, *11* (11), 11006–11027. https://doi.org/10.1021/acsami.9b01293.

(249) Jiang, X.; Yang, F.; Guo, Z. Superwetting Surfaces for Filtration Separation of High-Viscosity Raw Petroleum/Water Mixtures. *J. Mater. Chem. A* **2022**, *10* (27), 14273–14292. https://doi.org/10.1039/D2TA03444A.

(250) Tuteja, A.; Choi, W.; Ma, M.; Mabry, J. M.; Mazzella, S. A.; Rutledge, G. C.; McKinley, G. H.; Cohen, R. E. Designing Superoleophobic Surfaces. *Science* **2007**, *318* (5856), 1618–1622. https://doi.org/10.1126/science.1148326.

(251) Liu, D.; Yu, Y.; Chen, X.; Zheng, Y. Selective Separation of Oil and Water with Special Wettability Mesh Membranes. *RSC Advances* **2017**, *7* (21), 12908–12915. https://doi.org/10.1039/C7RA00237H.

(252) Li, Z.; Sang, S.; Jiang, S.; Chen, L.; Zhang, H. A Self-Detecting and Self-Cleaning Biomimetic Porous Metal-Based Hydrogel for Oil/Water Separation. *ACS Appl. Mater. Interfaces* **2022**, *14* (22), 26057–26067. https://doi.org/10.1021/acsami.2c05327.

(253) Song, J.; Huang, S.; Lu, Y.; Bu, X.; Mates, J. E.; Ghosh, A.; Ganguly, R.; Carmalt, C. J.; Parkin, I. P.; Xu, W.; Megaridis, C. M. Self-Driven One-Step Oil Removal from Oil Spill on Water via Selective-Wettability Steel Mesh. *ACS Appl. Mater. Interfaces* **2014**, *6* (22), 19858–19865. https://doi.org/10.1021/am505254j.

(254) Singh, A.; Singh, N.; Kaur, N.; Jang, D. O. Chitosan–Poly(Vinyl Alcohol)–Ionic Liquid-Grafted Hydrogel for Treating Wastewater. *New J. Chem.* **2023**, *47* (23), 11196–11209. https://doi.org/10.1039/D3NJ01384G.

(255) Mudiyanselage, T. K.; Neckers, D. C. Highly Absorbing Superabsorbent Polymer. *Journal of Polymer Science Part A: Polymer Chemistry* **2008**, *46* (4), 1357–1364. https://doi.org/10.1002/pola.22476.

(256) Zhang, J.; Qu, W.; Li, X.; Wang, Z. Surface Engineering of Filter Membranes with Hydrogels for Oil-in-Water Emulsion Separation. *Separation and Purification Technology* **2023**, *304*, 122340. https://doi.org/10.1016/j.seppur.2022.122340.

(257) Xiang, B.; Sun, Q.; Zhong, Q.; Mu, P.; Li, J. Current Research Situation and Future Prospect of Superwetting Smart Oil/Water Separation Materials. *J. Mater. Chem. A* **2022**, *10* (38), 20190–20217. https://doi.org/10.1039/D2TA04469B.

(258) Wang, Y.; Feng, Y.; Zhang, M.; Huang, C.; Yao, J. A Green Strategy for Preparing Durable Underwater Superoleophobic Calcium Alginate Hydrogel Coated-Meshes for Oil/Water Separation. *International Journal of Biological Macromolecules* **2019**, *136*, 13–19. https://doi.org/10.1016/j.ijbiomac.2019.06.039.

(259) Vásquez, L.; Dziza, K.; Loo, S.-L.; Binas, V.; Stefa, S.; Kiriakidis, G.; Athanassiou, A.; Fragouli, D. Highly Performant Nanocomposite Cryogels for

Multicomponent Oily Wastewater Filtration. *Separation and Purification Technology* **2022**, *303*, 122252. https://doi.org/10.1016/j.seppur.2022.122252.

(260) Liu, H.; Yu, H.; Yuan, X.; Ding, W.; Li, Y.; Wang, J. Amino-Functionalized Mesoporous PVA/SiO2 Hybrids Coated Membrane for Simultaneous Removal of Oils and Water-Soluble Contaminants from Emulsion. *Chemical Engineering Journal* **2019**, *374*, 1394–1402. https://doi.org/10.1016/j.cej.2019.05.161.

(261) Wang, Y.; He, Y.; Yan, S.; Yin, X.; Chen, J. Development of Alginate Hydrogel Modified Multifunctional Filtration Membrane with Robust Anti-Fouling Property for Efficient Water Purification. *Colloids and Surfaces A: Physicochemical and Engineering Aspects* **2019**, *582*, 123891. https://doi.org/10.1016/j.colsurfa.2019.123891.

(262) He, S.; Zhan, Y.; Hu, J.; Zhang, G.; Zhao, S.; Feng, Q.; Yang, W. Chemically Stable Two-Dimensional MXene@UIO-66-(COOH)2 Composite Lamellar Membrane for Multi-Component Pollutant-Oil-Water Emulsion Separation. *Composites Part B: Engineering* **2020**, *197*, 108188. https://doi.org/10.1016/j.compositesb.2020.108188.

(263) Zhan, Y.; Zhang, G.; Feng, Q.; Yang, W.; Hu, J.; Wen, X.; Liu, Y.; Zhang, S.; Sun, A. Fabrication of Durable Super-Hydrophilic/Underwater Super-Oleophobic Poly(Arylene Ether Nitrile) Composite Membrane via Biomimetic Co-Deposition for Multi-Component Oily Wastewater Separation in Harsh Environments. *Colloids and Surfaces A: Physicochemical and Engineering Aspects* **2021**, *624*, 126754. https://doi.org/10.1016/j.colsurfa.2021.126754.

(264) Ma, W.; Li, Y.; Gao, S.; Cui, J.; Qu, Q.; Wang, Y.; Huang, C.; Fu, G. Self-Healing and Superwettable Nanofibrous Membranes with Excellent Stability

toward Multifunctional Applications in Water Purification. *ACS Appl. Mater. Interfaces* **2020**, *12* (20), 23644–23654. https://doi.org/10.1021/acsami.0c05701.

(265) Ma, W.; Cao, W.; Lu, T.; Xiong, R.; Huang, C. Multifunctional Nanofibrous Membrane Fabrication by a Sacrifice Template Strategy for Efficient Emulsion Oily Wastewater Separation and Water Purification. *Journal of Environmental Chemical Engineering* **2022**, *10* (6), 108908. https://doi.org/10.1016/j.jece.2022.108908.

(266) Jiang, X.; An, Y.; Huang, Y.; Ding, W.; Sun, M.; Li, H.; Zheng, H. One Pot Synthesis of Cu–Ni–S@Ni Foam for the Simultaneous Removal and Detection of Norfloxacin. *Journal of Cleaner Production* **2023**, *382*, 135385. https://doi.org/10.1016/j.jclepro.2022.135385.

(267) Zhi, L.; Zuo, W.; Chen, F.; Wang, B. 3D MoS2 Composition Aerogels as Chemosensors and Adsorbents for Colorimetric Detection and High-Capacity Adsorption of Hg2+. *ACS Sustainable Chem. Eng.* **2016**, *4* (6), 3398–3408. https://doi.org/10.1021/acssuschemeng.6b00409.

(268) Dhakshinamoorthy, A.; López-Francés, A.; Navalon, S.; Garcia, H. Graphitic Carbon Nitride as Visible-Light Photocatalyst Boosting Ozonation in Wastewater Treatment. *Nanomaterials* **2022**, *12* (19), 3494. https://doi.org/10.3390/nano12193494.

(269) Rono, N.; Kibet, J. K.; Martincigh, B. S.; Nyamori, V. O. A Review of the Current Status of Graphitic Carbon Nitride. *Critical Reviews in Solid State and Materials Sciences* **2021**, *46* (3), 189–217. https://doi.org/10.1080/10408436.2019.1709414.

(270) Fronczak, M. Adsorption Performance of Graphitic Carbon Nitride-Based Materials: Current State of the Art. *Journal of Environmental Chemical Engineering* **2020**, *8* (5), 104411. https://doi.org/10.1016/j.jece.2020.104411.

(271) Liao, G.; He, F.; Li, Q.; Zhong, L.; Zhao, R.; Che, H.; Gao, H.; Fang, B. Emerging Graphitic Carbon Nitride-Based Materials for Biomedical Applications. *Progress in Materials Science* **2020**, *112*, 100666. https://doi.org/10.1016/j.pmatsci.2020.100666.

(272) Zhu, J.; Xiao, P.; Li, H.; Carabineiro, S. A. C. Graphitic Carbon Nitride: Synthesis, Properties, and Applications in Catalysis. *ACS Appl. Mater. Interfaces* **2014**, *6* (19), 16449–16465. https://doi.org/10.1021/am502925j.

(273) Sun, Y.; Ha, W.; Chen, J.; Qi, H.; Shi, Y. Advances and Applications of Graphitic Carbon Nitride as Sorbent in Analytical Chemistry for Sample Pretreatment: A Review. *TrAC Trends in Analytical Chemistry* **2016**, *84*, 12–21. https://doi.org/10.1016/j.trac.2016.03.002.

(274) Xiao, G.; Wang, Y.; Xu, S.; Li, P.; Yang, C.; Jin, Y.; Sun, Q.; Su, H. Superior Adsorption Performance of Graphitic Carbon Nitride Nanosheets for Both Cationic and Anionic Heavy Metals from Wastewater. *Chinese Journal of Chemical Engineering* **2019**, *27* (2), 305–313. https://doi.org/10.1016/j.cjche.2018.09.028.

(275) Cai, X.; He, J.; Chen, L.; Chen, K.; Li, Y.; Zhang, K.; Jin, Z.; Liu, J.; Wang, C.; Wang, X.; Kong, L.; Liu, J. A. A 2D-g-C3N4 Nanosheet as an Eco-Friendly Adsorbent for Various Environmental Pollutants in Water. *Chemosphere* **2017**, *171*, 192–201. https://doi.org/10.1016/j.chemosphere.2016.12.073.

(276) Daikopoulos, C.; Georgiou, Y.; Bourlinos, A. B.; Baikousi, M.; Karakassides, M. A.; Zboril, R.; Steriotis, T. A.; Deligiannakis, Y. Arsenite Remediation by an

Amine-Rich Graphitic Carbon Nitride Synthesized by a Novel Low-Temperature Method. *Chemical Engineering Journal* **2014**, *256*, 347–355. https://doi.org/10.1016/j.cej.2014.06.045.

(277) Ahmad, T.; Khan, S.; Rasheed, T.; Ullah, N. Graphitic Carbon Nitride Nanosheets as Promising Candidates for the Detection of Hazardous Contaminants of Environmental and Biological Concern in Aqueous Matrices. *Microchim Acta* **2022**, *189* (11), 426. https://doi.org/10.1007/s00604-022-05516-x.

(278) Tian, J.; Liu, Q.; Asiri, A. M.; Al-Youbi, A. O.; Sun, X. Ultrathin Graphitic Carbon Nitride Nanosheet: A Highly Efficient Fluorosensor for Rapid, Ultrasensitive Detection of Cu^{2+}. *Anal. Chem.* **2013**, *85* (11), 5595–5599. https://doi.org/10.1021/ac400924j.

(279) Rong, M.; Lin, L.; Song, X.; Wang, Y.; Zhong, Y.; Yan, J.; Feng, Y.; Zeng, X.; Chen, X. Fluorescence Sensing of Chromium (VI) and Ascorbic Acid Using Graphitic Carbon Nitride Nanosheets as a Fluorescent "Switch." *Biosensors and Bioelectronics* **2015**, *68*, 210–217. https://doi.org/10.1016/j.bios.2014.12.024.

(280) Li, M.; Wang, B.; An, X.; Li, Z.; Zhu, H.; Mao, B.; Calatayud, D. G.; James, T. D. A Practical Graphitic Carbon Nitride (g-C3N4) Based Fluorescence Sensor for the Competitive Detection of Trithiocyanuric Acid and Mercury Ions. *Dyes and Pigments* **2019**, *170*, 107476. https://doi.org/10.1016/j.dyepig.2019.04.021.

(281) Bian, W.; Zhang, H.; Yu, Q.; Shi, M.; Shuang, S.; Cai, Z.; Choi, M. M. F. Detection of Ag+ Using Graphite Carbon Nitride Nanosheets Based on Fluorescence Quenching. *Spectrochimica Acta Part A: Molecular and Biomolecular Spectroscopy* **2016**, *169*, 122–127. https://doi.org/10.1016/j.saa.2016.06.024.

(282) Dam, B.; Das, B.; K. Patel, B. Graphitic Carbon Nitride Materials in Dual Metallo-Photocatalysis: A Promising Concept in Organic Synthesis. *Green Chemistry* **2023**, *25* (9), 3374–3397. https://doi.org/10.1039/D3GC00669G.

(283) Liang, Q.; Li, Z.; Huang, Z.-H.; Kang, F.; Yang, Q.-H. Holey Graphitic Carbon Nitride Nanosheets with Carbon Vacancies for Highly Improved Photocatalytic Hydrogen Production. *Advanced Functional Materials* **2015**, *25* (44), 6885–6892. https://doi.org/10.1002/adfm.201503221.

(284) Dong, S.; Cai, W.; Sheng, L.; Wang, W.; Liu, H.; Xia, J. Aggregation Behavior of Graphitic C3N4 Nanosheets in Aqueous Environment: Kinetics and Mechanisms. *Environmental Pollution* **2020**, *263*, 114646. https://doi.org/10.1016/j.envpol.2020.114646.

(285) Lan, H.; Zhang, S.; Zhang, J.; Cui, Y.; Tang, Q.; An, X.; Liu, H.; Qu, J. Water-Soluble Carbon Nitride as Phase-Convertible Adsorbents for Removing Heavy Metals from Water. *Applied Surface Science* **2023**, *614*, 156172. https://doi.org/10.1016/j.apsusc.2022.156172.

(286) Ma, T. Y.; Tang, Y.; Dai, S.; Qiao, S. Z. Proton-Functionalized Two-Dimensional Graphitic Carbon Nitride Nanosheet: An Excellent Metal-/Label-Free Biosensing Platform. *Small* **2014**, *10* (12), 2382–2389. https://doi.org/10.1002/smll.201303827.

(287) Cao, Q.; Kumru, B.; Antonietti, M.; Schmidt, B. V. K. J. Graphitic Carbon Nitride and Polymers: A Mutual Combination for Advanced Properties. *Mater. Horiz.* **2020**, *7* (3), 762–786. https://doi.org/10.1039/C9MH01497G.

(288) Li, M.; Liao, H.; Deng, Q.; Wu, Y.; Xiao, F.; Wei, X.; Tu, D. Preparation of an Intelligent Hydrogel Sensor Based on G-C_3N_4 Nanosheets for Selective

Detection of Ag^{+}. *Journal of Macromolecular Science, Part A* **2018**, *55* (5), 408–413. https://doi.org/10.1080/10601325.2018.1453260.

(289) Song, P.; Wang, M.; Di, J.; Xiong, J.; Zhao, S.; Li, Z. Reusable Graphitic Carbon Nitride Nanosheet-Based Aerogels as Sorbents for Oils and Organic Solvents. *ACS Appl. Nano Mater.* **2020**, *3* (8), 8176–8181. https://doi.org/10.1021/acsanm.0c01592.

(290) Baig, U.; Faizan, M.; Sajid, M. Semiconducting Graphitic Carbon Nitride Integrated Membranes for Sustainable Production of Clean Water: A Review. *Chemosphere* **2021**, *282*, 130898. https://doi.org/10.1016/j.chemosphere.2021.130898.

(291) Ye, W.; Liu, H.; Lin, F.; Lin, J.; Zhao, S.; Yang, S.; Hou, J.; Zhou, S.; Bruggen, B. V. der. High-Flux Nanofiltration Membranes Tailored by Bio-Inspired Co-Deposition of Hydrophilic g-C3N4 Nanosheets for Enhanced Selectivity towards Organics and Salts. *Environ. Sci.: Nano* **2019**, *6* (10), 2958–2967. https://doi.org/10.1039/C9EN00692C.

(292) Baig, U.; Waheed, A.; Aljundi, I. H.; AbuMousa, R. A. Facile Fabrication of Graphitic Carbon Nitride Nanosheets and Its Integrated Polyamide Hyper-Cross-Linked TFC Nanofiltration Membrane with Intrinsic Molecular Porosity for Salts and Organic Pollutant Rejection from Water. *Journal of Materials Research and Technology* **2021**, *15*, 6319–6328. https://doi.org/10.1016/j.jmrt.2021.11.027.

(293) Bu, X.; Lu, Y.; Chen, S.; Li, D.; Zhang, Z.; Qian, P. Fabrication of Porous Carbon Nitride Foams/Acrylic Resin Composites for Efficient Oil and Organic Solvents Capture. *Chemical Engineering Journal* **2019**, *355*, 299–308. https://doi.org/10.1016/j.cej.2018.08.088.

(294) Hao, Q.; Chen, T.; Wang, R.; Feng, J.; Chen, D.; Yao, W. A Separation-Free Polyacrylamide/Bentonite/Graphitic Carbon Nitride Hydrogel with Excellent Performance in Water Treatment. *Journal of Cleaner Production* **2018**, *197*, 1222–1230. https://doi.org/10.1016/j.jclepro.2018.06.289.

(295) Olad, A.; Nouri, N.; Eslamzadeh, M. Polymer/Zeolite Nano-Composite Hydrogels as Promising Water Reservoir Materials: Effect of Clinoptilolite Content on Physicochemical Properties. *SN Appl. Sci.* **2019**, *1* (8), 868. https://doi.org/10.1007/s42452-019-0893-6.

(296) Wu, Z.; Zhang, P.; Zhang, H.; Li, X.; He, Y.; Qin, P.; Yang, C. Tough Porous Nanocomposite Hydrogel for Water Treatment. *Journal of Hazardous Materials* **2022**, *421*, 126754. https://doi.org/10.1016/j.jhazmat.2021.126754.

(297) Rogers, Z. J.; Bencherif, S. A. Cryogelation and Cryogels. *Gels* **2019**, *5* (4), 46. https://doi.org/10.3390/gels5040046.

(298) Haleem, A.; Pan, J.-M.; Shah, A.; Hussain, H.; He, W. A Systematic Review on New Advancement and Assessment of Emerging Polymeric Cryogels for Environmental Sustainability and Energy Production. *Separation and Purification Technology* **2023**, *316*, 123678. https://doi.org/10.1016/j.seppur.2023.123678.

(299) Loo, S.-L.; Krantz, W. B.; Lim, T.-T.; Fane, A. G.; Hu, X. Design and Synthesis of Ice-Templated PSA Cryogels for Water Purification: Towards Tailored Morphology and Properties. *Soft Matter* **2012**, *9* (1), 224–234. https://doi.org/10.1039/C2SM26859K.

(300) Lozinsky, V. I. Polymeric Cryogels as a New Family of Macroporous and Supermacroporous Materials for Biotechnological Purposes. *Russ Chem Bull* **2008**, *57* (5), 1015–1032. https://doi.org/10.1007/s11172-008-0131-7.

(301) Lozinsky, V. I. Cryogels on the Basis of Natural and Synthetic Polymers: Preparation, Properties and Application. *Russ. Chem. Rev.* **2002**, *71* (6), 489–511. https://doi.org/10.1070/RC2002v071n06ABEH000720.

(302) Lozinsky, V. I.; Galaev, I. Yu.; Plieva, F. M.; Savina, I. N.; Jungvid, H.; Mattiasson, B. Polymeric Cryogels as Promising Materials of Biotechnological Interest. *Trends in Biotechnology* **2003**, *21* (10), 445–451. https://doi.org/10.1016/j.tibtech.2003.08.002.

(303) Savina, I. N.; Ingavle, G. C.; Cundy, A. B.; Mikhalovsky, S. V. A Simple Method for the Production of Large Volume 3D Macroporous Hydrogels for Advanced Biotechnological, Medical and Environmental Applications. *Scientific Reports* **2016**, *6* (February), 1–9. https://doi.org/10.1038/srep21154.

(304) Carvalho, B. M. A.; Da Silva, S. L.; Da Silva, L. H. M.; Minim, V. P. R.; Da Silva, M. C. H.; Carvalho, L. M.; Minim, L. A. Cryogel Poly(Acrylamide): Synthesis, Structure and Applications. *Separation and Purification Reviews* **2014**, *43* (3), 241–262. https://doi.org/10.1080/15422119.2013.795902.

(305) Wolfe, J.; Bryant, G.; Koster, K. L. What Is "Unfreezable Water", How Unfreezable Is It, and How Much Is There? *Cryo Letters* **2002**, *23* (3), 157–166.

(306) Yao, K.; Yun, J.; Shen, S.; Wang, L.; He, X.; Yu, X. Characterization of a Novel Continuous Supermacroporous Monolithic Cryogel Embedded with Nanoparticles for Protein Chromatography. *Journal of Chromatography A* **2006**, *1109* (1), 103–110. https://doi.org/10.1016/j.chroma.2006.01.014.

(307) Loo, S. L.; Krantz, W. B.; Fane, A. G.; Hu, X.; Lim, T. T. Effect of Synthesis Routes on the Properties and Bactericidal Activity of Cryogels Incorporated with Silver Nanoparticles. *RSC Advances* **2015**, *5* (55), 44626–44635. https://doi.org/10.1039/c5ra08449k.

(308) Petrov, P.; Petrova, E.; Tsvetanov, C. B. UV-Assisted Synthesis of Super-Macroporous Polymer Hydrogels. *Polymer* **2009**, *50* (5), 1118–1123.

(309) Plieva, F. M.; Karlsson, M.; Aguilar, M.-R.; Gomez, D.; Mikhalovsky, S.; Galaev', I. Y. Pore Structure in Supermacroporous Polyacrylamide Based Cryogels. *Soft Matter* **2005**, *1* (4), 303–309. https://doi.org/10.1039/B510010K.

(310) Okay, O. Macroporous Copolymer Networks. *Progress in Polymer Science* **2000**, *25* (6), 711–779. https://doi.org/10.1016/S0079-6700(00)00015-0.

(311) Baigorri, R.; García-Mina, J. M.; González-Gaitano, G. Supramolecular Association Induced by Fe(III) in Low Molecular Weight Sodium Polyacrylate. *Colloids and Surfaces A: Physicochemical and Engineering Aspects* **2007**, *292* (2), 212–216. https://doi.org/10.1016/j.colsurfa.2006.06.027.

(312) Chen, Z.; Yu, C.; Dong, H.; Cai, X.; Liao, R.; Zeng, Z.; Ye, C. Sorption–Desorption Characteristics and Internal Mechanism of Lead Ions on Polycarboxylic Ion Exchange Resin. *J Polym Res* **2022**, *29* (12), 512. https://doi.org/10.1007/s10965-022-03360-4.

(313) Hirashima, Y.; Sato, H.; Suzuki, A. Atr-Ftir Spectroscopic Study on Hydrogen Bonding of Poly(n-Isopropylacrylamide-Co-Sodium Acrylate) Gel. *Macromolecules* **2005**, *38* (22), 9280–9286. https://doi.org/10.1021/ma051081s.

(314) Godwin Uranta, K.; Rezaei-Gomari, S.; Russell, P.; Hamad, F. Studying the Effectiveness of Polyacrylamide (PAM) Application in Hydrocarbon Reservoirs at Different Operational Conditions. *Energies* **2018**, *11* (9), 2201. https://doi.org/10.3390/en11092201.

(315) Socrates, G. *Infrared and Raman Characteristic Group Frequencies: Tables and Charts*; John Wiley & Sons, 2004.

(316) Qin, S.; Xiong, Y.; Li, J.; Wan, H.; Fang, S.; Duan, M.; Li, R.; Liao, D. Real-Time Adsorption and Photodegradation Investigation of Dye Removal on g-C3N4 Surface by Attenuated Total Reflectance Induced Evanescent Spectroscopy. *J. Phys. Chem. C* **2021**, *125* (7), 4027–4040. https://doi.org/10.1021/acs.jpcc.0c11482.

(317) Yan, H.; Yang, H. TiO2–g-C3N4 Composite Materials for Photocatalytic H2 Evolution under Visible Light Irradiation. *Journal of Alloys and Compounds* **2011**, *509* (4), L26–L29. https://doi.org/10.1016/j.jallcom.2010.09.201.

(318) Nayak, S.; Mohapatra, L.; Parida, K. Visible Light-Driven Novel g-C3N4/NiFe-LDH Composite Photocatalyst with Enhanced Photocatalytic Activity towards Water Oxidation and Reduction Reaction. *J. Mater. Chem. A* **2015**, *3* (36), 18622–18635. https://doi.org/10.1039/C5TA05002B.

(319) Hatamie, A.; Marahel, F.; Sharifat, A. Green Synthesis of Graphitic Carbon Nitride Nanosheet (g-C3N4) and Using It as a Label-Free Fluorosensor for Detection of Metronidazole via Quenching of the Fluorescence. *Talanta* **2018**, *176*, 518–525. https://doi.org/10.1016/j.talanta.2017.08.059.

(320) Wang, Y.; Liu, L.; Xue, J.; Hou, J.; Ding, L.; Wang, H. Enhanced Water Flux through Graphitic Carbon Nitride Nanosheets Membrane by Incorporating Polyacrylic Acid. *AIChE Journal* **2018**, *64* (6), 2181–2188. https://doi.org/10.1002/aic.16076.

(321) Carvalho, B. M. A.; Da Silva, S. L.; Da Silva, L. H. M.; Minim, V. P. R.; Da Silva, M. C. H.; Carvalho, L. M.; Minim, L. A. Cryogel Poly(Acrylamide): Synthesis, Structure and Applications. *Separation & Purification Reviews* **2014**, *43* (3), 241–262. https://doi.org/10.1080/15422119.2013.795902.

(322) Yao, K.; Yun, J.; Shen, S.; Wang, L.; He, X.; Yu, X. Characterization of a Novel Continuous Supermacroporous Monolithic Cryogel Embedded with Nanoparticles for Protein Chromatography. *Journal of Chromatography A* **2006**, *1109* (1), 103–110. https://doi.org/10.1016/j.chroma.2006.01.014.

(323) Xie, X.; Liu, L.; Zhang, L.; Lu, A. Strong Cellulose Hydrogel as Underwater Superoleophobic Coating for Efficient Oil/Water Separation. *Carbohydrate Polymers* **2020**, *229*, 115467. https://doi.org/10.1016/j.carbpol.2019.115467.

(324) Xue, Z.; Wang, S.; Lin, L.; Chen, L.; Liu, M.; Feng, L.; Jiang, L. A Novel Superhydrophilic and Underwater Superoleophobic Hydrogel-Coated Mesh for Oil/Water Separation. *Advanced Materials* **2011**, *23* (37), 4270–4273. https://doi.org/10.1002/adma.201102616.

(325) Zhang, W.; Cao, Y.; Liu, N.; Chen, Y.; Feng, L. A Novel Solution-Controlled Hydrogel Coated Mesh for Oil/Water Separation Based on Monolayer Electrostatic Self-Assembly. *RSC Adv.* **2014**, *4* (93), 51404–51410. https://doi.org/10.1039/C4RA09140J.

(326) Yousaf, Z.; Smith, M.; Potluri, P.; Parnell, W. Compression Properties of Polymeric Syntactic Foam Composites under Cyclic Loading. *Composites Part B: Engineering* **2020**, *186*, 107764. https://doi.org/10.1016/j.compositesb.2020.107764.

(327) S, L. Zur Theorie Der Sogenannten Adsorption Geloster Stoffe. *Kungliga Svenska Vetenskapsakademiens. Handlingar* **1898**, *24*, 1–39.

(328) Ho, Y. S.; McKay, G. Pseudo-Second Order Model for Sorption Processes. *Process Biochemistry* **1999**, *34* (5), 451–465. https://doi.org/10.1016/S0032-9592(98)00112-5.

(329) Azizian, S.; Eris, S. Chapter 6 - Adsorption Isotherms and Kinetics. In *Interface Science and Technology*; Ghaedi, M., Ed.; Adsorption: Fundamental Processes and Applications; Elsevier, 2021; Vol. 33, pp 445–509. https://doi.org/10.1016/B978-0-12-818805-7.00011-4.

(330) Wang, J.; Guo, X. Adsorption Isotherm Models: Classification, Physical Meaning, Application and Solving Method. *Chemosphere* **2020**, *258*, 127279. https://doi.org/10.1016/j.chemosphere.2020.127279.

(331) Tran, H. N. Comment on "Super-Adsorbent Hydrogel for Removal of Methylene Blue Dye from Aqueous Solution" by X.-S. Hu, R. Liang and G. Sun, J. Mater. Chem. A, 2018, 6, 17612–17624. *J. Mater. Chem. A* **2022**, *10* (12), 6809–6814. https://doi.org/10.1039/C9TA11420C.

(332) Fernández-Pérez, A.; Marbán, G. Visible Light Spectroscopic Analysis of Methylene Blue in Water; What Comes after Dimer? *ACS Omega* **2020**, *5* (46), 29801–29815. https://doi.org/10.1021/acsomega.0c03830.

(333) Fernández-Pérez, A.; Valdés-Solís, T.; Marbán, G. Visible Light Spectroscopic Analysis of Methylene Blue in Water; the Resonance Virtual Equilibrium Hypothesis. *Dyes and Pigments* **2019**, *161*, 448–456. https://doi.org/10.1016/j.dyepig.2018.09.083.

(334) Patil, K.; Pawar, R.; Talap, P. Self-Aggregation of Methylene Blue in Aqueous Medium and Aqueous Solutions of Bu 4 NBr and Urea. *Physical Chemistry Chemical Physics* **2000**, *2* (19), 4313–4317. https://doi.org/10.1039/B005370H.

(335) Limcharoensuk, T.; Sooksawat, N.; Sumarnrote, A.; Awutpet, T.; Kruatrachue, M.; Pokethitiyook, P.; Auesukaree, C. Bioaccumulation and Biosorption of Cd2+ and Zn2+ by Bacteria Isolated from a Zinc Mine in Thailand. *Ecotoxicology and*

Environmental Safety **2015**, *122*, 322–330. https://doi.org/10.1016/j.ecoenv.2015.08.013.

(336) Simonin, J.-P. On the Comparison of Pseudo-First Order and Pseudo-Second Order Rate Laws in the Modeling of Adsorption Kinetics. *Chemical Engineering Journal* **2016**, *300*, 254–263. https://doi.org/10.1016/j.cej.2016.04.079.

(337) Qin, S.; Xiong, Y.; Li, J.; Wan, H.; Fang, S.; Duan, M.; Li, R.; Liao, D. Real-Time Adsorption and Photodegradation Investigation of Dye Removal on g-C3N4 Surface by Attenuated Total Reflectance Induced Evanescent Spectroscopy. *J. Phys. Chem. C* **2021**, *125* (7), 4027–4040. https://doi.org/10.1021/acs.jpcc.0c11482.

(338) He, P.; Tang, X.; Chen, L.; Xie, P.; He, L.; Zhou, H.; Zhang, D.; Fan, T. Patterned Carbon Nitride–Based Hybrid Aerogel Membranes via 3D Printing for Broadband Solar Wastewater Remediation. *Advanced Functional Materials* **2018**, *28* (29), 1801121. https://doi.org/10.1002/adfm.201801121.

(339) Tang, L.; Jia, C.; Xue, Y.; Li, L.; Wang, A.; Xu, G.; Liu, N.; Wu, M. Fabrication of Compressible and Recyclable Macroscopic G-C3N4/GO Aerogel Hybrids for Visible-Light Harvesting: A Promising Strategy for Water Remediation. *Applied Catalysis B: Environmental* **2017**, *219*, 241–248. https://doi.org/10.1016/j.apcatb.2017.07.053.

(340) Mokhtar, A.; Abdelkrim, S.; Sardi, A.; Benyoub, A.; Besnaci, H.; Cherrak, R.; Hadjel, M.; Boukoussa, B. Preparation and Characterization of Anionic Composite Hydrogel for Dyes Adsorption and Filtration: Non-Linear Isotherm and Kinetics Modeling. *J Polym Environ* **2020**, *28* (6), 1710–1723. https://doi.org/10.1007/s10924-020-01719-6.

(341) Kołodyńska, D. Polyacrylate Anion Exchangers in Sorption of Heavy Metal Ions with the Biodegradable Complexing Agent. *Chemical Engineering Journal* **2009**, *150* (2), 280–288. https://doi.org/10.1016/j.cej.2008.12.027.

(342) Çavuş, S.; Gürdağ, G.; Yaşar, M.; Güçlü, K.; Gürkaynak, M. A. The Competitive Heavy Metal Removal by Hydroxyethyl Cellulose-g-Poly(Acrylic Acid) Copolymer and Its Sodium Salt: The Effect of Copper Content on the Adsorption Capacity. *Polym. Bull.* **2006**, *57* (4), 445–456. https://doi.org/10.1007/s00289-006-0583-6.

(343) Zhang, M.; Yang, P.; Lan, G.; Liu, Y.; Cai, Q.; Xi, J. High Crosslinked Sodium Carboxyl Methylstarch-g-Poly (Acrylic Acid-Co-Acrylamide) Resin for Heavy Metal Adsorption: Its Characteristics and Mechanisms. *Environ Sci Pollut Res* **2020**, *27* (31), 38617–38630. https://doi.org/10.1007/s11356-020-09945-0.

(344) Yu, Y.; Peng, R.; Yang, C.; Tang, Y. Eco-Friendly and Cost-Effective Superabsorbent Sodium Polyacrylate Composites for Environmental Remediation. *J Mater Sci* **2015**, *50* (17), 5799–5808. https://doi.org/10.1007/s10853-015-9127-5.

(345) Korus, I. Ultrafiltration Enhanced with Poly(Sodium Acrylate) as an Effective Method for Separation of Heavy Metals from Multicomponent Solutions. *DWT* **2021**, *242*, 38–46. https://doi.org/10.5004/dwt.2021.27866.

(346) Bobik, M.; Korus, I.; Synoradzki, K.; Wojnarowicz, J.; Biniaś, D.; Biniaś, W. Poly(Sodium Acrylate)-Modified Magnetite Nanoparticles for Separation of Heavy Metals from Aqueous Solutions. *Materials* **2022**, *15* (19), 6562. https://doi.org/10.3390/ma15196562.

(347) Kinniburgh, D. G. General Purpose Adsorption Isotherms. *Environ. Sci. Technol.* **1986**, *20* (9), 895–904. https://doi.org/10.1021/es00151a008.

(348) Allen, S. J.; Mckay, G.; Porter, J. F. Adsorption Isotherm Models for Basic Dye Adsorption by Peat in Single and Binary Component Systems. *Journal of Colloid and Interface Science* **2004**, *280* (2), 322–333. https://doi.org/10.1016/j.jcis.2004.08.078.

(349) Meghea, A.; Rehner, H. H.; Peleanu, I.; Mihalache, R. Test-Fitting on Adsorption Isotherms of Organic Pollutants from Waste Waters on Activated Carbon. *J Radioanal Nucl Chem* **1998**, *229* (1), 105–110. https://doi.org/10.1007/BF02389456.

(350) *Sci-Hub | Adsorption of acid dyes on chitosan—equilibrium isotherm analyses | 10.1016/s0032-9592(03)00152-3*. https://sci-hub.hkvisa.net/10.1016/s0032-9592(03)00152-3 (accessed 2023-11-28).

(351) Misak, N. Some Aspects of the Application of Adsorption Isotherms to Ion Exchange Reactions. *Reactive & Functional Polymers - REACT FUNCT POLYM* **2000**, *43*, 153–164. https://doi.org/10.1016/S1381-5148(99)00046-2.

(352) Berber-Mendoza, M. S.; Leyva-Ramos, R.; Alonso-Davila, P.; Fuentes-Rubio, L.; Guerrero-Coronado, R. M. Comparison of Isotherms for the Ion Exchange of Pb(II) from Aqueous Solution onto Homoionic Clinoptilolite. *Journal of Colloid and Interface Science* **2006**, *301* (1), 40–45. https://doi.org/10.1016/j.jcis.2006.04.037.

(353) Misak, N. Z. Langmuir Isotherm and Its Application in Ion-Exchange Reactions. *Reactive Polymers* **1993**, *21* (1), 53–64. https://doi.org/10.1016/0923-1137(93)90054-J.

(354) Sato, H.; Hirashima, Y.; Suzuki, A.; Goto, M.; Tokita, M. Effects of Repeated Water Exchange on the Swelling Behavior of Poly(Sodium Acrylate) Gels

Crosslinked by Aluminum Ions. *Journal of Polymer Science Part B: Polymer Physics* **2005**, *43* (7), 753–763. https://doi.org/10.1002/polb.20378.

(355) Wang, J.; Liu, Z.; Qu, B.; Li, Z.; Zhang, Y.; Xu, C.; Chen, Z.; Xie, Q.; Wang, M.-S.; Lu, M.; Zhao, J.; Wang, J.; Peng, D.-L.; Pan, F.; Hu, Y.-S. G-C3N4 in Situ Derived Ionic-Electronic Dual-Conducting Interlayer with N-Rich Sites for Long Lifespan Sodium Metal Anodes. *Energy Storage Materials* **2023**, *59*, 102793. https://doi.org/10.1016/j.ensm.2023.102793.

(356) Rao, X.; Dou, H.; Chen, W.; Long, D.; Zheng, S.; Chen, Z.; Abou Hassan, A.; Ruiz, E. O. M.; Zhang, Y. Embedding Sodium Ions in Graphitic Carbon Nitride Vacancies for Visible Light Photocatalytic H2 Evolution. *ACS Appl. Nano Mater.* **2020**, *3* (5), 4663–4669. https://doi.org/10.1021/acsanm.0c00667.

(357) Kurita, Y.; Aoki, M.; Ohtani, N. Fabrication of Sodium-Doped Graphitic Carbon Nitride for Photoelectrochemical Water Splitting into Hydrogen. *Jpn. J. Appl. Phys.* **2023**. https://doi.org/10.35848/1347-4065/acff00.

(358) Thomas, S. A.; Pallavolu, M. R.; Khan, M. E.; Cherusseri, J. Graphitic Carbon Nitride (g-C3N4): Futuristic Material for Rechargeable Batteries. *Journal of Energy Storage* **2023**, *68*, 107673. https://doi.org/10.1016/j.est.2023.107673.

(359) Alshehri, A. A.; Malik, M. A. Biogenic Fabrication of ZnO Nanoparticles Using Trigonella Foenum-Graecum (Fenugreek) for Proficient Photocatalytic Degradation of Methylene Blue under UV Irradiation. *J Mater Sci: Mater Electron* **2019**, *30* (17), 16156–16173. https://doi.org/10.1007/s10854-019-01985-8.

(360) Arunachalam, K. D. Bio-Adsorption of Methylene Blue Dye Using Chitosan-Extracted from Fenneropenaeus Indicus Shrimp Shell Waste. *JAMB* **2021**, *10* (4), 146–150. https://doi.org/10.15406/jamb.2021.10.00316.

(361) Ryu, S. R.; Noda, I.; Jung, Y. M. What Is the Origin of Positional Fluctuation of Spectral Features: True Frequency Shift or Relative Intensity Changes of Two Overlapped Bands? *Appl Spectrosc* **2010**, *64* (9), 1017–1021. https://doi.org/10.1366/000370210792434396.

(362) *Interpretation of Infrared Spectra, A Practical Approach - Coates - Major Reference Works - Wiley Online Library*. https://onlinelibrary.wiley.com/doi/10.1002/9780470027318.a5606 (accessed 2023-12-04).

(363) Sarma, G. K.; Sen Gupta, S.; Bhattacharyya, K. G. Removal of Hazardous Basic Dyes from Aqueous Solution by Adsorption onto Kaolinite and Acid-Treated Kaolinite: Kinetics, Isotherm and Mechanistic Study. *SN Appl. Sci.* **2019**, *1* (3), 211. https://doi.org/10.1007/s42452-019-0216-y.

(364) Işık, B.; Uğraşkan, V. Adsorption of Methylene Blue on Sodium Alginate–Flax Seed Ash Beads: Isotherm, Kinetic and Thermodynamic Studies. *International Journal of Biological Macromolecules* **2021**, *167*, 1156–1167. https://doi.org/10.1016/j.ijbiomac.2020.11.070.

(365) Yukselen, Y.; Kaya, A. Suitability of the Methylene Blue Test for Surface Area, Cation Exchange Capacity and Swell Potential Determination of Clayey Soils. *Engineering Geology* **2008**, *102* (1), 38–45. https://doi.org/10.1016/j.enggeo.2008.07.002.

(366) Raj, M. M.; Dharmaraja, A.; Kavitha, S. J.; Panchanatheswaran, K.; Lynch, D. E. Mercury(II)–Methylene Blue Interactions: Complexation and Metallate Formation. *Inorganica Chimica Acta* **2007**, *360* (6), 1799–1808. https://doi.org/10.1016/j.ica.2006.09.022.

(367) Shah, P.; Kumari Jha, S.; Bhattarai, A. Spectrophotometric Study of the Sodium Dodecyl Sulfate in the Presence of Methylene Blue in the Methanol–Water Mixed Solvent System. *Journal of Molecular Liquids* **2021**, *340*, 117200. https://doi.org/10.1016/j.molliq.2021.117200.

(368) Handa, T.; Ichihashi, C.; Yamamoto, I.; Nakagaki, M. The Location and Microenvironment of Dimerizing Cationic Dyes in Lipid Membranes as Studied by Means of Their Absorption Spectra. *BCSJ* **1983**, *56* (9), 2548–2554. https://doi.org/10.1246/bcsj.56.2548.

(369) Cheng, M.; Zeng, G.; Huang, D.; Yang, C.; Lai, C.; Zhang, C.; Liu, Y. Tween 80 Surfactant-Enhanced Bioremediation: Toward a Solution to the Soil Contamination by Hydrophobic Organic Compounds. *Critical Reviews in Biotechnology* **2018**, *38* (1), 17–30. https://doi.org/10.1080/07388551.2017.1311296.

(370) Daher, C. F.; Baroody, G. M.; Howland, R. J. Effect of a Surfactant, Tween 80, on the Formation and Secretion of Chylomicrons in the Rat. *Food and Chemical Toxicology* **2003**, *41* (4), 575–582. https://doi.org/10.1016/S0278-6915(02)00299-5.

(371) Dziza, K.; Santini, E.; Liggieri, L.; Jarek, E.; Krzan, M.; Fischer, T.; Ravera, F. Interfacial Properties and Emulsification of Biocompatible Liquid-Liquid Systems. *Coatings* **2020**, *10* (4), 397. https://doi.org/10.3390/coatings10040397.

(372) Lapčí-ková, B.; Valenta, T.; Lapčí-k, L.; Fuksová, M. Thermal Aging of Edible Oils: Spectrophotometric Study. *Potravinarstvo Slovak Journal of Food Sciences* **2018**, *12* (1), 372–378. https://doi.org/10.5219/871.

(373) Thakare, S. S.; Chakraborty, G.; More, A. B.; Chattopadhyay, S.; Mula, S.; Ray, A. K.; Sekar, N. Modulation of Optical Properties of BODIPY Fluorophore

via Intramolecular Charge Transfer. *Journal of Luminescence* **2018**, *194*, 622–630. https://doi.org/10.1016/j.jlumin.2017.09.024.

(374) Geethanjali, H. S.; Nagaraja, D.; Melavanki, R. M. Estimation of Dipole Moments and Quantum Yield of 5-Chloro-2-Methoxyphenyl Boronic Acid in Different Solvents Environment. *J Fluoresc* **2015**, *25* (3), 745–753. https://doi.org/10.1007/s10895-015-1561-x.

(375) Ghazali, S. R.; Kubulat, K.; Isa, M. I. N.; Samsudin, A. S.; Khairul, W. M. Contribution of Methyl Substituent on the Conductivity Properties and Behaviour of CMC-Alkoxy Thiourea Polymer Electrolyte. *Molecular Crystals and Liquid Crystals* **2014**, *604* (1), 126–141. https://doi.org/10.1080/15421406.2014.968058.

(376) Korus, I.; Rumińska, M. UV Spectrophotometric Studies of Cu(II) Ions Separation by Ultrafiltration Enhanced with Poly(Sodium Acrylate). *Desalination and Water Treatment* **2016**, *57* (3), 1436–1442. https://doi.org/10.1080/19443994.2014.989635.

(377) Khanlari, S.; Dubé, M. A. In Situ Poly(Sodium Acrylate)-Based Nanocomposite Formation by Redox-Initiated Solution Polymerization. *Polymer Engineering & Science* **2015**, *55* (6), 1230–1236. https://doi.org/10.1002/pen.24060.

(378) Shin, B. C.; Jhon, M. S.; Lee, H. B.; Yuk, S. H. pH/Temperature Dependent Phase Transition of an Interpenetrating Polymer Network: Anomalous Swelling Behavior above Lower Critical Solution Temperature. *European Polymer Journal* **1998**, *34* (11), 1675–1681. https://doi.org/10.1016/S0014-3057(98)00025-1.

(379) Li, X.; Zhang, J.; Shen, L.; Ma, Y.; Lei, W.; Cui, Q.; Zou, G. Preparation and Characterization of Graphitic Carbon Nitride through Pyrolysis of Melamine. *Appl. Phys. A* **2009**, *94* (2), 387–392. https://doi.org/10.1007/s00339-008-4816-4.

(380) Wang, X.; Maeda, K.; Thomas, A.; Takanabe, K.; Xin, G.; Carlsson, J. M.; Domen, K.; Antonietti, M. A Metal-Free Polymeric Photocatalyst for Hydrogen Production from Water under Visible Light. *Nature Mater* **2009**, *8* (1), 76–80. https://doi.org/10.1038/nmat2317.

(381) Shao, Z.; Liu, Q. Independent Characterization of the Elastic and the Mixing Parts of Hydrogel Osmotic Pressure. arXiv September 15, 2023. https://doi.org/10.48550/arXiv.2308.04533.

(382) Mittal, H.; Jindal, R.; Kaith, B. S.; Maity, A.; Ray, S. S. Flocculation and Adsorption Properties of Biodegradable Gum-Ghatti-Grafted Poly(Acrylamide-Co-Methacrylic Acid) Hydrogels. *Carbohydrate Polymers* **2015**, *115*, 617–628. https://doi.org/10.1016/j.carbpol.2014.09.026.

(383) Sadeghi, M.; Hosseinzadeh, H. Synthesis and Swelling Behavior of Starch-Poly (Sodium Acrylate-Co-Acrylamide) Superabsorbent Hydrogel. *Turkish Journal of Chemistry* **2008**, *32* (3), 375–388. https://doi.org/-.

(384) Zhang, M.-L.; Jin, F.; Zheng, M.-L.; Duan, X.-M. Inverse Opal Hydrogel Sensor for the Detection of pH and Mercury Ions. *RSC Adv.* **2014**, *4* (39), 20567. https://doi.org/10.1039/c4ra03013c.

(385) Lee, W.-F.; Wu, R.-J. Superabsorbent Polymeric Materials. I. Swelling Behaviors of Crosslinked Poly(Sodium Acrylate-Co-Hydroxyethyl Methacrylate) in Aqueous Salt Solution. *Journal of Applied Polymer Science* **1996**, *62* (7), 1099–1114. https://doi.org/10.1002/(SICI)1097-4628(19961114)62:7<1099::AID-APP16>3.0.CO;2-1.

(386) Wang, W. B.; Xu, J. X.; Wang, A. Q. A pH-, Salt- and Solvent-Responsive Carboxymethylcellulose-g-Poly(Sodium Acrylate)/Medical Stone Superabsorbent

Composite with Enhanced Swelling and Responsive Properties. *Express Polym. Lett.* **2011**, *5* (5), 385–400. https://doi.org/10.3144/expresspolymlett.2011.38.

(387) Sun, J.; Schmidt, B. V. K. J.; Wang, X.; Shalom, M. Self-Standing Carbon Nitride-Based Hydrogels with High Photocatalytic Activity. *ACS Applied Materials and Interfaces* **2017**, *9* (3), 2029–2034. https://doi.org/10.1021/acsami.6b14879.

(388) Jiang, J.; Zhang, Q.; Zhan, X.; Chen, F. A Multifunctional Gelatin-Based Aerogel with Superior Pollutants Adsorption, Oil/Water Separation and Photocatalytic Properties. *Chemical Engineering Journal* **2019**, *358*, 1539–1551.

(389) Ovchinnikov, O. V.; Evtukhova, A. V.; Kondratenko, T. S.; Smirnov, M. S.; Khokhlov, V. Yu.; Erina, O. V. Manifestation of Intermolecular Interactions in FTIR Spectra of Methylene Blue Molecules. *Vibrational Spectroscopy* **2016**, *86*, 181–189. https://doi.org/10.1016/j.vibspec.2016.06.016.